UNIVERSITY OF ALBERTA

RATIONAL APPROACH FOR DISSOLVED AIR FLOTATION CONTACT ZONE MODELING

by

AYMAN R. SHAWWA ©

A THESIS
SUBMITTED TO THE FACULTY OF GRADUATE STUDIES AND RESEARCH IN
PARTIAL FULFILLMENT OF THE REQUIREMENTS FOR THE DEGREE OF
DOCTOR OF PHILOSOPHY

in

ENVIRONMENTAL ENGINEERING

DEPARTMENT OF CIVIL AND ENVIRONMENTAL ENGINEERING

Edmonton, Alberta
Spring, 1998

National Library
of Canada

Acquisitions and
Bibliographic Services

395 Wellington Street
Ottawa ON K1A 0N4
Canada

Bibliothèque nationale
du Canada

Acquisitions et
services bibliographiques

395, rue Wellington
Ottawa ON K1A 0N4
Canada

Your file Votre référence

Our file Notre référence

The author has granted a non-exclusive licence allowing the National Library of Canada to reproduce, loan, distribute or sell copies of this thesis in microform, paper or electronic formats.

L'auteur a accordé une licence non exclusive permettant à la Bibliothèque nationale du Canada de reproduire, prêter, distribuer ou vendre des copies de cette thèse sous la forme de microfiche/film, de reproduction sur papier ou sur format électronique.

The author retains ownership of the copyright in this thesis. Neither the thesis nor substantial extracts from it may be printed or otherwise reproduced without the author's permission.

L'auteur conserve la propriété du droit d'auteur qui protège cette thèse. Ni la thèse ni des extraits substantiels de celle-ci ne doivent être imprimés ou autrement reproduits sans son autorisation.

0-612-29108-1

Canada

UNIVERSITY OF ALBERTA

FACULTY OF GRADUATE STUDIES AND RESEARCH

The undersigned certify that they have read, and recommended to the Faculty of Graduate Studies and Research, for acceptance, a thesis entitled: RATIONAL APPROACH FOR DISSOLVED AIR FLOTATION CONTACT ZONE MODELING submitted by: Ayman R. Shawwa in partial fulfillment of the requirement for the degree of DOCTOR OF PHILOSOPHY IN ENVIRONMENTAL ENGINEERING.

Daniel W. Smith

Dr. Daniel W. Smith - Supervisor

Dr. Stephen J. Stanley

Ian Buchanan

Dr. Ian D. Buchanan

Faye Hicks

Dr. Faye E. Hicks

Dr. Jerry J. Leonard

Dr. J. K. Bewtra -
External Examiner

Date 11 March 98

DEDICATION

This dissertation is dedicated to my parents Ahmad Rami and Bushra Shawwa for their love and support which provided me with the strength to carry out my journey toward this Ph.D. degree, and to my wife and best friend, Manal Amad who has been encouraging and patient throughout this work.

ABSTRACT

Dissolved air flotation (DAF) is considered an efficient clarification process for the treatment of drinking water supplies. Bench scale and pilot plant investigations demonstrated comprehensively that the DAF process is considered a viable choice when compared to the sedimentation process. It is considered very efficient for the treatment of soft, low alkalinity and algae-laden waters.

Over the past two decades, much research has been conducted on this unit process. Some of these studies were aimed at understanding the fundamental principles of dissolved air flotation for the application of drinking water treatment. Different mathematical models were developed to describe the bubble-particle collision and attachment inside the contact zone. One of these models was based on the single collector efficiency concept for a batch system. It has identified important design and operating variables which would affect the performance of the DAF process. However, model variables were based on theoretical calculations and therefore do not represent the actual conditions inside the contact zone.

The main objectives of this research were to develop a kinetic model for the DAF contact zone and to incorporate the model into a continuous-flow DAF system. The contact zone kinetic model included parameters which describe bubble-particle transport and attachment efficiencies, particle size, bubble size and volume concentration, and contact zone hydraulic loading. In addition, some of the model variables were measured experimentally for a range of conditions typically encountered in water treatment practice.

Model simulations predicted that contact zone height, particle stability and size, and bubble size and volume concentration would affect the DAF removal efficiency. Jar test experiments showed that algae particles must be destabilized for successful bubble attachment.

Model variables such as bubble size, volume concentration and rise velocity were measured, simultaneously, using a non-intrusive measurement method for different operational conditions. These experiments showed that the hydraulic loading, recycle ratio, saturator pressure and the nozzle orifice diameter have affected the measured variables and therefore would affect the DAF removal efficiency.

The contact zone kinetic model was tested, by using pilot-scale DAF system and synthetic water spiked with algae, by measuring the DAF particle removal efficiency. These experiments were conducted at different hydraulic loadings, recycle ratios and nozzle orifice diameters. Results indicated that removal efficiencies increased as bubble size decreased and bubble volume concentration increased.

To validate the kinetic model, the theoretical particle removal rate constant k_P was compared to the experimental values for the same operational conditions. The results showed that the theoretical and the experimental k_P values were equal when bubble-particle attachment efficiency α_{PB} was in the range of 0.35 to 0.40.

ACKNOWLEDGMENT

I am gratefully indebted to my mentor and supervisor Dr. Daniel W. Smith for his generous support and guidance throughout the research work. Dr. Smith has made countless contributions to my professional and personal life during the past five years.

I would like to thank my Ph.D. committee members, Dr. S. J. Stanley, Dr. I. D. Buchanan, Dr. F. E. Hicks, Dr. J. J. Leonard and Dr. J. K. Bewtra for their guidance and critical comments which improved the contents of this research.

A special thanks to Dr. Hassan H. Hamza, of the Western Research Center (CANMET), for his guidance and generous support for using their facilities to fabricate the pilot-scale DAF system that was used in this research.

I would also like to thank Mr. Nick Chernuka and Mr. Garry Solonynko, both of the Environmental Engineering Laboratory for their help with numerous laboratory tasks. Special thanks to Ms. Maria Demeter and Ms. Carla Schumacher for their help with the preparation of algae cultures and other laboratory tasks.

I am grateful to my good friend Dr. Lyndon Gyurek for his valuable help with the statistical analysis and computer work.

I would also like to thank the Town of St. Paul, Alberta, for their partial support through the Research Grant to Dr. Daniel W. Smith. In particular, I would like to thank Mr. Vaclav Matatko.

I am very grateful to the Natural Sciences and Engineering Research Council of Canada for providing me with the Post-Graduate Scholarship which supported two years of this Ph.D. work.

TABLE OF CONTENTS

ABSTRACT..

ACKNOWLEDGMENT...

LIST OF TABLES..

LIST OF FIGURES...

NOMENCLATURE..

CHAPTER

1. INTRODUCTION.. 1

1.1 Overview... 1

1.2 Research Objectives... 4

1.3 Research Approach... 5

2. LITERATURE REVIEW.. 8

2.1 Dissolved Air Flotation (DAF) for Drinking Water Treatment........ 8

2.1.1 Introduction.. 8

2.1.2 DAF Pre-treatment Process.. 10

2.1.2.1 Particle destabilization.. 11

2.1.2.2 Particle transport and flocculation.......................... 13

2.1.3 Flotation Process.. 16

2.1.3.1 Overview... 16

2.1.3.2 Bubbles formation and air supplied........................ 21

2.1.3.3 Bubble-particle interactions in the contact zone...... 28

2.1.3.3.1 Bubble rise velocity.............................. 32

2.1.3.3.2 Bubble-particle collision and attachment 36

2.1.3.4 Bubble-particle agglomerate rise in the flotation zone... 40

2.2 Measurement of Bubble Size, Concentration and Velocity with the Particle Dynamic Analyzer(PDA)... 44

2.2.1 Introduction 44
2.2.2 Velocity measurement 46
2.2.3 Size and concentration measurements 47
2.2.4 Data processing 50

3. CONTACT ZONE KINETIC MODEL 52
3.1 Introduction 52
3.2 Single Collector Efficiency Model 53
3.3 Hydrodynamic Characterization of DAF Contact Zone 58
3.4 DAF Contact Zone Kinetic Model 64

4. EXPERIMENTAL PROCEDURES 97
4.1 Design of Pilot-Scale DAF System 97
4.2 Tracer Study Experimental Set-Up 105
4.3 Bubble Size, Concentration and Velocity Measurements Using Particle Dynamic Analyzer (PDA) 109
4.3.1 PDA configuration and setting adjustment 109
4.3.1.1 Bubble size measurements using videophotography 114
4.3.2 PDA experimental set-up 115
4.3.2.1 Measurement of superficial liquid velocity 119
4.3.2.2 Measurement of bubble size, concentration and instantaneous rise velocity 122
4.4 DAF Kinetic Study 127
4.4.1 Synthetic water and algae culture preparation 127
4.4.2 Bench-scale DAF experimental set-up 131
4.4.3 Pilot-scale DAF experimental set-up 134

5. EXPERIMENTAL RESULTS 141
5.1 Hydrodynamic Characterization of DAF Contact Zone 141
5.2 Bubble Size, Concentration and Velocity Measurements in DAF Contact Zone 155

5.2.1 PDA configuration.... 155

5.2.2 Superficial liquid velocity measurements.... 163

5.2.3 Bubble size, concentration and velocity measurements.... 166

5.2.3.1 Effect of saturator pressure.... 166

5.2.3.2 Effect of recycle ratio.... 170

5.2.3.3 Effect of contact zone hydraulic loading rate.... 177

5.2.3.4 Effect of nozzle orifice diameter.... 190

5.2.3.5 Effect of contact zone height.... 197

5.2.3.6 Contact zone wall effect.... 210

5.3 DAF Kinetic Study.... 213

5.3.1 Optimum coagulant dose.... 213

5.3.2 DAF removal efficiency.... 216

6. DISCUSSION OF RESULTS.... 232

6.1 Hydrodynamic Characterization Study Results.... 232

6.2 Bubble Size, Concentration and Velocity Results.... 241

6.3 Particle Removal Efficiency Results and Model Prediction.... 248

6.4 Comparison of Theoretical and Experimental Particles Removal Rate Constant.... 253

7. CONCLUSIONS AND RECOMMENDATIONS.... 256

7.1 Limitation of Study.... 256

7.2 Conclusions.... 257

7.3 Recommendations.... 261

APPENDICES.... 262

A. DETAILED ANALYTICAL METHODS.... 262

A.1 Determination of Saturator Efficiency.... 263

B. SUMMARY OF DATA 267

B.1 Tracer Study Data.... 268

B.2 PDA Study Data.... 278

REFERENCES.......... 297

LIST OF TABLES

2.1. Key parameters used for DAF design and operation 19

2.2. Bubble mass, volume and number concentration 27

2.3. Effect of bubble diameter and temperature on bubble rise velocity, based on Stokes' law, and Reynolds number 34

2.4. Bubble-particle agglomerate velocity for different bubble and particle sizes assuming one bubble attached 43

3.1. Assumptions used for the contact zone kinetic model derivation 72

3.2. Reference values for contact zone kinetic model variables used for the sensitivity analysis 73

4.1. Summary of mixing and contact zone columns, and the separation tank dimensions 101

4.2. Summary of flocculator unit dimensions 105

4.3. Experimental arrangement for the tracer study 110

4.4. PDA configuration 112

4.5. Experimental arrangement for U_L measurements with the PDA 121

4.6. Experimental arrangements for studying the effect of recycle ratio and hydraulic loading on bubble size, concentration and rise velocity at probe volume coordinates (900,0,25) 123

4.7. Experimental arrangements for studying the effect of nozzle orifice diameter on bubble size, concentration and rise velocity 125

4.8. Experimental arrangements for studying the effect of contact zone column height on bubble size, concentration and rise velocity 126

4.9. Synthetic water chemical composition 129

4.10. Synthetic algae growth media 130

5.1. Summary of contact zone tracer study results 143

5.2. Comparison between U_L measured with the PDA, using TiO_2, at probe volume coordinates (900,0,25) and U_L calculated based on the measurement of the flow rate Q_{Total} 156

5.3. Bubble size distribution using videophotography technique for hydraulic loading 30 m/h, R_R = 10 %, P_{sat} = 484 kPa, $d_{Orifice}$ = 0.55 mm and probe volume coordinates (900,0,25) 158

5.4. Bubble size distribution using videophotography technique for hydraulic loading 70 m/h, R_R = 3 %, P_{sat} = 484 kPa, $d_{Orifice}$ = 0.55 mm and probe volume coordinates (900,0,25) 159

5.5. Comparison between bubble size measured with PDA and videophotography method 161

5.6. Consistency of bubble size and velocity measurements using the PDA for hydraulic loading = 50 m/h, R_R = 5 %, P_{sat} = 484 kPa, $d_{Orifice}$ = 0.55 mm and probe volume coordinates (900,0,25) 162

5.7. Effect of recycle water flow on U_L measurements using the PDA for hydraulic loading = 70 m/h and probe volume coordinates (900,0,25) 164

5.8. Superficial liquid velocity measured with the PDA for different contact zone heights, probe volume coordinates and hydraulic loading 165

5.9. Effect of saturator pressure on bubble size and concentration for hydraulic loading = 70 m/h, R_R = 5%, $d_{Orifice}$ = 0.55 mm and probe volume coordinates (900,0,0) 168

5.10. Effect of recycle ratio on bubble size, concentration and rise velocity for hydraulic loading = 30 m/h, $d_{Orifice}$ = 0.55 mm, 20°C, P_{Sat} = 484 kPa and probe volume coordinates (900,0,25) 172

5.11. Effect of recycle ratio on bubble size, concentration and rise velocity for hydraulic loading = 50 m/h, $d_{Orifice}$ = 0.55 mm, 20°C, P_{Sat} = 484 kPa and probe volume coordinates (900,0,25) 174

5.12. Effect of recycle ratio on bubble size, concentration and rise velocity for hydraulic loading = 70 m/h, $d_{Orifice}$ = 0.55 mm, 20°C, P_{Sat} = 484 kPa and probe volume coordinates (900,0,25) 175

5.13. Effect of recycle ratio on bubble size, concentration and rise velocity for hydraulic loading = 90 m/h, $d_{Orifice}$ = 1.03 mm, 20°C, P_{Sat} = 484 kPa and probe volume coordinates (900,0,25) 176

5.14. Effect of hydraulic loading on bubble size, concentration and rise velocity for $R_R = 7\%$, $d_{Orifice} = 0.55$ mm, 20°C, $P_{Sat} = 484$ kPa and probe volume coordinates (900,0,25) 181

5.15. Effect of hydraulic loading on bubble size, concentration and rise velocity for $R_R = 5\%$, $d_{Orifice} = 0.55$ mm, 20°C, $P_{Sat} = 484$ kPa and probe volume coordinates (900,0,25) 184

5.16. Effect of hydraulic loading on bubble size, concentration and rise velocity for $R_R = 3\%$, $d_{Orifice} = 0.55$ mm, 20°C, $P_{Sat} = 484$ kPa and probe volume coordinates (900,0,25) 186

5.17. Effect of hydraulic loading on bubble size, concentration and rise velocity for $R_R = 7\%$, $d_{Orifice} = 1.03$ mm, 20°C, $P_{Sat} = 484$ kPa and probe volume coordinates (900,0,25) 188

5.18. Effect of nozzle orifice diameter on bubble size, concentration and rise velocity for hydraulic loading = 50 m/h, $R_R = 7\%$, 20°C, $P_{Sat} = 484$ kPa and probe volume coordinates (400,0,25) 191

5.19. Effect of nozzle orifice diameter on bubble size, concentration and rise velocity for hydraulic loading = 70 m/h, $R_R = 5\%$, 20°C, $P_{Sat} = 484$ kPa and probe volume coordinates (400,0,0) 194

5.20. Effect of nozzle orifice diameter on bubble size, concentration and rise velocity for hydraulic loading = 70 m/h, $R_R = 5\%$, 20°C, $P_{Sat} = 484$ kPa and probe volume coordinates (900,0,0) 195

5.21. Effect of nozzle orifice diameter on bubble size, concentration and rise velocity for hydraulic loading = 90 m/h, $R_R = 3\%$, 20°C, $P_{Sat} = 484$ kPa and probe volume coordinates (900,0,25) 198

5.22. Effect of contact zone height and recycle ratio on bubble size, concentration and rise velocity for hydraulic loading = 30 m/h, $d_{Orifice} = 0.55$ mm, 20°C, $P_{Sat} = 484$ kPa and probe volume coordinates (900,0,25) and (400,0,25) 201

5.23. Effect of contact zone height and recycle ratio on bubble size, concentration and rise velocity for hydraulic loading = 50 m/h, $d_{Orifice} = 0.55$ mm, 20°C, $P_{Sat} = 484$ kPa and probe volume coordinates (900,0,25) and (400,0,25) 203

5.24. Effect of contact zone height on bubble size, concentration and rise velocity for hydraulic loading = 50 m/h, R_R = 10 %, $d_{Orifice}$ = 1.03 mm, 20°C, P_{Sat} = 484 kPa and probe volume coordinates (900,0,25) and (400,0,25) 206

5.25. Effect of contact zone height and recycle ratio on bubble size, concentration and rise velocity for hydraulic loading = 70 m/h, $d_{Orifice}$ = 0.55 mm, 20°C, P_{Sat} = 484 kPa and probe volume coordinates (900,0,25) and (400,0,25) 208

5.26. Contact zone wall effect on bubble size, concentration and rise velocity for hydraulic loading = 70 m/h, R_R = 5 %, $d_{Orifice}$ = 0.55 mm, 20°C and P_{Sat} = 484 kPa 211

5.27. Optimum coagulant dose experimental results 214

5.28. Experimental arrangements for the pilot-scale DAF kinetic study 217

5.29. Particle size distribution analysis (PSD) for the pilot-scale kinetic study for the following operational conditions: hydraulic loading = 90 m/h, R_R = 7 % and $d_{Orifice}$ = 1.03 mm 220

5.30. ANOVA results for pilot-scale DAF kinetic study using $d_{Orifice}$ =0.55 mm... 225

5.31. ANOVA results for pilot-scale DAF kinetic study using $d_{Orifice}$ = 1.03 mm.. 226

5.32. Contact zone removal efficiency calculations for hydraulic loading = 90 m/h, R_R = 7 % and $d_{Orifice}$ = 1.03 mm. The limiting overflow rate of the DAF separation zone U_{OS} is 5.6 m/h 230

5.33. Summary of contact zone removal efficiency results for DAF kinetic study 231

6.1. Effect of contact zone height and recycle ratio on contact zone axial dispersion coefficient D_a 242

6.2. Summary of results for superficial liquid velocity, bubble diameter, concentration and velocity measured by the PDA for different operational conditions 243

6.3. Results of the comparison between theoretical and experimental DAF removal efficiencies based on the contact zone kinetic model for different operational conditions 252

6.4. Results of the comparison between theoretical and experimental overall particle removal rate constant based on the contact zone kinetic model for different operational conditions 255

LIST OF FIGURES

2.1. Schematic diagram of the dissolved air flotation (DAF) process....................18

2.2. Effect of saturator pressure P_{Sat} on bubble volume concentration Φ_B as a function of recycle ratio R_R for bubbles with mean diameter of 50 μm and saturator efficiency of 70% at 20° C..29

2.3. Effect of saturator efficiency, *f*, on bubble volume concentration Φ_B as a function of recycle ratio R_R for bubbles with mean diameter of 50 μm and saturator pressure of 484 kPa at 20° C..30

2.4. Effect of water temperature on bubble volume concentration Φ_B as a function of recycle ratio R_R for bubbles with mean diameter of 50 μm, saturator efficiency of 70% and saturator pressure of 484 kPa at 20° C........................31

2.5. The fringe model and the probe volume..45

2.6. The fringe model of the phase shift..48

3.1. The single collector efficiency η_T as a function of particle diameter for the following conditions: $d_B = 60$ μm, $\rho_P = 1.01$ g/mL at 20° C..........................57

3.2. Effect of bubble diameter on η_T..59

3.3. Theoretical RTD for open-open boundary conditions....................................63

3.4. Horizontal element inside DAF contact zone..66

3.5. Effect of α_{PB} on particle removal efficiency for $d_P = 10$ μm, $d_B = 50$ μm, $\Phi_B = 4000$ ppm, $U_L = 70$ m/h and contact zone height of 3000 mm...............74

3.6. Effect of α_{PB} on DAF performance as a function of d_B....................................76

3.7. Effect of α_{PB} on DAF performance as a function of Φ_B....................................76

3.8. Effect of α_{PB} on DAF performance as a function of d_P....................................77

3.9. Effect of α_{PB} on DAF performance as a function of H....................................77

3.10. Effect of d_P on particle removal efficiency for $\alpha_{PB} = 0.5$, $d_B = 50$ μm, $\Phi_B = 4000$ ppm, $U_L = 70$ m/h and contact zone height of 3000 mm...............78

3.11. Effect of d_P on DAF performance as a function of α_{PB} 79

3.12. Effect of d_P on DAF performance as a function of H 79

3.13. Effect of d_P on DAF performance as a function of d_B 80

3.14. Effect of d_P on DAF performance as a function of Φ_B 80

3.15. Effect of d_B on particle removal efficiency for $\alpha_{PB} = 0.5$, $d_P = 10$ µm, $\Phi_B = 4000$ ppm, $U_L = 70$ m/h and contact zone height of 3000 mm 82

3.16. Effect of d_B on DAF performance as a function of d_P 83

3.17. Effect of d_B on DAF performance as a function of Φ_B 83

3.18. Effect of d_B on DAF performance as a function of H 84

3.19. Effect of d_B on DAF performance as a function of α_{PB} 84

3.20. Effect of Φ_B on particle removal efficiency for $\alpha_{PB} = 0.5$, $d_P = 10$ µm, $d_B = 50$ µm, $U_L = 70$ m/h and contact zone height of 3000 mm 85

3.21. Effect of Φ_B on DAF performance as a function of d_P 86

3.22. Effect of Φ_B on DAF performance as a function of α_{PB} 86

3.23. Effect of Φ_B on DAF performance as a function of H 87

3.24. Effect of Φ_B on DAF performance as a function of d_B 87

3.25. Effect of U_L on particle removal efficiency for $\alpha_{PB} = 0.5$, $d_P = 10$ µm, $d_B = 50$ µm, $\Phi_B = 4000$ ppm and contact zone height of 3000 mm 89

3.26. Effect of contact zone height on particle removal efficiency for $\alpha_{PB} = 0.5$, $d_P = 10$ µm, $d_B = 50$ µm, $\Phi_B = 4000$ ppm and $U_L = 70$ m/h 90

3.27. Effect of H on DAF performance as a function of α_{PB} 91

3.28. Effect of H on DAF performance as a function of Φ_B 91

3.29. Effect of H on DAF performance as a function of d_B 92

3.30. Effect of H on DAF performance as a function of d_P 92

4.1. Schematic diagram of the pilot-scale DAF system 98

4.2. Cross-section through the nozzle plate assembly 102

4.3. Schematic diagram of the tracer study set-up 106

4.4. Effect of air bubbles on conductivity measurements 108

4.5. PDA set-up 111

4.6. PDA experimental coordinate system 117

4.7. Location of probe volume coordinates inside the contact zone column 118

4.8. Bench-scale DAF recycle volumes as a function of timer settings at saturator pressure of 484 kPa 133

4.9. Bench-scale DAF unit paddle mixer velocity gradient as a function of speed at 20° C 133

4.10. Influent water flow meter calibration curve 139

4.11. Algae stock pump calibration curve 139

4.12. Coagulant pump calibration curve 140

4.13. Pilot-scale flocculator mixer velocity gradient as a function of speed 140

5.1. Typical SSR plot as a function of Pe for contact zone hydraulic loading = 70 m/h and $R_R = 0$ % 142

5.2. Contact zone mean residence time as a function of hydraulic loading at different heights across the contact zone and at $R_R = 0$ % 145

5.3. Residence distribution time variance as a function of hydraulic loading at different heights across the contact zone and at $R_R = 0$ % 146

5.4. Pe number for contact zone top port as a function of hydraulic loading for different R_R 147

5.5. Pe number for contact zone middle port as a function of hydraulic loading for different R_R 148

5.6. Pe number for contact zone bottom port as a function of hydraulic loading for different R_R 149

5.7. Experimental RTD curves for contact zone top port for different hydraulic loadings and R_R = 0 % 151

5.8. Experimental RTD curves for contact zone middle port for different hydraulic loadings and R_R = 0 % 152

5.9. Experimental RTD curves for contact zone bottom port for different hydraulic loadings and R_R = 0 % 153

5.10. Experimental and theoretical RTD curves for hydraulic loading 50 m/h and R_R = 0 % for different contact zone heights 154

5.11. Bubble size distribution for hydraulic loading 30 m/h, R_R = 10 %, P_{sat} = 484 kPa, $d_{Orifice}$ = 0.55 mm and probe volume coordinates (900,0,25) 160

5.12. Bubble size distribution for hydraulic loading 70 m/h, R_R = 3 %, P_{sat} = 484 kPa, $d_{Orifice}$ = 0.55 mm and probe volume coordinates (900,0,25) 160

5.13. Effect of saturator pressure on BSD for hydraulic loading = 70 m/h, R_R=5%, $d_{Orifice}$=0.55 mm, 20°C and probe volume coordinates (900,0,0) 169

5.14. Effect of recycle ratio on BSD for hydraulic loading = 30 m/h $d_{Orifice}$=0.55 mm, 20°C, Psat=484 kPa and probe volume coordinates (900,0,25) 173

5.15. Effect of recycle ratio on BSD for hydraulic loading = 50 m/h $d_{Orifice}$=0.55 mm, 20°C, Psat=484 kPa and probe volume coordinates (900,0,25) 178

5.16. Effect of recycle ratio on BSD for hydraulic loading = 90 m/h $d_{Orifice}$=1.03 mm, 20°C, P_{sat}=484 kPa and probe volume coordinates (900,0,25) 179

5.17. Effect of hydraulic loading on BSD at R_R=7%, P_{sat}=484 kPa, $d_{Orifice}$=0.55 mm, 20°C and probe volume coordinates (900,0,25) 182

5.18. Effect of hydraulic loading on BSD at R_R=5%, P_{sat}=484 kPa, $d_{Orifice}$=0.55 mm, 20°C and probe volume coordinates (900,0,25) 185

5.19. Effect of hydraulic loading on BSD at R_R=3%, P_{sat}=484 kPa, $d_{Orifice}$=0.55 mm, 20°C and probe volume coordinates (900,0,25) 187

5.20. Effect of hydraulic loading on BSD at R_R=7%, P_{sat}=484 kPa, $d_{Orifice}$=1.03 mm, 20°C and probe volume coordinates (900,0,25) 189

5.21. **Effect of nozzle orifice diameter on BSD for hydraulic loading =50 m/h, R_R=7%, P_{sat}=484 kPa, 20°C and probe volume coordinates (400,0,25) 192**

5.22. **Effect of nozzle orifice diameter on BSD for hydraulic loading =70 m/h, R_R=5%, P_{sat}=484 kPa, 20°C and probe volume coordinates (400,0,0) 196**

5.23. **Effect of nozzle orifice diameter on BSD for hydraulic loading =70 m/h, R_R=5%, P_{sat}=484 kPa, 20°C and probe volume coordinates (900,0,0) 196**

5.24. **Effect of nozzle orifice diameter on BSD for hydraulic loading =90 m/h, R_R=3 %, P_{sat}=484 kPa, 20°C and probe volume coordinates (900,0,0) 199**

5.25. **Effect of contact zone height on BSD for hydraulic loading =30 m/h, R_R=7 %, P_{sat}=484 kPa, 20°C, $d_{Orifice}$=0.55 mm and probe volume coordinates (900,0,25) and (400,0,25) 202**

5.26. **Effect of contact zone height on BSD for hydraulic loading =30 m/h, R_R=10 %, P_{sat}=484 kPa, 20°C, $d_{Orifice}$=0.55 mm and probe volume coordinates (900,0,25) and (400,0,25) 202**

5.27. **Effect of contact zone height on BSD for hydraulic loading =50 m/h, R_R=5 %, P_{sat}=484 kPa, 20°C, $d_{Orifice}$=0.55 mm and probe volume coordinates (900,0,25) and (400,0,25) 204**

5.28. **Effect of contact zone height on BSD for hydraulic loading =50 m/h, R_R=7 %, P_{sat}=484 kPa, 20°C, $d_{Orifice}$=0.55 mm and probe volume coordinates (900,0,25) and (400,0,25) 204**

5.29. **Effect of contact zone height on BSD for hydraulic loading =50 m/h, R_R=10 %, P_{sat}=484 kPa, 20°C, $d_{Orifice}$=1.03 mm and probe volume coordinates (900,0,25) and (400,0,25) 207**

5.30. **Effect of contact zone height on BSD for hydraulic loading =70 m/h, R_R=3 %, P_{sat}=484 kPa, 20°C, $d_{Orifice}$=0.55 mm and probe volume coordinates (900,0,25) and (400,0,25) 209**

5.31. **Effect of contact zone height on BSD for hydraulic loading =70 m/h, R_R=5 %, P_{sat}=484 kPa, 20°C, $d_{Orifice}$=0.55 mm and probe volume coordinates (900,0,25) and (400,0,25) 209**

5.32. Contact zone wall effect on BSD for hydraulic loading =70 m/h, R_R=5 %, P_{sat}=484 kPa, 20°C and $d_{Orifice}$=0.55 mm....212

5.33. Turbidity and particles removal efficiency as a function of PACl dose....215

5.34. R_{DAF} removal efficiency results for different hydraulic loadings, recycle ratios and nozzle orifice diameters....218

5.35. Particle number distribution for pilot-scale kinetic study for the following operational conditions: hydraulic loading = 90 m/h, R_R= 7% and $d_{Orifice}$ = 1.03 mm....221

5.36. Particle removal efficiency R_{DAFi} for d_{Pi} for the following operational conditions: hydraulic loading = 90 m/h, R_R= 7% and $d_{Orifice}$ = 1.03 mm....223

5.37. Hypothetical particles mass balance for contact and separation zones of the DAF process....228

6.1. Plot of the best fit of the experimental results for the correlation between t_m and U_L for contact zone top, middle and bottom ports, respectively....235

6.2. Plot of the best fit of the experimental results for the Pe and hydraulic loading correlation for contact zone top port and for different recycle ratios....237

6.3. Plot of the best fit of the experimental results for the Pe and hydraulic loading correlation for contact zone middle port and for different recycle ratios....238

6.4. Plot of the best fit of the experimental results for the Pe and hydraulic loading correlation for contact zone bottom port and for different recycle ratios....239

6.5. Plot for the best fit of the experimental results for the correlation between bubble relative rise velocity and the mean diameter for all data point (n=27)....247

6.6. Plot for the best fit of the experimental results for the correlation between bubble drag coefficient and Re for all data point (n=27)....249

NOMENCLATURE

1. Symbols

1.1 Roman Alphabet

a_B	projected area of spherical bubble with mean diameter d_B
A	correlation parameter determined by least square method
A_a	air mass
A_{CZ}	cross-sectional area of the DAF contact zone
A_{SZ}	cross-sectional area of the DAF separation zone
A_{Water}	cross-sectional area of main water inlet
A_{Sat}	cross-sectional area of saturated water inlet
A_H	Hamaker constant, 10^{-13} to 10^{-12} ergs
$A_{element}$	surface area of horizontal element inside DAF contact zone
B	correlation parameter determined by least square method
c	constant for a given water temperature, $(g\rho_f/18\mu)$
C	correlation parameter determined by least square method
C_x	concentration of tracer at an axial distance x downstream from the injection point at time t
C_R	concentration of air released in the flotation tank
C_a	concentration of air dissolved in water at atmospheric pressure based on Henry's law
C_{Sat}	mass concentration of dissolved air in the saturated stream
C_o	concentration of dissolved air in DAF influent raw water
C_{DB}	drag coefficient of a single air bubble
d_{PB}	equivalent spherical diameter of bubble-particle agglomerate
d_{PBi}	equivalent spherical diameter of bubble-particle agglomerate of size d_{Bi}

$d_{PB\ critical}$	critical diameter of bubble-particle agglomerate
d_{CZ}	inside diameter of the DAF contact zone
d_{SZ}	inside diameter of the DAF separation zone
d_{mc}	inside diameter of the DAF mixing column
d_B	mean bubble diameter
d_{Bi}	mean bubble diameter of size i
d_{Bc}	critical diameter of the bubble nucleous
$d_{PBi\ critical}$	critical diameter of bubble-particle agglomerate of size i
d_{Bv}	volumetric mean bubble diameter
d_{Pi}	mean particle diameter of size i
d_s	diameter of a solid sphere
$d_{orifice}$	inside diameter of nozzle orifice
dh	height of horizontal element inside DAF contact zone
dV	volume of horizontal element inside DAF contact zone
D	inside diameter of DAF contact zone column
D_a	axial dispersion coefficient
e_i	residuals of the regression model
E	correlation parameter determined by least square method
E(t)	residence time distribution density function
f	saturator efficiency factor
f_B	bubble's focal length
F_o	ratio of mean square to the mean square errors of the ANOVA model
F_D	drag force
F_A	force of attraction between colloids
F_μ	hydrodynamic resistance force between two identical spheres
G	mean velocity gradient
g	acceleration due to gravity, 9.8 m/s^2

H	height of flotation tank
H_s	separation distance between the center of two identical spheres
H_{CZ}	height of DAF contact zone column
H_{mc}	height of DAF mixing column
H_{SZ}	height of DAF separation zone tank
J_{PK}	rate of change of the total concentration of particles N with time t due to perikinetic flocculation
J_{OK}	rate of change of the total concentration of particles N with time t due to orthokinetic flocculation
k_P	overall particle removal rate constant
k_μ	empirical proportionality constant
K_B	Boltzman's constant, 1.381×10^{-23} J/K
K_H	Henry's constant, 4.18 kPa/mg/L at 20°C
L	path length inside contact zone
m_S	fraction of dead space inside the clarification zone of the DAF tank
M_{Sat}	momentum of saturated water flow
M_{Water}	momentum of main water flow inside DAF contact zone
M_P	particle mass
M_B	bubble mass
n_P	number of classes in the particle size distribution
n_B	number of bubbles attached to particles
$N_{element}$	number concentration of particles remaining in a fluid element inside DAF contact zone
N_B	bubble number concentration
N_{Bi}	bubble number concentration of size i
N_D	dispersion number
N_P	particle number concentration

N_{CZ}	number concentration of particles leavingthe contact zone at time t
$N_{CZ\ o,i}$	initial number concentration of particles of size i entering the DAF contact zone
$N_{CZ\ e,i}$	number concentration of particles of size i exiting the DAF contact zone
$N_{DAF\ e,i}$	DAF effluent particles number concentration of size i
P	total power dissipated
Pe	Peclet number
P_{Sat}	saturator gage pressure
P_{gas}	absolute pressure of gas above liquid inside the saturator
P_{Total}	total air pressure of saturator, sum of saturator gage pressure and one atmosphere
Q_{Sat}	volumetric flow rate of saturated water
Q_{Water}	volumetric flow rate of DAF influent water
Q_{Flocc}	flocculated water volumetric flow rate
Q_{Total}	total volumetric flow rate entering the DAF contact zone, sum of Q_{Sat} and Q_{Water}
Q_A	volumetric flow rate of air
Q_g	volumetric gas flow rate
r^2	statistical coefficient of determination for linear least squares regression
R	single bubble removal efficiency
$R_{CZ\ i}$	removal efficiency for DAF contact zone for particles of size d_{Bi}
R_{CZ}	overall removal efficiency for DAF contact zone
$R_{DAF\ i}$	DAF removal efficiency for particles of size d_{Bi}
R_{DAF}	overall DAF removal efficiency
R_R	recycle ratio, ratio of Q_{Sat} divided by Q_{water}
Re	Reynolds number

Re_B	Reynolds number of a single air bubble
Re_{PBi}	Reynolds Number of bubble-particle agglomerate of size d_{Bi}
S	suspended solid mass
S_D	spacing between PDA photodetector 1 and 2
S_F	projected fring spacing
t_m	mean residence time of DAF contact zone
T	absolute temperature, K
$U_{B\ inst}$	instantaneous bubble rise velocity due to advective flow and buoyancy
$U_{B\ rel}$	relative bubble rise velocity due to buoyancy
U_L	superficial liquid velocity, contact zone hydraulic loading
U_B	terminal rise velocity of a single bubble, or Stokes' rise velocity
U_{OS}	limiting overflow rate of the separation zone in the DAF tank
$U_{PB\ aggl}$	particle-bubble agglomerate rise velocity
$U_{PBi\ aggl}$	rise velocity of particle-bubble agglomerate of size d_{Bi}
$U_{B\ Stoke}$	Stokes' bubble rise velocity
U_{PB}	relative velocity of bubbles to particles of size d_P
U_{RMS}	root mean square velocity
U_1	PDA photodetector at position 1
U_2	PDA photodetector at position 2
v_B	mean volume of a single air bubble
V	flotation tank volume, reactor volume
V_{CZ}	DAF contact zone volume
V_{SZ}	DAF separation zone volume
V_{MC}	DAF mixing column volume
X_{gas}	mole fraction of gas in saturated liquid
y	response variable used in the linear regression model

1.2 Greek Alphabet

α_i	effect of the i^{th} level of the first independent variable
α_{PP}	particle-particle collision efficiency
α_{PB}	particle-bubble collision efficiency factor
$\alpha\beta_{ij}$	two-way interaction of the i^{th} and the j^{th} level
βj	effect of the j^{th} level of the second independent variable
β_1	the intercept of the linear regression model
β_2	the slope of the linear regression model
$\hat{\beta}_1$	estimated intercept of the linear regression model
$\hat{\beta}2$	estimated slope of the linear regression model
η_D	single collector efficiency for Brownian diffusion
η_I	single collector efficiency for interception
η_S	single collector efficiency for sedimentation
η_{IN}	single collector efficiency for inertia
η_T	total single collector transport efficiency
μ	fluid dynamic viscosity
μ_a	overall average effect of the ANOVA model
σ	surface tension of bubble
σ_t^2	variance of residence time distribution curve
σ_{UB}	standard deviation of $U_{B\,inst}$ or the root mean square velocity for bubbles
σ_{UL}	standard deviation of U_L or the root mean square velocity for water
ΔP	pressure difference across the nozzle
ΔN_i	particle count per milliliter in channel i
ρ_{Sat}	density of saturated air
ρ_B	density of air bubble

ρ_f	density of liquid
ρ_P	density of particle
ρ_{PBi}	density of particle-bubble agglomerate of size d_{Bi}
ρ_{PB}	particle-bubble agglomerate density
ν	kinematic viscosity of the fluid
θ	dimensionless time, (t/τ)
ϕ_{1-2}	phase shift for detector pairs U1-U2
ϕ_{1-3}	phase shift for detector pairs U1-U3
τ	theoretical residence time inside DAF contact zone
Φ_B	bubble volume concentration
Φ_P	particle volume concentration
ε_f	volume fraction of air bubbles in the saturated water stream
ε_u	linear regression model experimental random errors
ε_{ij}	ANOVA model random errors

2. Abbreviation

ANOVA	analysis of variance
BSD	bubble size distribution
DAF	dissolved air flotation
DOC	dissolved organic carbon
DLVO	Derjaguin, Landau, Verwey and Overbeck theory
EDLF	electrical double layer force
EPM	electrophoretic mobility
IEP	isoelectric point
HRT	hydraulic residence time inside the DAF contact zone
LOF	lack of fit errors

LDA	laser Doppler anemometry
LRHF	long range hydrodynamic force
LVDW	London-van der Waals molecular force of attraction
NOM	natural organic matter
PE	pure errors
PBT	population balance model in turbulent flow
PDA	particle dynamic analyzer
PSD	particle size distribution
PACl	polyaluminum chloride
PHF	pressing hydrodynamic force
PMT	PDA photomultipliers
RPM	revolution per minute
RTD	residence time distribution of the liquid
SRHF	short range hydrodynamic force
SSR	sum of squares of residuals
SCE	single collector efficiency model
UTCC	University of Toronto culture collection

CHAPTER 1

INTRODUCTION

1.1 Overview

Dissolved air flotation, DAF, is an alternative process for solid-liquid separation whereby particles are removed by means of their attachment to air bubbles. This process was recognized as early as 1924 for the recovery of fibers and white paper in the paper industry (Gregory, 1997). It has become increasingly important in the field of drinking water treatment since the mid-1960's especially in Scandinavia and the UK. It is an emerging technology in North America which is used successfully for treating soft, low alkalinity, naturally colored and algae-laden waters.

In the DAF process, water is saturated with air under pressure and recycled back into a circular or rectangular flotation tank through a nozzle or a valve. The resultant pressure reduction releases air from solution as small or micro-bubbles, i.e. bubbles with diameters less than 150 μm. These bubbles collide with the flocculated particles in the flotation tank forming bubble-floc aggregates as the result of successful attachments.

Kitchner and Gochin (1981) listed three possible mechanisms for forming bubble-floc aggregates: (1) entrapment of bubbles in large floc structures, which is more important for sludge thickening and municipal wastewater which involves large flocs and concentrated suspensions; (2) growth of bubble nuclei and their formation on particles or within flocs; and (3) particle collision and adhesion with pre-formed bubbles. The third mechanism is applicable to the treatment of dilute suspensions typically found in drinking water sources. Also, air bubbles are formed very quickly (within 1 second) after injecting the air saturated water into the flotation tank (Rykaart and Haarhoff, 1995) which makes the last mechanism more applicable.

The controlling step for flotation to proceed is bubble-particle attachment which is determined by the surface chemical and hydrodynamic parameters that exist in the flotation tank. There are two views that describe the bubble-particle attachment: the contact angle and the heterogeneous system of small particles and micro-bubbles (Edzwald, 1995). The contact angle between the adsorbed bubble and the particle must be finite and large enough so that attachment of an air bubble to the surface of the particle is thermodynamically feasible (Gochin, 1981). However, the magnitude of the contact angle depends on the size scale of the bubbles and particles.

The second view of bubble-particle attachment of colloidal particles to micro-bubbles was presented by Derjaguin et al. (1984) where a finite contact angle is not required and therefore the term contactless flotation was used. In this model, reduction of electrical charge interactions and attraction by London-van der Waals forces are required for attachment as particles are transported to the bubble surface.

Regardless of the view taken, there are two important conditions for successful bubble-particle attachment (Edzwald, 1995): charge neutralization of the particles (particle destabilization) and the production of hydrophobic particles.

As the above discussion illustrates, the performance of the DAF process is dependent on complex interactions involving many physical and chemical processes. Due to these complex interactions, the establishment of a suitable design model based on the fundamentals of the DAF process is almost impossible. Therefore, the design and operation of the DAF process is heavily based on bench and pilot scale testing. However, many researchers have attempted to model the DAF performance mathematically for the application to drinking water treatment.

Edzwald and co-workers (Edzwald et al., 1990; Malley and Edzwald, 1991; Edzwald, 1995; Edzwald, 1997) have described a conceptual model for particle collection by bubbles in the DAF tank. They have divided the flotation tank, for the purpose of modeling, into two zones: the contact or the reaction zone and the separation or the clarification zone. The purpose of the contact zone is to collide and attach particles to bubbles, while the purpose of the separation zone is to provide relatively quiescent conditions for particle-bubble agglomerates to rise to the surface of the tank. Their model is based on the single collector efficiency concept which is used to describe particle-bubble collision and attachment. This concept has been used successfully to describe dispersed air flotation (Flint and Howarth, 1971; Reay and Ratcliff, 1973) and also used to model particle removal by deep bed filtration (Yao, 1971).

The single collector efficiency model, SCE, is based on the convective-diffusion equation and particle trajectory analysis. These were used to derive individual particle transport expressions for the single collector efficiency for Brownian diffusion, η_D, interception, η_I, sedimentation, η_S, and inertia, η_{IN}. The SCE model shows that transport by inertia and sedimentation are not significant for particles and bubbles less than 100 μm. Also, the model has shown that the total single collector transport efficiency, η_T, is controlled by interception for particles larger than 1 μm, which are typically found in water treatment.

The SCE model indicated that η_T is proportional to bubble size according to d_B^{-2} and dependent on particle size according to d_P^2 for interception. Based on the SCE model, a particle removal rate equation was developed which was expressed in a first-order rate form. This approach was used successfully for describing the flotation system as analogous to a chemical reactor where the overall rate of particle removal by bubbles is a first-order process (Gochin, 1981). This simple first-order equation, which was applied to a batch flotation conditions, has identified important design and operational parameters affecting the flotation performance.

A more complicated approach for modeling bubble-particle collisions was considered by Tambo and co-workers (Tambo and Matsui, 1986; Fukushi et al., 1993). Their model, called the population balance model in turbulent flow or the PBT model, described the bubble-particle collisions in the contact zone as a heterogeneous flocculation process where the bulk fluid flow is characterized by turbulent flow. They have developed flocculation rate equations for particle transport based on collisions caused by the bulk water velocity differences caused by the turbulent mixing.

The actual difference between the PBT and the SCE models is the bubble-particle collision rate. This is due to the differences in the flow condition assumptions used in each model. The SCE model considers the transport of particles in the vicinity of the bubble surface where the relative motion of the fluid to the bubble creates streamlines of flow around the bubble, which occurs under laminar flow conditions. Both approaches are reasonable and valid for modeling particle removal by bubbles for design with appropriate safety factors. However, they need to be applied properly for the particular flow conditions.

A recent study by Edzwald (1995) entitled "Principles and Applications of Dissolved Air Flotation" discussed comprehensively the fundamentals of the DAF process for drinking water treatment and also compared the differences between the PBT and the SCE models. This study highlighted the need for further research in this area by considering alternative models that would describe bubble-particle collision in the contact zone. It also suggested that those models need to be tested and verified at the pilot scale level.

1.2 Research Objectives

The research presented here is a rational approach for modeling bubble-particle interactions in the DAF contact zone for drinking water treatment applications. The primary objectives of this study are: (1) to develop a kinetic model for the DAF contact zone based on fundamental principles and the single collector efficiency model incorporated into a continuous flow system; and (2) to validate the contact zone kinetic model by comparing the experimental removal rate constant to the theoretical values, using synthetic water spiked with algae, for the same operational conditions.

To achieve the main objectives, three supplemental objectives were established in this research: (1) to design a continuous-flow pilot-scale DAF system where the contact and the separation zones are physically delineated; (2) to characterize the hydrodynamics inside the contact zone for different operational conditions; and (3) to measure, simultaneously, bubble size, concentration, and rise velocity inside the DAF contact zone for different operational conditions.

1.3 Research Approach

The research approach involved six major components which included: (1) the development of a contact zone kinetic model incorporated into a continuous-flow DAF system; (2) the design of a complete pilot-scale DAF system; (3) tracer studies to characterize the hydrodynamics inside the contact zone for operational conditions typically encountered in water treatment practice; (4) simultaneous measurements of bubble size, concentration and rise velocity inside the contact zone for different operational conditions; (5) experimental studies using synthetic water to measure DAF removal efficiency under different operational conditions; and (6) comparison of the experimental to the theoretical removal efficiencies to verify the contact zone kinetic model.

The development of the contact zone kinetic model was based primarily on the fundamentals of the DAF process and the SCE model that was developed by Edzwald and co-workers (Edzwald et al., 1990; Malley and Edzwald, 1991; Edzwald, 1995; Edzwald, 1997). In this research, the SCE model was modified by incorporating it into a continuous-flow DAF system.

Four major considerations were incorporated into the design of the continuous-flow pilot-scale DAF system: (1) the design was based on the integrated treatment concept (Edzwald, 1995) where the design of the pre-treatment processes, i.e. coagulation and flocculation processes, was integrated with the flotation process; (2) the contact and the separation zones were physically delineated by designing the DAF tank as a coaxial column, where the inner column was considered part of the contact zone; (3) the mixing of the flocculated water and the supersaturated water was accomplished in a separate column, called the mixing column, where large bubbles were separated from the micro-bubbles; and (4) the influent section to the contact zone column was designed as a circular cone to minimize turbulence.

Tracer studies were conducted to characterize the hydrodynamics inside the DAF contact zone. These experiments involved the measurements of the mixing time, in terms of mean residence time, and the degree of mixing, in terms of Peclet number, at three different heights of the contact zone column. That was achieved by conducting a pulse-input test where sodium chloride, NaCl, was injected into the fluid influent line just upstream from the contact zone column after reaching steady-state conditions. The conductance of the fluid inside the column was monitored as a function of time by means of a conductivity probe.

Simultaneous measurements of bubble size, concentration and rise velocity inside the DAF contact zone were accomplished by using a particle dynamic analyzer, PDA. This non-intrusive instrument is based on the laser Doppler anemometry , LDA, technique. These experiments involved four components: (1) configuration and settings adjustment for the PDA instrument; (2) measurements of bubble size using the videophotography technique to verify the PDA settings adjustment, under the same experimental conditions; (3) measurement of liquid superficial velocity inside the contact zone for different hydraulic loading rates; and (4) measurement of bubble size, concentration and rise velocity for different hydraulic loading rates, saturated flow rates, saturator pressures and nozzle orifice diameters.

The DAF contact zone kinetic experiments involved the measurement of contact zone particle removal efficiency and the overall particle removal rate constant. These experiments involved four components: (1) preparation of laboratory grown algae cultures and synthetic water preparation; (2) determination of the optimum coagulant dose using a bench scale DAF unit (Aztec Environmental Control Ltd., UK); and (3) measurement of contact zone particle removal efficiencies for different hydraulic loading rates, saturated flow rates and nozzle orifice diameters; and (4) measurement of the overall particle removal rate constant for different hydraulic loading rates, saturated flow rates and nozzle orifice diameters.

Finally, the contact zone kinetic model was verified by comparing the theoretical particle removal rate constant to the experimental values for all operational conditions tested.

In the subsequent chapters, a thorough literature review, detailed discussion on the model development, detailed description of experimental procedures, results, discussions, conclusions and recommendation for further research are presented.

CHAPTER 2

LITERATURE REVIEW

This chapter will provide the background information necessary for understanding the research objectives, the approach used to address thesis objectives and interpretation of the results obtained in this study. The literature review will focus on two main areas including dissolved air flotation, DAF, pretreatment process and the fundamentals of the flotation process.

2.1 Dissolved Air Flotation (DAF) for Drinking Water Treatment

2.1.1 Introduction

The dissolved air flotation process was developed first in the mining industry as an economical means for separating mineral ores. As the understanding of the DAF process increased, its application spread to other areas including: industrial waste treatment such as refinery wastewater, recycled paper de-inking and paper mill wastewater and municipal waste treatment such as activated sludge thickening, tertiary wastewater treatment and combined sewer and storm waters (Malley, 1988; Edzwald; 1995).

DAF was first used for drinking water clarification in Scandinavia and South Africa in the 1960's (Longhurst and Graham, 1987). It is considered now a proven drinking water treatment technology in Belgium, The Netherlands, Australia and the United Kingdom while it is considered as an emerging technology in North America (Edzwald, 1995).

There are currently ten operating DAF plants for drinking water treatment in the United States with capacities ranging from 136 ML/d to about 4 ML/d with others under design and construction (Nickols, 1997). Several large DAF plants are proposed for construction in Canada within the next few years which include the Seymor water treatment plant in Vancouver with 1000 ML/d capacity, the Glenmore water treatment plant in Calgary with 300 ML/d capacity and the Deacon water treatment plant in Winnipeg with 700 ML/d capacity (Adkins, 1997).

Extensive laboratory, pilot and field scale studies were performed by many researchers to asseses the effectiveness of DAF for the treatment of drinking water. These studies showed that DAF was effective for the treatment of algae-laden waters, low turbidity, soft and high organic content (including color) waters that produce light flocs (Hyde et al., 1977; Zabel, 1985; Heinanen, 1988; Edzwald and Malley, 1990; Arora et al., 1994).

There are several advantages of DAF over conventional clarification processes such as sedimentation. DAF is more efficient for the separation of low-density particles such as algae and precipitated aluminum hydroxide. These particles are considered to be a problem in conventional treatment processes, especially under cold water conditions. DAF requires smaller tanks since less time is required for flotation than sedimentation, which translates into lower capital costs (Zabel, 1985). Hydraulic loading rates are 10 times higher than sedimentation and hydraulic detention times are much shorter, typically 5 to 15 minutes (Edzwald and Walsh, 1992).

Also, smaller flocculation tanks with shorter retention times are required since smaller flocs are required for flotation (Edzwald, 1995). The solids concentration of the sludge produced in DAF is higher than that of settling tank, which reduces the cost of sludge disposal (Edzwald and Wingler, 1990). Other potential advantages of DAF are the removal of volatile organics and taste and odor by air stripping during flotation.

Fundamentally, the DAF process can be divided into two integrated sub-processes: the pretreatment process, or the coagulation process, and the flotation process. The concept of integrating DAF into the overall treatment process was emphasized by Edzwald (1995) who stressed that what is done ahead of flotation with coagulant addition and flocculation (i.e. the pretreatment process) affects the flotation performance and in turn affects the design and performance of subsequent treatment processes.

In the following sections, the fundamentals of each process, including the important process variables that are related to the treatment of drinking water, will be discussed in detail.

2.1.2 DAF Pretreatment Process

The DAF pretreatment process involves two steps: particle destabilization and particle flocculation (Edzwald, 1995). In water treatment literature, these two steps define the coagulation process. The term flocculation applies only to the transport and agglomeration aspects of the overall process of coagulation. On the other hand, the chemical engineering literature defines coagulation as the process of destabilization by the double layer compression and flocculation as the process of destabilization by the bridging mechanism (AWWARF, 1991).

In the DAF pretreatment process, particle destabilization occurs during the rapid mixing stage, after the addition of chemical coagulants, while flocculation and the growth of aggregates occur during the slow mixing stage. The objective of the rapid mixing step is to disperse the coagulants uniformly and quickly so as to cause destabilization of colloidal particles in the raw water. On the other hand, the principal aim of slow mixing is the transport of the destabilized particles and to promote collisions and floc formation.

2.1.2.1 Particle destabilization

The particulates and colloidal materials typically found in raw waters include inorganics such as clays, silica, iron and manganese, and natural organics such as viruses, algae, bacteria and synthetic organic chemicals. Colloidal systems contain particles with a high surface area to volume ratio and ranging in size from approximately 1.0 nm to 1.0 µm or more in diameter. These particles are known to carry a negative electrical surface charge in aqueous solutions. These charges are counter balanced by charges in the aqueous layer, resulting in an electrical double layer at every interface between the solid and the water. Repulsive electrical forces and van der Waals forces interact between particles producing a barrier that prevent aggregation.

There are four distinct mechanisms that can cause particle destabilization of colloidal suspensions (O'Melia, 1972):

I. compression of the double layer surrounding the colloid;
II. adsorption to produce charge neutralization;
III. enmeshment of the colloid or sweep coagulation; and
IV. adsorption to permit interparticle bridging.

In water treatment, coagulation by inorganic coagulants and polymeric inorganic coagulants occurs predominantly by two mechanisms: (1) adsorption of the hydrolysis species on the colloid causing charge neutralization and (2) sweep coagulation where interactions occur between the colloid and the precipitating hydroxide (AWWARF, 1991).

For water treatment with the DAF process, charge neutralization is considered to be the main particle destabilization mechanism where small destabilized pinpoint flocs are produced at low dosages of chemical coagulants (Edzwald, 1995). Since charge neutralization occurs very rapidly, within 1 second after the addition of the coagulant, the coagulant must be dispersed in the raw water stream as rapidly as possible, within less than 0.1 seconds, so that the hydrolysis products that develop in 0.01 to 1 seconds will cause destabilization of the colloids (AWWARF, 1991).

For colloidal particles to be destabilized by the charge neutralization mechanisms, transport or collisions between the colloids and the incipiently forming products of the hydrolysis reactions must occur through rapid mixing. The energy required for mixing is related to the well recognized mean velocity gradient, G, concept of Camp and Stein (1943). It is defined in terms of the power input per unit volume as:

$$G = \sqrt{\frac{P}{V\mu}} \tag{2.1}$$

where P is the total power dissipated, μ is water dynamic viscosity and V is the volume of the rapid mix reactor.

Johnson and Amirtharajah (1983) suggested that high intensities of mixing with mean G values of 3000 to 4000 s^{-1} for very short time, i.e. less than 1 second, would probably be beneficial for effective charge neutralization. Coagulant dosages and pH conditions required for particle destabilization by charge neutralization depend on coagulant type and raw water quality characteristics, such as particle concentration, hardness and the content and type of natural organic matter, NOM.

Trivalent aluminum or iron salts can destabilize particles via the charge neutralization mechanism. Aluminum salts are widely used as coagulants in the water treatment field, of these alum is the most commonly used in water treatment. Alum is the generic term for the coagulant aluminum sulfate $Al_2(SO_4)_3.17H_2O$. When alum is dissolved in water it forms SO_4^{-2} ions and six coordinate aquo-aluminum complexes commonly written as Al^{+3} (Stumm, 1967). These ions are acidic and can undergo additional hydrolysis reactions (O'Melia, 1972). The interaction between the positively charged ions with the negatively charged colloids produces two points of zero zeta potential, or the isoelectric point, IEP, at pH values of 4.8 and 6.8 (AWWA, 1990). Favorable particle destabilization by charge neutralization can be expected to be at or close to these pH values.

However, for cold and soft waters, pre-formed aluminum polymers, such as polyaluminum chloride, PACl, have an advantage over alum. They are also very effective over greater pH range (5 to 10) because of the basicity of the solution. PACl is prepared by the partial neutralization of $AlCl_3$ by the addition of a base resulting in the formation of stable polymeric aluminum species (Malley, 1988). PACl can destabilize particles via the charge neutralization mechanism if it contains primarily the polymer $Al_{13}O_4(OH)^{+7}$ species. This is analogous to the action of cationic organic polyelectrolytes used in water treatment (Edzwald, 1985). In comparison to alum, PACl is considered to be a more effective coagulant at lower dosages because of the higher charge on its species.

The coagulation requirements, or more fundamentally the particle destabilization requirements, for the DAF process are similar to the sedimentation and direct filtration processes. However, higher coagulant dosages are required in sedimentation processes for sweep floc conditions (Edzwald, 1995).

2.1.2.2 Particle transport and flocculation

The particle transport or flocculation step of the coagulation process is the rate- determining step for the formation of aggregates and is an important factor in treatment facility design (Camp, 1955). Destabilized colloids must be brought into contact with one another for aggregation to occur. There are three major physical processes for particle transport and aggregation: (1) Brownian diffusion or perikinetic flocculation where the driving force of this mechanism is the thermal energy of the fluid, (2) bulk fluid shear or orthokinetic flocculation where the driving force of this mechanism is a velocity gradient induced by mechanical mixing, and (3) differential settling where the driving force is the gravity.

The importance of particle concentration on flocculation mechanisms can be summarized in the following equations for particles of uniform size (O'Melia, 1972):

$$J_{PK} = \frac{dN_P}{dt} = -\frac{4}{3}\frac{\alpha_{pp}.K_B.T.N_P^2}{\mu} \qquad (2.2)$$

$$J_{OK} = \frac{dN_P}{dt} = -\frac{2}{3}\alpha_{pp}.G.d_P^3.N_P^3 \qquad (2.3)$$

where J_{PK} and J_{OK} are the rates of change of the total concentration of particles N_P with time, t, due to perikinetic and orthokinetic flocculation, respectively, α_{PP} is the particle-particle collision efficiency factor, K_B is Boltzmann's constant, T is the absolute temperature and d_P is the mean diameter of particles.

The significance of particle size can be seen from the ratio of J_{OK} to J_{PK} which is equal to 1.0 for particles with 1 μm diameter at 25 °C and a mean velocity gradient, G, of 10 s^{-1}. It can be concluded that for particles with diameters less than 1 μm, perikinetic flocculation is predominant and conversely with diameters greater than 1 μm , orthokinetic flocculation predominates. In conventional water treatment, the size of the flocs produced is larger than 1 μm and therefore the orthokinetic flocculation predominates in the particle aggregation process.

Since the driving force in othokinetic flocculation is the velocity gradient, the mean velocity gradient, G, is used to characterize the mixing intensity inside the flocculator. Letterman (1981) has summarized the overall effect of mixing intensity on the rate of orthokinetic flocculation. At high mean G values, a relatively rapid disappearance of primary particles and a rapid formation of relatively small and high density flocs occur.

On the other hand, a lower mean G value causes slower rate of floc formation, however, producing larger floc size.

These characteristics of floc formation are the reason for tapered flocculation used in conventional water treatment with the higher G value in the first compartment and progressively smaller G values in the remaining compartments. This tapering causes the build up of progressively larger size flocs which improves the clarification process by sedimentation. However, tapering of flocculation is not needed for the DAF pretreatment process because large flocs are not needed. Thus, higher mean G values are desirable for improved clarification by the DAF process (Edzwald, 1995).

Gregory and Zabel (1990) found an optimum mean G of 70 s^{-1} using alum as the coagulant which was independent of water type. While Janssens (1991) reported that optimum G conditions for DAF depend on the type of the coagulant used: 70 to 80 s^{-1} for alum, 70 s^{-1} for ferric chloride and greater than 30 s^{-1} for PACl. Klute et al. (1994) found that velocity gradients of 50 s^{-1} produced a narrower floc size distribution concentrated around diameters of 30 μm, compared to the wider size distribution produced by lower G values of 15 s^{-1}. Ødegaard (1994) found that DAF efficiency increased with increasing flocculation G to a maximum value and decreased above that value.

Since the floc size required for DAF is smaller than for conventional treatment, a shorter flocculation retention time is required. Flocculation times of 5 to 20 minutes have been reported for pilot-plant and full scale studies (Malley and Edzwald, 1991; Janssens, 1991; van Craenenbroek et al., 1993), compared to an average of 30 minutes for conventional treatment (Malley and Edzwald, 1991). These small, strong, low-density flocs can better resist the high shear and turbulence at the outflow openings of the DAF nozzles (Bunker et al., 1994).

Recent research by Edzwald and co-workers (Edzwald and Wingler, 1990; Edzwald et al., 1992; Bunker et al., 1994; Edzwald et al., 1994a) supported the above work indicating an optimum G value in the range of 55 to 100 s^{-1}. Their research has confirmed that small and strong flocs with particle size distributions of 10 to 30 μm are effectively removed by flotation and that flocculation detention times of 5 minutes are optimal.

2.1.3 Flotation Process

2.1.3.1 Overview

Flotation can be defined as a solid-liquid separation process in which gas bubbles attach to solid particles to cause the apparent density of the bubble-solid agglomerates to be less than that of the water, thereby allowing the agglomerate to float to the surface (AWWA, 1990). Although in principle any gas that is not highly soluble in the liquid phase can be employed, in practice air is the most commonly used gas because of its availability, safety of use and cost (Zabel, 1984).

Flotation terminology and nomenclature is often confusing because they can be classified in different terms. Flotation can be classified according to application, e.g. coal flotation, in terms of the presence or absence of froth and in terms of the method of producing gas bubbles, e.g. dispersed air flotation, microflotation and dissolved air flotation (Mangravite et al., 1972). The discussion in this section will focus only on flotation based on the method of bubble formation.

Dispersed air flotation relies on bubble formation by mechanical means which produces bubble sizes in the range of 0.1 to 1.0 mm and uses surfactants to produce particle-bubble adhesion. It is primarily used in the mining industry for ore separation and it is not suitable for drinking water treatment because of the addition of surfactants.

Microflotation uses very low gas flow rates and frothing agents to produce microbubbles of about 40 μm. It is not applicable to drinking water treatment because of the addition of chemical collectors and frothers. Microflotation had received extensive attention in the 1960's and 1970's (Rubin and Johnson, 1967; Rubin, 1968; Rubin and Lackey, 1969; Rubin and Lapp, 1971). These researchers found that the electrolytic flotation, or microflotation, could effectively remove bacteria, algae, metals and metal precipitates, silica, humic acids and other organic colloids from solution. This extensive research of the microflotation process has provided valuable information regarding the physical and chemical mechanisms used in flotation and it provided insight into the use of flotation for drinking water treatment.

In dissolved air flotation, DAF, bubbles are generated by the reduction in pressure of a water stream saturated with air. The air precipitates in the form of fine bubbles usually of less than 100 μm in diameter. There are two types of DAF: vacuum flotation and pressure flotation. Pressure flotation is the most widely used in the field of water treatment. There are three basic pressure dissolved air flotation systems (Zabel, 1984): full flow, split-flow and recycle-flow pressure flotation. For drinking water treatment, the recycle-flow pressure flotation is the most appropriate system.

In recycle-flow pressure flotation, as shown in the schematic diagram of the DAF process in Figure 2.1, part of the clarified effluent is recycled, with recycle ratios typically ranging from 6 to 10 percent of the raw water flow. The recycled flow is pressurized in a special tank called the saturator at typically 480 kPa gage pressure (Edzwald and Walsh, 1992). The pressurized recycle water is introduced to the flotation tank through a pressure release device, needle valves or specially designed nozzles, where the pressure is reduced to near atmospheric pressure releasing the air in the form of fine bubbles, i.e. 20 to 100 μm in diameter (AWWA, 1990).

The key parameters used in DAF design and operation for water treatment applications are shown in Table 2.1 (Edzwald and Walsh, 1992; Haarhoff and van Vuuren, 1994).

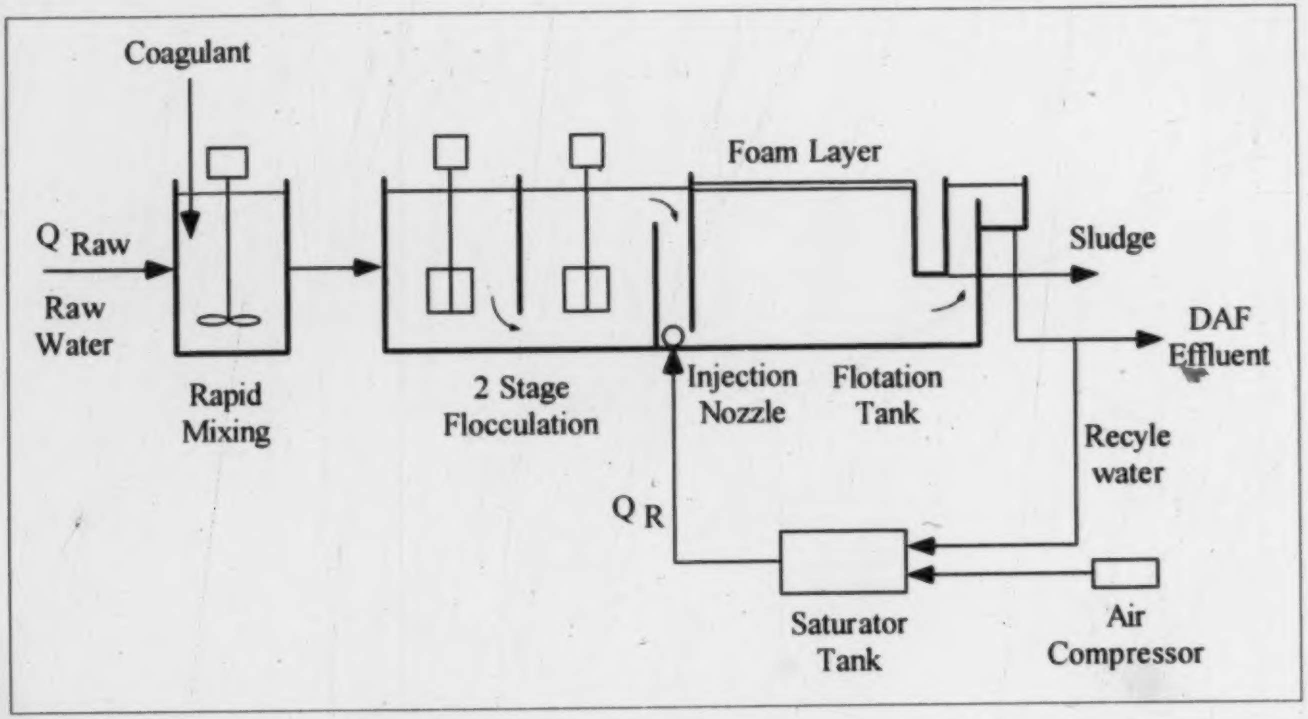
Coagulant
Q Raw
Raw Water
Rapid Mixing
2 Stage Flocculation
Foam Layer
Injection Nozzle
Flotation Tank
Sludge
DAF Effluent
Recyle water
Q R
Saturator Tank
Air Compressor

Figure 2.1 Schematic diagram of the dissolved air flotation (DAF) process

Table 2.1 Key parameters used in DAF design and operation.

		Design Values	
Parameter	Units	Range	Typical
Chemical Pretreatment:			
Coagulant Dose	(mg/L)	determined by DAF jar test	
Flocculation Time[#]	(min)	10 to 30	10
G-value[#]	(s^{-1})	10 to 150	70
Flotation Tank Design:			
Contact or Reaction Zone:			
Detention Time	(min)	1 to 4	1.5
Hydraulic Loading Rate[*]	(m/h)	40 to 100	70
Separation or Flotation Zone:			
Detention Time	(min)	5 to 15	10
Hydraulic Loading Rate[**]	(m/h)	5 to 11	8
Cross-Flow Velocity	(m/h)	20 to 100	30
Air Saturation System:			
Operating Pressure[#] (kPa)		206 to 620	480
Recycle Rate[#]	(%)	7 to 30	8
Bubble Size	(µm)	10 to 120	40
Saturator Efficiency	(%)	40 to 90	70
Sludge Removal:			
Percent Solids	(%)	0.2 to 6	3
Layer Thickness	(mm)	5 to 15	10
Sludge Scraper Speed	(m/h)	15 to 50	30

[*] Based on total flow (feed plus recycle) and the maximum cross-sectional area of the contact zone.

[**] Data from Haarhoff and van Vurren (1994) based on total flow (including recycle) and effective flotation area.

[#] Data from Edzwald and Walsh (1992).

The flotation tank is divided into the contact or the reaction zone, and the separation or the clarification zone. Delineation of the boundary between the contact zone and the clarification zone is often difficult and arbitrary where the zones are not clearly separated by baffles (Harrhoff and van Vuuren, 1994). The contact zone can take many shapes, such as a section of pipe before the flotation tank, where bubbles and flocs mix intimately forming bubble-floc agglomerates, as a result of collision and contact between rising bubbles and flocs, which would rise into the clarification zone. The contact zone is considered very important and the growth of bubble-floc agglomerates within this zone is dependent on mixing time and mixing intensity.

Mixing time in the contact zone is based on the mean residence time while the degree of mixing is dependent on the complex hydrodynamics within the contact zone, which is related to the mean velocity of water. Mixing time usually ranges from 1 to 4 min. The mean velocity of water, or hydraulic loading rate, is based on the maximum cross-sectional area of the contact zone. Typical hydraulic loading rates range from 40 to 100 m/h (Harrhoff and van Vuuren, 1994).

Two parameters are considered important for the clarification zone. The first is the cross-flow velocity from the contact zone into the clarification zone. A very high velocities will induce a circulation pattern within the clarification zone and excessive turbulence may disrupt the air/floc agglomerate. Typical values ranges from 20 to 100 m/h (Harrhoff and van Vuuren, 1994).

The second parameter is the hydraulic loading rate. A very high hydraulic loading will result in a downward flow velocity toward the outlet which may exceed the rising velocity of the bubble-floc agglomerates. Hydraulic loading can be based on the total flow rate (feed plus the recycle flow). Typical values range from 5 to 11 m/h (Harrhoff and van Vuuren, 1994).

In the flotation process, three distinct phases can be distinguished: (1) bubble formation and supplied air concentration; (2) bubble-particle interactions in the contact or the reaction zone; and (3) bubble-particle agglomerate rise in the flotation or the separation zone. Phase two can be further divided into three sub-phases: (a) bubble rise velocity; (b) bubble-particle collisions; and (c) bubble-particle attachment. The following sections will discuss these phases in detail.

2.1.3.2 Bubbles formation and air supplied

A bubble can be defined as a region in space occupied by a gas and enclosed by a gas-liquid interface. Bubble's shapes can be divided into three distinct types: spherical, ellipsoidal and spherical capped bubbles. Very small bubbles with mean diameters less than 1000 μm are considered spherical in appearance and rise with a steady rectilinear motion (Clift et al., 1978). The shape of the bubble is determined by the balance between the normal and tangential stresses, in each phase, at the interface. Factors which contribute to the shape of the bubble include fluid forces, viscosity, surface tension and adsorbed surface agents.

Small air bubbles in the range of 10 to 100 μm are formed when the pressurized recycle water is injected into the flotation tank using needle valves or specially designed nozzles. The bubble formation process can be described in two consecutive steps: nucleation and growth (Raaykart and Haarhoff, 1994). The first step commences spontaneously after the pressure reduction through the nozzle producing bubble nuclei according to the thermodynamic principle of minimizing the free energy change (Edzwald, 1995). Assuming air to be ideal gas, the critical diameter of the bubble nucleus d_{Bc} for homogeneous nucleation is:

$$d_{Bc} = \frac{4\,\sigma}{\Delta P} \tag{2.4}$$

where σ is the surface tensionand ΔP is the pressure difference across the nozzle. Equation 2.4 shows that as the pressure change increases, smaller bubble nuclei are formed. However, there is a diminishing return in reducing the bubble size above saturator pressure of 500 kPa (Heinanen et al., 1992).

After all the excess air in the saturated recycle water is transferred from the dissolved to the gas phase, the second step, or bubble growth, begins. During the second step, the total air volume remains constant but the bubbles continue to grow due to coalescence. Additional bubble growth may occur due to the decrease in the hydrostatic pressure as the bubbles rise in the flotation tank. Both of these factors have negligible effects on the small bubbles formed in the DAF system (Takahashi et al.,1979).

Measurements of bubble size distribution for DAF system indicate that bubbles maintain steady state size of 10 to 100 μm with mean bubble diameter of 40 μm (Edzwald, 1995). This steady state depends on the saturation pressure, recycle flow rate and nozzle geometry (Takahashi et al.,1979). The study by Takahashi and co-workers (1979) showed that the mean bubble diameter decreased as the saturation pressure and the recycle flow rate through the nozzle increased. It was also found that bubble diameter increased with nozzle length.

In order to ensure small bubbles, or microbubbles, in the flotation tank, saturator gage pressure, P_{Sat}, of 400 to 600 kPa are recommended (Edzwald et al., 1992). Also, the recycle flow, or the saturated water flow, Q_{Sat}, must be high enough to provide a rapid pressure drop and to prevent backflow and bubble growth in the vicinity of the injection system. However, the production of large bubbles, or macrobubbles, which are significantly larger than the mean bubble diameter is inevitable. These macrobubbles rise rapidly to the surface and as a result interfere with the slowly rising agglomerates of flocs and microbubbles and also could disrupt the float layer at the top of the flotation tank.

Macrobubbles contain a significant quantity of air of which the rest of the system is deprived. Their formation and presence in the flotation tank should be minimized because they would lower the overall efficiency of the DAF process. Raaykart and Haarhoff (1994) in their studies of numerous bubble size distributions have suggested that the boundary between macro- and micro-bubbles in the DAF process should be set at 150 μm.

The concentration of supplied air bubbles resulting from mixing the pressurized recycle flow, or the saturated water flow, with the influent raw water, Q_{Water}, affects bubble-particle collisions and consequently the removal of the attached bubble-particle. It is considered to be an important design and operating parameter in the DAF process (Edzwald, 1995).

The concentration of the supplied air can be described in terms of air volume supplied, A, per mass of suspended solids, S, or the A to S ratio, A/S, which has been used in wastewater treatment applications. Typical values for A/S in wastewater applications range from 0.005 to 0.06 mL/mg (Metcalf and Eddy, 1979). However, for drinking water treatment, the suspended solids concentration is low resulting in A/S on the order of 0.4 mL/mg. Therefore, the A/S ratio concept is not useful for dilute suspensions experienced in drinking water treatment applications (Zabel, 1985).

The air supplied for the DAF process in drinking water treatment applications can be described in terms of (Edzwald et al., 1992): (1) the recycle ratio , R_R; (2) the mass concentration of the air released in flotation , C_R; (3) the air bubble volume concentration, Φ_B; and (4) the number concentration of air bubbles, N_B.

In practice, the recycle ratio is used as a surrogate measure of the air supplied for a constant saturator pressure, which is defined as the ratio of Q_{Sat} to Q_{water}. The equilibrium mass concentration of dissolved air for saturated water can be calculated using Henry's law, which states that the solubility of a gas in a non-reactive gas solvent mixture is directly proportional to the partial pressure of the gas above the liquid (Chang, 1981). Henry's law can be expressed as:

$$P_{gas} = K_H \,.\, X_{gas} \tag{2.5}$$

where P_{gas} is the absolute pressure of the gas above the liquid inside the saturator, K_H is Henry's constant (4.18 kPa/mg-L at 20 °C) and X_{gas} is the mole fraction of the dissolved gas defined as the number of moles of gas divided by the sum of the number of moles of gas and liquid.

Air solubility is affected by temperature and total dissolved solids. In general, the highest solubility will be observed at lower temperature and lower dissolved solids. The maximum concentration of air that can be dissolved, based on Henry's law and assuming 100 percent saturation, ranges from 215 mg/L at about 0 °C to 126 mg/L at 25 °C (Malley, 1988).

Using Henry's law as a basis, equations can be developed for the saturation and the release of dissolved air bubbles. Assuming air is a single ideal gas, the equilibrium mass concentration in the saturated stream, C_{Sat}, can be calculated as follows:

$$C_{Sat} = f \,.\, \frac{P_{total}}{K_H} \tag{2.6}$$

where P_{total} is the total air pressure of the saturator, i.e. the sum of the saturator gage pressure P_{Sat} and one atmosphere, f is the saturator efficiency factor. In practice, f is typically 70 percent for unpacked saturators and up to 90 percent for packed saturators (Hyde et al., 1977).

Work by Zabel (1984) has indicated that the highest possible efficiency in most air saturator systems is 90 percent of the theoretical saturation, i.e. based on Henry's law.

This is due to the fact that air is a mixture of gases consisting primarily of nitrogen and oxygen. Oxygen has higher solubility than nitrogen, dissolving more rapidly producing a nitrogen enriched atmosphere inside the saturator. At equilibrium, the saturator air is composed of approximately of 88 percent nitrogen and 12 percent oxygen causing a reduction by about 9 percent in the dissolution of air compared to 100 percent saturation with atmospheric air (Edzwald, 1995).

Other factors that account for lower than 100 percent saturation efficiency, which result in reducing the effective air concentration below the applied air concentration, have been identified by Haarhoff and Steinbach (1997). These factors are : (1) the slow adjustment of the saturator air composition from atmospheric to equilibrium; (2) the method whereby saturator efficiency is estimated; (3) the air precipitation efficiency of the injection nozzle, which simply relates the actual air mass precipitated to the maximum air mass that could be theoretically precipitated; (4) the nature of the bubble suspension produced by the injection nozzle; and (5) the oxygen concentration in the raw water feed.

The concentration of the air released, C_R, in the contact zone of the DAF process can be calculated based on a mass balance approach using the following equation:

$$C_R = \frac{(C_{Sat} - C_a) \cdot R_R - (C_a - C_o)}{1 + R_R} \tag{2.7}$$

where C_a is the concentration of air in the flotation tank which will remain in solution at atmospheric pressure and C_o is the concentration of air in the raw water.

Since the flotation process relies on the bubble-particle collisions, it is more instructive to describe the mass of air released in terms of bubble volume or number concentration. Bubble volume concentration, Φ_B, which is an important design and operating parameter (Edzwald et al., 1990), is typically expressed in parts air per million parts of water (ppm) or the volume of air supplied in mL per volume of water in m^3. It can be calculated as follow:

$$\Phi_B = \frac{C_R}{\rho_{Sat}} \tag{2.8}$$

where ρ_{Sat} is the density of saturated air. High values of Φ_B ensure high collision opportunities between particles and bubbles and consequently higher flotation efficiency.

The bubble number concentration, N_B, can be estimated by dividing Φ_B by the average volume of a single bubble, v_B. Since bubbles with diameters less than 100 μm rise like solid spherical particles in water at low Reynolds number (Levich, 1962; Tsukada et al., 1984), the following expression for N_B can be used:

$$N_B = \frac{6\,\Phi_B}{\pi\, d_{Bv}^{\,3}} \tag{2.9}$$

where d_{Bv} is the volumetric mean bubble diameter which is calculated using the following equation:

$$d_{Bv} = \left[\frac{\Sigma (N_{Bi} \times d_{Bi}^{\,3})}{\Sigma N_{Bi}}\right]^{1/3} \tag{2.10}$$

where N_{Bi} is the number of bubbles with diameter d_{Bi}.

Table 2.2 presents a summary of calculations of the mass concentration, C_R, the bubble volume concentration, Φ_B, and the bubble number concentration, N_B, based on Equations 2.6 through 2.9 for recycle ratios of 3 to 15 percent, saturator pressure of 480 kPa, saturator efficiency of 70 percent and at 20 °C. These calculations were based on an average bubble diameter of 50 μm.

Table 2.2 Bubble mass, volume and number concentration

R_R %	C_R mg/L	Φ_B ppm	N_B bubbles/mL
1	0.72	608	9.3E+03
3	2.13	1790	2.7E+04
5	3.48	2927	4.5E+04
7	4.78	4021	6.1E+04
10	6.65	5587	8.5E+04
12	7.84	6585	1.0E+05
15	9.54	8016	1.2E+05

* Saturator pressure of 480 kPa, saturator efficiency of 70%, mean bubble diameter of 50 μm and at 20 °C.

Figures 2.2 to 2.4 show the effect of saturator pressure, saturator efficiency and water temperature on bubble volume concentration as a function of the recycle ratio.

The quantity of air available for the DAF process is controlled by both the saturator pressure and the flow of the recycle or saturated water. Experiments varying the recycle ratio and pressure showed that the treated water quality was only dependent upon the total quantity of air introduced to the system, and not upon the individual values of the pressure or the recycle flow (Zabel, 1984). The main practical way to control and vary the amount of air supplied to the DAF process is through the recycle rate.

Edzwald et al. (1992) have examined air requirements for treating three different water types including fulvic acid water at dissolved organic carbon, DOC, concentration of 2 to 15 mg/L, clay turbidity waters with clay solids at 20 to 100 mg/L and algae type waters with algae at cell concentrations of 20,000 to 500,000 cells/mL. Their experimental results showed that a recycle ratio of 8% at a saturator pressure of 483 kPa with 70% saturator efficiency, which correspond to bubble volume concentration of about 4600 ppm and bubble number concentration of 1.2×10^5 bubbles/mL, was sufficient to treat successfully all types of waters.

2.1.3.3 Bubble-particle interactions in the contact zone

As it was explained earlier, the purpose of the contact zone of the DAF process is to provide collision and contact opportunities between the rising air bubbles and flocs leading to attachment and formation of bubble-particle agglomerates with densities less than that of water. The interactions of bubbles and particles in the contact zone can be divided, for the purpose of this work, into two steps: (1) the transport of bubbles to the particles, characterized by the bubble rise velocity, and (2) collision and attachment between bubbles and particles. The following sections provide detailed discussion of each step.

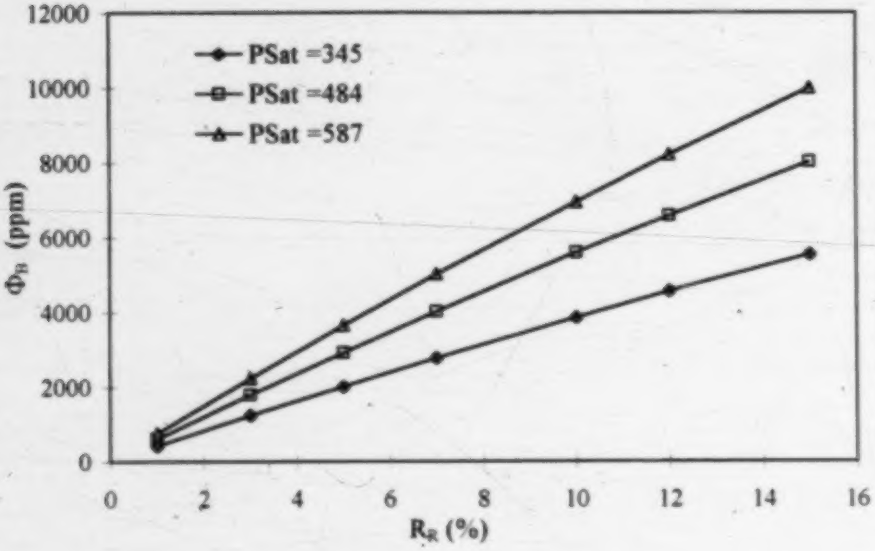

Figure 2.2 Effect of saturator pressure P_{Sat} on bubble volume concentration Φ_B as a function of the recycle ratio R_R for bubbles with mean diameter of 50 μm and saturator efficiency of 70 % at 20°C (Note: units of pressure are in kPa).

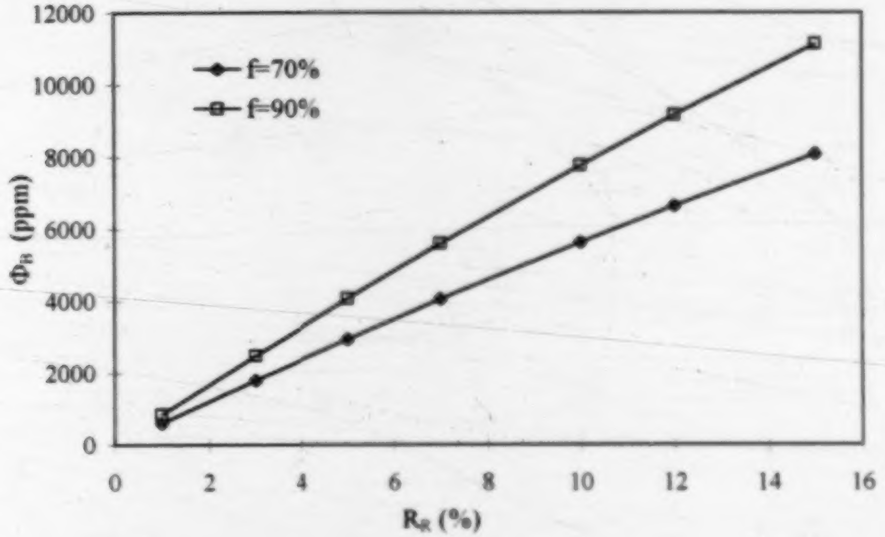

Figure 2.3 Effect of saturator efficiency *f* on bubble volume concentration Φ_B as a function of the recycle ratio R_R for bubbles with mean diameter of 50 μm and saturator pressure of 480 kPa at 20°C.

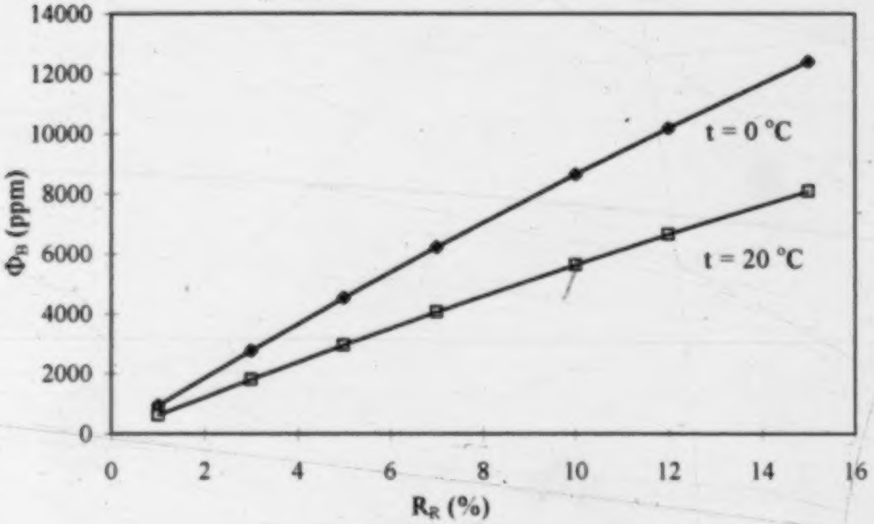

Figure 2.4 Effect of water temperature on bubble volume concentration Φ_B as a function of the recycle ratio R_R for bubbles with mean diameter of 50 μm saturator efficiency of 70 % and saturator pressure of 480 kPa .

2.1.3.3.1 Bubble rise velocity

After bubble generation and growth, the next step in the flotation process, which occurs inside the contact zone, is the transport of bubbles to the particles. The rate at which the air bubble rises can be calculated by solving the Navier-Stokes equation. Small bubbles of about 100 μm or less are formed in DAF process, which rise as rigid spheres under laminar flow conditions, i.e. Reynolds number Re << 1, and therefore follow Stokes law (Clift et al., 1978). Larger bubbles have higher rise velocities and exist as ellipsoids (1 to 10 mm) and spherical caps (> 10 mm).

Assuming that the bubble is held in a spherical shape by surface tension, the problem becomes similar to that posed by solid sphere moving steadily through a viscous liquid (Clift et al., 1978). When a bubble rises in a viscous fluid, it is acted upon by three forces: a gravitational force acting downward, a buoyant force acting upwards and a drag force, F_D, acting downward. When the terminal velocity is reached, the drag force is equal to the difference between the gravitational attraction and the Archimedes buoyancy. For a bubble with diameter d_B and.density ρ_B rising in a fluid of density ρ_f, the drag force can be expressed as:

$$F_D = \frac{\pi}{6} d_B^3 (\rho_f - \rho_B) g \tag{2.11}$$

At low Reynolds Number, i.e laminar flow, the drag on a bubble with diameter d_B is due entirely to viscous forces within the fluid (Levich, 1962) resulting in the following expression:

$$F_D = 3 \pi d_B \mu U_B \tag{2.12}$$

where μ is the fluid dynamic viscosity and U_B is the terminal rise velocity of the bubble, also called Stokes' rise velocity, in the laminar flow region. Substituting Equation 2.11 into Equation 2.12 and solving for U_B would give:

$$U_B = \frac{g\,(\rho_f - \rho_B)\,d_B^{\,2}}{18\,\mu} \tag{2.13}$$

Equation 2.13 gives good results for Reynolds Numbers up to 1.0 (Edzwald, 1995) which correspond to bubble diameters of about 120 μm at 20 °C. Also, it indicates that the rise velocity of the bubbles is proportional to $d_B^{\,2}$. In addition, water temperature would affect ρ_f and μ and as a result U_B. The effect of bubble diameter and water temperature on bubble rise velocity is summarized in Table 2.3. As shown, bubble sizes of 150 μm and below, at 4 °C, and bubble sizes of 120 μm and below at 20 °C, will ensure laminar flow, i.e $Re \leq 1.0$.

For bubble with diameter in excess of 120 μm at 20 °C, the rise velocity deviates from that indicated by Stokes' model (Levich, 1962). The drag force on the rising bubble with diameter d_B can be expressed in terms of the bubble drag coefficient, C_{DB}:

$$F_D = C_{DB}\,\frac{\pi\,d_B^{\,2}}{4}\,\rho_f\,\frac{U_B^{\,2}}{2} \tag{2.14}$$

where $\rho_f\,(U_B^{\,2}/2)$ is the dynamic pressure on the bubble. At the terminal rise velocity, U_B, Equation 2.11 can be substituted into Equation 2.14. Solving for C_{DB} would give:

$$C_{DB} = \frac{4}{3}\,\frac{g\,d_B}{U_B^{\,2}} \tag{2.15}$$

Table 2.3 Effect of bubble diameter and temperature on bubble rise velocity, based on Stokes' Law, and Reynolds Number, Re.

d_B	4 °C		20 °C	
(μm)	U_B (m/s)	Re	U_B (m/s)	Re
10	3.10E-05	0.0003	5.51E-05	0.0005
20	1.24E-04	0.0025	2.20E-04	0.0044
30	2.79E-04	0.0083	4.96E-04	0.0148
40	4.95E-04	0.0197	8.82E-04	0.0350
50	7.74E-04	0.0384	1.38E-03	0.0684
60	1.11E-03	0.0664	1.98E-03	0.1182
70	1.52E-03	0.1055	2.70E-03	0.1878
80	1.98E-03	0.1574	3.53E-03	0.2803
90	2.51E-03	0.2242	4.46E-03	0.3991
100	3.10E-03	0.3075	5.51E-03	0.5474
110	3.75E-03	0.4093	6.67E-03	0.7286
120	4.46E-03	0.5314	7.94E-03	0.9459
130	5.23E-03	0.6756	9.31E-03	1.2027
140	6.07E-03	0.8438	1.08E-02	1.5021
150	6.97E-03	1.0379	1.24E-02	1.8475
200	1.24E-02	2.4601	2.20E-02	4.3794
500	7.74E-02	38.4390	1.38E-01	68.4274

For low Re, i.e. laminar flow, substitution of Equation 2.12 into Equation 2.14 yields the following equation:

$$C_{DB} = \frac{24}{Re_B} \tag{2.16}$$

where Re_B is the Reynolds number of bubble with diameter d_B defined as:

$$Re_B = \frac{\rho_f \, d_B \, U_B}{\mu} \tag{2.17}$$

In the previous discussion, Stokes' equation, given by Equation 2.13, describes the relative velocity between fluid and a bubble rising in a quiescent flotation column, i.e. hydraulic loading or superficial liquid velocity, U_L, is equal to zero. The terminal rise velocity based on Stokes' equation will be termed the relative bubble rise velocity, $U_{B\,rel}$, in this research.

Under actual operational conditions, bubble rise velocity would be affected by the contact zone hydraulic loading. Therefore, the instantaneous bubble rise velocity $U_{B\,inst}$, which can be measured using a laser Doppler anemometer, would describe the actual bubble rise velocity inside the contact zone. The instantaneous bubble rise velocity $U_{B\,inst}$ can be defined as:

$$U_{B\,inst} = U_{B\,rel} + U_L \tag{2.18}$$

where U_L is defined as the total flow rate, Q_{Total}, divided by the maximum cross-sectional area of the contact zone, A_{CZ}. The total flow rate is the sum of Q_{Sat}, Q_{water} and the volumetric flow rate of air, Q_A, which is defined as the bubble volume concentration, Φ_B, multiplied by Q_{Sat}. Since calculations of Q_A indicated that it was much smaller than both Q_{Sat} and Q_{water}, it was not included in Q_{total}.

2.1.3.3.2 Bubble-particle collision and attachment

There are three mechanisms that describe the collision and attachment of air bubbles to the particles which include: (1) collision and adhesion of large particles to large bubbles, which is termed contact flotation (Derjaguin et al., 1984); (2) collision and surface attachment of rising bubbles to the pre-formed flocs, which is termed contactless flotation (Derjaguin et al., 1984); and (3) growth of bubble nuclei within the floc structure (Kitchener and Gochin, 1981).

The first two mechanisms are applied to water treatment applications while the third mechanism is applied to wastewater treatment and sludge thickening. The first mechanism, which is important in the separation of mining mineral ores, is observed for particles larger than 100 μm and can be described as a two step process (Derjaguin et al., 1984). The first step of the contact flotation process is that the particle inertia would rapidly rupture the intervening water layer between the bubble and the particle and as a result the particle would make contact with the bubble surface. The second step is the formation of a three phase wetting perimeter, or contact angle, through the interaction of surface tension forces. The contact angle must be finite and large enough such that the work or energy of adhesion of water to the solid particle is less than the work or energy of cohesion of the water (Kitchener, 1984). A large contact angle indicates hydrophobicity and good attachment.

The second mechanism is considered the primary mechanism of bubble-particle collision and attachment in water treatment. Contactless flotation, also termed inertialess flotation is analogous to a hetrocoagulation model involving the stability of bubbles and particles (Edzwald, 1995). It can be described as a three step process flotation (Derjaguin et al., 1984). First, particles are transported to the vicinity of the bubble surface. Second, the intervening water layer is thinned to a critical thickness by the particle-bubble collision and hydrodynamic forces. Third, the surface forces of attraction and repulsion become dominant once the critical thickness is reached and the intervening water layer either ruptures resulting in bubble-particle attachment by surface forces or the particle-bubble surfaces repel each other resulting in no attachment. Therefore, the third step of the process depends on the surface chemistry of the particles and bubbles. The surface chemistry and the chemical aspects of the attachment will be discussed later in this section.

The bubble-particle collision in contacless flotation is affected by the hydrodynamic forces. Theses forces are: the long range hydrodynamic forces, LRHF, short range hydrodynamic forces, SRHF, and the pressing hydrodynamic forces, PHF. The LRHF causes particles approaching the bubble to deviate from their rectilinear path due to the curving of the fluid streamlines which is caused due to the fact that the fluid velocity at the bubble surface approaches zero.

The long range forces occur at distances on the order of the bubble size upstream of the bubble surface. The LRHF does not affect the transport of large particles to the bubble surface because the inertial forces of these particles are much greater than the LRHF. However, transport of 100 μm particles and smaller is greatly affected by the LRHF (Derjaguin et al., 1984).

The short range hydrodynamic force is caused by the hydrodynamic resistance force Fμ between two identical spheres and can be given as (Taylor, 1953):

$$F\mu = \frac{k_\mu U_{PB} \mu d_s^2}{(H_s - d_s)} \tag{2.19}$$

where k_μ is an empirical proportionality constant, U_{PB} is the particle-bubble approach velocity, μ is the dynamic viscosity of water, d_S is the sphere diameter and H_S is the separation distance between the center of the spheres. Equation 2.19 shows that Fμ increases as U_{PB} and d_S increase and H_S decreases. Also, Equation 2.19 indicates that as temperature decreases, i.e. as μ increases Fμ increase. For large particles, inertia forces overcome the SRHF so that Fμ is zero (Derjaguin et al., 1984).

The pressing hydrodynamic forces result from the differential velocity of the approaching particle and fluid. The velocity of the particle is slowed as it approaches the bubbles by the hydrodynamic forces so that the radial velocity of the fluid is higher than the velocity of the particle. As a result, the radial flow of the fluid envelops the particle and presses it toward the bubble surface. This force would result in the initial thinning of the intervening water layer, which is counteracted by the LRHF. PHF alone is not sufficient to overcome the SRHF, so that the effect of both PHF and the surface forces is required for collision and attachment.

Surface forces and the hydrophobic and hydrophilic nature of the particles play an important role in the attachment of bubbles and particles (Gaudin, 1957; Anderson and Rubin, 1981). When solid particles are immersed in water, an electric double layer forms at the solid-liquid interface (Stumm and Morgan, 1981). This electrical double layer generally arises from three mechanisms: chemical reaction at the surface resulting in ionization of surface groups, or complexation with solutes, or isomorphic replacement of atoms within the crystalline lattice.

Electroneutrality of the solid-liquid interface results in the formation of a second diffuse layer containing oppositely charged counter ions adjacent to the surface. The interaction of the overlapping electrical double layers raises the electrical double layer force, EDLF, which is a repulsive force. The EDLF is counteracted by the London-van der Waals, LVDW, molecular force of attraction, which results from the dipole interaction between atoms and molecules. The LVDW force is an attraction force for most of solids in water (Gregory, 1969).

Small particle and bubble interactions are assumed to behave the same way as the particle-particle interactions described by the Derjaguin-Landaue and Verwey-Overbeck, DLVO, theory (Derjaguin et al., 1984). The DLVO theory, after the classical works by Derjaguine and Landau (1941), and Verwey and Overbeek (1948), involves estimating the energy of attraction from the LVDW forces and the energy of repulsion from the EDL forces. The theory shows that the repulsion energy is an exponential function of the distance between two identical spheres with a range on the order of the thickness of the double layer. On the other hand, the attraction energy decreases as the reciprocal of the distance between the spheres.

There are two conditions for contactless flotation to occur. First, particles should be unstable, i.e. have low electrophoretic mobility (EPM). The second condition is related to the balance between the LVDW attraction forces and the hydrodynamic resistance forces. This can be explained by first presenting the LVDW attraction force, F_A, by the following equation:

$$F_A = \frac{-A_H \, d_s}{24 \, H_s^2} \tag{2.20}$$

where A_H is the Hamaker constant which ranges between 10^{-13} to 10^{-12} ergs. Comparison between Equations 2.19 and 2.20 indicates that the attraction force increases as the reciprocal of $H_s^{\,2}$ whereas the hydrodynamic force increases as the reciprocal of H_s to the first power. Since U_{PB} is small and does not significantly affect F_μ at small $(H_s\text{-}d_s)$ values, therefore, F_A can overcome F_μ and contactless flotation can be achieved.

Edzwald (1995) has suggested, based on experimental evidence, that there are two important conditions for bubble-particle attraction and flotation: (1) charge neutralization through efficient coagulation and flocculation, and (2) production of hydrophobic particle surfaces or hydrophobic spots on the particle surfaces. For many particles, hydrophopicity is simply increased by reducing the charge. However, there are particles, such as amorphous $Al(OH)_3$ which have polar surface groups that bond to water molecules and therefore render them hydrophilic. This poly-molecular layer of water would hinder the bubble-particle attachment. However, work by Kitchener and Gochin (1981) suggestes that naturally occurring organic matter present in water act as surfactants or collectors and can adsorb onto the surfaces of metal hydroxide flocs, and therefore render them hydrophobic.

2.1.3.4 Bubble-particle agglomerates rise in the clarification zone

After bubble attachment and reduction in particle density, the formed bubble-particle agglomerates rise to the surface of the flotation tank in the clarification or separation zone. Bratby and Marais (1975) have developed a concept for the motion of these agglomerates inside the flotation tank. In the contact zone column, the hydraulic flow is upward and in the same direction as the buoyancy. In this stage, the flocs have no chance to settle whether they are attached to air bubbles or not. However, in the clarification zone the hydraulic flow turns downward or opposite to the buoyancy. If the velocity of the bubble-particle agglomerates is higher that the hydraulic loading inside the clarification zone, then these agglomerates rise and are collected in the foam layer on the surface.

Bratby and Marais (1975) called the velocity that just keeps the agglomerate in the foam layer as the limiting overflow rate of the separation zone, U_{OS}, i.e. the hydraulic loading based on the surface area of the separation zone. Haarhoff and van Vuuren (1994) have recommended the hydraulic loading in the clarification zone to be 5.0 to 11.0 m/h based on the total flow, i.e. including the recycle flow.

The U_{OS} depends basically on the volume and the amount of air bubbles attached to the particles. The volume of an air bubble is important in lowering the particle density and therefore producing flotation. The following equations are used to demonstrate the effect of bubble-particle attachment on the particle density. First, the mass of particles and bubbles are determined based on volume and density:

$$M_P = \frac{\rho_P \pi d_P^3}{6} \tag{2.21}$$

and

$$M_B = \frac{\rho_B \pi d_B^3}{6} \tag{2.22}$$

where M_P is the particle mass, M_B is the bubble mass, ρ_P is the particle density, ρ_B is the bubble density, d_P is the particle equivalent spherical diameter, and d_B is the bubble mean diameter. Assuming n_B bubbles are attached to one particle, Equations 2.21 and 2.22 are combined with equations for bubble and particle volume, resulting in the following equation for the particle-bubble density ρ_{PB}:

$$\rho_{PB} = \frac{[\rho_P d_P^3 + n_B(\rho_B d_B^3)]}{[d_P^3 + n_B(d_B^3)]} \tag{2.23}$$

The equivalent spherical diameter of the bubble-particle agglomerate, d_{PB}, can be calculated using the following formula:

$$d_{PB} = [\, d_P^3 + n_B(d_B^3)]^{1/3} \tag{2.24}$$

The rise velocity of the bubble-particle agglomerate, $U_{PB\,aggl}$, assuming Stokes' drag conditions, i.e. $Re_{PB} \le 1.0$, is calculated by:

$$U_{PB\,aggl} = \frac{g(\rho_w - \rho_{PB})\, d_{PB}^2}{18\mu} \tag{2.25}$$

For transition flow conditions, i.e. $1 < Re_{PB} < 50$, the rise velocity of the bubble-particle agglomerate would be (Edzwald, 1995):

$$U_{PB\ aggl} = \frac{g^{0.8}[(\rho_w - \rho_{PB})/\rho_w]^{0.8}\ d_{PB}^{1.4}}{10\upsilon^{0.6}} \tag{2.26}$$

where υ is the kinematic viscosity.

For alum flocs with initial density of 1.01 g/mL at 20°C, and size less than 100 μm, one bubble of size 60 μm would easily reduces the floc density to less than 1 gm/mL. Table 2.4 summarizes calculations for bubbles with different mean diameters and particles varying in size from 10 to 100 μm assuming only one bubble attachment per particles.

Removal of bubble-particle agglomerates in the separation zone occurs under plug flow conditions when:

$$U_{PB\ aggl} \geq \frac{U_{OS}}{1 - m_S} \tag{2.27}$$

where m_S is the fraction of dead space inside the clarification tank. For practical purposes, the dead space can be neglected (Baeyens et al., 1995)

It can be assumed that there is a critical bubble-floc agglomerate diameter $d_{PB\ critical}$ when $U_{PB\ aggl} = U_{OS}$. Agglomerates having $d_{PB} > d_{PB\ critical}$ will have $U_{PB\ aggl}$ higher than U_{OS} and therefore will be separated from the effluent. On the other hand, agglomerates with $d_{PB} < d_{PB\ critical}$ will be carried with the effluent. The critical bubble-floc agglomerate diameter can be calculated using Equations 2.28 and 2.29:

$$d_{PB\ Critical}\ \text{for } Re_{PB}<1 = \left[\frac{18\mu U_{OS}}{g(\rho_w - \rho_{PB})}\right]^{0.5} \tag{2.28}$$

and

Table 2.4 Bubble-particle agglomerate velocity for different bubble and particle sizes assuming only one bubble attached

	d_B = 40 μm			d_B = 60 μm			d_B =80 μm		
d_P * μm	ρ_{PB} g/mL	d_{PB} μm	$U_{PB\ aggl}$ m/h	ρ_{PB} g/mL	d_{PB} μm	$U_{PB\ aggl}$ m/h	ρ_{PB} g/mL	d_{PB} μm	$U_{PB\ aggl}$ m/h
8	0.009	40.1	3.2	0.004	60.0	7.1	0.002	80.0	12.7
10	0.017	40.2	3.2	0.006	60.1	7.1	0.003	80.1	12.7
15	0.052	40.7	3.1	0.017	60.3	7.1	0.008	80.2	12.7
20	0.113	41.6	3.0	0.037	60.7	7.1	0.017	80.4	12.6
30	0.300	45.0	2.8	0.113	62.4	6.9	0.052	81.4	12.5
50	0.668	57.4	2.2	0.371	69.9	6.1	0.199	86.0	11.8
70	0.851	74.1	1.6	0.620	82.4	5.1	0.406	94.9	10.6
100	0.949	102.1	1.0	0.831	106.7	3.8	0.668	114.8	8.6

* Assuming particle density of 1.01 g/mL at 20°C

$$d_{PB\ Critical} \text{ for } 1<Re_{PB}<50 = \left[\frac{10\upsilon^{0.6}\,U_{OS}}{g^{0.8}\left[(\rho w-\rho_{PB})/\rho_w\right]^{0.8}}\right]^{0.7} \tag{2.29}$$

Studies performed by Heinänen et al. (1992) indicated that the mean rising velocity of bubble-particle agglomerate was about 27 m/h in the clarification tank. Visual observations showed that the number of attached air bubbles varied from 1 to about 20 per agglomerate. Furthermore, there was hardly any separation or detachment of air bubbles from the agglomerates. Therefore, following the recommendations of Haarhoff and van Vurren (1994) for a maximum clarification zone hydraulic loading of 11 m/h and designing the tank in a circular shape, to minimize the dead zone, it can be assumed that all the agglomerates entering the clarification tank are removed.

2.2 Measurement of Bubble Size, Concentration and Velocity with the Particle Dynamic Analyzer (PDA)

2.2.1 Introduction

Bubble size distribution, BSD, and bubble velocity distribution can be measured simultaneously by using the particle dynamic analyzer, PDA, instrument which is based on phase Doppler anemometry which itself is an extension of laser Doppler anemometry, LDA.

The operating principles of the PDA is explained through the use of the simple fringe model. The PDA consists of an optical system which splits a continuous laser beam into two parallel beams which pass through a spherical lens that causes these beams to intersect at the focal point of the lens. As a result, a set of plane parallel interference fringes are produced at the intersection point of the two beams. Figure 2.5 shows the fringe plane which is also called the instrument measurement volume or

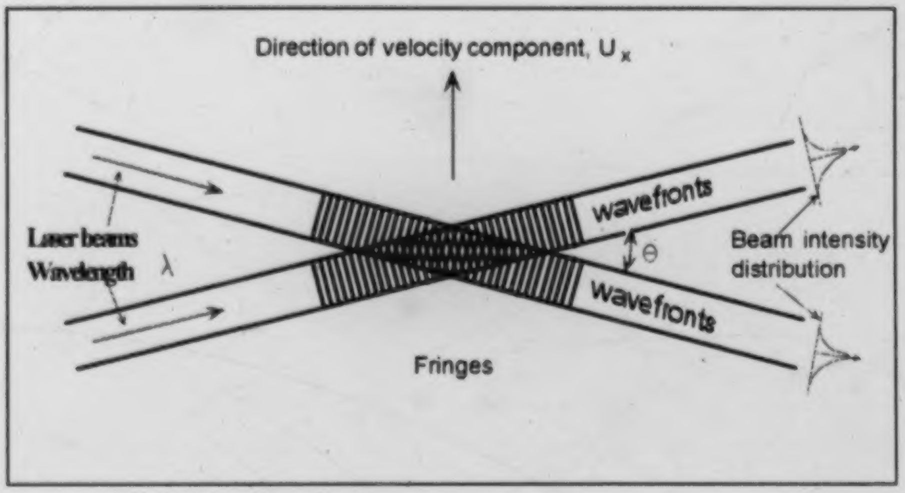
Direction of velocity component, U_x
Laser beams
Wavelength λ
wavefronts
wavefronts
Θ
Beam intensity distribution
Fringes

Figure 2.5 The fringe model and the probe volume
(Adapted from DANTEC, 1989)

simply the probe volume. The spacing between the interference fringes depends on the wavelength of the laser and the angle between the two beams θ.

2.2.2 Velocity measurements

Bubbles moving across the fringe pattern will scatter light in different directions. The scattered light, which has another frequency due to the Doppler effect, is collected by the receiving optics and is converted into an electrical signal by a high speed photodetector. The frequency of the electrical signal, which is proportional to the particle velocity, is then measured with an electrical device.

In this study, one of the objectives is to measure the instantaneous bubble rise velocity and therefore it is important to determine the sign of the velocity of the bubble. Since the fringe pattern produced at the crossing of the two beams will be stationary, the frequency of the scattered light carries no information of the sign of the velocity of the bubble.

To obtain information on the sign of the velocity, a small frequency shift is introduced in the transmitting optics to one of the crossing laser beams. Consequently, the fringe pattern moves perpendicularly to the fringe plane such that the light intensity at any point is modulated at the shift frequency. As a result, bubbles moving in the probe volume will scatter light modulated such that the difference between the modulation frequency and the shift frequency is proportional to the velocity of the bubble.

Therefore, a bubble moving in the opposite direction to the fringe movement increases the modulation while a bubble moving in the same direction reduces it. In the PDA system used for this study (DANTEC, Denmark), a 40 MHz shift is produced using a Bragg cell.

2.2.3 Size and concentration measurements

To measure bubble size, simultaneously with the velocity, the PDA utilizes the phase of the scattered light, which contains information regarding bubble size. The operating theory can be explained using the simple fringe model. If the interference fringes in the probe volume are considered to be light rays, they are projected into space by the transparent bubble as shown in Figure 2.6.

As the bubble moves through the probe volume, the projected fringes are swept through space. A stationary photodetector, the same photodetector used for converting velocity frequencies into electrical signals, will observe alternately light and dark fringes moving with different frequency due to the Doppler effect. If two detectors U_1 and U_2 are placed at a separate locations, they will observe the same frequency but with a relative phase shift proportional to the detectors spacing, S_D, divided by the projected fringe spacing, S_F. The separation of the projected fringes at a large distance, R, from the probe volume is inversely proportional to the effective focal length of the bubble, f_B. For a spherical bubble, the focal length is proportional to the bubble diameter, d_B, and therefore the measured phase shift is proportional to the bubble diameter.

The position and the spacing of the two detectors has an effect on distinguishing between small and large bubbles as well as on size resolution. Choosing a wide detector spacing such as U_1-U_2 gives a phase shift, φ_{1-2}, which varies rapidly with bubble diameter and permits high resolution measurements to be made. However, large particles would be indistinguishable from small particles, because they have phase shifts larger than 360°, they will fold-down and give incorrect results.

In order to extend the unambiguous range, which has a maximum φ of 360°, while retaining a high resolution, a three detector configuration is used. The closely spaced detector pair, U_1-U_3, has a slowly varying phase shift φ_{1-3} and is used to resolve ambiguity in the measurement from the primary detector pairs, U_1-U_2.

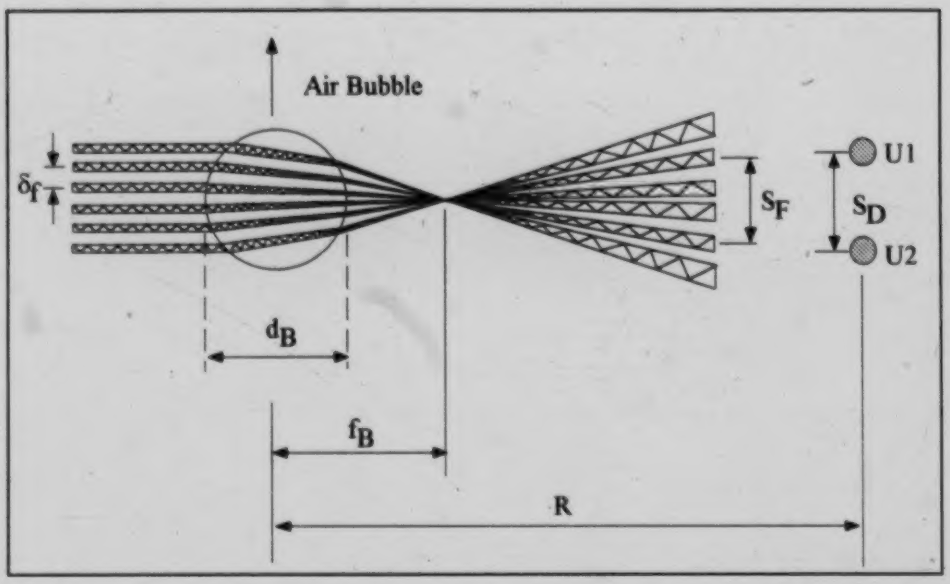
Air Bubble
δ_f
d_B
f_B
R
S_F
S_D
U1
U2

Figure 2.6 Fring model of phase shift (Adapted from DANTEC, 1989)

Also, U_2-U_3 can be used for self consistency and validation checks.

To calculate the exact relation between phase shift and bubble diameter, it is necessary to consider the light scattering process. This process is approximated by ray optics which divides the light scattering into reflection, refraction, 2nd order refraction and diffraction in the forward direction. Different scattering orders, with the exception of diffraction, produce a linear phase vs. diameter curve each with a unique slope.

In order to calculate the exact relation between phase shift and bubble diameter, a linear phase response curve should be obtained (DANTEC, 1989). In order to achieve that, a scattering angle must be chosen where a single scattering order is dominant. For bubbles, which are transparent and have refractive index less than that for water, the best phase-diameter linearity and the highest signal levels are obtained at a scattering angle of 70° from the true forward, i.e. forward scatter configuration.

In order to measure bubble number concentration, N_B, the bubble arrival rate, velocity and the instrument cross section must be known. The concentration is given by the arrival rate normalized by the velocity times the instrument cross section.

The main difficulty is in determining the instrument cross section since it depends not only on the laser power but also on the bubble size. Bubbles passing through the edge of the laser beam scatter less light than those passing through the center. For a bubble to be detected, the light level must be above a fixed detection threshold. Since large bubbles scatter more light than small ones, they can pass further from the laser beam center and still be detected. Thus there is a counting bias in favor of larger bubbles.

To get the correct size and concentration distribution, the bias must be completely eliminated. This is accomplished by normalizing the distribution with a function of the measured bubble residence time.

2.2.4 Data Processing

In order to calculate the velocity and size values, the signals obtained from the receiving optics must be processed. The most common processors used include frequency trackers, counters, burst spectrum analyzer and covariance processors. The function of these processors is to demodulate the PDA signal to determine the Doppler frequency and phase.

In this study, the system used was a covariance processor which provides a wide range of bandwidths, high data rates and is able to handle low signal-to-noise ratios. This processor uses a covariance processing technique in which the phase and the frequency detectors utilize powerful analog correlation techniques (Lading and Anderson, 1988).

In the frequency detector, the electrical signal from the main photodetector is split into two signals, one of which is delayed by a known amount of time. This corresponds to adding a phase of the delay time multiplied by the unknown frequency. The two signals are input to a phase detector, which measures their phase difference, which is divided by the delay time to yield the unknown frequency. In the phase detector, signals from the two photodetectors are fed into an analog cross correlator. The output of the cross correlator is proportional to the cosine of the phase difference between the two signals.

Raw data collected by the PDA instrument are validated. This validation is based on the signal to noise levels and the fringe counts. Each time a bubble passes through the probe volume and produces a validated signal, an instantaneous bubble velocity and the corresponding size are determined.

Since the measured velocity distribution may be correlated with the magnitude and the direction of the bubble velocity, fast moving bubbles are more likely to be detected than slower ones. Also, bubbles passing through the outer edges of the probe volume are less likely to be detected. Therefore, to account for the velocity bias, mean velocities are calculated based on residence time weighting.

CHAPTER 3

CONTACT ZONE KINETIC MODEL

3.1 Introduction

The dissolved air flotation, DAF, process has been designed empirically, based largely on experience. Models that describe the main variables affecting the performance of the DAF process are needed in order to improve DAF design and operations. As it is discussed in Section 2.1.3, the DAF tank is divided into the contact and the clarification zones. Modeling of the clarification zone is similar to the sedimentation process where Stokes' law type expressions are used to describe the rise velocity of the bubble-particle agglomerates (Edzwald, 1997). On the other hand, modeling of the contact zone is considered more complicated because there are many interrelated chemical and physical variables that describe the collision and attachments between bubbles and floc particles.

Two approaches have been used to model the contact zone for DAF applications for drinking water treatment: single collector collision efficiency based model, in which bubbles are viewed as collectors of particles, and flocculation type model for collisions among bubbles and particles (Edzwald, 1995).

The single collector efficiency (SCE) model is based on the single collector collision efficiency concept which describes mass transport from the bulk water to the bubble surface in which bubbles act as collectors (analogous to deep bed filtration where sand particles act as collectors. This model has been used by Flint and Howarth (1971) and Reay and Ratcliff (1973) for flotation and also has been used as a modeling approach for the removal of particles by deep bed filtration (Yao et al., 1971). The SCE model identifies important design and operating variables which would affect the performance of the DAF process.

A more complicated approach for modeling bubble-particle collisions was considered by Tambo and co-workers (Tambo and Matsui, 1986; Fukushi et al., 1994). Their model, called the population balance model in turbulent flow or the PBT model, describes the bubble-particle collisions in the contact zone as a heterogeneous flocculation process where the bulk fluid flow is characterized by turbulent flow. They have developed flocculation rate equations for particle transport based on collisions caused by the bulk water velocity differences caused by the turbulent mixing.

The actual difference between the PBT and the SCE models is the bubble-particle collision rate. This is due to the differences in the flow condition assumptions used in each model. The SCE model considers the transport of particles in the vicinity of the bubble surface where the relative motion of the fluid to the bubble creates streamlines of flow around the bubble, which occurs under laminar flow conditions. Also, the SCE model uses simpler mathematical representation for the bubble-particle collision rate. For these reasons, the SCE model is chosen as the basis for developing the contact zone kinetic model.

In this chapter, a kinetic model describing bubble-particle interactions inside the contact zone is developed based on the SCE model incorporated into a continuous flow DAF system. In order to achieve this objective, the SCE model is discussed in detail with all the assumptions used in its derivation. Also, the hydrodynamic characterization for the continuous flow contact zone is discussed in detail.

3.2 Single Collector Efficiency Model

The single collector efficiency (SCE) model has been described in details by Edzwald and co-workers (Edzwald et al, 1990; Malley and Edzwald, 1991; Edzwald, 1995). The SCE model describes the mass transport of particles from the bulk water to bubble surfaces. A basic assumption is used in this model where bubbles are formed rapidly and almost instantaneously in the contact zone. This assumption may be valid due to the large pressure differences across the nozzle used to inject the saturated water into the DAF tank.

The single bubble removal efficiency, R, can be described mathematically as:

$$R = \alpha_{PB} \cdot \eta_T \tag{3.1}$$

where η_T is the total single bubble collector efficiency, which represents the total transport rate and can be expressed as:

$$\eta_T = \frac{\text{Bubble} - \text{particle collision rate}}{\text{Bubble} - \text{particle approach rate}} \tag{3.2}$$

and α_{PB}, the collision efficiency factor between particles and bubbles, is given by:

$$\alpha_{PB} = \frac{\text{Bubble} - \text{particle attachment rate}}{\text{Bubble} - \text{particle collision rate}} \tag{3.3}$$

The α_{PB} factor is usually determined empirically and is strongly dependent on coagulant type, dosage and pH (Edzwald, 1997). It ranges from zero, which indicates no collisions are successful and there is no bubble-particle attachment, to one, which indicates that all collisions lead to attachment. Typical α_{PB} values found in water treatment range from 0.3 to 0.5 (Liers et al., 1996).

In order to quantify η_T, the convective-diffusion equations, which were based on the work of Smoluchowski (1917) and Levich (1962), and the particle trajectory analysis, which was based on the work of Flint and Howarth (1971), were used to derive individual particle transport expressions for the single collector efficiency. The individual particle transport mechanisms that were considered are: Brownian diffusion of particles, fluid shear or interception of particles by a rising bubble, differential settling of particles onto a bubble and collision due to inertia.

To use this approach, different assumptions have to be utilized. It is assumed that the bubbles act as rigid spheres and that the particles are moving in a uniform flow field of velocity relative to the bubble. In addition, Stokes' laminar flow conditions are assumed applicable for bubbles of 120 µm and smaller at 20°C. Also, the London-van der Waals, the electric double layer and the hydrodynamic forces are all included in the α_{PB} term.

The mathematical representation for all transport mechanisms, expressed as single collector efficiency, can be summarized in the following equations (Edzwald et al., 1990):

$$\eta_D = 6.18\left(\frac{K_B\,T}{g(\rho_f-\rho_B)d_P}\right)^{2/3}\cdot\frac{1}{{d_B}^2} \tag{3.4}$$

$$\eta_I = \frac{3}{2}\left(\frac{d_P}{d_B}\right)^2 \tag{3.5}$$

$$\eta_S = \left(\frac{\rho_P-\rho_f}{\rho_f-\rho_B}\right)\cdot\left(\frac{d_P}{d_B}\right)^2 \tag{3.6}$$

$$\eta_{IN} = \frac{g\rho_P\,\rho_f\,d_B\,{d_P}^2}{324\mu^2} \tag{3.7}$$

where η_D is the single collector collision efficiency for Brownian diffusion, η_I is the single collector collision efficiency for interception, η_S is the single collector collision efficiency for differential settling, η_{IN} is the single collector collision efficiency for inertia, K_B is Boltzman's constant, T is the absolute temperature, d_P is the particle diameter, ρ_P is the particle density, d_B is the bubble diameter, ρ_B is the bubble density, ρ_f is the water density and μ is the water dynamic viscosity.

The total single collector efficiency, η_T, is equivalent to the sum of the single collector efficiencies due to Brownian diffusion, interception, differential settling and inertia. η_T can be described mathematically as:

$$\eta_T = \eta_D + \eta_I + \eta_S + \eta_{IN} \tag{3.8}$$

Equations 3.4 to 3.7 indicate that η_T is affected by particle and bubble diameter, particle density and water temperature, which would affect water viscosity. The effect of particle size on η_T is shown graphically in Figure 3.1 for a bubble diameter of 60 μm, water temperature of 25°C and ρ_P of 1.01 g/mL. The following important conclusions can be drawn from studying the η_T graph carefully:

(1) η_T reaches a minimum value for particles of about 1 μm with increasing values for smaller and larger particles;
(2) η_T is controlled by Brownian diffusion for particle diameters below 1 μm and is controlled by interception for particles larger than 1 μm;
(3) η_T reaches its maximum value of 1.0 for particles 35 μm or larger when d_B is 60 μm;
(4) transport by inertia is not significant for particles and bubbles that are less than 100 μm. This indicates that the bubble-particle transport and attachment in DAF for water treatment applications is contactless or inertialess flotation;
(5) transport by differential settling is also not significant for particles less than 50 μm; and
(6) for DAF water treatment applications, where typical floc particle size is in the order of 10 μm (Edzwald, 1995), the transport by interception is the most significant term in the total single collector collision efficiency.

Therefore, η_T in Equation 3.8 can be approximated by η_I :

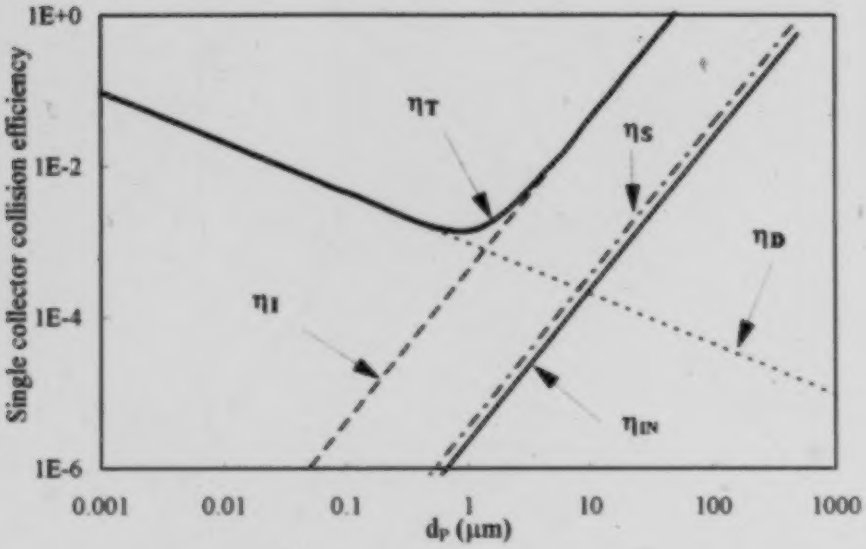

Figure 3.1 The single collector collision efficiency η_T as a function of particle diameter for the following conditions: d_B = 60 μm an ρ_P = 1.01 g/mL at 20 °C

$$\eta_T \approx \eta_I = \frac{3}{2}\left(\frac{d_P}{d_B}\right)^2 \tag{3.9}$$

The effect of bubble size on η_T is illustrated in Figure 3.2, which shows that η_T increases as the bubble sizes decreases for a given particle size. The effect of particle density and water temperature on η_T, for a typical water treatment condition, is not significant (Malley, 1988).

Equations 3.4, 3.5 and 3.6 indicate that η_T is dependent on bubble size according to d_B^{-2} for all cases and is dependent on particle size according to $d_P^{-2/3}$ for Brownian diffusion and d_P^2 for interception and differential settling. Hydrodynamic retardation, i.e. tendency to decrease particle collisions as particle moves toward bubble, is not significant and therefore was not included in the SCE model (Edzwald, 1995).

3.3 Hydrodynamic Characterization of the Contact Zone

The contact zone is considered very important for the overall performance of the DAF process (Haarhoff and van Vurren, 1994; Edzwald, 1995). In this zone, the saturated water and the flocculated water are mixed in order to provide collision opportunities between bubbles and flocs. The mechanism of bubble-particle interactions is highly dependent on the hydrodynamic conditions in the contact zone, which are governed by flow conditions and geometry.

Many workers in this area (Kitchener and Gochin, 1981; Haarhoff and van Vurren, 1994) have agreed on several aspects regarding the preferred hydrodynamic conditions inside the contact zone: (1) sufficient mixing should be provided to blend the incoming flocculated water and the saturated water; (2) degree of mixing levels should be high enough to provide sufficient collision opportunities for bubbles and flocs for attachment;

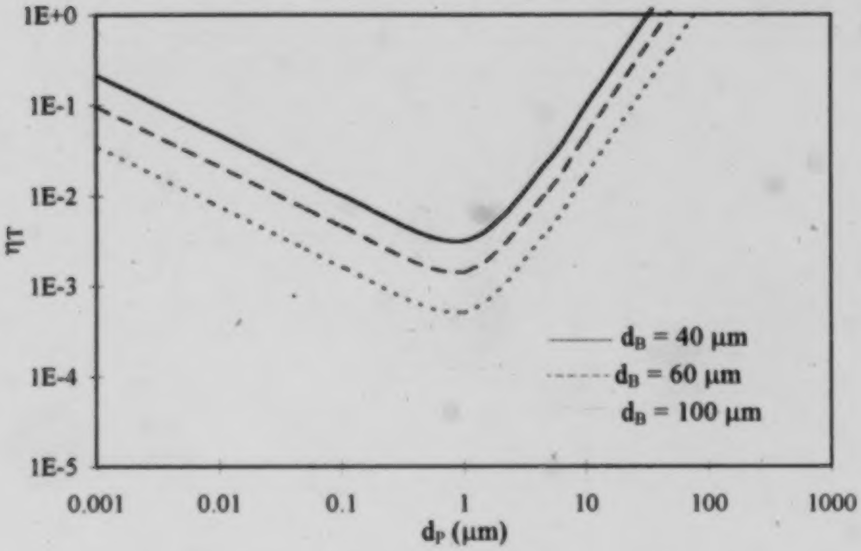

Figure 3.2 Effect of bubble diameter on η_T

and (3) sufficient residence time should be provided to increase collision opportunities between bubbles and particles.

Traditionally, the hydraulic loading or the superficial liquid velocity, U_L, defined as the total water flow rate, Q_{Total}, divided by the cross sectional area of the contact zone, A_{CZ}, is used as a surrogate measure for the degree of mixing. For typical rectangular flotation tanks, the hydraulic loading rate ranges from 200 m/h near the injection nozzle to 70 m/h at the top of the sloping baffle (Fawcett, 1997).

Another method for estimating the degree of mixing or dispersion inside the contact zone involves measuring Peclet number, Pe, which is a dimensional group defined as the ratio of advective to diffusive transport. For that purpose, theoretical models that would describe non-ideal flow conditions through a vessel or a reactor have to be used. Two frequently used models are the axial dispersion model and the tanks in series model. For flotation columns, the axial dispersion model is often used (Finch and Dobby, 1990). In this model, mixing occurs only along the axis of the column.

To characterize the spreading of the fluid, a diffusion-like process is assumed and is superimposed on plug flow (Levenspiel, 1972). When a pulse or stimulus of tracer is introduced into the fluid influent line just upstream from the DAF contact zone column, the concentration of the tracer, C_x, at an axial distance x downstream from the injection point at time t is:

$$\frac{\partial C_x}{\partial t} = D_a \frac{\partial^2 C_x}{\partial x^2} - U_L \frac{\partial C_x}{\partial x} \tag{3.10}$$

where D_a is the axial dispersion coefficient, which represents the spreading process (units of Length^2 time^{-1}). In this one-dimensional model, radial dispersion and non-uniform velocity profiles are not considered.

If the concentrations of the tracer inside the reactor are measured simultaneously with the tracer injection time, where time zero corresponds to the impulse injection, then a residence time distribution, RTD, of the liquid is obtained. The collected concentrations are then normalized to produce a curve enclosing an area of unity above the time axis. This can be represented mathematically as the residence time distribution density function, E(t) such that:

$$\int_0^\infty E(t)\,.\,dt = 1 \tag{3.11}$$

The RTD curve is often characterized by the mean residence time, t_m, and the variance ,σ_t^2, (Levenspiel, 1972). They represent the location and the spread of residence time distribution, respectively. Mathematically, they can be calculated from the discrete pulse-input tracer test data as follow:

$$t_m = \frac{\Sigma\, C_i\, t_i\, \Delta t_i}{\Sigma\, C_i\, \Delta t_i} \tag{3.12}$$

and

$$\sigma_t^{\,2} = \frac{\Sigma\, C_i\, t_i^{\,2}\, \Delta t_i}{\Sigma\, C_i\, \Delta t_i} - t_m^{\,2} \tag{3.13}$$

RTD distribution can also be obtained theoretically by using a single parameter, the dispersion number N_d, which is the inverse of Pe, defined as:

$$N_d = \frac{1}{Pe} = \frac{D_a}{U_L \cdot L} \tag{3.14}$$

where L is the distance between the point of the tracer injection and the contact zone column's port where the measurements were taken.

The correct form of the equation to be used for the theoretical prediction is determined by the type of experimental conditions (Levenspiel, 1972). In this study, the contact zone is assumed to have open-open boundary conditions in relation to the residence time distribution. This is due to the fact that the mixing process extends over its boundary both in the inlet and outlet section (Westertrep et al., 1984). The corresponding theoretical RTD curve is an analytical solution for equation 3.10 for x = L (Levenspiel, 1972):

$$E(\theta) = \frac{1}{2\sqrt{\frac{\pi}{Pe}\theta}} \exp\left[-Pe\frac{(1-\theta)^2}{4\theta}\right] \tag{3.15}$$

where θ is the dimensionless time defined as:

$$\theta = \frac{t}{\tau} = \frac{t}{(V_{CZ}/Q)} \tag{3.16}$$

where τ is the theoretical residence time inside the contact zone column and V_{CZ} is the contact zone volume.

For situations of large deviations from plug flow, i.e. Pe < 100, the pulse response is broad and it passes the measurement point slowly enough that it changes shape, or it spreads. That gives a non-symmetrical E-curve (Levenspiel, 1972). Also, for open-open boundary conditions, the mean residence time, t_m, is larger than the theoretical residence time, τ, of the vessel.

The RTD's for reactors having values of N_d between zero and ∞, and the same dimensionless time $\theta = 1$, are shown in Figure 3.3. When $N_d = 0$ or $Pe = \infty$ plug flow conditions are observed in the reactor and when $N_d = \infty$ or $Pe = 0$ completely mixed flow conditions prevail in the reactor. In actual DAF contact zones, the flow conditions are neither perfect plug flow nor completely mixed.

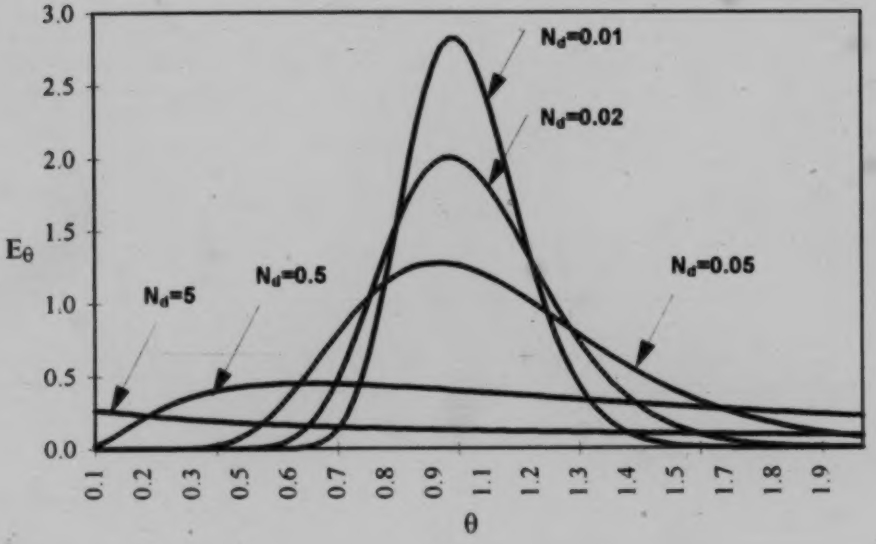

Figure 3.3 Theoritical RTD for open-open boundary conditions

The simplest way of calculating Pe is to make use of the statistical characteristics of the distribution, i.e. t_m and σ_t^2. However, the long tail often encountered in experimental tracer studies lowers the accuracy of the calculations (Mavros, 1992). Another accurate way of determining Pe is to fit the experimental data to theoretical calculated profiles, using Equation 3.15. The best fit is determined by minimizing the sum of squares of residuals, SSR:

$$SSR(Pe) = \sum (E(\theta)_{experimental} - E(\theta)_{theoretical})^2 \qquad (3.17)$$

where SSR(Pe) is the sum of squares of residuals function. The Peclet Number is found by solving equation 3.17 by trial and error and the Pe value which corresponds to the minimum SSR(Pe) value is accepted to characterize the system considered. However, prior to the least square minimization, the tracer data should be normalized by applying the trapezoidal integration rule to pair the experimental observations and model predictions on the same numerical scale.

3.4 DAF Contact Zone Kinetic Model

The complexity of the physical and chemical processes that occur inside the DAF contact zone has made the establishment of a suitable design model from the fundamentals of bubble-particle interactions almost impossible. However, an approach that has given some success is to regard the DAF process as analogous to a chemical reactor (Gochin,1981). Several attempts have been made by different researchers (Sutherland,1948; Collins and Jameson,1976; Gochin, 1981; Edzwald et al., 1990) to describe the particle overall removal rate in batch systems using the first-order expression with respect to the concentration of particles:

$$\frac{dN_P}{dt} = - k_P \cdot N_P \qquad (3.18)$$

where N_P is the particle number concentration for particle size, d_P, and k_P is a lumped parameter, called the overall particles removal rate constant, which involves physical, chemical and surface properties of the process (Gochin, 1981). The rate constant, k_P, is always determined experimentally for the system under investigation.

An expression for k_P has been derived by Collins and Jameson (1977) for a batch flotation process with a continuous input of bubbles:

$$k_P = \frac{3\,R\,H\,Q_g}{2\,V\,d_B} \tag{3.19}$$

where R is the single bubble removal efficiency for particle size, d_P, defined as the ratio of particles collected by a bubble to the particles approaching the bubble, and mathematically defined by Equation 3.1, H and V are the flotation tank height and volume respectively, Q_g is the volumetric gas flow rate and d_B is the mean bubble diameter. An analogous expression for k_P was developed by Yuu et al. (1977) for batch flotation system:

$$k_P = \frac{3\,R\,U_B\,\Phi_B}{2\,d_B} \tag{3.20}$$

where U_B is the terminal rise velocity of the bubble and Φ_B is the bubble volume concentration.

The previous k_P expressions were derived for a batch flotation system. However, dissolved air flotation processes are usually considered continuous flow systems. Therefore, an expression for overall removal rate constant under continuous flow conditions is required. If one considers a horizontal element, which is located inside the contact zone of the DAF tank, that has a height dh, surface area $A_{element}$ and volume dV, as shown in Figure 3.4, the following expression represents the mass balance for particle

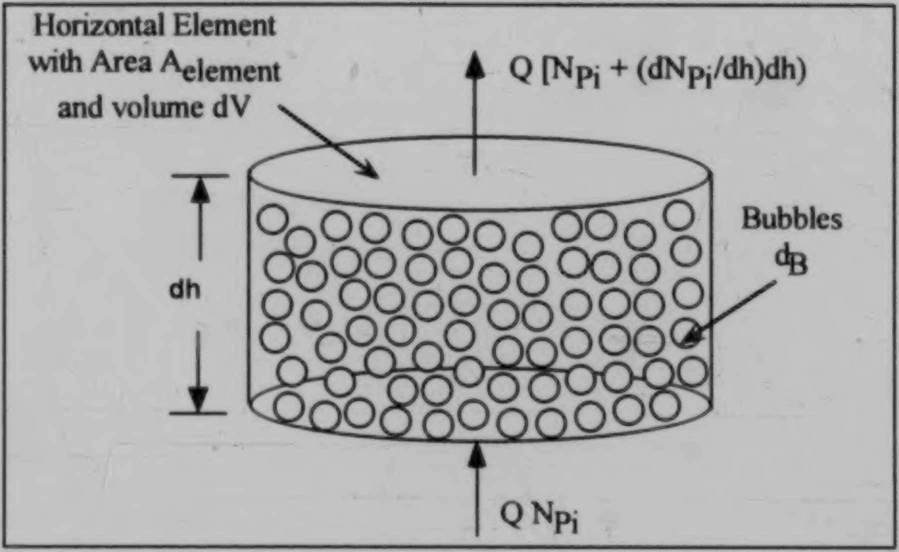
Horizontal Element
with Area $A_{element}$
and volume dV
$Q\,[N_{Pi} + (dN_{Pi}/dh)dh)$
dh
Bubbles
d_B
$Q\,N_{Pi}$

Figure 3.4 Horizontal element inside DAF contact zone

concentration, N_p, with mean particle diameter, d_P, and total liquid flow, Q_{Total}, across the element:

$$\frac{\partial N_P}{\partial t}\partial V = Q_{Total}\,N_P - Q_{Total}\,(\,N_P+\frac{\partial N_P}{\partial h}\partial h) - \text{Particle removal of size } d_P \qquad (3.21)$$

where the particle removal term is defined as the number of particles of size d_P removed by a single bubble multiplied by the number of bubbles in the element. The number of particles of size, d_P, removed by a single bubble is defined as:

$$\text{Number of particles removed by one bubble} = R\;.\;U_{PB}\;.\;a_B\;.\;N_P \qquad (3.22)$$

where a_B is the projected area of a spherical bubble with a mean diameter d_B and U_{PB} is the relative velocity of bubbles to particles of size, d_P . For particles having density very close to that of water, e.g. alum flocs which have density ≈ 1.01 g/mL at 20°C, the particles would follow the water stream line and therefore would move with a velocity very close to the superficial liquid velocity. Therefore, U_{PB} can be approximated by the instantaneous bubble rise velocity, $U_{B\,inst}$, which is defined as:

$$U_{PB} \approx U_{B\,Inst} = \frac{\partial h}{\partial t} = U_L + U_{B\,rel} \qquad (3.23)$$

where U_L is the liquid superficial velocity, which is equivalent to the contact zone hydraulic loading rate defined as:

$$U_L = \frac{Q_{Total}}{A_{CZ}} \qquad (3.24)$$

where A_{CZ} is the cross sectional area of the contact zone, $U_{B\,rel}$ is the relative bubble rise velocity approximated by Stoke's rise velocity for a spherical bubble with diameter, d_B:

$$U_{B\,rel} \approx U_{B\,Stoke} = \frac{g\,(\rho_f - \rho_B)\,d_B^{\,2}}{18\,\mu} \approx \frac{g\,\rho_f\,d_B^{\,2}}{18\,\mu} = c\,.\,d_B^{\,2} \qquad (3.25)$$

where c is a constant for a given water temperature.

Substituting Equations 3.1 and 3.23 and the projected area of a spherical bubble with diameter d_B into Equation 3.22 and rearranging gives:

$$\text{Number of particles removed} = \alpha_{PB}\,\eta_T\,(U_L + U_{B\,Stoke})\frac{\pi\,d_B^{\,2}}{4}N_P \qquad (3.26)$$

The number of bubbles in the element can be defined as:

$$\text{Number of bubbles} = \frac{\Phi_B(A_{element}\ dh)}{v_B} \qquad (3.27)$$

where, v_B is the volume of a single bubble with diameter d_B and Φ_B is the bubble volume concentration defined as:

$$\Phi_B = \sum_{i=1}^{n}(N_B\,.\,v_B)_i \approx N_B\,.\,v_B \qquad (3.28)$$

where N_B is the bubble number concentration. Substituting the volume of a single bubble with diameter d_B into Equation 3.27 gives:

$$\text{Number of bubbles} = \frac{6.\Phi_B.(A_{element}\ dh)}{\pi.d_B^{\,3}} \qquad (3.29)$$

From Equations 3.26 and 3.29, the particle removal term in Equation 3.21 can be written as, after simplification:

$$\text{Particle removal} = \frac{3}{2}\alpha_{PB}\,\eta_T\,(U_L + U_{B\,Stoke})\,N_P\,\Phi_B\,\frac{A_{element}\,.\,dh}{d_B} \tag{3.30}$$

Substituting Equation 3.30 into Equation 3.21 would describe the mass balance for particle concentration, N_P, inside the element:

$$\frac{\partial N_P}{\partial t}\partial V = Q_{Total}\,N_P - Q_{Total}\left(N_P + \frac{\partial N_P}{\partial h}\partial h\right) - \frac{3}{2}\alpha_{PB}\,\eta_T\,(U_L + U_{B\,Stoke})\,N_P\,\Phi_B\,\frac{A_{element}\,.\,\partial h}{d_B} \tag{3.31}$$

Equation 3.31 can be further simplified, after multiplying through the parenthesis and dividing each term by ($A_{element}\,\partial h$) and canceling, into:

$$\frac{\partial N_P}{\partial t} = -\frac{Q_{Total}}{A_{element}}\frac{\partial N_P}{\partial h} - \frac{3}{2}\alpha_{PB}\,\eta_T\,(U_L + U_{B\,Stoke})\,\frac{\Phi_B}{d_B}\,N_P \tag{3.32}$$

For the batch system case, i.e. $Q_{Total} = 0$, Equation 3.32 can be rewritten as:

$$\frac{dN_P}{dt} = -\frac{3}{2}\alpha_{PB}\,\eta_T\,U_{B\,Stoke}\,\frac{\Phi_B}{d_B}\,N_P \tag{3.33}$$

Equation 3.33 is called the single collector efficiency DAF model (Malley, 1988). When Equation 3.33 is expressed in the simple rate form, defined in Equation 3.18, the overall rate constant, k_P, is found to be similar to k_P defined in Equation 3.20.

The overall particle removal rate, dN_P/dt, for the applied particle size range can be defined as:

$$\frac{dN_P}{dt} = \sum_{i=1}^{i=n}\left(\frac{dN_P}{dt}\right)_i = \sum_{i=1}^{i=n} - k_P.(N_P)_i \tag{3.34}$$

where n_P is the number of classes in the particle size distribution. Equation 3.34 assumes that k_P is the first-order removal rate constant for particle size equal to the mean of the particle size distribution, PSD. Also, it assumes that the collision efficiency factor α_{PB} is the same for all particles in the applied particle size range.

The overall removal rate constant, k_P, can be calculated by substituting $\partial h = (U_L + U_{B\,Stoke})\,\partial t$ into Equation 3.32 and rearranging:

$$\frac{dN_P}{dt} = -\frac{3}{2}\alpha_{PB}\,\eta_T\left[\frac{(U_L+U_B)^2}{(2U_L+U_B)}\right]\frac{\Phi_B}{d_B}\,N_p \qquad (3.35)$$

Substituting η_T for particle size, d_P, (Equation 3.9) and $U_{B\,Stoke}$ (Equation 3.25) into Equation 3.35 would yield:

$$\frac{dN_P}{dt} = -\frac{9}{4}\alpha_{PB}\left[\frac{(U_L+c.d_B^{\,2})^2}{(2U_L+c.d_B^{\,2})}\right]\frac{d_P^{\,2}}{d_B^{\,3}}\,\Phi_B\,N_P \qquad (3.36)$$

When Equation 3.36 is expressed in the simple rate form, the overall removal rate constant, k_P, for mean particle size, d_P, can be defined as:

$$k_P = \frac{9}{4}\alpha_{PB}\left[\frac{(U_L+c.d_B^{\,2})^2}{(2U_L+c.d_B^{\,2})}\right]\frac{d_P^{\,2}}{d_B^{\,3}}\,\Phi_B \qquad (3.37)$$

The particle removal rate can also be expressed in terms of the particle removal per contact zone height, dh. Considering steady state conditions, i.e. U_L is constant, and substituting ∂t by $\partial h/(U_L + U_{B\,Stoke})$, and substituting η_T (as given in Equation 3.9) and $U_{B\,Stoke}$ (as given in Equation 3.25) into Equation 3.32 and rearranging would yield:

$$\frac{dN_P}{dt} = -\frac{9}{4}\alpha_{PB}\left[\frac{(U_L + c.d_B^2)}{(2U_L + c.d_B^2)}\right]\Phi_B N_P \tag{3.38}$$

Equation 3.38 can be solved analytically after defining the boundary conditions, which are: $N_P = N_{CZo}$ at $h = 0$ and $N_P = N_{CZe}$ at $h = H_{CZ}$ where N_{CZo} is the initial number concentration of particles of size, d_P, entering the contact zone, N_{CZe} is the number concentration of particles of size d_P exiting the contact zone and H_{CZ} is the height of the contact zone column. The resulting analytical solution for continuous-flow DAF system is:

$$\frac{N_{CZe}}{N_{CZo}} = \sum_{i=1}^{i=n}\left(\frac{N_{CZe}}{N_{CZo}}\right)_i = \exp\left\{-\frac{9}{4}\alpha_{PB}\left[\frac{(U_L + c.d_B^2)}{(2U_L + c.d_B^2)}\right]\frac{d_P^2}{d_B^3}\Phi_B H_{CZ}\right\} \tag{3.39}$$

Equation 3.39 is the contact zone kinetic model for the continuous flow DAF system at steady state conditions. This model was derived based on many assumptions which may affect its validity. Therefore, it is important to list these assumptions with related references, as shown in Table 3.1.

The model identifies important design and operating variables that would affect the flotation performance. These variables are the attachment efficiency factor α_{PB}, the mean particle diameter d_P, the mean bubble diameter d_B, the bubble volume concentration Φ_B, the superficial liquid velocity U_L and the contact zone height H_{CZ}. To describe the effect of each variable on the model, sensitivity analysis is employed. A set of reference or standard values, based on experimental experience and literature, were chosen for each of the model variables. These values are summarized in Table 3.2.

The effect of α_{PB} on particle removal is shown in Figure 3.5. The results suggest that particle destabilization is required because as α_{PB} approaches zero the particle removal is reduced. DAF performance increases rapidly with increasing α_{PB} and the calculated removal efficiency was higher than 95 % for α_{PB} values in the range of

Table 3.1 Assumptions used for the contact zone kinetic model derivation

	Assumption	Reference
1	Based on the single collector efficiency concept for DAF application in water treatment	Edzwald et al. (1990) Malley and Edzwald (1991)
2	Bubbles are formed instantly after the injection of saturated water into the DAF tank	Raaykart and Haarhoff (1994)
3	The empirical factor α_{PB} included LVDW and hydrodynamic forces and it was assumed 0.5	Edzwald (1993)
4	$\alpha_{Pi\,B}$ for particles with size d_{Pi} is equal to α_{PB} for the applied particle size range	Liers et al. (1996)
5	η_T equal approximately η_I for particle size d_P larger than 1 μm and smaller than 100 μm	Edzwald (1997)
6	Φ_B remains constant inside the contact zone at steady state conditions ($\Phi_B >> \Phi_P$)	Edzwald (1997)
7	Bubbles with $d_B < 1000$ μm are spherical in shape and rise with steady rectilinear motion	Clift et al. (1978)
8	$U_{B\,rel}$ is approximated by $U_{B\,Stoke}$ for bubbles with $d_B < 100$ μm	Edzwald et al. (1990)
9	Bubble size remains constant with respect to contact zone height	Takahashi et al. (1979)
10	U_{PB} is approximated by $U_{B\,rel}$ for algae flocs with ρ_P almost equal to ρ_W, i.e. $U_{P\,rel} = 0$	
11	Contact zone was assumed to have open-open boudary conditions in relation to the RTD	Westertrep et al. (1984)
12	k_P was assumed to be constant for narrow range of particle size and for single value of hydrophobicity	Finsh and Dobby (1990)
13	d_P should be < 100 μm because detachement forces were not included in the model	Edzwald (1997)

Table 3.2 Reference values for contact zone kinetic model variables used for the sensitivity analysis

Model Variables	Note	Reference Value
α_{PB}		0.5
d_P	1	10 μm
d_B		50 μm
Φ_B	2	4000 ppm
U_L	3	70 m/h
H_{CZ}	4	3000 mm

Note 1 d_P was based on the mean diameter of the PSD of the flocculated algae used in this research

Note 2 Φ_B was calculated based on saturator efficiency factor of 0.84, P_{Sat} = 484 kPa and R_R = 7 %

Note 3 U_L was calculated based on average hydraulic loading recommended by Haarhoff and van Vurren (1994)

Note 4 H_{CZ} was calculated based on mean contact zone residence time of 150 sec (Haarhoff and van Vurren, 1994)

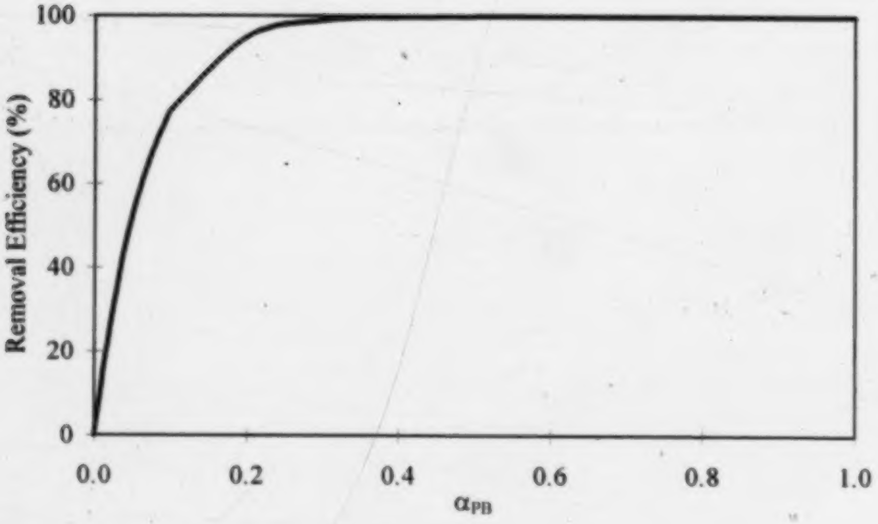

Figure 3.5 Effect of α_{PB} on particle removal efficiency for $d_P = 10\ \mu m$, $d_B = 50\ \mu m$, $\Phi_B = 4000$ ppm, $U_L = 70$ m/h and contact zone height of 3000 mm

0.1 to 0.3. α_{PB} is strongly dependent on the coagulant type, dosage and pH. Particle-bubble attachment is favored under optimum coagulation conditions which produce particles of little or no charge and are relatively hydrophobic (Edzwald, 1997).

To investigate the effect of α_{PB} on DAF performance as a function of other variables, Figures 3.6 to 3.9 were plotted for different values of d_B, Φ_B, d_P, and H_{CZ}, respectively. These figures show that the bubble diameters larger than 80 μm, Φ_B lower than 2000 ppm, d_P lower than 10 μm and H_{CZ} lower than 1000 mm would reduce particle removal efficiency, especially at lower α_{PB} values.

The effect of d_P on DAF performance is shown in Figure 3.10. The results indicate that particle removal improves sharply as d_P increases. The model predicts that greater than 95 % of particles are removed for particle sizes larger than 10 μm. As expected, the removal efficiency increases as d_P is increased because η_T, which is approximated by η_I for particle size larger than 1 μm, is proportional to d_P^2. However, the model can not be used to predict particle removal for particle sizes larger than 100 μm because detachment forces for large flocs on small bubbles must be considered. Also, these particles or flocs require a larger number of attached bubbles to reduce the bubble-particle agglomerate density to less than water in order for flotation to occur. For these reasons, it is suggested that flocculation tanks with lower detention times and higher mixing conditions be used with DAF in order to produce smaller particles (Edzwald, 1997).

To investigate the effect of d_P on DAF performance as a function of other variables, Figures 3.11 to 3.14 were plotted for different values for α_{PB}, H_{CZ}, d_B and Φ_B, respectively. These figures show that with α_{PB} lower than 0.1, H_{CZ} lower than 1000 mm, bubble diameter larger than 80 μm and Φ_B lower than 2000 ppm would reduce particle removal efficiency, especially for low d_P values.

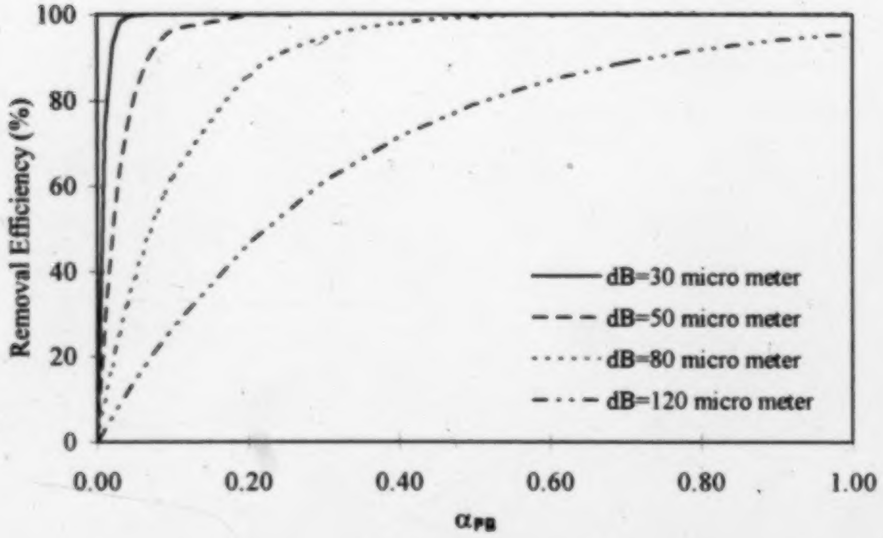

Figure 3.6 Effect of α_{PB} on DAF performance as a function of d_B for Φ_B=4000 ppm, U_L=70 m/h, d_P=10 μm and contact zone height = 3000mm (Note: dB=d_B)

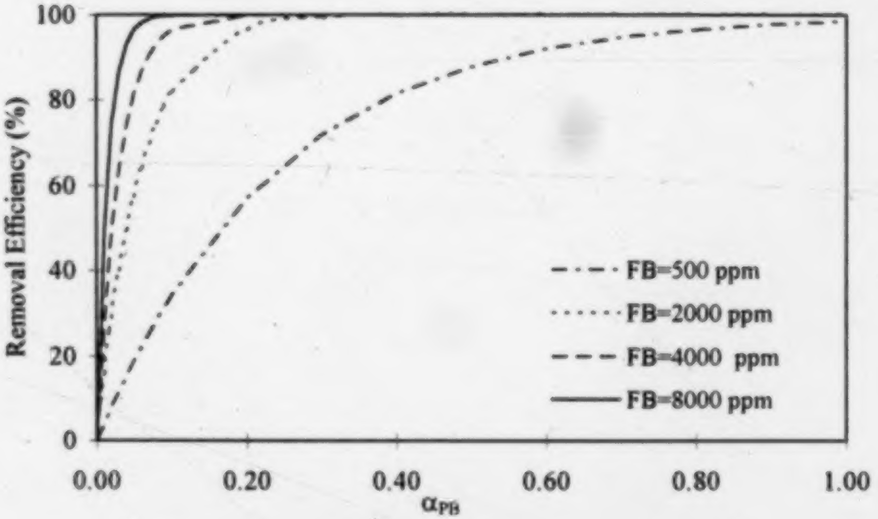

Figure 3.7 Effect of α_{PB} on DAF performance as a function of Φ_B for d_B=50 μm, U_L=70 m/h, d_P=10 μm and contact zone height = 3000mm (Note: FB=Φ_B)

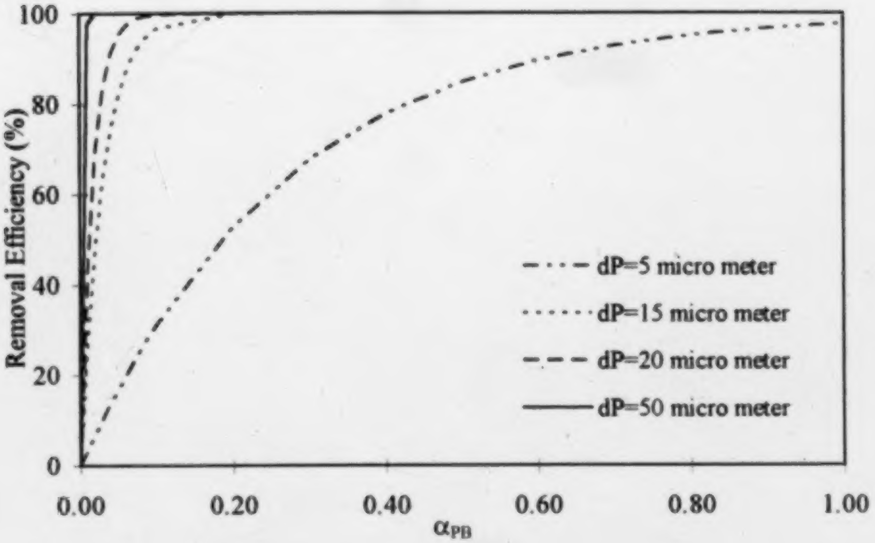

Figure 3.8 Effect of α_{PB} on DAF performance as a function of d_P for d_B=50 μm, U_L=70 m/h, Φ_B=4000 ppm and contact zone height = 3000mm (Note: dP=d_P)

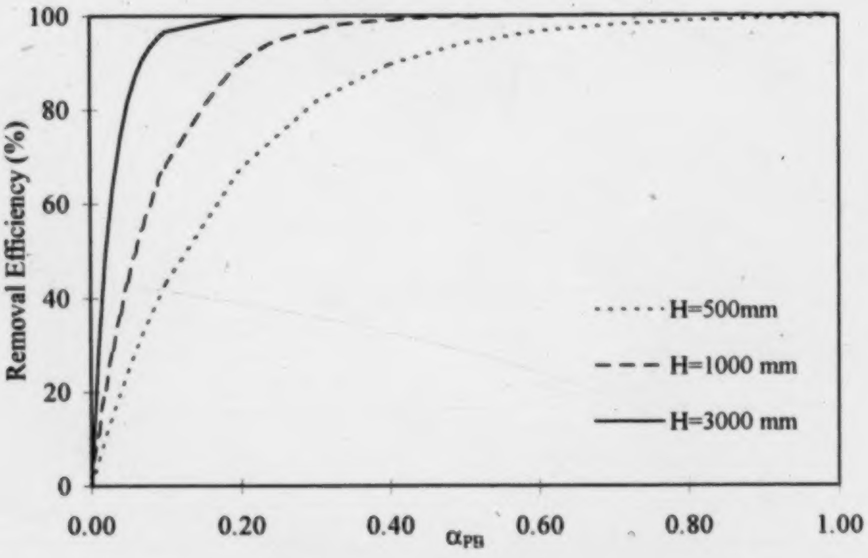

Figure 3.9 Effect of α_{PB} on DAF performance as a function of H_{CZ} for d_B=50 μm, U_L=70 m/h, Φ_B=4000 ppm and d_P=10 μm (Note: H=H_{CZ})

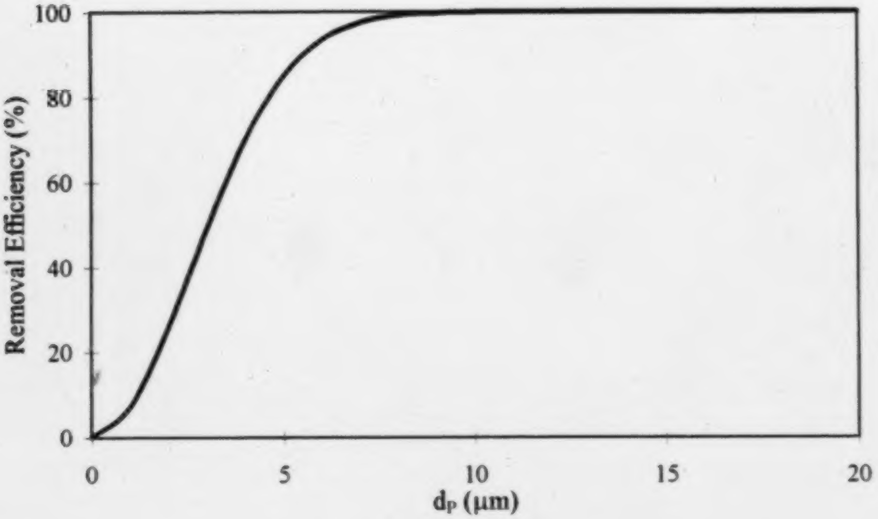

Figure 3.10 Effect of d_P on particle removal efficiency for $\alpha_{PB} = 0.5$, $d_B = 50$ μm, $\Phi_B = 4000$ ppm, $U_L = 70$ m/h and contact zone height of 3000 mm

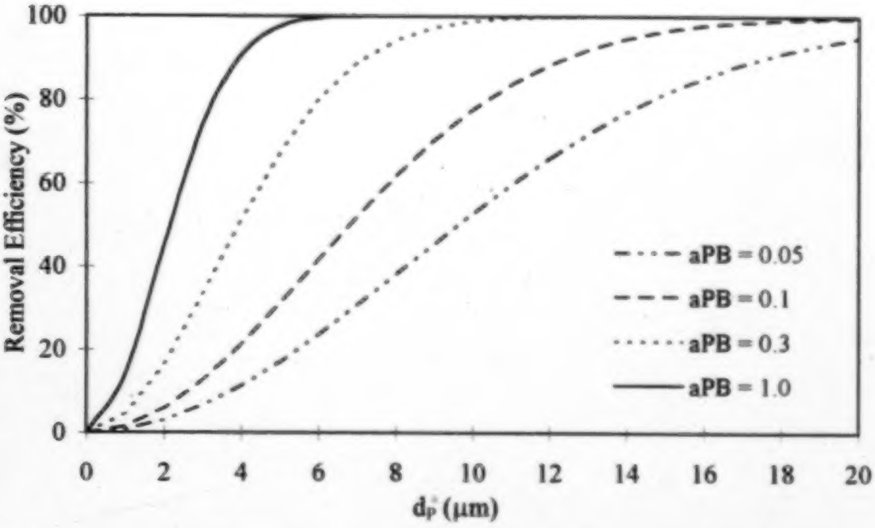

Figure 3.11 Effect of d_P on DAF performance as a function of α_{PB} for d_B = 50 μm, Φ_B = 4000 ppm, U_L = 70 m/h and contact zone height of 3000 mm (Note: aPB=α_{PB})

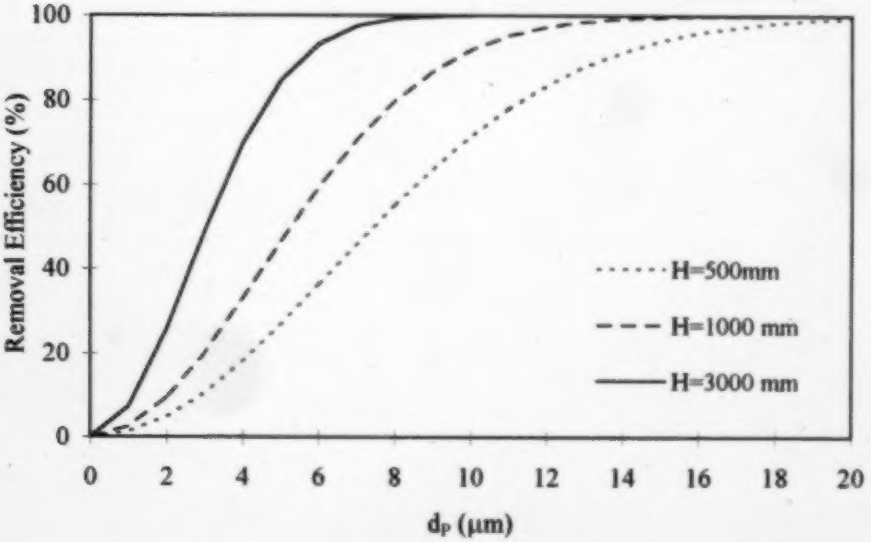

Figure 3.12 Effect of d_P on DAF performance as a function of H_{CZ} for d_B = 50 μm, Φ_B = 4000 ppm, U_L = 70 m/h and α_{PB}=0.5 (Note: H=H_{CZ})

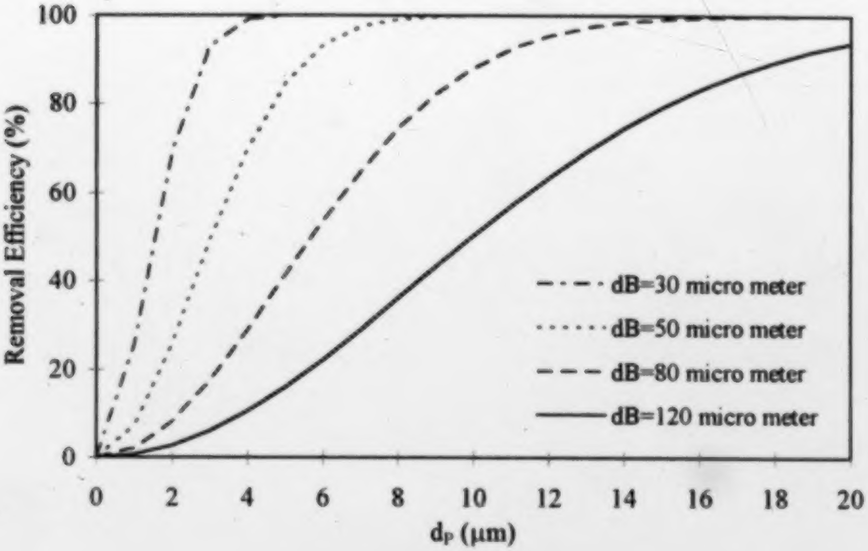

Figure 3.13 Effect of d_P on DAF performance as a function of d_B for $\alpha_{PB} = 0.5$, $\Phi_B = 4000$ ppm, $U_L = 70$ m/h and contact zone height of 3000 mm (Note: $dB=d_B$)

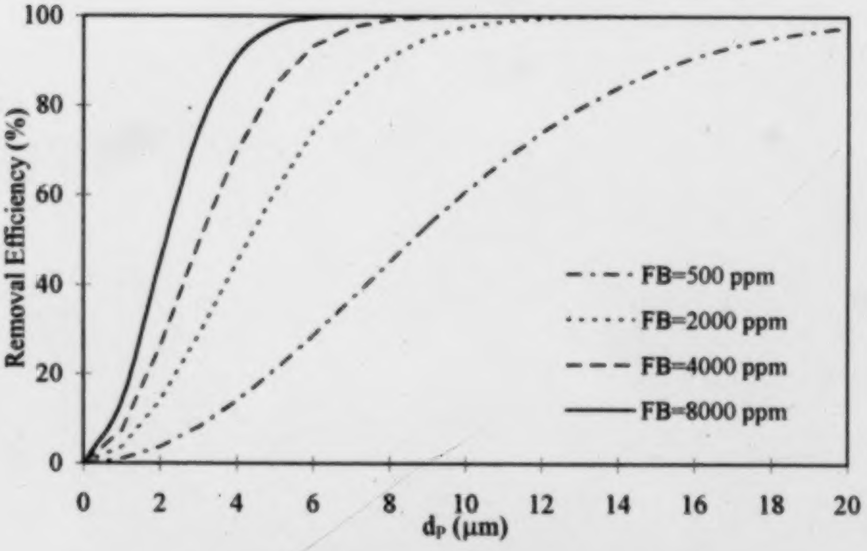

Figure 3.14 Effect of d_P on DAF performance as a function of Φ_B for $d_B = 50$ μm, $\alpha_{PB} = 0.5$, $U_L = 70$ m/h and contact zone height of 3000 mm (Note: $FB=\Phi_B$)

The contact zone kinetic model shows that the particle removal rate depends on d_B^{-3}. Therefore, a significant improvement in DAF performance is expected with decreasing bubble diameter, which is shown in Figure 3.15. To investigate the effect of d_B on DAF performance as a function of other variables, Figures 3.16 to 3.19 were plotted for different values for d_P, Φ_B, contact zone height and α_{PB}, respectively. These figures show that d_P lower than 10 μm, Φ_B lower than 2000 ppm, contact zone height lower than 1000 mm and α_{PB} lower than 0.1 would reduce particle removal efficiency, especially for d_B values larger than 50 μm.

The effect of bubble volume concentration is illustrated in Figure 3.20. The model simulation indicates that particle removal rate increases sharply with increasing Φ_B and that more than 95 % removal is achieved at approximately Φ_B equal to 2000 ppm. Bubble volume concentration is controlled by the saturator pressure and the recycle ratio. Since the saturator pressure does not vary much in practice, the recycle ratio is considered the more important design and operating parameter. For the condition used in this simulation, a recycle ratio of 7 % is considered to be the optimum value for pilot and full scale DAF water treatment facilities (Zabel, 1984).

As the volume of bubbles attached to the particles increases, the density of the agglomerate would decrease and as a result the rise velocity would increase. In water treatment practice, Φ_B is much greater than the particle volume concentration Φ_P, at a ratio of more than several 100 to 1 (Edzwald, 1997). As a result, the probability of bubble-particle collision and attachment is higher in the contact zone. This provides higher DAF performance.

To investigate the effect of Φ_B on DAF performance as a function of other variables, Figures 3.21 to 3.24 were plotted for different values for d_P, α_{PB}, contact zone height and d_B, respectively. These figures show that d_P lower than 10 μm, α_{PB} lower than 0.1, contact zone height lower than 1000 mm and bubble diameter larger than 80 μm

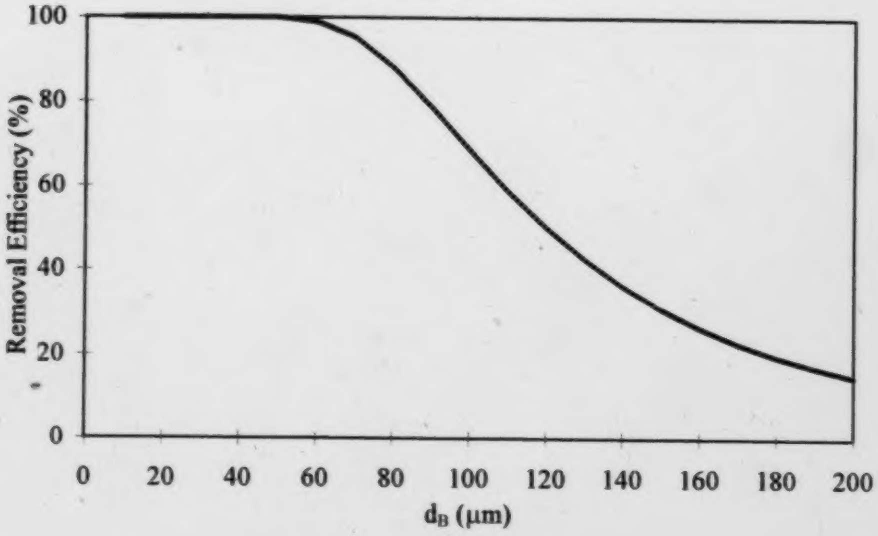

Figure 3.15 Effect of d_B on particle removal efficiency for $\alpha_{PB} = 0.5$, $d_P = 10$ μm, $\Phi_B = 4000$ ppm, $U_L = 70$ m/h and contact zone height of 3000 mm

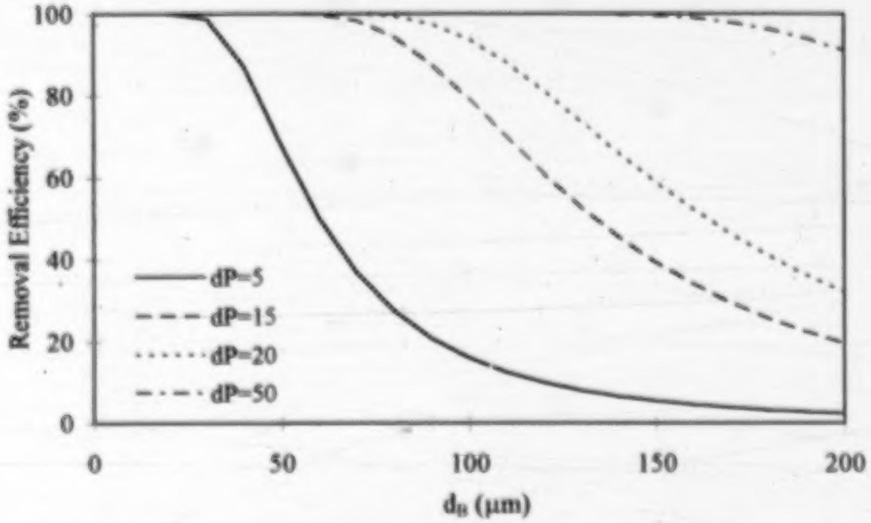

Figure 3.16 Effect of d_B on DAF performance as a function of d_P for $\alpha_{PB} = 0.5$, $\Phi_B = 4000$ ppm, $U_L = 70$ m/h and contact zone height of 3000 mm (Note: dP=dP, units are in μm)

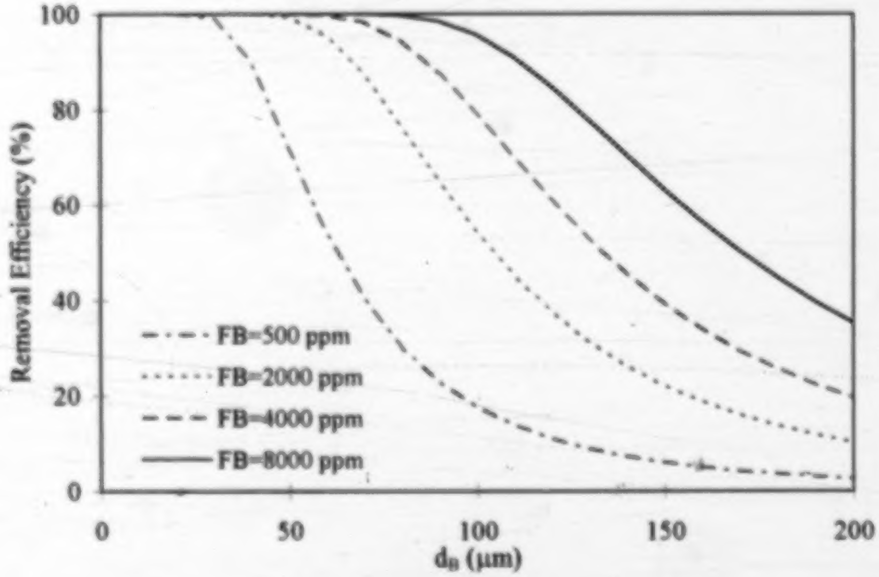

Figure 3.17 Effect of d_B on DAF performance as a function of Φ_B for $\alpha_{PB} = 0.5$, $d_P = 10$ μm, $U_L = 70$ m/h and contact zone height of 3000 mm (Note: FB=Φ_B)

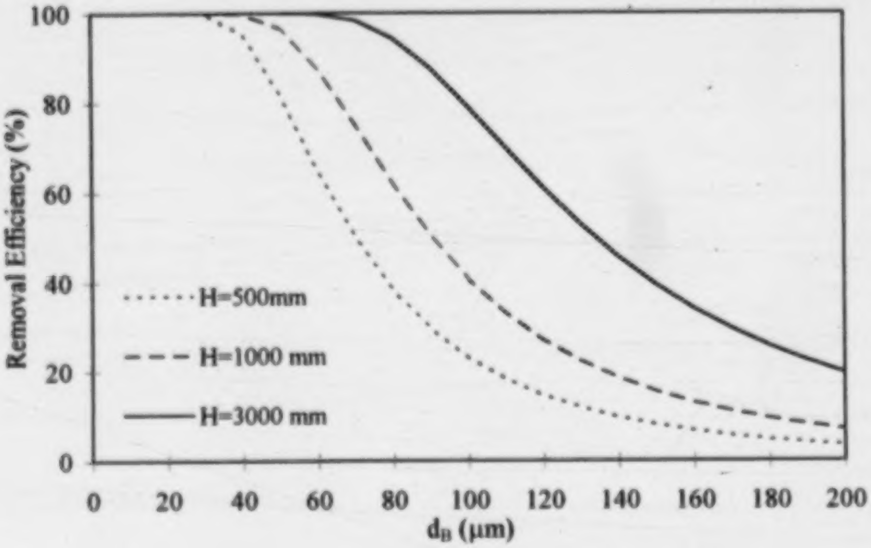

Figure 3.18 Effect of d_B on DAF performance as a function of H_{CZ} for $\alpha_{PB} = 0.5$, $d_P = 10$ μm, $U_L = 70$ m/h and $\Phi_B = 4000$ ppm (Note: $H=H_{CZ}$)

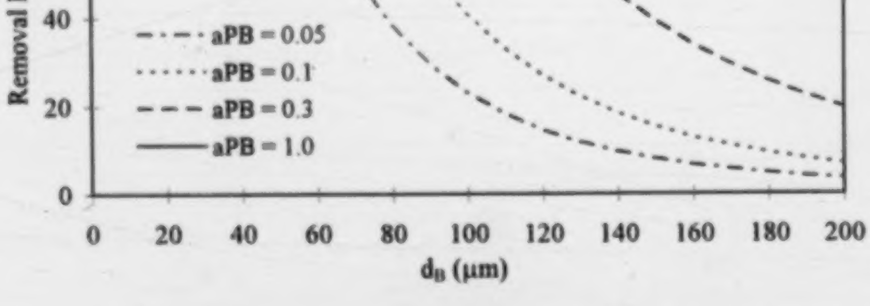

Figure 3.19 Effect of d_B on DAF performance as a function of α_{PB} for $\Phi_B = 4000$ ppm, $d_P = 10$ μm, $U_L = 70$ m/h and contact zone height of 3000 mm (Note: $aPB=\alpha_{PB}$)

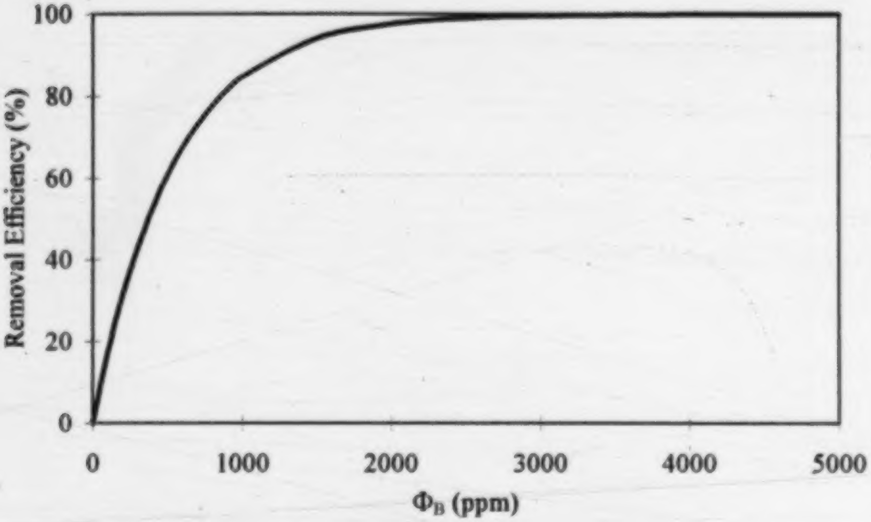

Figure 3.20 Effect of Φ_B on particle removal efficiency for $\alpha_{PB} = 0.5$, $d_P = 10\ \mu m$, $d_B = 50\ \mu m$, $U_L = 70$ m/h and contact zone height of 3000 mm

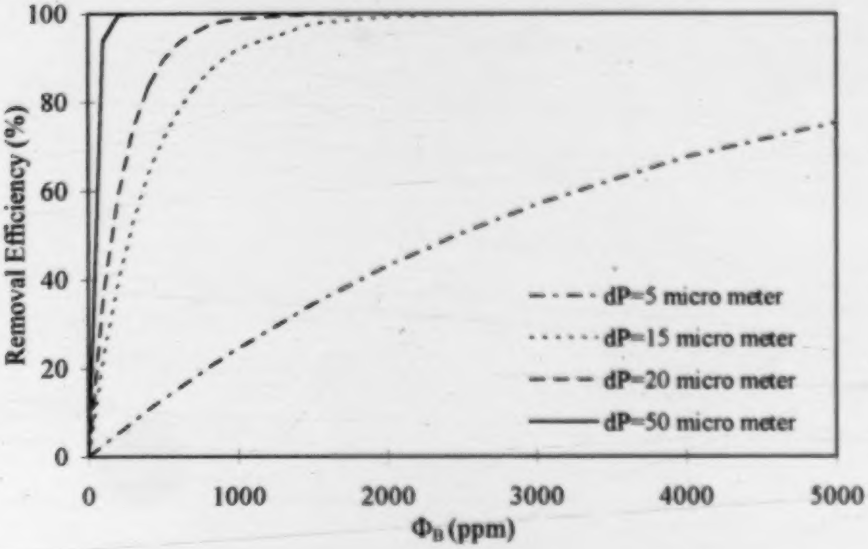

Figure 3.21 Effect of Φ_B on DAF performance as a function of d_P for $\alpha_{PB} = 0.5$, $d_B = 50\ \mu m$, $U_L = 70$ m/h and contact zone height of 3000 mm (Note: $dP=d_P$)

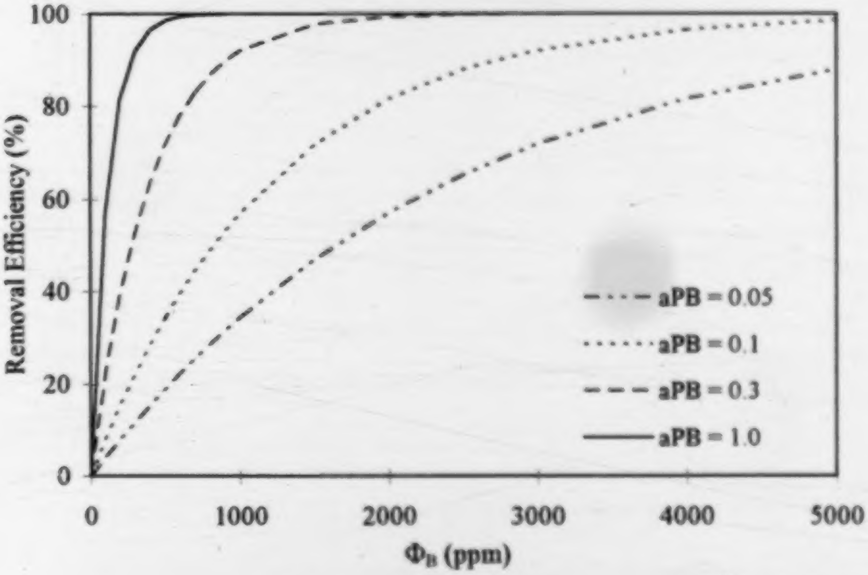

Figure 3.22 Effect of Φ_B on DAF performance as a function of α_{PB} for $d_P = 10\ \mu m$, $d_B = 50\ \mu m$, $U_L = 70$ m/h and contact zone height of 3000 mm (Note: $aPB=\alpha_{PB}$)

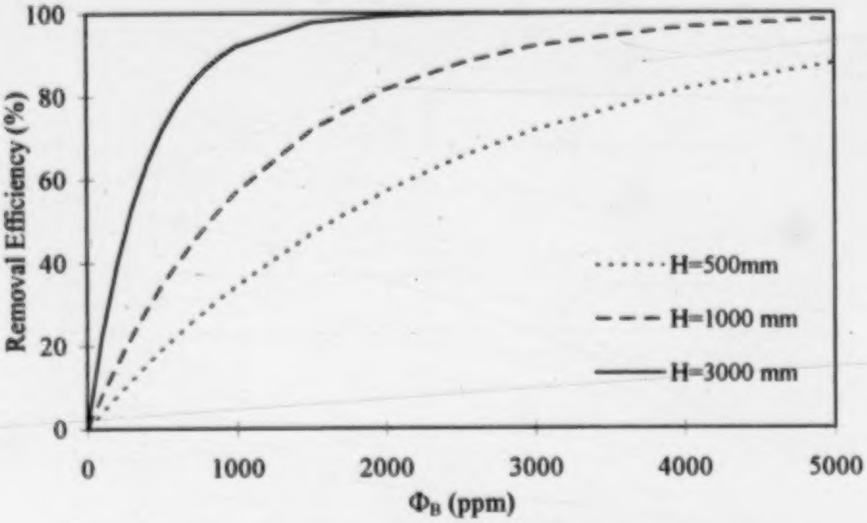

Figure 3.23 Effect of Φ_B on DAF performance as a function of H_{CZ} for $d_P = 10$ μm, $d_B = 50$ μm, $U_L = 70$ m/h and $\alpha_{PB}=0.5$ (Note: dB=d_B)

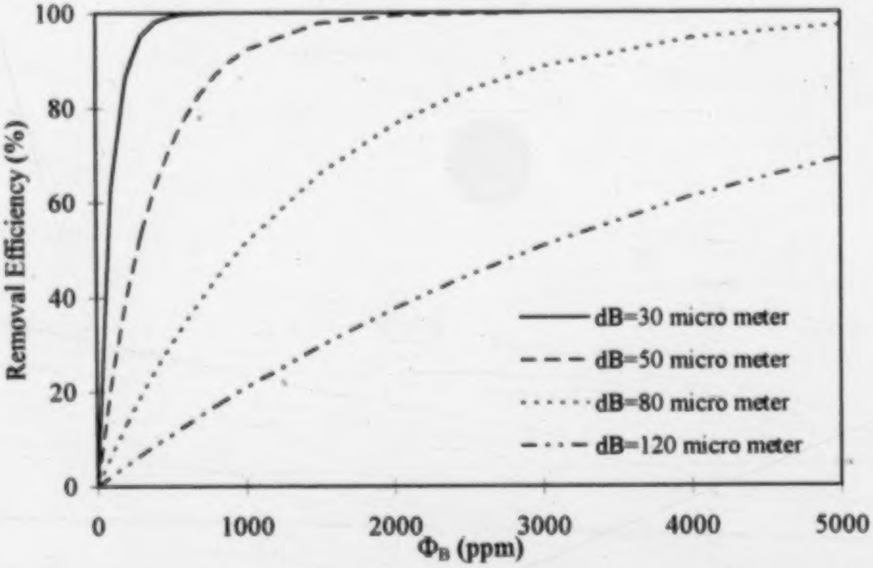

Figure 3.24 Effect of Φ_B on DAF performance as a function of d_B for $d_P = 10$ μm, $\alpha_{PB} = 0.5$, $U_L = 70$ m/h and contact zone height of 3000 mm (Note: dB=d_B)

reduce particle removal efficiency significantly, especially for Φ_B lower than 4000 ppm. These figures demonstrate the strong relationship between DAF performance and Φ_B. A larger concentration of bubbles with diameter equal to 50 μm would achieve very high particle removal even for low d_P and α_{PB}.

Superficial liquid velocity U_L or the hydraulic loading in the contact zone is considered to be an important design and operating parameter. Increasing U_L would increase Pe or decrease dispersion number, N_d, and as a result the RTD would approximate a plug flow condition, as shown in Figure 3.3. Particle removal rate increases as the flow conditions approach plug flow, as explained later in this section. However, increasing U_L would decrease the contact time required for bubble-particle collision and attachment and, therefore, particle removal rate would decrease. This is shown in Figure 3.25 where DAF performance decreases slightly as U_L is increased. In all cases of U_L simulated, more than 95 % of particles were removed.

The effect of contact zone height on DAF performance is very similar to the effect of contact zone residence time. The deeper the contact zone, the longer time the bubbles and particles will have for contact, at a given U_L value. This is shown in Figure 3.26 where particle removal rate has increased rapidly as the contact zone height is increased. More than 95 % removal was achieved at contact zone depth of 2000 mm, which corresponds to about 100 seconds of contact time for U_L of 70 m/h. This falls in the range of 60 to 240 seconds of contact time recommended by Haarhoff and van Vurren (1994).

To investigate the effect of contact zone height on DAF performance as a function of other variables, Figures 3.27 to 3.30 were plotted for different values for α_{PB}, Φ_B, d_B and d_P, respectively. These figures show that α_{PB} lower than 0.1, Φ_B lower than 2000 ppm, d_B larger than 80 μm and d_P lower than 10 μm would reduce particle removal efficiency, especially for contact zone height lower than 1000 mm.

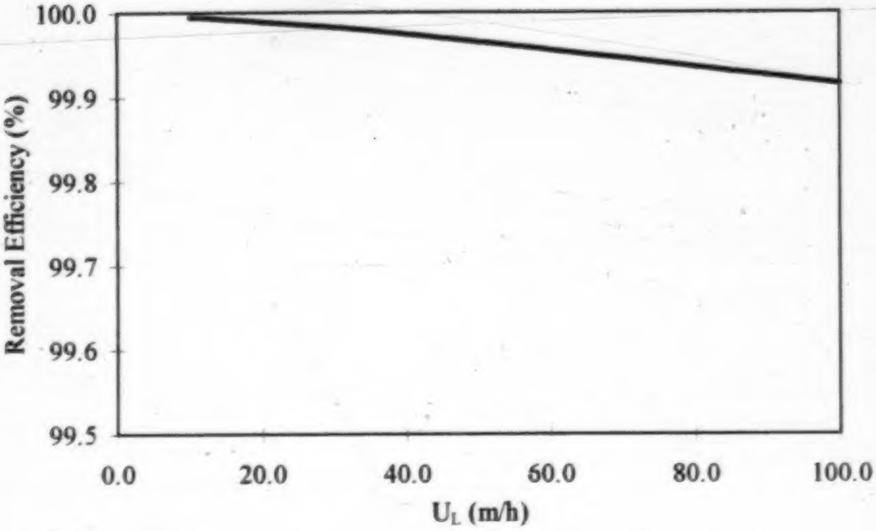

Figure 3.25 Effect of U_L on particle removal efficiency for $\alpha_{PB} = 0.5$, $d_P = 10$ μm, $d_B = 50$ μm, $\Phi_B = 4000$ ppm and contact zone height of 3000 mm

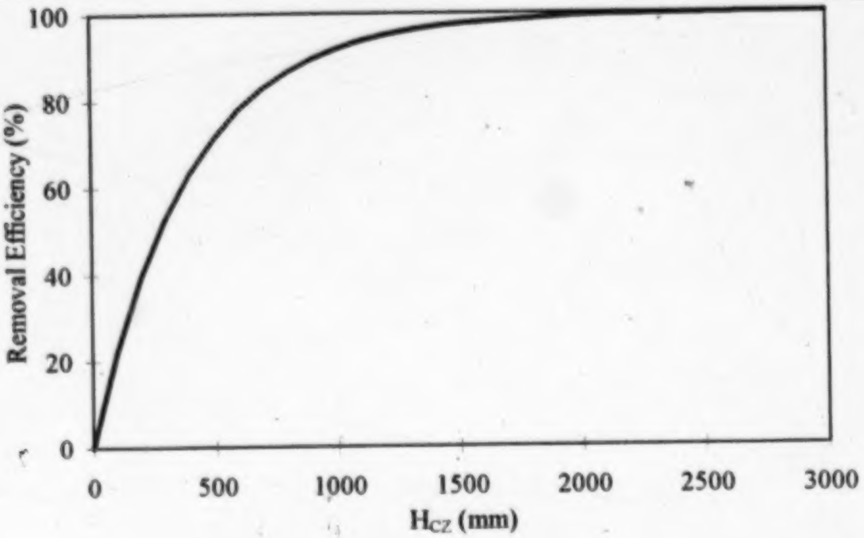

Figure 3.26 Effect of contact zone height on particle removal efficiency for $d_P = 10$ μm, $d_B = 50$ μm, $U_L = 70$ m/h, $\alpha_{PB} = 0.5$ and Φ_B of 4000 ppm

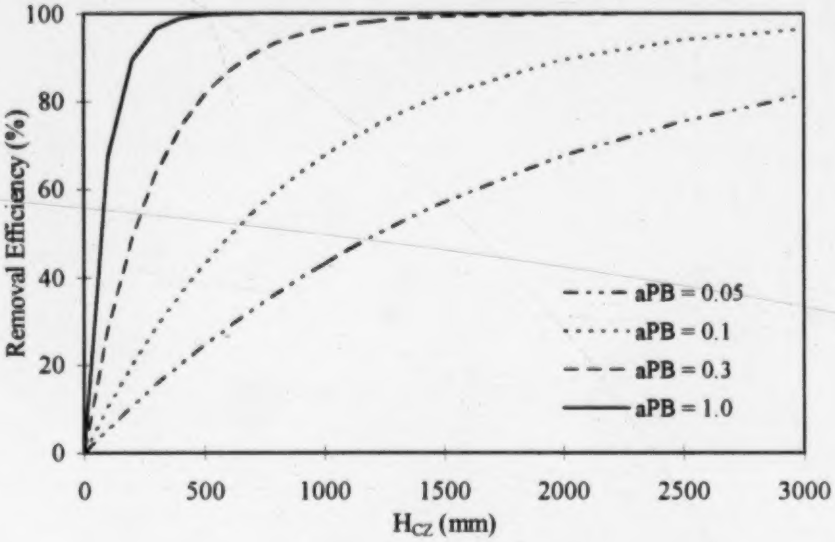

Figure 3.27 Effect of H on DAF performance as a function of α_{PB} for $d_P = 10\ \mu m$, $d_B = 50\ \mu m$, $U_L = 70$ m/h and Φ_B=4000 ppm (Note: aPB=α_{PB})

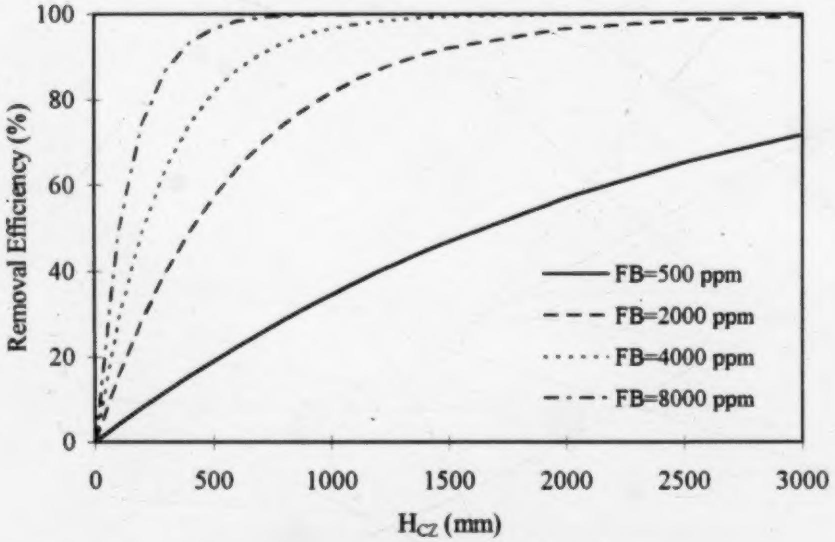

Figure 3.28 Effect of H on DAF performance as a function of Φ_B for $d_P = 10\ \mu m$, $d_B = 50\ \mu m$, $U_L = 70$ m/h and $\alpha_{PB} = 0.5$ (Note: FB=Φ_B)

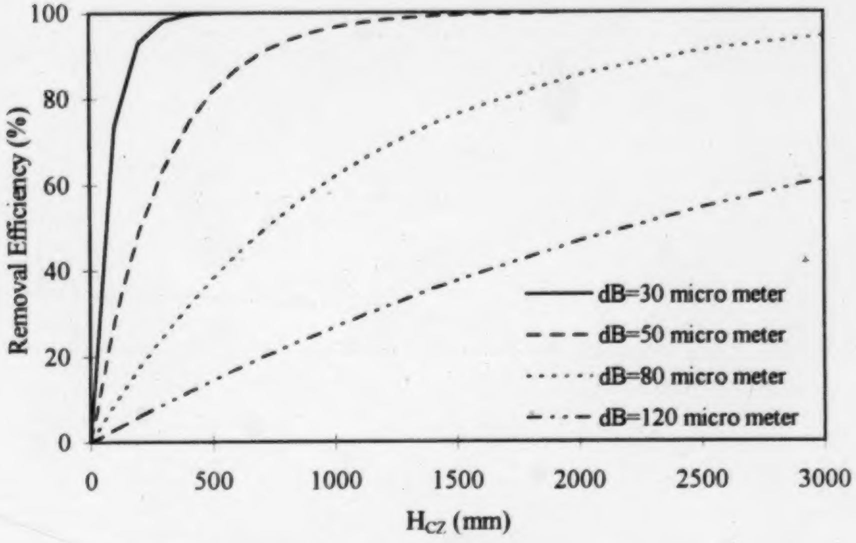

Figure 3.29 Effect of H on DAF performance as a function of d_B for $d_P = 10$ μm, $U_L = 70$ m/h, $\alpha_{PB} = 0.5$ and Φ_B=4000 ppm (Note: dB=d_B)

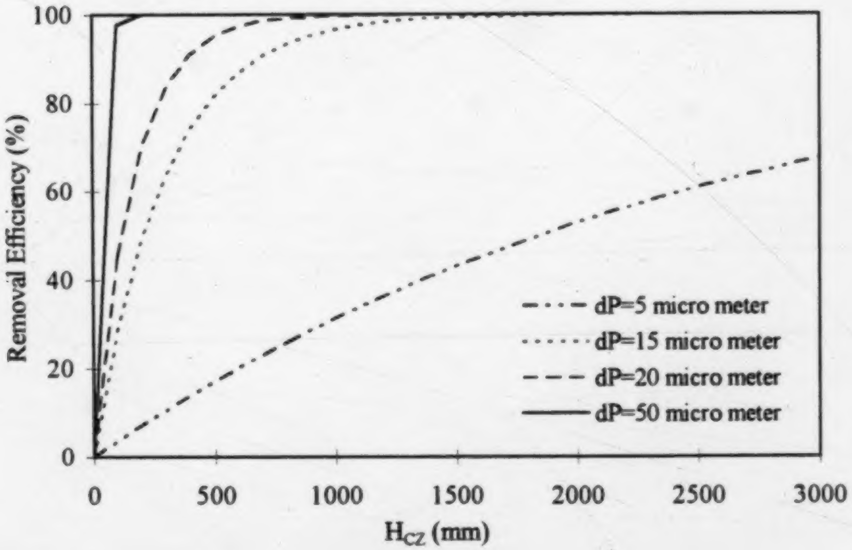

Figure 3.30 Effect of H on DAF performance as a function of d_P for $\Phi_B = 4000$ ppm, $d_B = 50$ μm, $U_L = 70$ m/h and α_{PB}=0.5 (Note: dP=d_B)

Using Equation 3.39, the particle removal efficiency for the DAF contact zone, $R_{CZ\,i}$, for particle size, d_{pi}, can be calculated using the following equation:

$$R_{CZ\,i} = 1 - \frac{N_{CZ\,e,i}}{N_{CZ\,o,i}} = 1 - \exp\left\{ - \frac{9}{4}\,\alpha_{PB} \left[\frac{(U_L + c\,.d_B^{\,2})}{(2U_L + c\,.d_B^{\,2})} \right] \frac{d_P^{\,2}}{d_B^{\,3}}\, \Phi_B\, H_{CZ} \right\} \tag{3.40}$$

and for the applied particle size range, the overall removal efficiency for the contact zone, R_{CZ}, can be expressed as:

$$R_{CZ} = \sum_{i=1}^{i=n} R_{CZ\,i} = 1 - \sum_{i=1}^{i=n} \left(\frac{N_{CZ\,e}}{N_{CZ\,o}} \right)_i \tag{3.41}$$

For a continuous flow DAF system, the actual R_{CZ} is determined by three factors: the overall particle removal rate constant, the mean residence time of particles inside the contact zone and mixing conditions inside the contact zone. Therefore, it is important to incorporate the hydrodynamics with the overall removal rate constant, k_P, inside the contact zone in order to estimate the contact zone removal efficiency, and ultimately the overall DAF removal efficiency, for different operational conditions.

Assuming steady-state conditions inside the DAF contact zone, the hydrodynamics can be approximated using the concepts of residence time distribution (Himmelblau and Bischoff, 1968). The bubble-particle suspension is regarded as consisting of a large number of identical fluid elements in which the interaction and the removal of the particles by the bubbles is taking place. The extent of particles removal in any particular element is proportional to the length of time it stays in the DAF contact zone, or its residence time. The residence time distribution, RTD, function E(t), which was discussed in Section 3.3, can be used to describe the overall fluid movement through the contact zone. The RTD function for open-open boundary conditions was defined by Equation 3.15.

Using the same fluid element described in Figure 3.4, the number concentration of particles, N_{CZ}, leaving the contact zone, under steady-state conditions and with total flow rate, Q_{Total}, can be written as:

$N_{CZ} = \Sigma\ N_{element}$ { N_P remaining in element of age t→t+dt and leaving contact zone} x

E(t) {fraction of exit stream which consists of elements of age t→t+dt}, or

$$N_{CZ} = \int_0^{\infty} N_{element} \cdot E(t).dt \qquad (3.42)$$

where $N_{element}$ is obtained from the solution of Equation 3.18 which is:

$$N_{element} = N_{CZ\,o} \cdot \exp(-k_P . t_m) \qquad (3.43)$$

where $N_{CZ\,o}$ is the initial particle number concentration of size, d_P, entering the contact zone.

There are two extremes of mixing conditions that can occur in a chemical reactor: completely mixed and plug flow. In completely mixed reactors there is a distribution of residence time, beginning with time zero, and the concentration is the same through the reactor. At this operational condition, E(t) can be calculated from (Gochin, 1981):

$$E(t) = \frac{Q}{V} . \exp(-\frac{Qt}{V}) = \frac{\exp(-\frac{t}{t_m})}{t_m} \qquad (3.44)$$

and therefore Equation 3.42 can be written as:

$$N_{CZ} = \int_0^{\infty} N_{CZo} \exp(-k_p t_m) \frac{\exp(-\frac{t}{t_m})}{t_m} dt \qquad (3.45)$$

and the solution of Equation 3.42 is given by:

$$\frac{N_{CZ\,e}}{N_{CZ\,o}} = \frac{1}{1 + k_p t_m} \qquad (3.46)$$

and the overall particles removal efficiency is given by:

$$R_{CZ} = 1 - \sum_{i=1}^{i=n} \left(\frac{N_{CZ\,e}}{N_{CZ\,o}} \right)_i = \frac{k_p t_m}{1 + k_p t_m} \qquad (3.47)$$

The other extreme of mixing is plug flow where the residence time of all elements of the bubble-particles suspension is the same inside the contact zone. Consequently, a concentration gradient of bubble-particle agglomerates exists along the axis of DAF contact zone. Therefore, Equation 3.42 becomes:

$$N_{CZ} = N_{element} . \int_0^{\infty} E(t).dt = N_{element} \times 1 = N_{element} \qquad (3.48)$$

or

$$N_{CZ\,e} = N_{CZ\,o} . \exp(-k_P.t_m) \qquad (3.49)$$

Hence the overall removal efficiency for plug flow is given by:

$$R_{CZ} = 1 - \sum_{i=1}^{i=n} \left(\frac{N_{CZ\,e}}{N_{CZ\,o}} \right)_i = 1 - \exp(-k_P.t_m) \qquad (3.50)$$

It is evident from Equations 3.47 and 3.50 that theoretically a plug flow contact zone is more efficient than a perfectly mixed system provided that first-order kinetics applies and k_P and t_m are the same. However, in actual DAF contact zones the fluid flow is intermediate between perfectly mixed flow and plug flow. In this case, the mixing parameter Pe is used to quantify the mixing effect on particle removal efficiency. For first-order reactions and for vessels with any kind of entrance and exit conditions, the overall removal efficiency for DAF contact zones, R_{CZ}, can be defined as (Levenspiel, 1972):

$$R_{CZ} = 1 - \sum_{i=1}^{i=n}\left(\frac{N_{CZe}}{N_{CZo}}\right)_i = 1 - \frac{4a\exp\left(\frac{Pe}{2}\right)}{(1+a)^2\exp\left(\frac{a\,Pe}{2}\right) - (1-a)^2\exp - \left(\frac{a\,Pe}{2}\right)} \qquad (3.51)$$

where

$$a = \sqrt{1 + \frac{4k_P t_m}{Pe}} \qquad (3.52)$$

Equation 3.51 can be used to calculate the overall particle removal rate constant, k_P, by measuring R_{CZ} under different operational conditions. Later, the experimental k_P values obtained from Equation 3.51, will be compared with the theoretical values obtained from Equation 3.37.

CHAPTER 4

EXPERIMENTAL PROCEDURE

4.1 Design of Pilot-Scale DAF System

The continuous-flow pilot-scale DAF system used in this research, as shown in Figure 4.1, included three units: (1) the DAF unit which included: the mixing column, the contact or reaction zone column, the clarification or separation zone tank and the air dosing system; (2) the flocculation unit; and (3) the rapid mixing unit.

The design of the continuous-flow pilot-scale DAF system was based on four major considerations: (1) an integrated treatment concept (Edzwald, 1995) where the design of the pre-treatment processes, i.e. coagulation and flocculation processes, was integrated with the flotation process; (2) the contact and the separation zones were physically delineated by designing the DAF tank as a coaxial column, where the inner column was considered part of the contact zone; (3) the mixing of the flocculated water and the supersaturated water was accomplished in a separate column, called the mixing column, where large bubbles were separated from the micro-bubbles; and (4) the influent section to the contact zone column was designed as a circular cone to minimize turbulence.

In conventional DAF units, delineation of the boundary between the contact and the separation zones is often difficult and arbitrary. For the purpose of this study, the contact and the separation zones were physically delineated by designing the DAF tank as a coaxial flotation column. The inner column was the contact zone column and the outside column was the separation zone tank. The dimensions of the contact zone column was based on length to diameter, L/D, ratio larger than 10. At this ratio, the Peclet number would be in excess of 25 and the flow would approximate a plug flow (Liers et al.,1996). The column's diameter was chosen to be 100 mm to minimize wall effects.

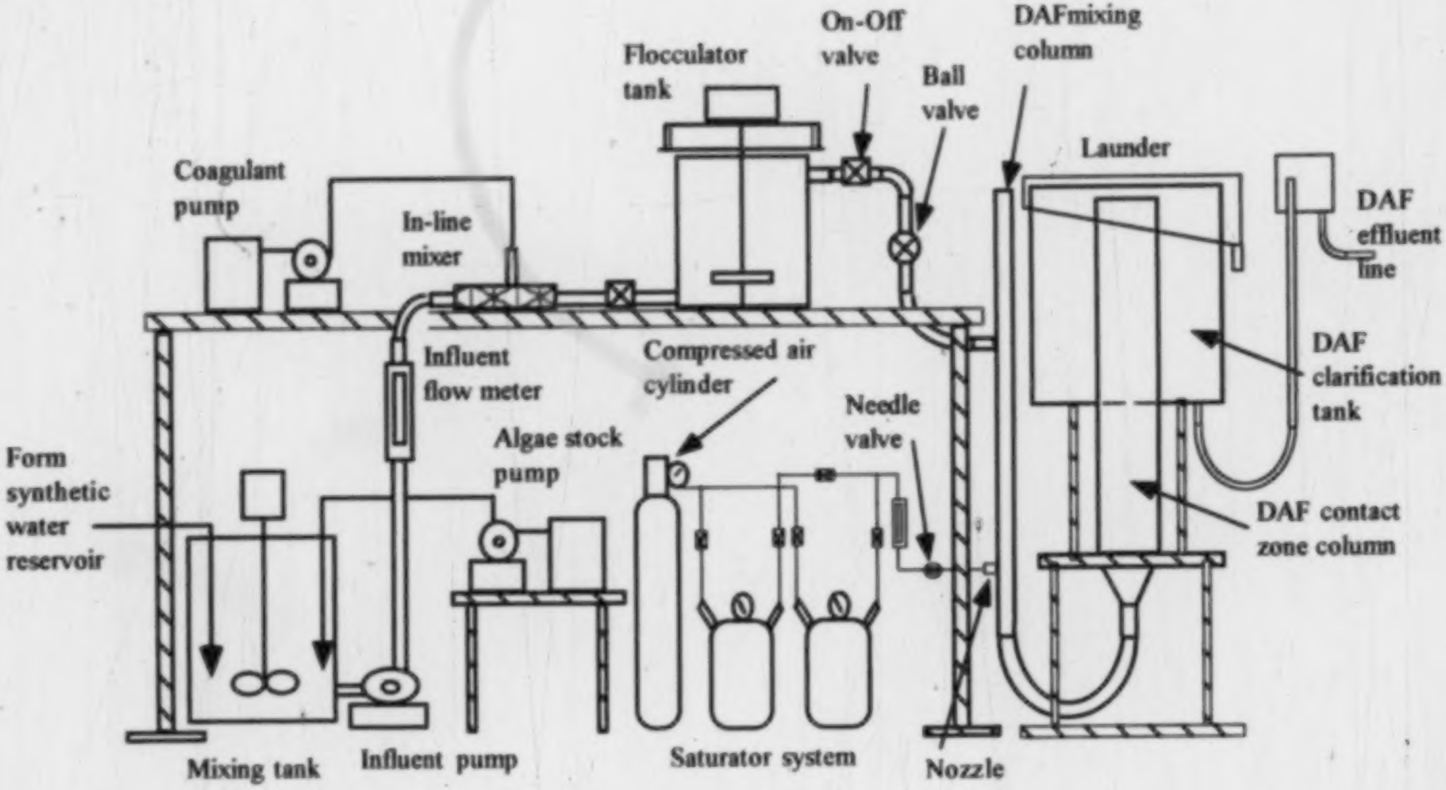
Coagulant pump
In-line mixer
Flocculator tank
On-Off valve
Ball valve
DAFmixing column
Launder
DAF effluent line
DAF clarification tank
DAF contact zone column
Influent flow meter
Compressed air cylinder
Needle valve
Algae stock pump
Form synthetic water reservoir
Mixing tank
Influent pump
Saturator system
Nozzle

Figure 4.1 Schematic diagram of the pilot-scale DAF system

In order to minimize the degree of turbulence inside the inlet section to the contact zone column, the inlet section was designed as a circular cone. The height and the side slopes of the cone were determined based on the assumption that the influent water would follow a natural jet growth.

In order to avoid the presence of large bubbles of diameter greater than 150 μm in the contact zone, the saturated water was injected into a separate column, called the mixing column, where the influent or the flocculated water, coming from the flocculator, was directed downward. The mixing column diameter was determined based on the assumption that bubbles with diameters larger than 150 μm would rise in the mixing column even at the highest flow rates. Therefore, only micro-bubbles (bubbles with size less than 150 μm) would flow to the contact zone column. The section of the mixing column, where saturated water was mixed with the flocculated water, was considered to be part of the contact zone.

The contact zone hydraulic loading was based on the total water flow rate Q_{Total}, which included influent water flow rate, Q_{Water}, plus the saturated water flow rate, Q_{Sat}, divided by the maximum cross-sectional area of the contact zone. In this study, hydraulic loading rates ranged from 30 to 90 m/h. The Q_{Water} was simply determined by measuring the DAF column overflow rate, under steady-state conditions. The overflow rate was controlled by means of a ball valve located upstream of the mixing column and just after the flocculation tank.

In order to perform the bubble size and rise velocity measurements in the contact zone column, using the PDA instrument, three considerations were taken into the design of the column: (1) the clarification tank could be easily replaced with a launder which would fit on the top of the contact zone column to collect and discharge overflow water; (2) the column was made of clear acrylic; and (3) the column was surrounded by a clear acrylic rectangular tank and the gap between them was filled with tap water.

The design of the separation zone tank was based on two important parameters: (1) the cross-flow velocity from the contact zone into the separation zone. Haarhoff and van Vurren (1994) suggested that the cross-flow velocity should be less than or equal to the maximum hydraulic loading of the contact zone; and (2) the hydraulic loading or the limiting overflow rate of the separation zone, U_{OS}. The separation zone hydraulic loading rate was based on the total flow rate, Q_{Total}. The U_{OS} velocity should not exceed the rising velocity of the bubble-floc agglomerates. The maximum value suggested by Haarhoff and van Vurren (1994) was 11 m/h.

Table 4.1 summarizes the dimensions of the mixing and contact zone columns, and the separation tank dimensions.

The DAF air dosing system was used to produce supersaturated water which was injected into the contact zone to produce fine bubbles. It consisted of two 18 L pressurized tanks, called saturator tanks, with a pressure gauge, compressed air source with a pressure regulator, flow meter, metering valve and a nozzle assembly. The design of the nozzle assembly followed exactly the same details of the bench-scale DAF unit nozzle assembly (Aztec Environmental Control Ltd., UK). Figure 4.2 shows a cross-section through the nozzle assembly.

To design the diameter of the saturated water inlet, or the nozzle inlet, to the mixing column, the hydrodynamic requirements for mixing or blending the saturated water and the main water were taken into consideration. Mixing is considered to be achieved when the momentum of the saturated water flow M_{Sat} divided by the momentum of the main water flow M_{Water} is ≥ 0.14 (Fawcett, 1997). The momentum ratio can be defined as:

$$\frac{M_{Sat}}{M_{Water}} = (1-\varepsilon_f)\left(\frac{Q_{Sat}}{Q_{Water}}\right)^2 \frac{A_{Water}}{A_{Sat}} \qquad (4.1)$$

Table 4.1 Summary of mixing and contact zone columns, and the separation tank dimensions

Design Parameter	Units	Dimensions
Contact Zone Column		
H_{CZ}	mm	1200
Max.d_{CZ}	mm	100
Min.d_{CZ}	mm	40
Max. A_{CZ}	m^2	0.00785
V_{CZ}	m^3	0.00942
Height of cone	mm	300
Mixing column		
H_{MC}	mm	500
d_{MC}	mm	40
V_{MC}	mm	0.0006
Separation Zone Tank		
H_{SZ}	mm	700
d_{SZ}	mm	400
V_{SZ}	m^3	0.0879
A_{SZ}	m^2	0.1256

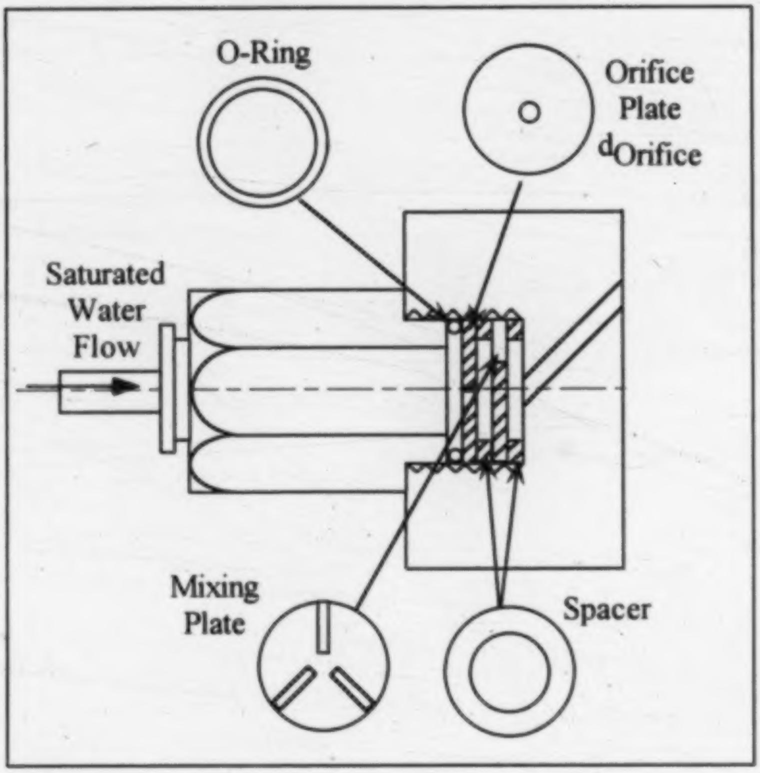
O-Ring
Orifice Plate
$d_{Orifice}$
Saturated Water Flow
Mixing Plate
Spacer

Figure 4.2 Cross-section through the nozzle plate assembly

where ε_f is the volume fraction of air bubbles in the saturated water, Q_{Sat} is the saturated water flow, Q_{Water}, is the main water flow rate, A_{Water} is the cross sectional area of the main water inlet and A_{Sat} is the cross sectional area of the saturated water inlet. Equation 4.1 was used to calculate the required diameter of the nozzle inlet.

As was discussed in Chapter 2, bubble volume concentration can be controlled by the saturator efficiency, saturator pressure and the saturated water flow rate or the recycle ratio. The saturator efficiency of the unpacked saturator used for this study was determined by following the batch method used by Henry and Gehr (1981). The experimental procedure and the results are summarized in Appendix A.1. The saturator pressure was controlled by the pressure regulator. The maximum operational pressure for the saturator tank was 620 kPa. The recycle ratio was controlled by a metering valve while the calibrated flow meter was used to measure the Q_{Sat}.

The flocculator was designed to provide about 5 minutes of residence time at a flow rate of 0.7 m^3/h. The tank was designed with an overflow weir so that the water head in the flocculator, and consequently in the DAF column was always constant. The flocculator effluent flow rate, Q_{Water}, was controlled by a ball valve located downstream of the flocculator effluent line. The overflow was collected in a launder and was discharged to the waste line. The flocculator was elevated to create a pressure head for the water to flow by gravity to the DAF column.

The flocculation mixing unit consisted of a vertical shaft connected to a variable speed motor. Mixing was accomplished by using a flat turbine with six-flat-blade. The following design criteria for the mixing unit were taken into consideration:
(1) maximum impeller tip speed did not exceed 1.52 m/s;
(2) impeller diameter to equivalent tank diameter ratio was 0.35;
(3) impeller power number was 5.0; and
(4) variable speed motor provided a G range of 30 to 150 s^{-1}.

The velocity gradient of the flocculator mixer was determined following Malley's (1988) procedures. Table 4.2 summarized the flocculator unit dimensions and design specifications.

The rapid mixing unit used in this study was an in-line static mixer. The objective of the rapid mixing unit was to disperse the coagulant in raw water as rapidly as possible so that the hydrolysis products that developed in 0.01 to 1 second would cause destabilization of the colloid via the charge neutralization mechanism. For that purpose, Johnson and Amirtharajah (1983) recommended high intensities of mixing, G values of 3000 to 4000 s^{-1}, for very short times, less than 1 second.

4.2 Tracer Study Experimental Set-up

The tracer study was conducted using the pilot-scale DAF system that was described in detail in Section 4.1. Figure 4.3 shows a schematic diagram of the tracer study set-up.

The RTD may be described experimentally by either pulse-input tests or step-input test. The results from these tests are usually interrelated and provide similar information on the residence time distribution of fluid elements inside a reactor (Levenspiel, 1972). In this research, the pulse-input test was used, where the liquid residence time was determined by the impulse and response technique.

Initially, deionized water was pumped from a storage tank into an elevated stainless steel tank. This tank provided enough pressure head for the water to flow by gravity to the mixing column at the desired flow rates. The flow rate entering the column was controlled by means of a ball valve located at the elevated tank's effluent line. Saturated water was injected into the mixing column, by means of a nozzle, below the

Table 4.2 Summary of flocculator unit dimensions

Design Parameter	Units	Dimensions
Tank side depth	mm	470
Tank width	mm	350
Tank length	mm	350
Tank volume	m^3	0.0582
Baffles number		4
Baffles width	mm	35
Impeller diameter	mm	120
Impeller height above tank's bottom	mm	120
Flat blades number		6
Blade width	mm	25
Blade length	mm	30

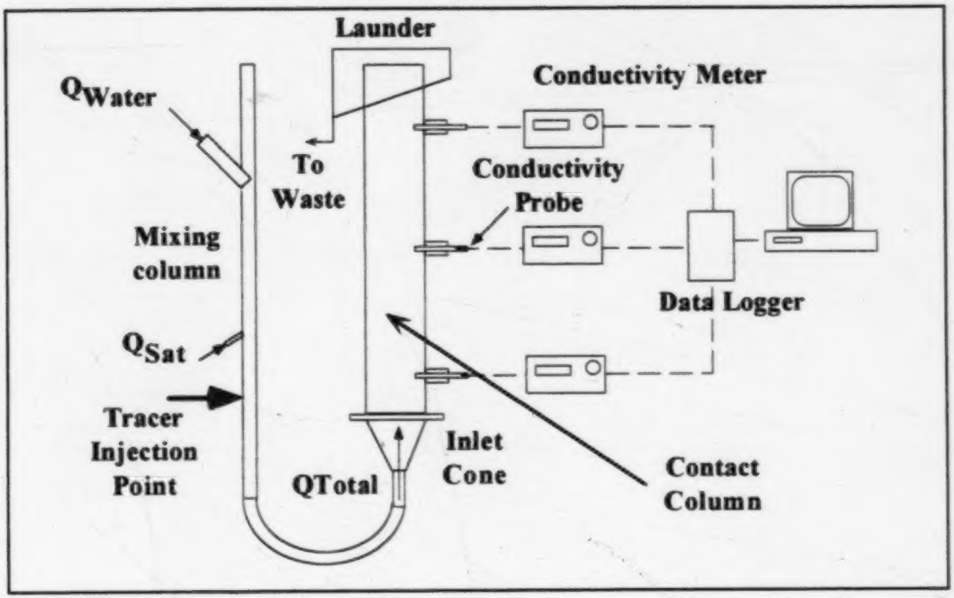
Launder
Q_{Water}
Conductivity Meter
To Waste
Conductivity Probe
Mixing column
Data Logger
Q_{Sat}
Tracer Injection Point
QTotal
Inlet Cone
Contact Column

Figure 4.3 Schematic diagram of the tracer study set-up

deionzed water feeding point. The saturated water flow rate was regulated by means of a needle valve. Total water flow ,Q_{Total}, which includes deionized water flow rate ,Q_{Water}, and saturated water flow rate, Q_{Sat}, entered the contact column from the bottom through a circular cone section. Constant deionized water and saturated water flow conditions were considered to be achieved after about eight turnovers of contact zone volume.

A pulse, consisting of 20 mL of 25 % aqueous NaCl was injected just below the saturated water injection point, as shown in Figure 4.3. The system response, as a function of time, was monitored by recording the change of the conductivity of water at three different heights inside the contact zone column. This was achieved by means of three conductivity probes, which consisted of a pair of electrodes, which were fitted into three sealed ports along the side wall of the column. Each probe was connected to a conductivity meter (YSI model 34). These conductivity meters were connected to a data logger (Chart Pac™ data recording module CP-X, Lakewood Systems, Houston, Texas) where conductance values were recorded and stored.

Experimentally obtained conductivity-time profiles were translated into concentration-time (of tracer) profiles. That was achieved using a special computer software (Lakewood data logger processing software version 4.38, Lakewood Systems, Houston, Texas). In order to do the translation, each probe had to be calibrated by measuring the voltage at different concentrations of NaCl solution and the results were fed into the software. To correct for background noise, the conductance of deionized water was subtracted from the conductance measured after the injection of the tracer.

Before starting the experiments, the effect of air bubbles on conductivity readings was evaluated. This was accomplished by comparing the conductivity readings at different NaCl concentrations with and without the presence of air bubbles. The effect of air bubbles was insignificant as is shown in Figure 4.4.

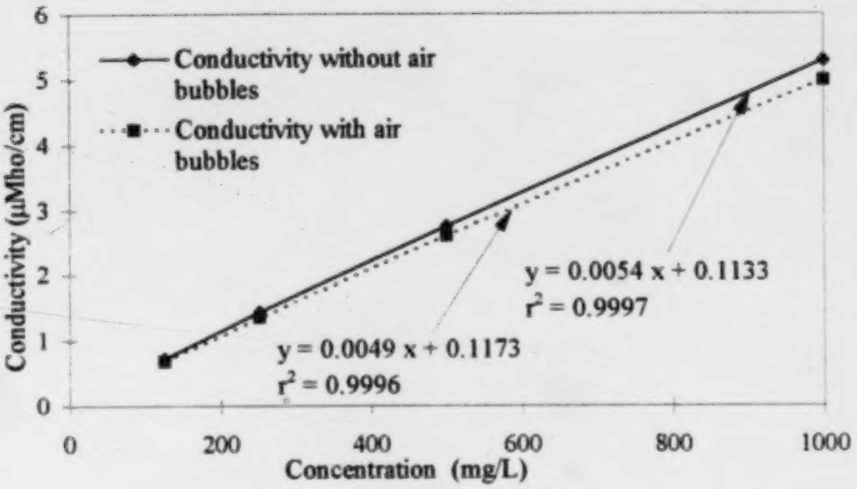

Figure 4.4 Effect of air bubbles on conductivity measurements

The RTD of the contact zone, at the top, middle and the bottom of the contact column, was evaluated at four different hydraulic loading rates: 30, 50, 70 and 90 m/h. Also,at each hydraulic loading, saturated water flow rate, Q_{Sat} varied from 5 % to 10 % of the influent water flow rate, Q_{Water}, i.e. recycle ratios were 5 % to 10 %. All these experiments were performed under constant P_{Sat} of 484 kPa. All experiments were performed at least five times. Table 4.3 summarizes the arrangement of the tracer study experiments.

4.3 Bubble Size, Concentration and Velocity Measurements Using PDA

4.3.1 PDA configuration and setting adjustment

The system used in this study was the 2-D DANTEC particle dynamic analyzer (DANTEC, Denmark). It consisted of the following components: 55x modular LDA transmitting optics, 55x10 receiving optics, 55x08 photomultipliers and 58N10 processor. Figure 4.5 shows the set-up for the PDA used in this study.

In order to perform accurate measurements of bubble sizes and velocity, the PDA settings must be properly adjusted for the flow being studied. PDA instrument configuration and adjustment included transmitting optics, receiving optics and electronics adjustment. In order to optimize these settings, it was necessary to go through an iterative procedure where the instrument measurement ranges were set very wide to get an indication of the characteristic velocity and size values present. Then the instrument was finely adjusted to match the measurement range to the flow being studied. The PDA configuration and settings adjustment used in this research are outlined in Table 4.4.

The laser wavelength for the velocity component in the direction of the rising bubbles, i.e. the x-direction, was 514.5 nm Argon-Ion laser. The transmitting optics

Table 4.3 Experimental arrangements for the tracer study

Run #	Hydraulic Loading (m/h)	Q_{Total} (L/min)	Recycle Ratio (%)	Q_{Sat} (mL/min	Q_{Water} (L/min)	HRT (min)		
						Top[1] Port	Middle[2] Port	Bottom[3] Port
1	30	3.9	0	0	3.9	2.9	1.9	1.0
2	30	3.9	5	187	3.7	2.9	1.9	1.0
3	30	3.9	10	357	3.6	2.9	1.9	1.0
4	50	6.5	0	0	6.5	1.7	1.1	0.6
5	50	6.5	5	312	6.2	1.7	1.1	0.6
6	50	6.5	10	595	5.9	1.7	1.1	0.6
7	70	9.2	0	0	9.2	1.2	0.8	0.4
8	70	9.2	5	436	8.7	1.2	0.8	0.4
9	70	9.2	10	833	8.3	1.2	0.8	0.4
10	90	11.8	0	0	11.8	1.0	0.6	0.3
11	90	11.8	5	561	11.2	1.0	0.6	0.3
12	90	11.8	10	1070	10.7	1.0	0.6	0.3

1 HRT calculations are based on the contact zone volume from the point of trace injection to the top port

2 HRT calculations are based on the contact zone volume from the point of tracer injection to the middle port

3 HRT calculations are based on the contact zone volume from the point of tracer injection to the bottom port

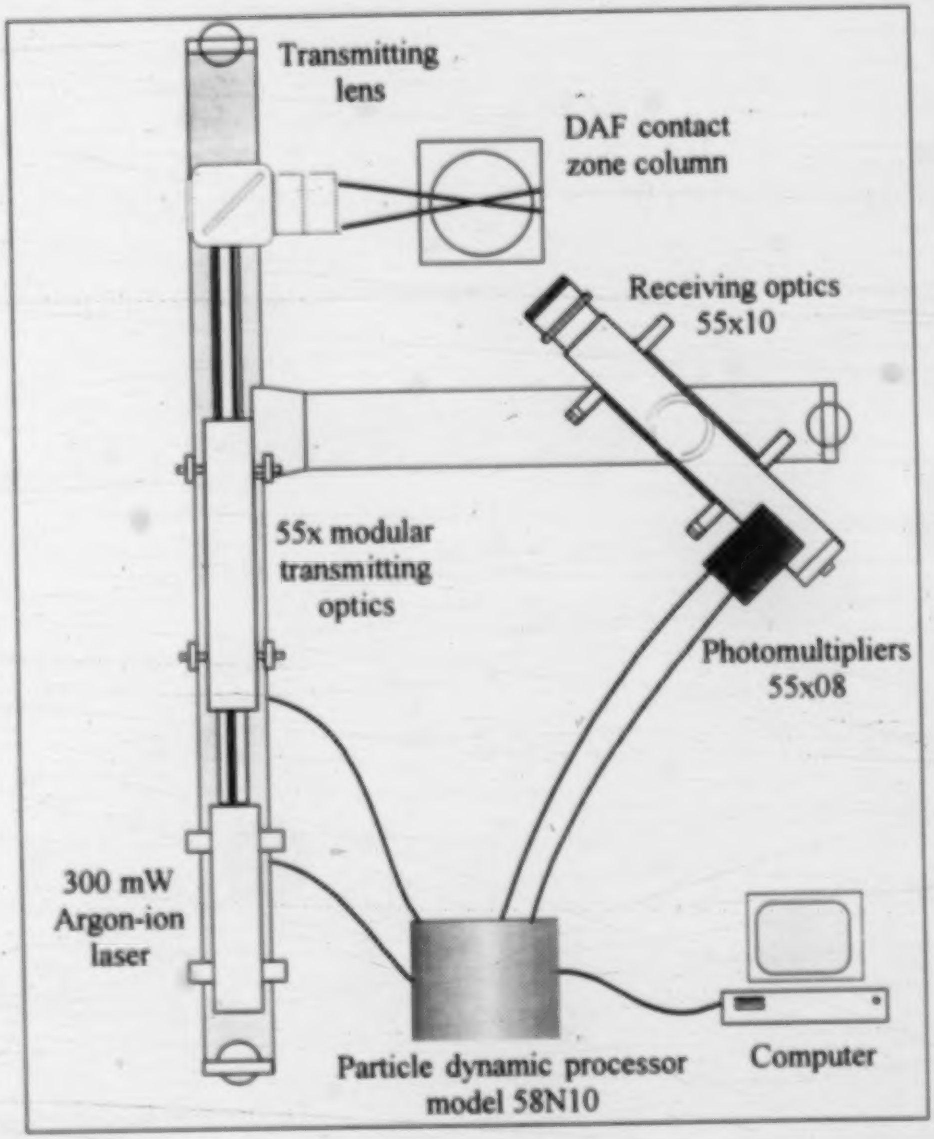
Transmitting lens
DAF contact zone column
Receiving optics 55x10
55x modular transmitting optics
Photomultipliers 55x08
300 mW Argon-ion laser
Particle dynamic processor model 58N10
Computer

Figure 4.5 PDA set-up

Table 4.4 PDA configuration

PDA Component	Units	Setting
Transmitting Optics Setup:		
Front lens focal length	mm	310
Laser beam spacing	mm	52
Fringe spacing	μm	3.1
Number of fringes		40
Measurement volume	mm	0.1219 x 0.1219 x 1.9421
Frequency shift sign		negative
Polarization	degree	0.
Polarization orientation		parallel to fringes
Laser wavelength	nm	$\lambda = 514.5$
Laser power	mW	300
Gaussian beam diameter	mm	0.82
Beam collimation		1.2
Beam expansion		1.85
Receiving Optics Setup:		
Front lens focal length	mm	310
Polarization	degree	0
Scattering angle (δ)	degree	70 (forward scatter deflection)
Electronic Setup:		
Signal bandwidth	MHz	0.12
S/N ratio	dB	-3

included a short focal length lens (310 mm) to maximize the light intensity in the measuring volume. With a beam spacing of 52 mm for the 310 mm lens, this produced an instrument or probe measurement volume of 0.12 mm x 0.12 mm x 1.94 mm. The direction of the fringe motion affected the sign of the phase shift. Therefore, the sign of the phase shift was determined by the direction of the fringe motion. The direction of the fringe motion was opposite to the direction of the positive velocity, which was the positive x-axis in this particular setup. Therefore, the sign of the fringe motion and phase shift was negative. Polarization in the receiving optics was set relative to the scattering plane, or the probe measurement volume. For air bubbles moving in the positive x-axis, the transmitted beams would lie in a horizontal plane and the fringes would lie in a horizontal plane which was also the scattering plane. Since air bubbles have near forward scatter, the polarization was set parallel to the scattering plane.

Regarding the receiving optics configurations, the receiving lens was chosen with short focal length, i.e. 310 mm, to increase bubble size resolution and to improve the signal-to-noise ratio of the Doppler signals. The polarization was set to match that of the transmitting optics. As shown in Figure 4.5, the PDA was operated in the forward scatter mode with a deflection angle of 70° from the true forward scatter because this angle was considered to be the optimum scattering angle for air bubbles (DANTEC, 1988).

The PDA electronics were adjusted to match the size and velocity ranges that were investigated in this study. The band pass filters were set at a signal bandwidth of 0.12 Mhz. This bandwidth was chosen to optimize the data rate, to minimize noise and to ensure that all velocities encountered were contained within the selected bandwidth. The system as configured required four photomultipliers, PMT. Each PMT had an individual high voltage supply, with each being adjusted to account for normal variations in sensitivity between PMT's. Adjustment were made by comparing signals on a two channel oscilloscope.

The previous PDA configuration and settings were based on running many experiments using the pilot-scale DAF column. Comparison between measured liquid superficial velocities, at different hydraulic loading rates, to those calculated based on the measured flow rates verified that the PDA was configured correctly. Also, it was important to verify that the PDA was configured correctly for the mean bubble size measurements. In order to do that, video images of air bubbles were taken and the mean bubble diameter was measured and compared to that measured by the PDA. The results obtained by the videophotography method were used to refine the PDA settings. The videophotography method used for measuring bubble size is discussed next.

4.3.1.1 Bubble size measurements using the video photography method

The measurements taken by this method were performed under the same operational conditions, i.e. hydraulic loading, saturator pressure and recycle ratio, as those measured by the PDA. Bubble size measurements were taken at column height of 900 mm, measured from the square base of the column, using a CCD camera (768(H) x 494 (V) pixels). The camera was mounted with a micro lens (Zoom 6000, D.O. Industries, New York) with 63.5x magnification with a 20-inch monitor. The CCD video camera was capable of capturing 30 frames per second.

In order to accurately position the video photographic equipment, a support was fabricated which consisted of an aluminum rack and pinion assembly used to focus the micro lens. The assembly was mounted on a hinge provided with screw adjustment for leveling the CCD camera and the micro lens. The entire assembly was bolted to a scissors jack which allowed raising or lowering of the assembly. For stability, the jack was bolted to a heavy base plate. Adequate light was provided using a fiber optic source which was positioned at an oblique angle such that air bubbles would appear as black solid spheres in the monitor. The micro lens was focused on a line scribed on the inside of the column.

The captured video images of air bubbles were recorded using a high quality VCR. The VCR was connected to a video capture board, via a PC computer, where video images were captured using Media Studio VE software (version 2, Ulead Systems). Using the same software, individual frames containing air bubbles images were selected and saved in separate files for bubble size analysis.

Bubble size analysis was performed first by selecting the individual air bubbles which were sharply focused and digitizing them using a digitizing images software. The software was used to measure the (x,y) coordinates at different points around the circumference of the individual bubble so that the length of the straight line connecting any two points could be calculated. However, it was important to determine the scale factor by which all measurement should be multiplied in order to obtain the actual readings. The scale factor was determined by measuring the length of a stage micrometer slide with 10 µm divisions. The stage micrometer slide was attached to the inside of the contact zone column at the same location were air bubble images were taken. Also, the same magnification was used for both the slide micrometer and air bubbles images. To measure the bubble diameter, the length across the spherical bubble was measured in several directions, such that these lines intersected near the center of the bubble. These measurements were multiplied by the scale factor and the average was taken as the mean bubble diameter.

4.3.2 PDA experimental set-up

The experimental set-up consisted of the same pilot-scale DAF contact zone column that was used for the tracer test study. The 100 mm acrylic column was surrounded by a 150mm x 150mm acrylic tank where the gap between the column and the square tank was filled with tap water. This installation was important so that accurate bubble size and velocity measurements with the PDA could be achieved (the same installation was used for bubble size measurements using the videophotography method).

As was explained earlier, the PDA was operated in the forward scatter mode with a scattering angle of 70° from the true forward scatter direction. This is shown in Figure 4.6 with relation to the contact zone column. This figure also shows the measurement coordinate system used in this study. The laser beams are in the X-Z plane with the bisector, or the probe volume, along the Z-axis. The fringe plane, which is also the scattering plane, is parallel to the Y-Z plane. The flow velocity measured is the component perpendicular to the fringe plane, i.e. in the direction of the X-axis.

The receiving lens is rotated so that its axis forms an angle of 70° with the forward scatter line. In this set-up, the transmitting optic lens is parallel to side 1-3 of the square tank (called the transmitting window) as shown in the plan view of Figure 4.6. The receiving optic lens makes 20° with side 1-2 of the square tank (called the receiving window).

Bubble size and velocity and water velocity were measured at different points inside the contact zone column as well as at different heights. To locate the exact probe volume coordinates, two marked grid systems were used, as shown in Figure 4.7. The Y-Z grid system consisted of a 100 mm circular plate, placed at the top of the column, with pre-drilled holes at different (y,z) coordinates. A thin nylon string was attached to the plate at the desired (y,z) coordinate and a small plumb was used to keep the line in a vertical position.

The X-Z grid was simply a transparent grid paper with 10 mm divisions attached to the outside square tank of the DAF column facing the transmitting optic lens. The center of the grid was marked with a line representing the center of the contact zone column. The position of the desired probe volume coordinate was determined by moving the DAF column manually until the two laser beams intersected with the nylon string at the desired (y,z) coordinates and the middle point of the two laser beams, on the transparent grid paper, coincides with the desired (x,z) coordinates.

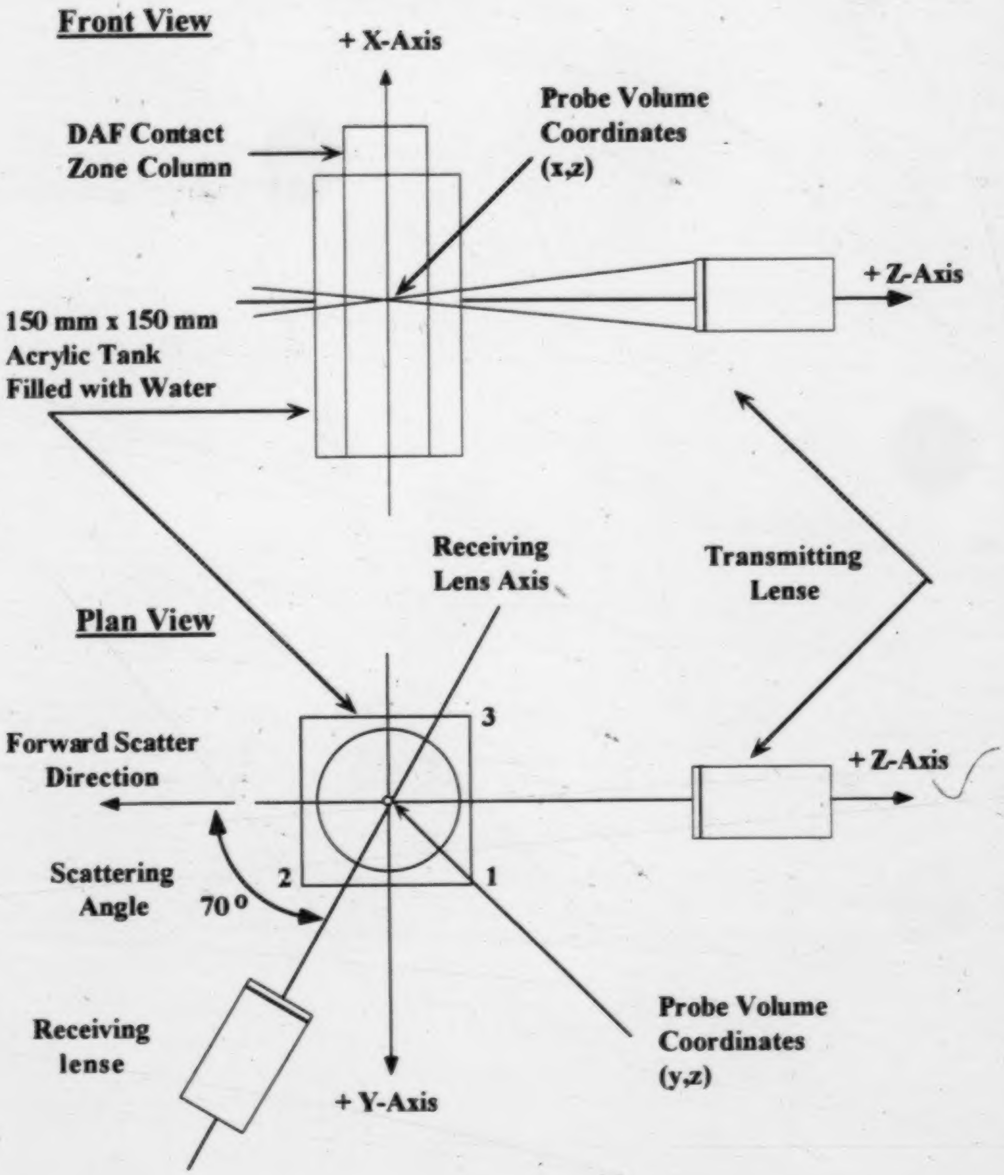
Front View
+ X-Axis
DAF Contact
Zone Column
Probe Volume
Coordinates
(x,z)
+ Z-Axis
150 mm x 150 mm
Acrylic Tank
Filled with Water
Receiving
Lens Axis
Transmitting
Lense
Plan View
3
Forward Scatter
Direction
+ Z-Axis
Scattering
Angle
70 o
2
1
Receiving
lense
+ Y-Axis
Probe Volume
Coordinates
(y,z)

Figure 4.6 PDA experimental coordinate system

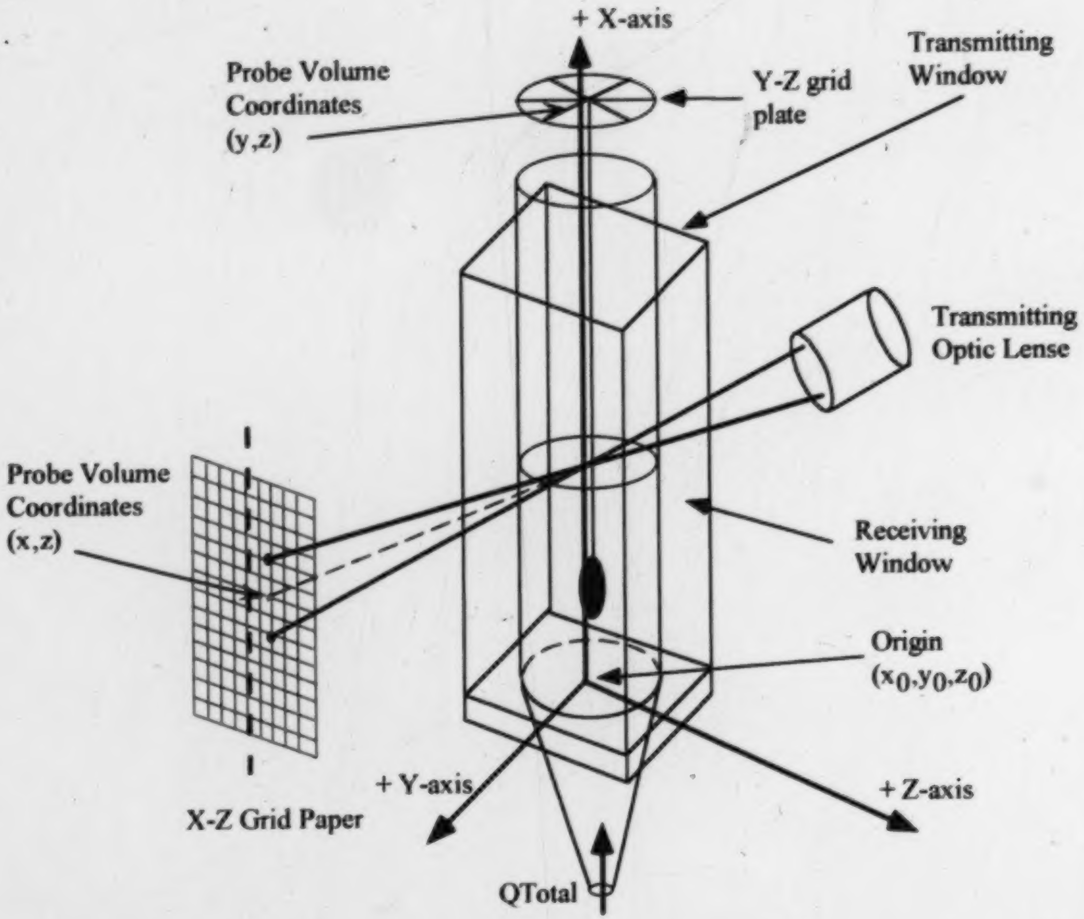
+ X-axis
Probe Volume Coordinates (y,z)
Y-Z grid plate
Transmitting Window
Transmitting Optic Lense
Probe Volume Coordinates (x,z)
Receiving Window
Origin (x_0,y_0,z_0)
+ Y-axis
X-Z Grid Paper
+ Z-axis
QTotal

Figure 4.7 Location of probe volume coordinates inside the contact zone column

Since the PDA set-up was fixed, the x coordinate remained constant, i.e. the height at which the measurements were taken was fixed, and only the (y,z) coordinates were be changed. In order to take measurements at a lower height inside the column, the whole column had to be raised by placing it on the top of a wooden box with height equal to the desired height at which the measurements were taken.

In this experiment, two heights were investigated, 900 and 400 mm from the base of the DAF column, where the (x_o,y_o,z_o) origin was considered to be the point at the center of the column base, as shown in Figure 4.7. The height of the laboratory ceiling restricted taking measurements at lower heights.

After determining the desired position of the probe volume, i.e. the (x,y,z) coordinates, the required PDA settings were fed into the PDA computer. The next step would be taking the superficial water velocity, bubble size, concentration and instantaneous rise velocity which is discussed in details in the following sections.

4.3.2.1 Measurement of superficial liquid velocity

Superficial liquid velocity in the X-direction, U_L, was measured at different contact zone hydraulic loading rates. Desired hydraulic loading rates were determined by measuring the water flow rate, Q_{Total}, exiting the contact zone column, using the stop watch and the bucket method, then dividing the flow by the maximum cross sectional area of the contact zone. The influent water was seeded with TiO_2, at very low concentrations, due to its good light scattering properties.

In these experiments, the saturated flow rate, Q_{Sat}, was zero, i.e. $R_R=0$. Therefore, the total flow rate, Q_{Total}, entering the contact zone was equal to the seeded deionized water flow rate, Q_{water}, fed from the elevated storage tank. This tank provided enough pressure head for the water to flow by gravity to the mixing column first and then to the contact zone column. The flow rate entering the column was controlled by means of a ball valve located at the elevated tank's effluent line.

Superficial liquid velocities were measured at two heights: 900 and 400 mm, from the base of the contact zone column. That was accomplished by manually positioning the column, as was explained in the previous section. Measurements were taken after reaching steady state condition which was determined at approximately eight times the theoretical residence time of the contact zone. Measurements were replicated five times and the average was taken as the mean value for U_L. Table 4.5 summarizes the experimental arrangements for U_L measurements.

For this part of the study, U_L measurements in the contact zone did not require the presence of air bubbles and therefore Q_{Sat} was equal to zero. That means there was no water flow through the nozzle in the mixing zone. Therefore, it was important to check whether this condition would affect U_L measurements inside the contact zone. That was accomplished by measuring the U_L with the PDA under two different operational conditions.

The first condition involved pumping deionized water, using a peristaltic pump, into the mixing column and through the nozzle at a rate equal to 5% of the seeded deionized water flow rate, Q_{water}. The contact zone hydraulic loading was 50 m/h and the corresponding Q_{Total} was 6.5 L/min.

The second operational condition was performed without pumping deionized water through the nozzle, where $Q_{Total} = Q_{water} = 6.5$ L/min. U_L were measured at the same probe volume coordinates for both operational conditions. Results were compared using the t-test at 1% level of statistical significance.

Table 4.5 Experimental arrangements for U_L measurements with the PDA

Experiment #	Contact zone hydraulic loading (m/h)	Probe volume coordinates (x,y,z) in mm
1	30	(900,0,25)
2	30	(400,0,25)
3	50	(900,0,25)
4	50	(400,0,25)
5	70	(900,0,25)
6	70	(400,0,25)
7	70	(900,0,-45)
8	70	(900,0,-25)
9	70	(900,0,0)
10	70	(900,0,45)
11	90	(900,0,25)
12	90	(400,0,25)

4.3.2.2 Measurement of bubble size, concentration and instantaneous rise velocity

Bubble size, concentration and instantaneous rise velocity, $U_{B\ inst}$, in the x-direction were measured at different operational conditions: (1) different saturator pressures, P_{Sat}, at constant contact zone hydraulic loading and constant recycle ratio, R_R; (2) different contact zone hydraulic loading rates at constant P_{Sat} and R_R; (3) different recycle ratios at constant contact zone hydraulic loading rate and P_{Sat}; and (4) different nozzle orifice diameters at constant contact zone hydraulic loading rate, R_R and P_{sat}. Also, the effect of contact zone column height and wall effects on bubble size, concentration and rise velocity were measured.

Bubble size, concentration and $U_{B\ Inst}$ were measured at three different value of P_{sat}: 345, 484 and 587 kPa. These experiments were performed under constant contact zone hydraulic loading of 70 m/h and R_R = 5 %, that corresponded to Q_{Total} = 9.2 L/min (Q_{Water} = 8.7 L/min and Q_{Sat} = 0.5 L/min). These measurements were taken at probe volume coordinates (900,0,0). Measurements were taken after reaching steady state condition which was determined at approximately eight times the theoretical residence time of the contact zone. Also, to ensure that the saturator had reached a steady state condition, the measurements were started after reaching a steady data rate and validation percentage on the PDA software. Measurements were replicated four times and the average was taken as the mean value for bubble diameter, concentration and $U_{B\ inst}$.

In all experiments, two 18 liter saturator tanks were used so that a continuous supply of saturated water flow could be provided in case achieving steady state conditions required longer time.

Also, bubble size, concentration and $U_{B\ inst}$ were measured at different contact zone hydraulic loading rates and recycle ratios, as summarized in Table 4.6. All experiments were performed under constant saturator pressure of 484 kPa. After locating the probe

Table 4.6 Experimental arrangements for studying the effect of recycle ratio and hydraulic loading on bubble size, concentration and rise velocity at probe volume coordinates (900,0,25)

Experiment #	Contact zone hydraulic loading (m/h)	R_R (%)	Nozzle orifice diameter $d_{Orifice}$ (mm)
Effect of R_R experimental arrangement			
1	30	7	0.55
	30	10	0.55
2	50	5	0.55
	50	7	0.55
3	70	3	0.55
	70	5	0.55
4	90	3	1.03
	90	5	1.03
	90	7	1.03
Effect of hydraulic loading experimental arrangement			
1	30	7	0.55
	50	7	0.55
2	50	5	0.55
	70	5	0.55
3	70	3	0.55
	90	3	0.55
4	70	7	1.03
	90	7	1.03

volume coordinates, which was (900, 0, 25), deionized water flow rate, Q_{Water}, and the saturated water flow rate, Q_{Sat}, were adjusted so that the required contact zone hydraulic loading rate and R_R were achieved.

Saturated water was injected into the mixing column through the nozzle, which had an orifice with the required diameter, $d_{Orifice}$. Q_{Sat} was controlled by means of a needle valve and was measured using a calibrated flow meter. Measurements were taken after reaching steady state condition which was determined at approximately eight times the theoretical residence time of the contact zone. Measurements were replicated four times and the average was taken as the mean value for bubble diameter, concentration and $U_{B\ inst}$.

The effect of nozzle orifice diameter, $d_{Orifice}$, on bubble size and concentration was investigated. Two different values of $d_{Orifice}$ were used in this study: 0.55 and 1.03 mm. Before each experiment, the orifice plate with the desired $d_{Orifice}$ was placed inside the nozzle, as shown in Figure 4.1. The orifice with 0.55 mm diameter had a maximum flow rate of 480 mL/min at P_{Sat} of 484 kPa while the orifice with the 1.03 mm diameter had a maximum flow rate of 1010 mL/min at the same P_{Sat}. Table 4.7 summarizes the experimental arrangements for studying the effect of $d_{Orifice}$ on bubble size and concentration.

To study the effect of contact zone height on bubble size, concentration and $U_{B\ inst}$, PDA measurements were taken at two different heights: 900 and 400 mm, measured from the base of the DAF column to the probe volume. Measurements taken at 400 mm were achieved by placing the DAF column on top of a 500 mm support. At the same time, the elevated water tank was raised by 500 mm to maintain the same head pressure.

Table 4.8 summarizes the experimental arrangements for studying the effect of contact zone height on bubble size, concentration and $U_{B\ inst}$. All measurements were

Table 4.7 Experimental arrangements for studying the effect of nozzle orifice diameter on bubble size, concentration and instantaneous rise velocity

Experiment #	Contact zone hydraulic loading (m/h)	R_R (%)	Nozzle orifice diameter $d_{Orifice}$ (mm)
1	50	7	0.55
	50	7	1.03
2	70	5	0.55
	70	5	1.03
3	70	5	0.55
	70	5	1.03
4	90	3	0.55
	90	3	1.03

Table 4.8 Experimental arrangements for studying the effect of contact zone column height on bubble size, concentration and instantaneous rise velocity

Experiment #	Contact zone hydraulic loading (m/h)	R_R (%)	Probe volume coordinates (x,y,z) in mm	Nozzle orifice diameter $d_{Orifice}$ (mm)
1	30	7	(900,0,25)	0.55
	30	7	(400,0,25)	0.55
2	30	10	(900,0,25)	0.55
	30	10	(400,0,25)	0.55
3	50	5	(900,0,25)	0.55
	50	5	(400,0,25)	0.55
4	50	7	(900,0,25)	0.55
	50	7	(400,0,25)	0.55
5	50	10	(900,0,25)	1.03
	50	10	(400,0,25)	1.03
6	70	3	(900,0,25)	0.55
	70	3	(400,0,25)	0.55
7	70	5	(900,0,25)	0.55
	70	5	(400,0,25)	0.55
8	70	7	(900,0,25)	1.03
	70	7	(400,0,25)	1.03

performed at P_{Sat} of 484 kPa. Measurements were taken after reaching steady state condition which was determined at approximately eight times the theoretical residence time of the contact zone. Measurements were replicated four times and the average was taken as the mean value for bubble diameter, concentration and $U_{B\,ins}$.

4.4 DAF Kinetic Experiments

The objectives of these experiments were to determine the effect of different operational conditions on DAF performance, in terms of particle removal, to measure the overall DAF removal efficiency, R_{DAF}, and to estimate the contact zone removal efficiency, R_{CZ}.

These experiments were conducted at optimum coagulant dosage using synthetic water spiked with algae. They were performed using the same pilot-scale DAF system that was used in both the tracer studies and the particle dynamic analyzer measurements. However, the set-up was modified by attaching the separation or the clarification tank to the contact zone column. Figure 4.1 is the schematic diagram of the complete pilot-scale DAF system that was used in this part of the study.

In the following sections, detailed experimental procedures for the preparation of the synthetic water and the algae culture, the bench-scale DAF experiments, which were used to determine the optimum coagulant dosage, and the pilot-scale DAF experiments, which were used to measure R_{DAF} and to estimate R_{CZ}, are presented.

4.4.1 Synthetic water and algae culture preparation

The synthetic water used in this study consisted of *Chlorella vulgaris* suspended in chemically conditioned deionized water. The synthetic water used in these experiments had an inorganic composition similar to that found in a typical Alberta prairie lake. Table 4.9 summarizes synthetic water composition without algae suspension.

Chlorella vulgaris is a small unicellular, non-motile green algae which may grow singly or in clusters is commonly found in Alberta prairie lakes and causes taste and odor. It was chosen as the model algae because it was easily cultured in the laboratory. *Chlorella v.* cells are approximately spherical in shape, an advantage for measuring cell size and numbers using the particle counter, with a diameter range of about 2 to 10 μm with a mean diameter of 5.28 μm and mean density very close to water of 1.07 g/mL (Edzwald and Malley, 1990).

Axenic *Chlorella vulgaris* cultures were purchased from the University of Toronto Culture Collection, UTCC. The algae for this research was cultured and grown in the laboratory in 500 mL Erlenmeyer flasks containing 400 mL of the synthetic algae growth media based on the work performed by Edzwald and Malley (1990). Details of the synthetic algae growth media are shown in Table 4.10.

A batch growth culture method was used to grow *Chlorella vulgaris* to high cell number concentrations. Fresh stock cultures were prepared by aseptic transfer of an aliquot of algae culture to a culture vessel containing 400 mL of algae growth media. The cultures were shaken continuously using a shaker and the temperature was maintained at 22 °C (± 2 °C). The cultures were illuminated with at least 77.5 μEinestien/m^2 (600 foot candles) of fluorescent light at all times.

Algae growth phase was monitored using a Hiac/Royco particle counter (Model 8000, Pacific Scientific). This instrument was based on the light obscuration or light extinction technique for particle counting. The particle counter had a light obscuration sensor (Model HRLD-150) which had a size range of 1 to 150 μm with a maximum particle concentration of 16,000 particles greater than 1.0 μm/mL. The flow rate of the

Table 4.9 Synthetic water chemical composition

Inorganic Component	Chemical compound	Concentration
Alkalinity and buffer	$NaHCO_3$	10^{-3} M
Calcium hardness	$CaCl_2$	1.2×10^{-3} M (120 mg/L as $CaCO_3$)
Ionic strength	NaCl	4.5×10^{-3} M (TDS = 180 mg/L)

Table 4.10 Synthetic algae growth media

Chemical Compound	Stock Concentration	mL Stock/ L media
$CaCl_2 . 2H_2O$	1.25 g/500 mL	10
$MgSO_4 . 7H_2O$	3.75 g/500mL	10
K_2HPO_4	3.75 g/500mL	10
KH_2PO_4	8.75 g/500mL	10
$NaNO_3$	12.5 g/500mL	10
NaCl	1.25 g/500mL	10
Na_2EDTA and	10 g/L	1
KOH	6.2 g/L	
H_3BO_3	5.75 g/500 mL	0.7
$FeSO_4.7H_2O$ and	4.98 g/L	1
H_2SO_4	1 mL/L	
Trace Metal Mix		1
$CuSO_4 . 5 H_2O$	0.079 g/L	
$ZnSO_4 . 7 H_2O$	0.222 g/L	
$CoCl_2 . 6 H_2O$	0.0494 g/L	
$MnCl_2 . 4H_2O$	1.81 g/L	
$Na_2MoO_4 . 2 H_2O$	0.390 g/L	
H_3BO_3	2.86 g/L	

sample through the sensor was 25 mL/min. The log growth phase was used for this particular study following the work done by Edzwald and Malley (1990).

Chlorella v. was grown for a sufficient period of time, 7 to 10 days, to obtain cell number concentration of approximately 10^7 cell/mL for log growth phase conditions. The algae in the stock cultures were at sufficiently high cell number concentrations to permit spiking it into the synthetic water to yield an experimental cell concentration of 10^5 cells/mL. It should be noted that an algae count of 10^5 cells/mL in a lake is high (normally less than 10^4 cells/mL). However, this number was chosen so there would be sufficient number of particles remaining following DAF treatment for accurate counts in which removal of 90% were obtained.

4.4.2 Bench-scale DAF experimental set-up

The objective of this experiment was to determine the optimum coagulant dose for the synthetic water in terms of reduction of turbidity and particle count. The coagulant selected for this study was STERNPAC PACl (Polyaluminum hydroxchlorosulphate). The stock solution had an aluminum concentration of 7.7×10^4 mg/L and a specific gravity of 1.2. The bench-scale DAF unit (Aztec Environmental Control Ltd., UK) was used for these experiments.

The components of the bench-scale DAF unit included a compressed air cylinder, pressurization tank (saturator) and four coagulation-flocculation-flotation jars, which were constructed of high strength acrylic with a maximum capacity of 1400 mL. The DAF unit was equipped with a series of solenoid valves and recycle timers which allowed control of the air-saturated liquid flow from the saturator to the jars. This flow was termed recycle by convention although there was technically no recycle in this system. The volume of recycle as a function of timer setting and saturator pressure was measured for this system at saturator pressures of 484 kPa, as shown in Figure 4.8. Each jar of the DAF unit was equipped with a retractable paddle mixer. The mixers were connected to a single speed control that could be operated at 20, 30, 40, 50, 60, 80, 100, 200, 300, or 400 rpm. Velocity gradients were determined for the paddle mixers as a function of rpm at 20° C, as shown in Figure 4.9. The DAF unit included a pressurization tank which served as an unpacked saturator. The saturator was connected to an organic-free compressed air cylinder as the air source.

Bench-scale DAF experiments were conducted by placing 4 L of deionized water in the saturator and the air pressure was raised to 484 kPa. The saturator was then shaken for about 30 seconds. The pressure would fall as the air was absorbed by the water and then raised again to the regulated pressure. The saturator was shaken two to three times in this way while keeping the air supply on. It was allowed to stand for a minimum of 10 minutes, shaking intermittently. Each of the flotation jars was connected to the DAF unit via the saturated water inlets at the back of each jar. To purge the feed lines, Timer 1 was set to between 5 and 10 seconds and valves 1 to 4 were energized. The synchronized recycle control was selected so that all solenoid valves were controlled by Timer 1. The recycle button was activated so that all the feed lines were purged with the saturated water. The residual liquid in each jar was removed by removing the lower port stopper. At this point, the jars were ready to be filled with synthetic water.

To determine the optimum PACl dose, the following experimental procedures were followed:

(1) the volume of algae stock was determined based on spiking 1 L of synthetic water to produce algae cell count of approximately 10^5 cells/mL. The algae cell count was determined using the particle counter during the log growth phase of the algae;

(2) the PACl stock solution, with stock concentration = 7.7×10^4 mg/L as Al, was diluted using deionized water. The working solution concentration was determined based on dosing 1 L of synthetic water to produce PACl concentration in the ranges of 0.5 to 10 mg/L;

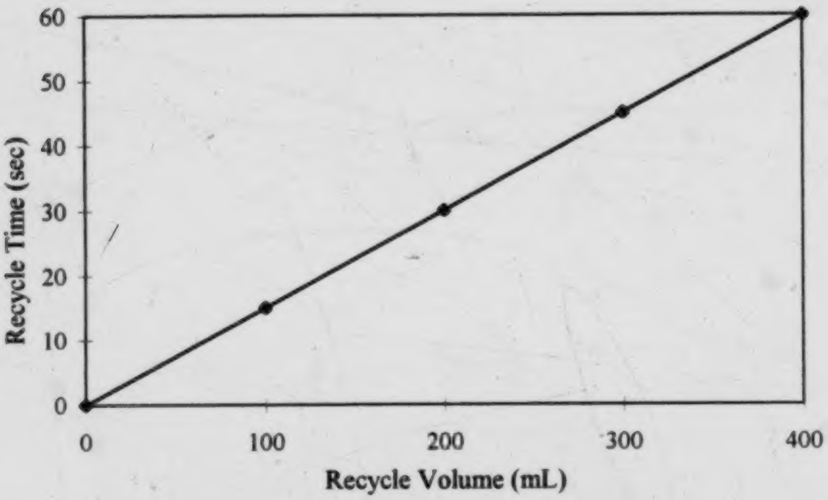

Figure 4.8 Bench-scale DAF recycle volumes as a function of timer settings at saturator pressure of 484 kPa

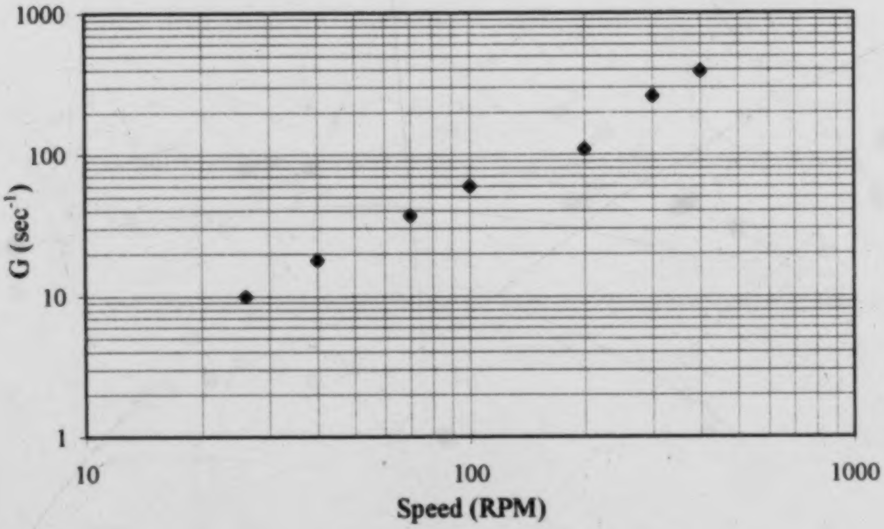

Figure 4.9 Bench-scale DAF unit paddle mixer velocity gradient as a function of speed at 20 °C

(3) an appropriate volume of algae stock culture was added to each jar to produce algae cell counts of approximately 10^5 cells/mL;

(4) using the control DAF jar, the characteristics of the synthetic water spiked with algae was determined by measuring turbidity, particle size distribution and particle concentration;

(5) an appropriate volume of the PACl working solution was added to each jar to produce the desired coagulant dose and the paddle mixers were lowered;

(6) rapid mixing was performed at 400 rpm, G value of 350 s^{-1}, for 2 minutes;

(7) slow mixing was performed at 100 rpm, G value of 70 s^{-1} for 6 minutes;

(8) following slow mixing, the paddles were removed and the flotation solenoids were activated. A flotation recycle ratio of 10 % (i.e. 100 mL of saturated water released into 1000 mL of sample water) was used in all experiments. The jars were allowed to stand for 10 minutes before samples were taken; and

(9) samples were taken from the bottom tap at the base of each jar. Prior to sampling, the sample tubing was purged with approximately 100 mL of sample to insure the line was clear. The following parameters were measured for each sample: pH, turbidity and particle count.

The optimum PACl dose was determined based on the following criteria: treated water turbidity of 0.1 NTU or lower and lowest particle count in treated water (or highest particles log reduction). Whenever the optimum dose could not be determined in the selected range, a new coagulant dose range was selected and the experiment was repeated.

4.4.3 Pilot-scale DAF experimental set-up

The experimental set-up used in these experiments is shown in Figure 4.1. It consisted of a 120 L mixing tank that was used to mix both the synthetic water and the algae stock solution. Mixing was achieved by using a general purpose high speed mixer. The synthetic water was pumped from a 200 L reservoir into the mixing tank by means of a calibrated variable-flow pump. At the same time, algae stock was pumped from a stirred flask to the mixing tank by means of a small variable-flow peristaltic pump. The water volume inside the mixing tank was kept constant by adjusting the flow rate of the synthetic water so that it would equal the flow rate of the water pumped to the flocculator. Also, the flow rate of the algae stock solution was adjusted so that the desired number concentration of the algae cells in the mixing tank was achieved.

The synthetic water containing algae was pumped, using a variable-flow pump, first to the in-line static mixer and then to the flocculator. The flow rate was determined by using a calibrated variable area flow meter. The coagulant was pumped from a small reservoir into the in-line mixer, through a one-way valve, by using a small peristaltic pump. The in-line mixer provided rapid mixing of the coagulant with the feed water, which was required for particle charge neutralization.

After that, the coagulated water entered the flocculator which had a detention time of about 5 minutes at a flow rate of 11.8 L/min. The tank provided slow mixing by using a six-flat-blade turbine connected to a vertical shaft, which was connected to a variable speed motor. The flocculator was elevated to create enough pressure head for the water to flow by gravity to the DAF mixing column at the desired flow rates. The flow rate entering the column was controlled by means of a ball valve located at the flocculator effluent line. The flocculator was designed with an overflow weir so that the water head in the tank was always constant. The overflow water was collected in a launder and discharged to the waste line.

Saturated water was injected into the DAF mixing column, by means of a nozzle, below the flocculated water feeding point. The saturated water flow rate was regulated by means of a needle valve. Total water flow rate, Q_{Total}, which included the flocculated water flow rate, Q_{Flocc}, and the saturated water flow rate, Q_{Sat}, entered the contact column from the bottom through a circular cone section. The rising bubble-floc agglomerates were collected on the top of the separation zone tank. The clarified water exited through the bottom of the clarification tank through a plastic tube connected to a level adjustment pipe. This pipe was used to control the water level inside the clarification tank so that water level could be raised in order to remove the foam layer through the launder.

The DAF removal efficiency, $R_{DAF\,i}$, for each particle size, d_{Pi}, was determined as a function of different hydraulic loading rates, recycle ratios and nozzle's orifice diameters. All these experiments were conducted with the following procedure:

(1) the synthetic water was prepared by dissolving the appropriate amounts of the chemicals, as listed in Table 4.9, in deionized water in the 200 L reservoir tank. The contents were thoroughly mixed using a general purpose mixer;

(2) the algae stock solution was prepared by transferring several 400 mL algae cultures, grown for about 10 days, into a 6 L flask. The contents were thoroughly mixed using a magnetic stirrer and the number concentration of the algae cells was measured using the particle counter;

(3) at the beginning of each experiment, the Q_{Flocc} was set by pumping tap water, from a separate tank, to the flocculator at a flow rate of 11.8 L/min. The calibration curve shown in Figure 4.10 was used to read the flow meter settings. The Q_{Flocc} was regulated by means of a ball valve located at the flocculation tank effluent line. It was adjusted by measuring the flow rate exiting the DAF effluent line using the bucket and the stop watch method and adjusting the ball valve accordingly;

(4) once the desired Q_{Flocc} was set, the on-off valve located after the flocculator was turned off and the influent water pump was shut off. The flocculator and the DAF columns were drained completely;

(5) next, the synthetic water was pumped from the 200 L reservoir into the 120 L mixing tank with a flow rate approximately equal to Q_{Flocc} so that constant water volume in the mixing tank was achieved. The contents of the synthetic water reservoir were constantly replenished during the course of the experiment;

(6) once the flocculator and the DAF columns were filled with the synthetic water, the algae stock solution pump was started. The flow rate was adjusted so that the desired

number concentration of the algae cells in the mixing tank, which was approximately 10^5 cell/mL, was achieved. The calibration curve shown in Figure 4.11 was used to determine the pump control settings. The synthetic water and the algae stock solution were thoroughly mixed inside the mixing tank. Samples were collected frequently to measure the number concentration of the algae cells;

(7) the coagulant pump was immediately started after adding the algae stock and the coagulant flow rate was adjusted so that the concentration of the PACl solution entering the in-line mixer was equal to the optimum coagulant dose, which was determined using the bench-scale DAF unit. The calibration curve shown in Figure 4.12 was used to measure the pump control settings;

(8) at the same time, the flocculation mixer was started and the mixer speed was adjusted so that the required revolution per minute of the motor, which would correspond to a G value of 70 s^{-1}, was achieved. The calibration curve shown in Figure 4.13 was used to determine the required motor speed;

(9) the saturated water flow rate, Q_{Sat}, was started by turning on the on-off valve and the required flow rate, which would correspond to the required recycle ratio, was adjusted by means of a needle valve. Q_{Sat} was measured using a calibrated flow meter located just before the nozzle. The required nozzle orifice diameter, $d_{Orifice}$, was achieved by replacing the orifice plate inside the nozzle assembly with the one with the required $d_{Orifice}$, just before starting these experiments. Also, the saturator tanks, which were filled with deionized water, were pressurized at 484 kPa well a head of the start of the experiment to allow enough time for saturation. They were also shaken, intermittently, for about 10 minutes;

(10) after 15 minutes of adding the algae stock and the coagulant, a water sample was carefully collected from the top of the flocculator, just before the tank effluent line. The sample's total particle count and particle size distribution, PSD, were immediately measured using the particle counter. The corresponding measurements would determine the initial particle number concentration entering the contact zone $N_{CZ\,o,i}$ for particle size, d_{Pi}. In these experiments, the applied particle size range was 1 to 150 μm. Preliminary particle size and concentration measurements at different

times, indicated that measurements remained almost constant after 15 minutes of adding the algae stock and the coagulant; and

(11) after about three times the total residence time of the pilot-scale DAF system, a water sample was collected from the DAF effluent line for particle count and PSD analysis. The corresponding particle count measurements would determine the particle number concentration for the DAF effluent, $N_{DAF\ e,i}$, for particle size, d_{Pi}.

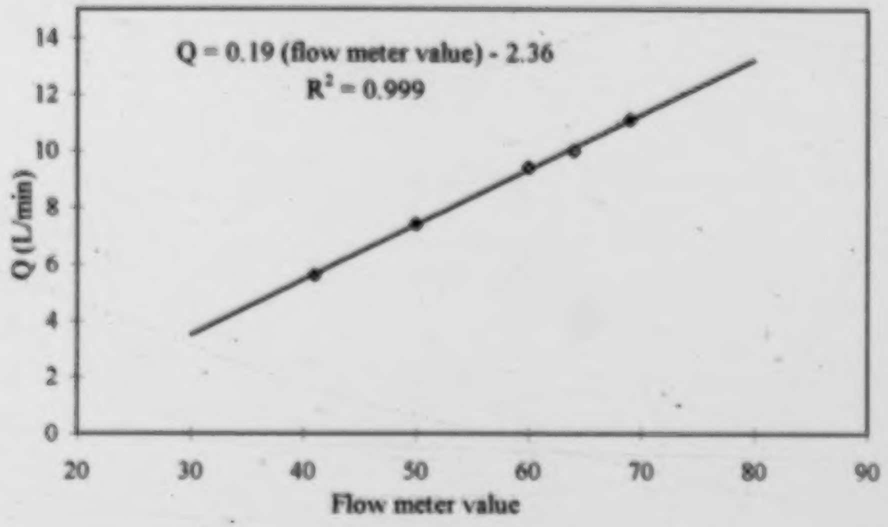

Figure 4.10 Influent water flow meter calibration curve

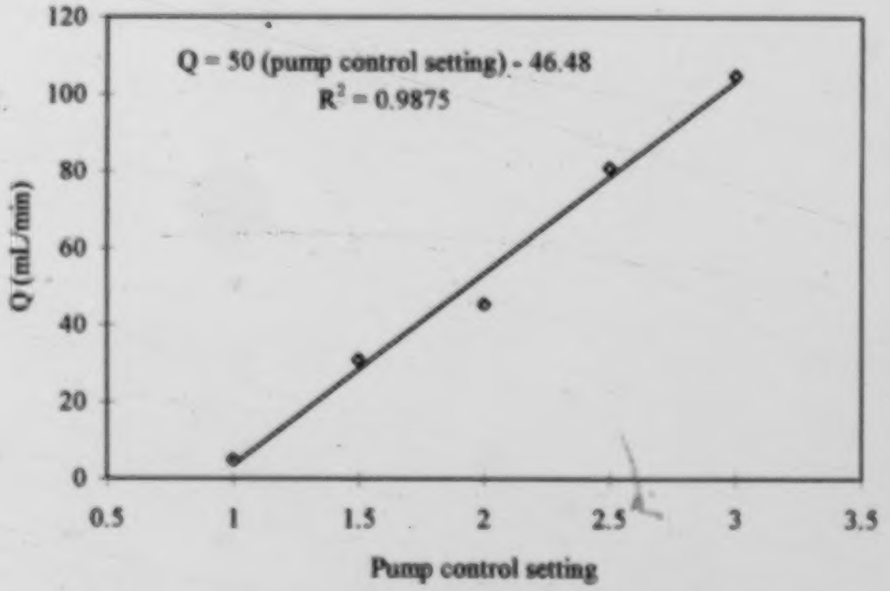

Figure 4.11 Algae stock pump calibration curve

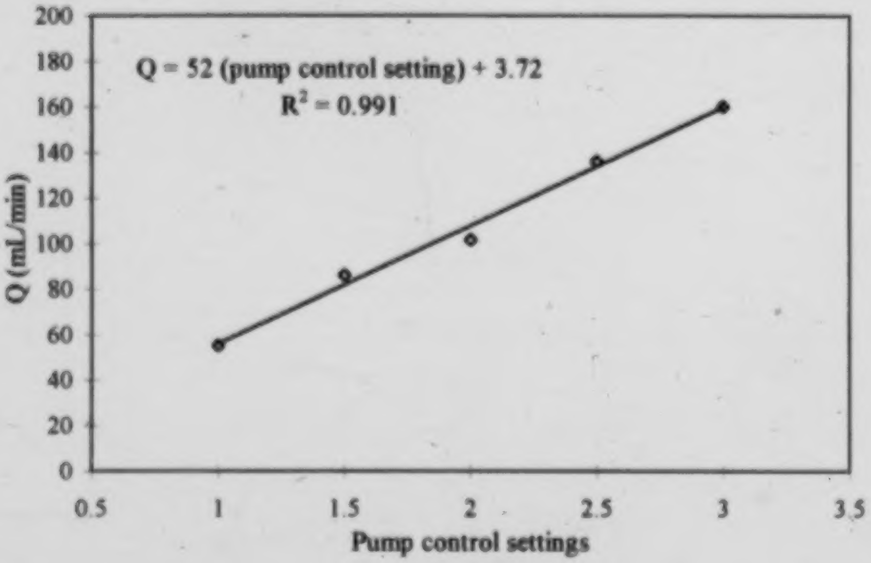

Figure 4.12 Coagulant pump calibration curve

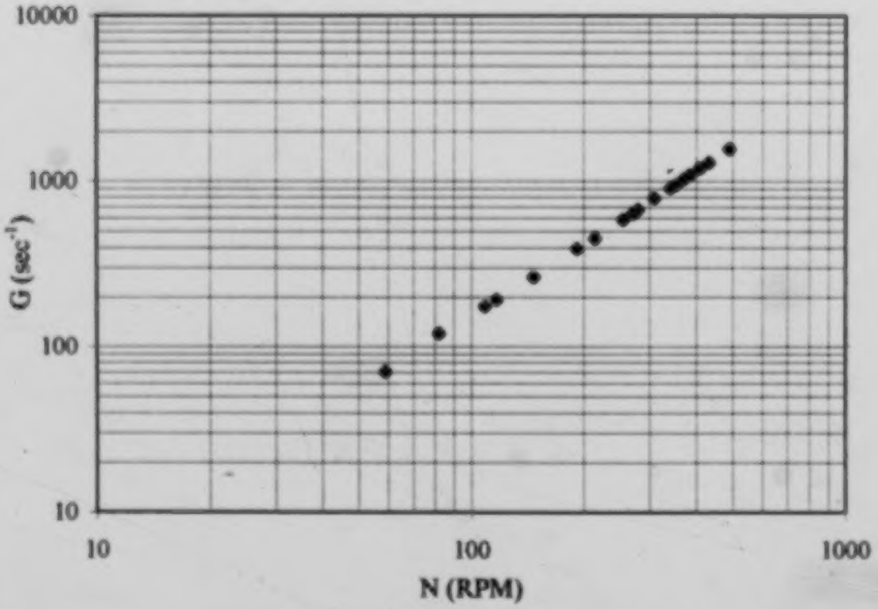

Figure 4.13 Pilot-scale flocculator mixer velocity gradient as a function of speed at room temperature

CHAPTER 5

EXPERIMENTAL RESULTS

5.1 Hydrodynamic Characterization of DAF Contact Zone

The tracer experiments were conducted by first varying contact zone hydraulic loading U_L from 30 to 90 m/h at saturated water flow rate $Q_{Sat} = 0$, i.e. recycle ratio $R_R = 0$ %. This corresponded to contact zone hydraulic residence time, HRT, from 0.4 to about 3 minutes. Later, Q_{Sat} was varied, at each U_L, from 5 % to 10 % of the influent water flow rate, Q_{Water}, at saturator pressure of 484 kPa. That corresponded to theoretical bubble volume concentration, Φ_B, from 2947 to 5625 ppm, i.e. cubic meter of air bubble volume per 10^6 cubic meter of treated water, and bubble number concentration ,N_B, from 9×10^4 to 2×10^5 bubbles/mL at 20°C.

After the collected conductivity-time profiles were translated into concentration-time profiles, equation 3.15 was used as the model to characterize the axial dispersion in the contact zone in terms of Peclet number. The least square minimization technique was used in this study to estimate the Pe. Figure 5.1 represents a typical plot of SSR as a function of Pe for hydraulic loading rate of 70 m/h and $Q_{Sat} = 0$ for top, middle and bottom ports, respectively. In all the tracer experiments in this study, a minimum SSR was always obtained indicating that there was no problem associated with model divergence. The contact zone mean residence time, t_m, and the variance of the residence time distribution, σ^2_t, at different heights across the contact zone, were calculated based on equations 3.12 and 3.13.

The tracer study results, which represent the average of four trials per run, are summarized in Table 5.1. Also, the results for all experimental trials are summarized in Tables B1.1 to B1.4 in Appendix B.1.

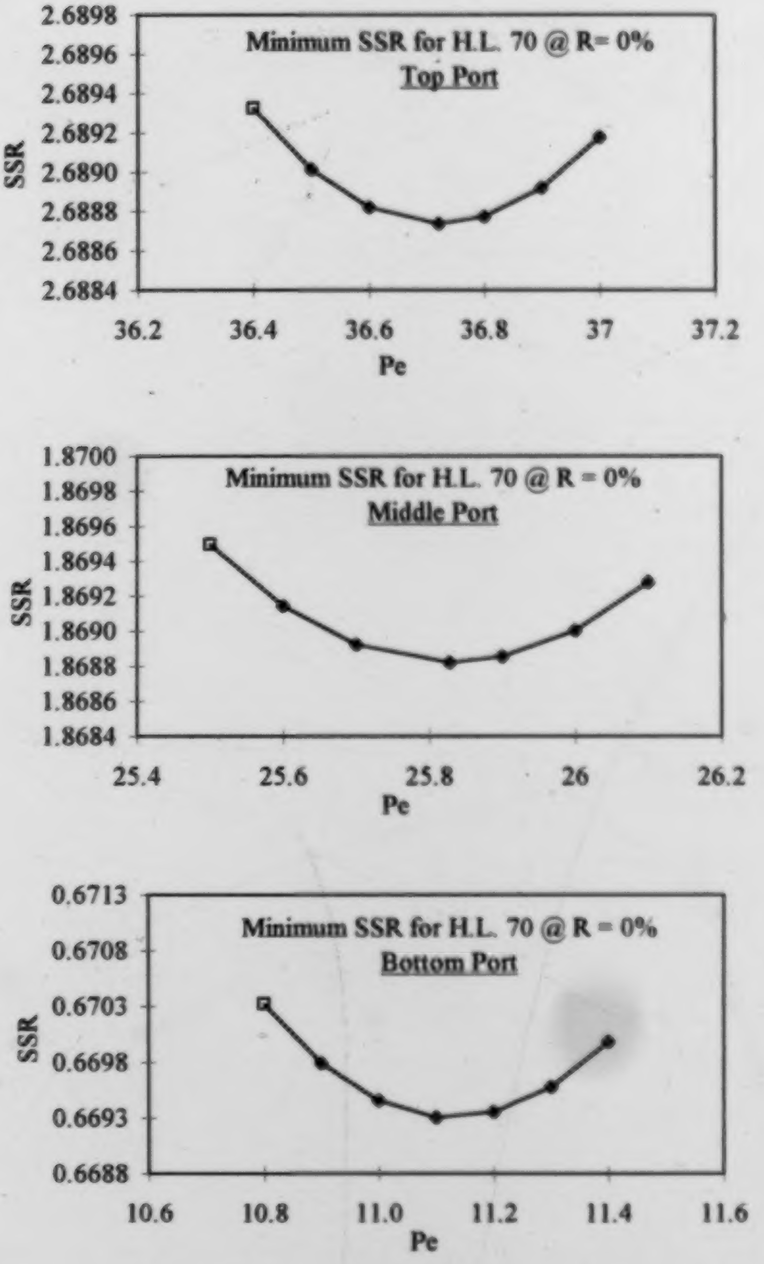

Figure 5.1 Typical SSR plot as a function of Pe for contact zone hydraulic loading rate = 70 m/h and R_R = 0%

Table 5.1 Summary of contact zone tracer study results

Run	Hydraulic Loading	R_R	Φ_B	HRT (min.)			t_m (min)			σ_t^2			Pe		
No.	(m/h)	(%)	(ppm)	T*	M#	B"	T	M	B	T	M	B	T	M	B
1	30	0	0	2.9	1.9	1.0	3.7	2.7	2.1	1.18	1.36	1.54	13.9	9.4	4.9
2	30	5	2947	2.9	1.9	1.0	3.8	2.8	2.0	1.19	1.38	1.61	11.2	8.3	3.6
3	30	10	5625	2.9	1.9	1.0	3.8	2.8	2.2	1.19	1.39	1.58	10.6	7.1	3.2
4	50	0	0	1.7	1.1	0.6	2.1	1.4	1.1	0.37	0.38	0.56	35.1	24.9	9.2
5	50	5	2947	1.7	1.1	0.6	2.1	1.6	0.9	0.39	0.40	0.58	29.6	22.3	7.7
6	50	10	5625	1.7	1.1	0.6	2.2	1.6	1.1	0.39	0.42	0.58	26.3	20.2	6.7
7	70	0	0	1.2	0.8	0.4	1.4	1.0	0.7	0.20	0.21	0.30	36.7	25.8	11.1
8	70	5	2947	1.2	0.8	0.4	1.5	1.0	0.6	0.22	0.24	0.31	33.7	25.0	13.6
9	70	10	5625	1.2	0.8	0.4	1.5	1.1	0.7	0.21	0.24	0.30	31.5	23.7	9.5
10	90	0	0	1.0	0.6	0.3	1.2	0.8	0.5	0.10	0.12	0.16	41.4	28.7	13.8
11	90	5	2947	1.0	0.6	0.3	1.2	0.9	0.5	0.12	0.14	0.19	39.5	28.1	12.3
12	90	10	5625	1.0	0.6	0.3	1.3	0.8	0.6	0.11	0.13	0.19	37.2	27.3	11.5

* Contact zone top port

# Contact zone middle port

" Contact zone bottom port

As shown in Figure 5.2, contact zone t_m decreased as U_L was increased. For the same U_L, t_m decreased from the top port to the bottom port and in all cases, t_m was always larger than HRT. Since t_m represents the average residence time of fluid elements inside the contact zone, non-ideal or non-plug flow conditions prevailed (Levenspiel, 1972). The experimental results indicated that as U_L increased, t_m approached HRT. In these experiments, contact zone t_m ranged from 1.3 to 3.7 minutes.

Also, as the contact zone hydraulic loading rate increased, the mean residence time inside the contact zone decreased. This would lower the collision opportunities between bubbles and particles. However, Tambo (1990) suggested that only 15 to 20 seconds of mixing or contact time is needed for maximum bubble-particle attachment. In this study the contact time was always higher than the suggested value, even at the highest U_L. As a result, higher hydraulic loading rates inside the contact zone would provide flow conditions closer to plug flow and at the same time would provide enough contact time between bubbles and particles.

The variance, σ^2_t, of the residence time distribution decreased significantly as U_L increased, as shown in Figure 5.3. Since σ^2_t represents the spread out of the distributions with time, the smaller the σ^2_t the narrower the distribution and its shape becomes more symmetrical and closer to plug flow conditions. Therefore, the flow conditions inside the contact zone approached plug flow conditions as U_L increased. Also, σ^2_t decreased from the bottom port to the top port of the contact zone, at same U_L, indicating that the flow approached plug flow conditions as contact zone t_m increased and the contact zone cross-sectional area increased.

Mixing inside the contact zone was measured in terms of Pe. As U_L increased, Pe also increased. This is shown in Figures 5.4 to 5.6 for contact zone top, middle and bottom ports, respectively. From equation 3.14, one can see that Pe is inversely proportional to the dispersion number, N_d.

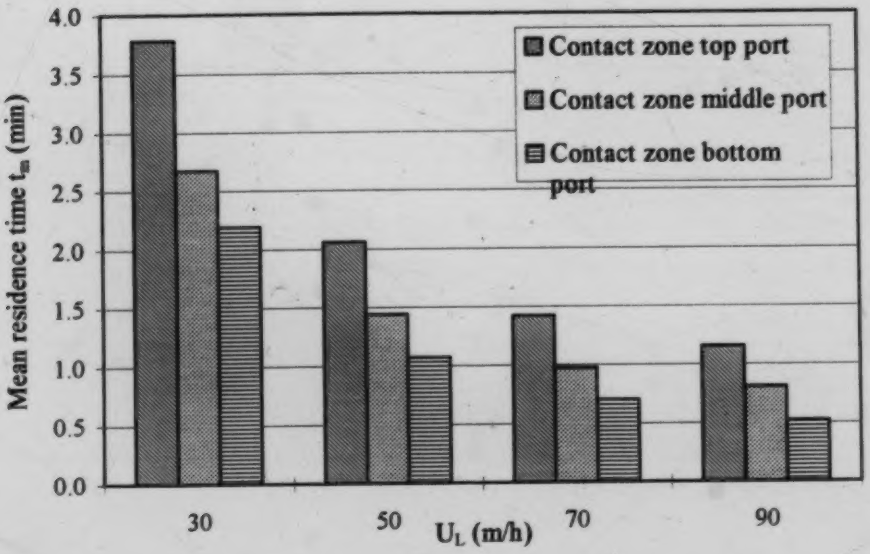

Figure 5.2 Contact zone mean residence time, t_m, as a function of hydraulic loading rate at different heights across the contact zone and at $R_R = 0$ %

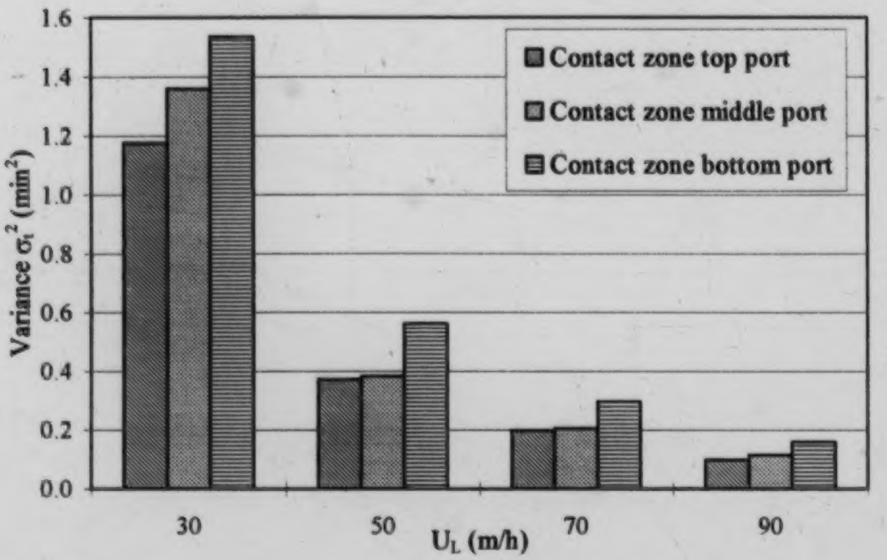

Figure 5.3 Residence distribution time variance, σ^2_t, as a function of hydraulic loading rate at different heights across the contact zone and at $R_R = 0$ %

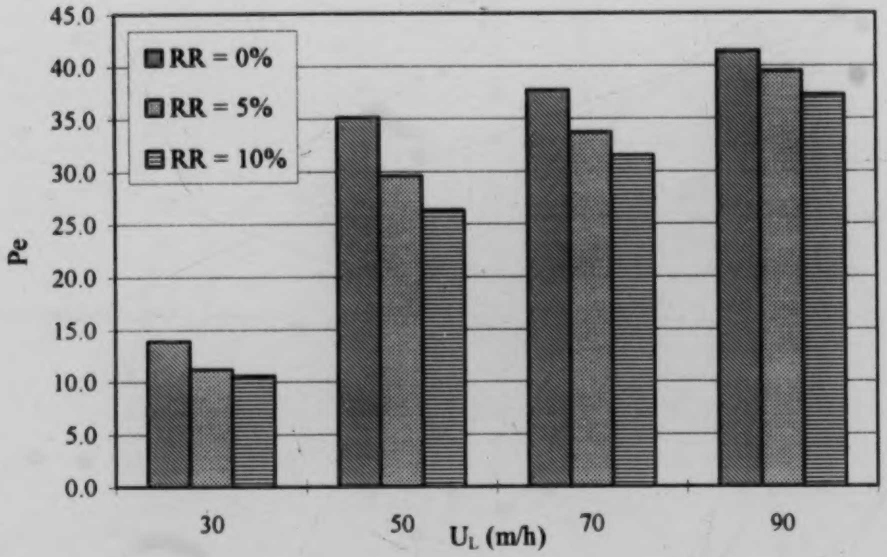

Figure 5.4 Peclet number for contact zone top port as a function of hydraulic loading at different recycle ratios (Note: RR=R_R)

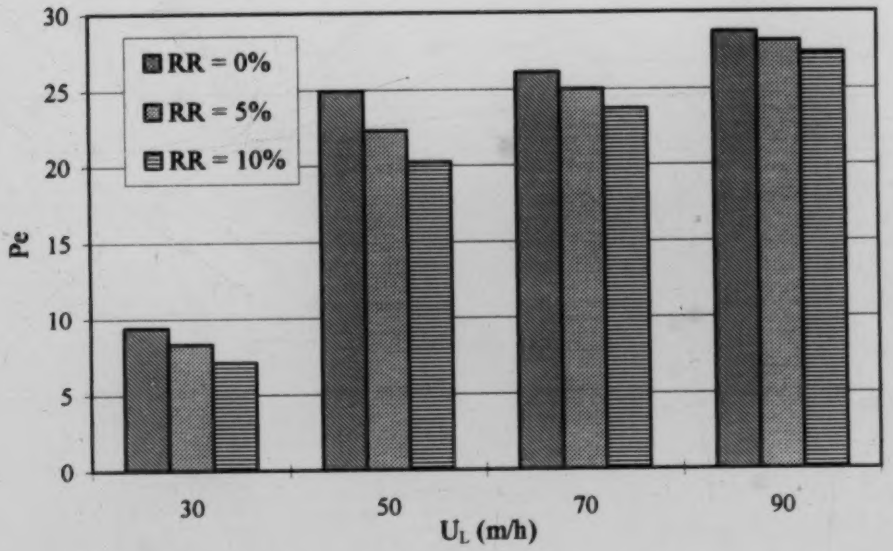

Figure 5.5 Peclet number for contact zone middle port as a function of hydraulic loading at different recycle ratios (Note: $RR=R_R$)

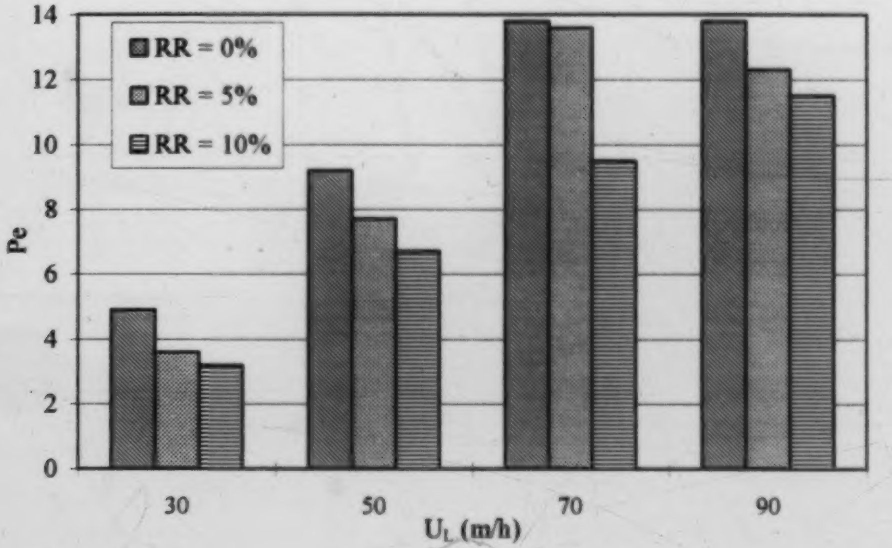

Figure 5.6 Peclet number for contact zone bottom port as a function of hydraulic loading at different recycle ratios (Note: $RR=R_R$)

Since the effect of the dispersion coefficient is insignificant for U_L lower than 100 m/h (Shah et al., 1982), the Pe should be directly proportional to U_L, which is the case in this study. This means that as U_L increases, the degree of mixing inside the contact zone decreases.

In addition, Pe decreased as the saturated water flow rate, Q_{Sat}, increased, which is equivalent to increasing the recycle ratio, R_R. Increasing R_R from 5 % to 10 % caused an increase in the number concentration of bubbles N_B from about 9×10^4 to 2×10^5 bubbles/mL and also increased the rise velocity of bubbles. As a result, the degree of mixing inside the contact zone had slightly increased.

Figures 5.7 to 5.9 depict typical plots of E-θ curves for top, middle and bottom ports as a function of U_L. As shown, the curves look like the Gaussian curve with somewhat asymmetrical shape due to the existence of a long tail after the occurrence of concentration peak. As U_L increased, the shape of the curve became more symmetrical and narrower, and the peak values of E_θ increased. Also, experimental RTD curves were more symmetrical at the top of the contact column than at the middle or the bottom sections, indicating lower degree of mixing. The shape of the experimental RTD curves for the bottom of the contact column, for all tracer tests, were highly asymmetrical with a long tail indicating that there was higher degree of mixing.

To demonstrate the good conformity between the experimental measurements and model predictions, experimental and theoretical RTD curves for $U_L = 50$ m/h and $Q_{Sat} = 0$ were plotted for the top, middle and the bottom of the contact column, as shown in Figure 5.10. The solid curves represent the model predictions based on the best estimate of Pe while the scattered points represent the experimental results. It can be seen that the experimental results matched closely to the model predictions for the top and the middle of the contact column while there were some discrepancies for the bottom section. The conformity between the experimental measurements and model predictions suggest that

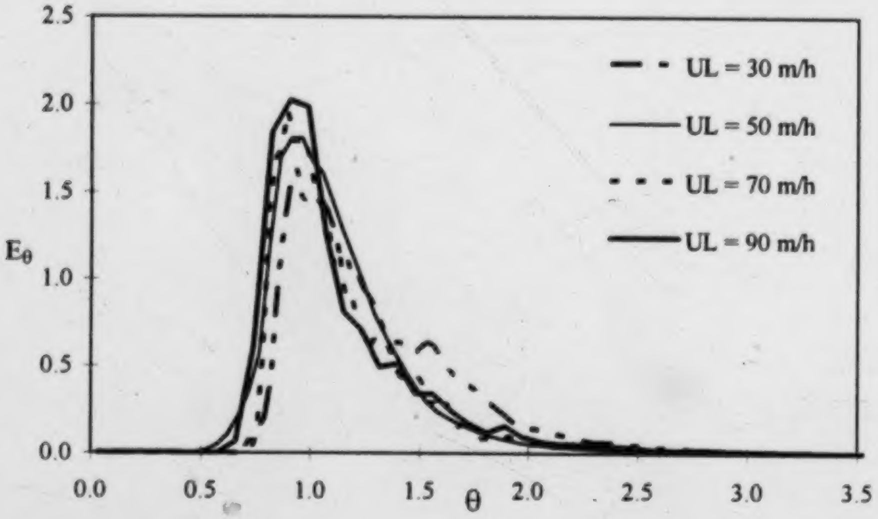

Figure 5.7 Experimental RTD curves for contact zone top port for different hydraulic loading rates and for R_R = 0% (Note: UL=U_L)

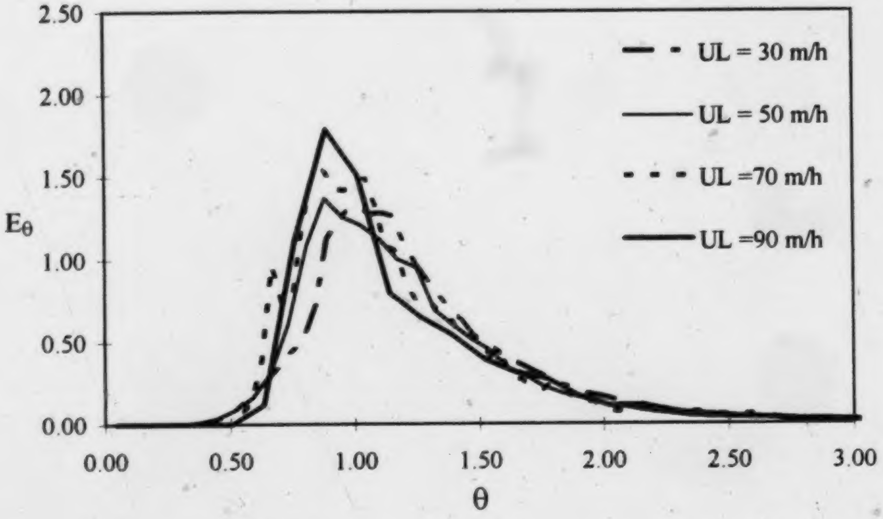

Figure 5.8 Experimental RTD curves for contact zone middle port for different hydraulic loading rates and for R_R = 0% (Note: UL=U_L)

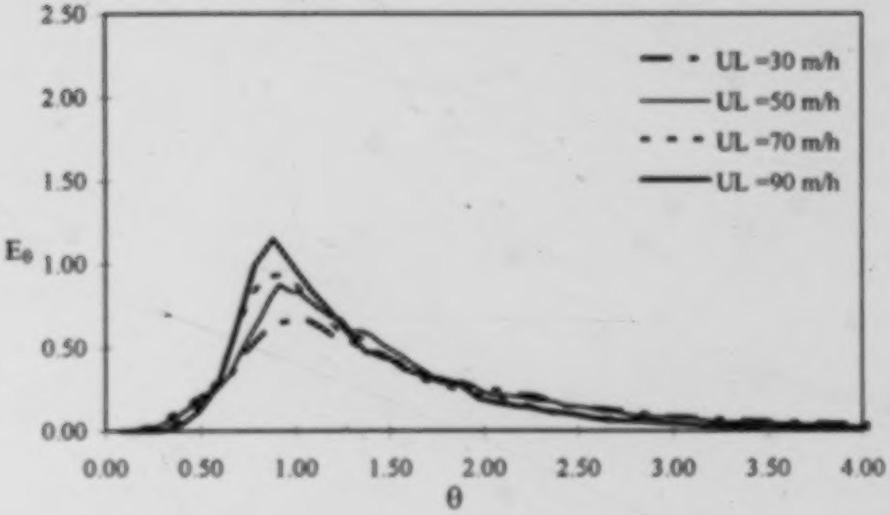

Figure 5.9 Experimental RTD curves for contact zone bottom port for different hydraulic loading rates and for R_R = 0% (Note: UL=U_L)

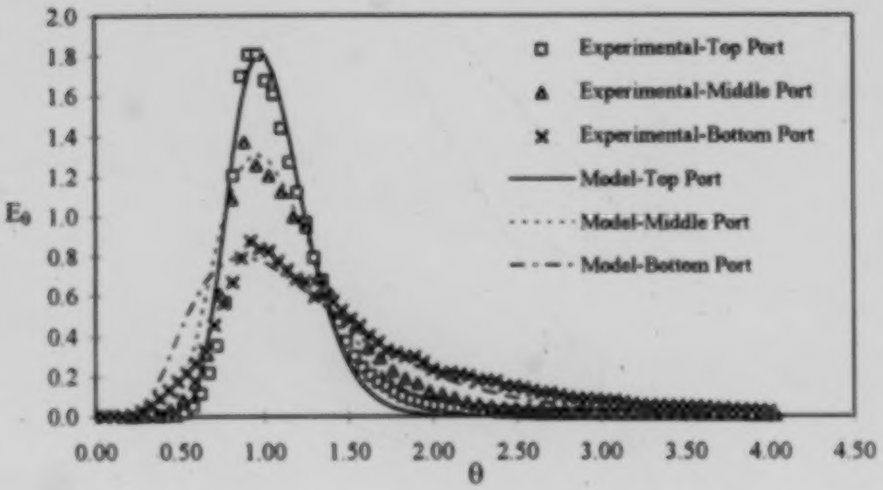

Figure 5.10 Experimental and theoritical RTD curves for hydraulic loading rate of 50 m/h and R_R = 0 % for different contact zone heights

the axial dispersion model can well characterize the hydrodynamics inside the contact zone.

5.2 Bubble Size, Concentration and Velocity Measurements in DAF Contact Zone

5.2.1 PDA configuration

Accurate measurements of water velocity and bubble size, concentration and instantaneous rise velocity required precise configuration of the PDA settings. These settings were optimized by maximizing the data bubble arrival rate and the validation percentage of the collected samples and by minimizing the instrument range, level and consistency errors (as discussed in Section 4.3.1).

After optimizing the PDA settings, superficial liquid velocities ,U_L, measured using TiO_2, were compared with calculated contact zone hydraulic loading rate based on the measured flow rate, Q_{Total}. Also, bubble sizes measured with the PDA were compared with those obtained using the videophotography method. The purpose of the previous comparison was to establish confidence in using the PDA instrument and also for further optimization of the PDA settings.

Table 5.2 summarizes the results of U_L measured by the PDA instrument and U_L calculated based on the measured Q_{Total} . The PDA measurements were performed by seeding the influent water with TiO_2, at low concentrations, and measuring the instantaneous velocity at the probe volume coordinate (900,0,25). Actual flow rates were measured using the stop watch and the bucket method. The calculated U_L was based on the measured Q_{total} divided by the maximum cross section of the contact zone column.

The results indicate good agreement between U_L measured with PDA and those calculated based on the measured Q_{total}. The results also indicate that as the Q_{total}

Table 5.2 Comparison between U_L measured by the PDA, using TiO_2, at probe volume coordinates (900,0,25) and U_L calculated based on the measuement of the flow rate, Q_{Total}

Theoretical hydraulic loading (m/h)	30	50	70	90
Measured Q_{Total} (L/min)	3.82	6.58	9.30	11.81
U_L - based on measured Q_{Total} (m/s)	8.11E-03	1.40E-02	1.97E-02	2.51E-02
U_L - based on PDA (m/s)	1.05E-02	1.65E-02	2.18E-02	2.55E-02
% difference	23	15	9	2

increased, i.e. as contact zone hydraulic loading increased, the percentage difference between measured and calculated U_L decreased.

Bubble sizes measured with the PDA were compared with those measured with the videophotography method. Both measurements were performed under identical operational conditions: hydraulic loading rates of 30 and 70 m/h at R_R of 10 % and 3 %, respectively, P_{Sat} of 484 kPa and nozzle orifice diameter of 0.55 mm. For PDA measurements, the probe volume coordinates were (900,0,25) while video images were taken at the same contact zone height but were focused on a line scribed on the inside of the column.

The results of bubble size using the videophotography method for hydraulic loading of 30 m/h and R_R =10 % and hydraulic loading of 70 m/h and R_R =3 % are shown in Tables 5.3 and 5.4, respectively. Three different bubble mean diameters were calculated based on the video images: the arithmetic mean, the mean surface and the mean volume diameter. Also, bubble size distributions for both hydraulic loading rates are shown in Figures 5.11 and 5.12. These results show that the mean volume diameter was larger than the arithmetic mean diameter and also show that the mean bubble diameter decreased as the hydraulic loading rate increased.

Results of bubble size measurements obtained by the PDA were compared with those obtained by the video images. Table 5.5 summarizes the mean volume diameters measured by PDA and videophotography methods for hydraulic loading rate 30 m/h and R_R =10 % and hydraulic loading of 70 m/h and R_R =3 %. The results indicate good agreement between the two methods and the difference was found insignificant at 1% level of statistical significance.

The previous results suggested that the PDA measurements can be used with high confidence. Consistency of PDA bubble size and instantaneous rise velocity measurements were confirmed by repeating measurements at different times and

Table 5.3 **Bubble size distribution using videophotography technique for hydraulic loading rate of 30 m/h, R_R=10%, P_{Sat}=484 kPa, $d_{Orifice}$ = 0.55 mm and probe volume coordinate (900,0,25)**

					Frequency			
Class	(µm)	d_{Bi}	d_{Bi}^2	d_{Bi}^3	f_i	$f_i\,d_{Bi}$	$f_i\,d_{Bi}^2$	$f_i\,d_{Bi}^3$
1	10.0-20.0	15	225	3375	0	0	0	0
2	20.0-30.0	25	625	15625	0	0	0	0
3	30.0-40.0	35	1225	42875	13	455	15925	557375
4	40.0-50.0	45	2025	91125	20	900	40500	1822500
5	50.0-60.0	55	3025	166375	64	3520	193600	10648000
6	60.0-70.0	65	4225	274625	107	6955	452075	29384875
7	70.0-80.0	75	5625	421875	135	10125	759375	56953125
8	80.0-90.0	85	7225	614125	92	7820	664700	56499500
9	90.0-100.0	95	9025	857375	39	3705	351975	33437625
10	100.0-110.0	105	11025	1157625	11	1155	121275	12733875
11	110.0-120.0	115	13225	1520875	4	460	52900	6083500
12	120.0-130.0	125	15625	1953125	1	125	15625	1953125
13	130.0-140.0	135	18225	2460375	1	135	18225	2460375
14	140.0-150.0	145	21025	3048625	0	0	0	0
		--------	--------	--------	--------	--------	--------	--------
	Σ	1120	1E+05	12628000	487	35355	3E+06	2.13E+08

Arithmetic mean diameter (µm) 72.6

Mean area diameter (µm) 74.3

Mean volume diameter (µm) 75.9 σ_d (µm) 15.4

Table 5.4 Bubble size distribution using videophotography technique for hydraulic loading rate of 70 m/h, R_R=30%, P_{Sat}=484 kPa, $d_{Orifice}$ = 0.55 mm and probe volume coordinate (900,0,25)

					Frequency			
Class	(µm)	d_{Bi}	d_{Bi}^2	d_{Bi}^3	f_i	$f_i\, d_{Bi}$	$f_i\, d_{Bi}^2$	$f_i\, d_{Bi}^3$
1	10.0-20.0	15	225	3375	0	0	0	0
2	20.0-30.0	25	625	15625	2	50	1250	31250
3	30.0-40.0	35	1225	42875	24	840	29400	1029000
4	40.0-50.0	45	2025	91125	63	2835	127575	5740875
5	50.0-60.0	55	3025	166375	105	5775	317625	17469375
6	60.0-70.0	65	4225	274625	156	10140	659100	42841500
7	70.0-80.0	75	5625	421875	90	6750	506250	37968750
8	80.0-90.0	85	7225	614125	28	2380	202300	17195500
9	90.0-100.0	95	9025	857375	11	1045	99275	9431125
10	100.0-110.0	105	11025	1157625	10	1050	110250	11576250
11	110.0-120.0	115	13225	1520875	8	920	105800	12167000
12	120.0-130.0	125	15625	1953125	2	250	31250	3906250
13	130.0-140.0	135	18225	2460375	1	135	18225	2460375
14	140.0-150.0	145	21025	3048625	0	0	0	0
	Σ	1120	1E+05	12628000	500	32170	2E+06	1.62E+08

Arithmetic mean diameter (µm) 64.3

Mean area diameter (µm) 66.5

Mean volume diameter (µm) 68.7 σ_d (µm) 20.7

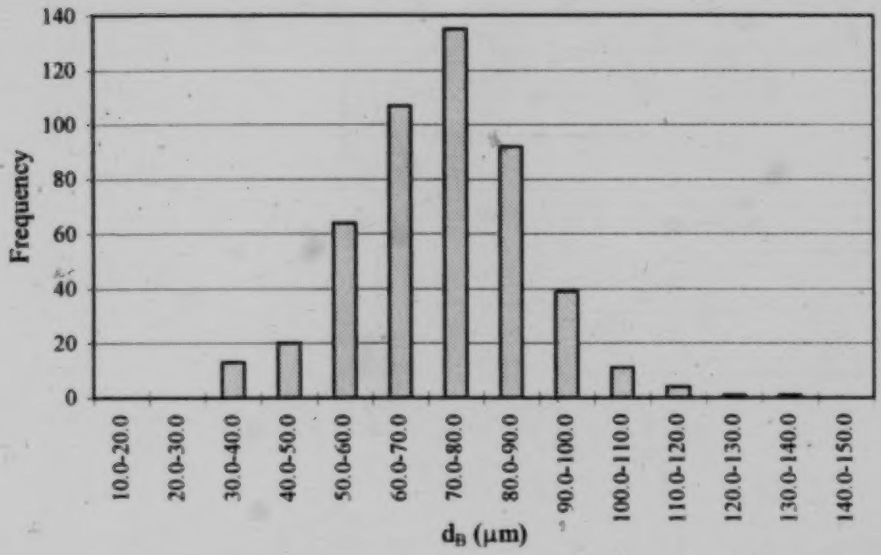

Figure 5.11 Bubble size distribution for hydraulic loading rate 30 m/h, R_R=10% P_{Sat} =484 kPa, nozzle orifice diameter=0.55 mm and probe volume coordinates (900,0,25)

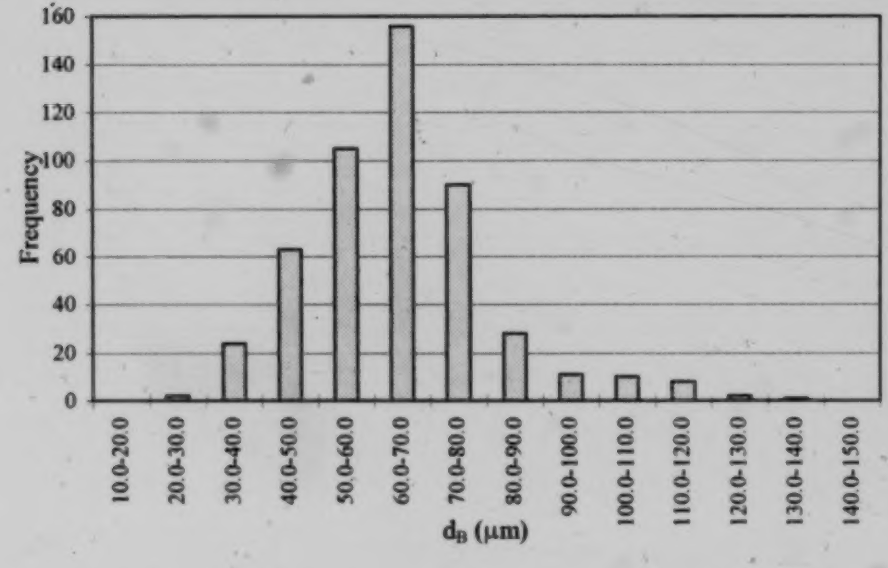

Figure 5.12 Bubble size distribution for hydraulic loading rate 70 m/h, R_R=3% P_{Sat} =484 kPa, nozzle orifice diameter=0.55 mm and probe volume coordinates (900,0,25)

Table 5.5 Comparison between bubble size measured with PDA and videophotography method

	Hydraulic loading rate = 30 m/h R_R = 10 %		Hydraulic loading rate = 70 m/h R_R = 3 %	
	Videophotography	PDA	Videophotography	PDA
Mean volume diameter, d_B (μm)	75.9	73.7	68.7	66.0
σ_B (μm)	15.4	14.4	20.7	22.7
Number of measured bubbles	487	5787	500	1855

Table 5.6 **Consistency of bubble size and velocity measurements using the PDA for hydraulic loading rate = 50 m/h, R_R = 5%, P_{Sat} = 484 kPa, $d_{Orifice}$ = 0.55 mm and probe volume coordinates (900,0,25)**

Day 1	Trial 1	Trial 2	Trial 3	Trial 4	Avg
Validated Samples	4018	3946	4022	4033	4005
Validation % *	80	79	80	81	80
Data Rate ** (bubble/sec)	97	112	104	110	106
$U_{B\,bst}$ (m/s)	1.71E-02	1.85E-02	1.71E-02	1.72E-02	1.75E-02
σ_{UB} (m/s)	2.15E-03	2.62E-03	2.73E-03	2.59E-03	2.52E-03
d_B (μm)	70.0	70.2	70.5	70.6	70.3
σ_{dB}(μm)	16.1	15.3	15.0	14.7	15.3

Day 2	Trial 1	Trial 2	Trial 3	Trial 4	Avg
Validated Samples	3928	3887	3945	3917	3919
Validation %	79	78	79	78	78
Data Rate (bubble/sec)	89	97	99	102	97
$U_{B\,bst}$ (m/s)	1.75E-02	1.68E-02	1.72E-02	1.72E-02	1.72E-02
σ_{UB} (m/s)	3.16E-03	2.18E-03	2.41E-03	2.34E-03	2.52E-03
d_B (μm)	69.4	70.7	69.6	69.9	69.9
σ_{dB}(μm)	16.9	17.2	15.8	16.1	16.5

* **validation percentage is the number of measurements validated by the PDA software divided by the number of measurements transferred to the computer RAM**

** **data rate is the bubble arrival rate as counted by the PDA processor before software validation**

comparing the results. Table 5.6 summarizes the results of PDA measurements collected at two different times for hydraulic loading rate = 50 m/h, R_R = 5%, P_{Sat} = 484 kPa, nozzle orifice diameter = 0.55 mm and probe volume coordinates (900,0,25). These measurements were taken after reaching steady state condition, i.e. steady validated samples and bubble arrival rate. The results showed that the difference between PDA measurements, for both bubble size and velocity, at different times was insignificant at the 1% level of statistical significance.

5.2.2 Superficial liquid velocity measurements

The U_L in the x-direction was measured with the PDA by seeding the influent water with TiO_2. These experiments did not require the presence of air bubbles in the contact zone and therefore, Q_{Sat} was zero, i.e. $R_R = 0$. In order to determine whether this condition would have any effect on U_L measurements, PDA measurements were performed with and without recycling deionized water through the nozzle and the results were compared by performing a t-test.

Table 5.7 summarizes the results of the effect of recycled water flow on U_L measurements for hydraulic loading rate = 70 m/h and probe volume coordinates (900,0,25). The results showed that the difference between U_L measured with recycled water and those measured without recycled water was insignificant at the 1% level of statistical significance. Therefore, it was decided to perform all U_L measurements without recycling water through the DAF nozzle.

Superficial liquid velocities were measured to characterize the water flow inside the contact zone column at different hydraulic loading rates and also to calculate the relative bubble rise velocity at different operational conditions. U_L was measured at two different contact zone heights and at different probe volume coordinates. Table 5.8 summarizes the results of U_L measurements.

Table 5.7 Effect of recycled water flow on U_L measurements using PDA for hydraulic loading rate of 70 m/h and probe volume coordinates (900,0,25)

Without recycled water

$Q_{\text{Influent water}}$ = 9.1 L/min
$Q_{\text{recycled water}}$ = 0
Q_{Total} = 9.1 L/min

	Trial 1	Trial 2	Trial 3	Trial 4	Avg
U_L (m/s)	2.12E-02	2.22E-02	2.09E-02	2.11E-02	2.13E-02
σ_{UL} (m/s)	2.85E-03	2.34E-03	2.59E-03	2.89E-03	2.67E-03

With recycled water

$Q_{\text{Influent water}}$ = 8.7 L/min
$Q_{\text{recycled water}}$ = 435 mL/min
Q_{Total} = 9.1 L/min

	Trial 1	Trial 2	Trial 3	Trial 4	Avg
U_L (m/s)	2.18E-02	2.12E-02	2.22E-02	2.20E-02	2.18E-02
σ_{UL} (m/s)	2.52E-03	3.25E-03	2.79E-03	2.60E-03	2.79E-03

Table 5.8 Superficial liquid velocity, U_L, measured with PDA at different contact zone column heights, probe volume coordinates and hydraulic loading rates

Exp. #	Measured * Q_{Total} (L/min)	Calculated ** hydraulic loading rate (m/h)	Probe volume coordinates (x,y,z) in mm	Measured mean U_L (m/s)	U_{RMS} (m/s)
1	3.960	30.2	(900,0,25)	1.05E-02	2.95E-03
2	3.940	30.1	(400,0,25)	1.07E-02	4.10E-03
3	6.590	50.3	(900,0,25)	1.65E-02	2.33E-03
4	6.580	50.2	(400,0,25)	1.62E-02	4.43E-03
5	9.160	69.9	(900,0,25)	2.18E-02	2.83E-03
6	9.210	70.3	(400,0,25)	2.13E-02	7.15E-03
7	9.180	70.1	(900,0,-45)	1.67E-02	3.45E-03
8	9.180	70.1	(900,0,-25)	2.13E-02	2.52E-03
9	9.160	69.9	(900,0,0)	2.22E-02	2.52E-03
10	9.180	70.1	(900,0,45)	1.70E-02	3.32E-03
11	11.800	90.1	(900,0,25)	2.55E-02	3.31E-03
12	11.810	90.2	(400,0,25)	2.43E-02	7.51E-03

* Based on measuring the flow rate of water exiting the contact zone column using th stop watch and the bucket method

** Based on measured Q_{Total} divided by the maximum cross sectional area of the contact zone column

Results indicated that the measured mean U_L values were always larger than the calculated hydraulic loading rates. This may be due to the fact that the calculated hydraulic loading rates were based on the maximum cross sectional area of the contact zone, while the actual cross section varied from 40 to 100 mm. Also, the results show that there are insignificant differences between mean U_L measured at 900 and 400 mm. However, the results of the standard deviation of the measured U_L, σ_{UL}, which is also termed the root mean square velocity ,U_{RMS}, indicate that as the contact zone column height increased deviations of the measured U_L from the mean decreased.

5.2.3 Bubble size, concentration and velocity measurements

Bubble size, concentration and instantaneous rise velocity $U_{B\,inst}$ were measured at different operational conditions: (1) different saturator pressures P_{Sat} at constant contact zone hydraulic loading rate and constant recycle ratio R_R; (2) different contact zone hydraulic loading rates at constant P_{Sat} and R_R; (3) different recycle ratios at constant contact zone hydraulic loading rate and P_{Sat}; and (4) different nozzle orifice diameters at constant contact zone hydraulic loading rate, R_R and P_{Sat}. Also, the effect of contact zone column height and wall effects on bubble size, concentration and rise velocity were measured. All PDA experimental data and results are summarized in Tables B2.1 to B2.28 in Appendix B.2.

The results of experiments that were designed to assess and measure the effect of each operational condition are presented in the following sections.

5.2.3.1 Effect of saturator pressure

One of the important operational parameters that affect bubble size and concentration inside the contact zone, and ultimately the overall performance of the DAF process, is the saturator pressure. In these experiments, the saturator pressure, P_{Sat}, was expressed as gauge pressure. The objective of these experiments was to evaluate the effect of P_{Sat} on bubble size and concentration and also to determine the optimum P_{Sat} that would be used in all other experiments.

Three different values of P_{Sat} were evaluated at a constant hydraulic loading rate of 70 m/h and R_R of 5 %. All measurements were taken at probe volume coordinates of (900,0,0) and the nozzle orifice diameter was 0.55 mm. Table 5.9 summarizes the results which show that bubble mean volume diameter d_B did not change significantly as P_{Sat} increased. However, the standard deviation of bubble diameter σ_{dB} decreased as the P_{Sat} increased. Also, the bubble size distribution BSD, as shown in Figure 5.13, became narrower and with higher percentage of air bubbles.

The results in Table 5.9 also show that, as P_{Sat} increased both measured bubble volume and number concentrations increased. As P_{Sat} increased, the equilibrium mass concentration in the saturated stream C_{Sat} increased and, as a result, the concentration of the air released in the contact zone C_R increased. Since the bubble volume concentration Φ_B is proportional to C_R, as shown in equation 2.8, Φ_B increased. Based on Equation 2.9, bubble number concentration, N_B, is proportional to Φ_B and since d_B did not change significantly as P_{Sat} increased, N_B also increased.

When the theoretical and measured N_B and Φ_B values at different values of P_{Sat} were compared, there were differences. Theoretical N_B and Φ_B were calculated based on Equations 2.6, 2.7 and 2.8 and using the following data: (1) bubble mean volume diameter measured with the PDA; (2) P_{Sat} under investigation; (3) R_R of 5 % for contact zone hydraulic loading rate of 70 m/h; (4) saturator efficiency factor of 0.84; and (5) water temperature of 20°C. On the other hand, measured N_B values were obtained directly from the PDA software and the measured or experimental Φ_B were calculated by multiplying the measured bubble number concentration by the bubble mean volume.

Table 5.9 **Effect of saturator pressure P_{Sat} on bubble size and concentration for hydraulic loading rate= 70 m/h, R_R=5%, $d_{Orifice}$ = 0.55 mm and probe volume coordinates (900,0,0)**

P_{Sat} kPa (Psi)	345 (50)	484 (70)	587 (85)
d_B (μm)	63.0	64.5	64.1
σ_{dB}(μm)	21.9	18.0	15.5
$U_{B\ Inst}$ (m/s)	2.34E-02	2.39E-02	2.37E-02
U_L (m/s)	2.22E-02	2.22E-02	2.22E-02
$U_{B\ Relative}$ (m/s)	1.20E-03	1.66E-03	1.52E-03
$U_{B\ Stoke}$ (m/s)	2.19E-03	2.30E-03	2.27E-03
Measured N_B (bubbles/mL)	5.43E+03	1.31E+04	1.48E+04
Theoretical N_B (bubbles/mL	2.00E+04	2.66E+04	3.31E+04
Measured Φ_B (ppm)	710	1841	2038
Theoretical Φ_B (ppm)	2618	3727	4558

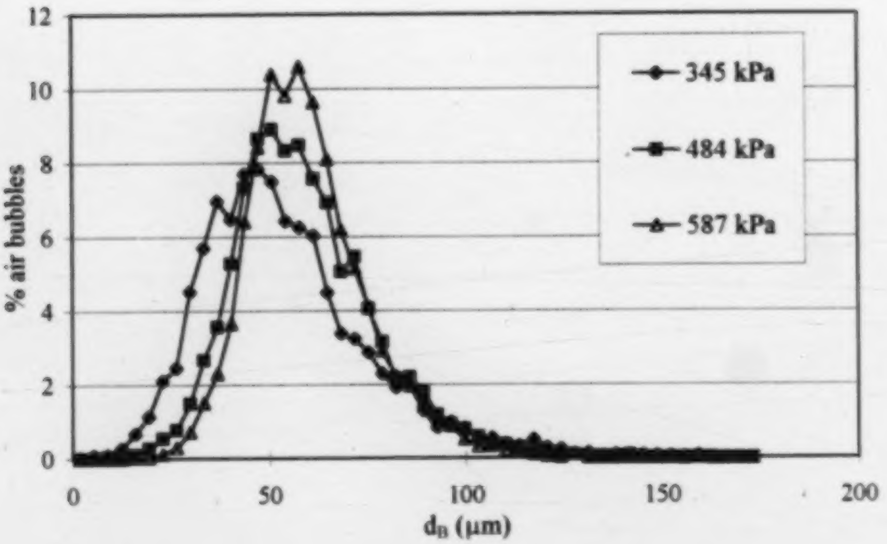

Figure 5.13 Effect of saturator pressure on BSD for hydraulic loading rate = 70 m/ R_R = 5 %, d $_{Orifice}$ = 0.55 mm, 20°C and probe volume coordinates (900,0,0)

The differences between the theoretical and measured N_B values may be due to the production of macro bubbles, 150 μm and larger, in the vicinity of the nozzle. This phenomena was observed in all experiments conducted with the DAF column, especially at low R_R and P_{Sat}. Also, it was observed that many bubbles were sticking to the inside walls of the mixing column, just below the nozzle. As a result, larger bubbles were formed, by coalescence, which would rise in the mixing column due to their high buoyancy. Therefore, bubble coalescence inside the mixing column may contribute to the reduction of the measured N_B and Φ_B values.

Another factor that may have contributed to the discrepancy between theoretical and measured N_B was the method of data processing with the PDA. As was explained in Section 2.2.3, N_B measurements required information on bubble arrival rate, velocity and the instrument cross section. The most difficult of these was to determine the instrument cross section which was a function of many variables such as the laser power and alignment. Therefore, the N_B value determined by the PDA may not have been the actual bubble concentration inside the contact zone. However, measured N_B values followed the same trend as the theoretical values.

The results in Table 5.9 show that as P_{Sat} increased the difference between measured N_B and Φ_B and theoretical values decreased. As P_{Sat} increased, the pressure across the nozzle increased causing larger bubbles to break up and produce higher concentrations of bubbles.

5.2.3.2 Effect of recycle ratio

The second operational parameter investigated in this study was the recycle ratio, R_R . The effect of R_R on bubble size, concentration and $U_{B\,sed}$ was measured by varying R_R at constant contact zone hydraulic loading rate and P_{Sat}. However, there were difficulties in choosing the R_R range to be studied, for different hydraulic loading rates.

This was due to operational limitations with the PDA instrument. As R_R increased, 10 % and higher, the contact zone contained very high concentration of bubbles and became cloudy. As a result, the signals received by the PDA receiving optics became weaker to the point that the PDA was not able to collect any data. This limitation did not allow the investigation of the effect of higher R_R on bubble size, concentration and $U_{B\ inst}$.

The results of the effect of recycle ratio on bubble size, concentration and $U_{B\ inst}$, for a hydraulic loading rate of 30 m/h, are shown in Table 5.10. These experiments were performed at P_{Sat} of 484 kPa and the measurements were taken at probe volume coordinates (900,0,25). The results show that as R_R increased from 7 % to 10 %, the mean bubble diameter decreased. This is clearly shown in Figure 5.14, which illustrates BSD for both recycle ratios. At higher R_R, the flow through the nozzle increased and as a result bubbles with smaller diameters were produced. Also, it is shown that the U_{RMS} decreased as a result of the decrease in σ_{dB}.

In addition, the measured Φ_B increased as R_R increased, as shown in Table 5.10. This was expected because as R_R increased C_R also increased, based on Equation 2.7, causing an increase in Φ_B. Also, N_B increased as R_R increased due to the production of smaller bubbles.

The effect of recycle ratio on bubble size, concentration and $U_{B\ inst}$ at higher contact zone hydraulic loading rates was also investigated. The results of these experiments are summarized in Tables 5.11 to 5.13 for hydraulic loading rates of 50, 70 and 90 m/h, respectively. These experiments were performed at P_{Sat} of 484 kPa and the measurements were taken at a probe volume coordinates (900,0,25). Nozzle orifice diameter of 0.55 mm was used for hydraulic loading rates 50 and 70 m/h while $d_{Orifice}$ of 1.03 mm was used for hydraulic loading rate of 90 m/h.

In all these experiments, the results showed that the mean bubble diameter d_B decreased as R_R increased but the change was not as significant as that of d_B when the

Table 5.10 **Effect of recycle ratio on bubble size, concentration and rise velocity for hydraulic loading rate of 30 m/h, d $_{Orifice}$ = 0.55 mm, 20°C, P_{Sat} = 484 kPa and probe volume coordinates (900,0,25)**

R_R (%)	7	10
d_B (μm)	85.5	73.7
σ_{dB}(μm)	15.4	14.4
$U_{B\ inst}$ (m/s)	1.42E-02	1.40E-02
U_{RMS} (m/s)	5.57E-03	4.68E-03
U_L (m/s)	1.05E-02	1.05E-02
$U_{B\ Relative}$ (m/s)	3.73E-03	3.45E-03
$U_{B\ Stoke}$ (m/s)	4.04E-03	3.00E-03
Measured N_B (bubbles/mL)	1.04E+04	1.79E+04
Theoretical N_B (bubbles/mL	1.57E+04	3.40E+04
Measured Φ_B (ppm)	3405	3748
Theoretical Φ_B (ppm)	5120	7114

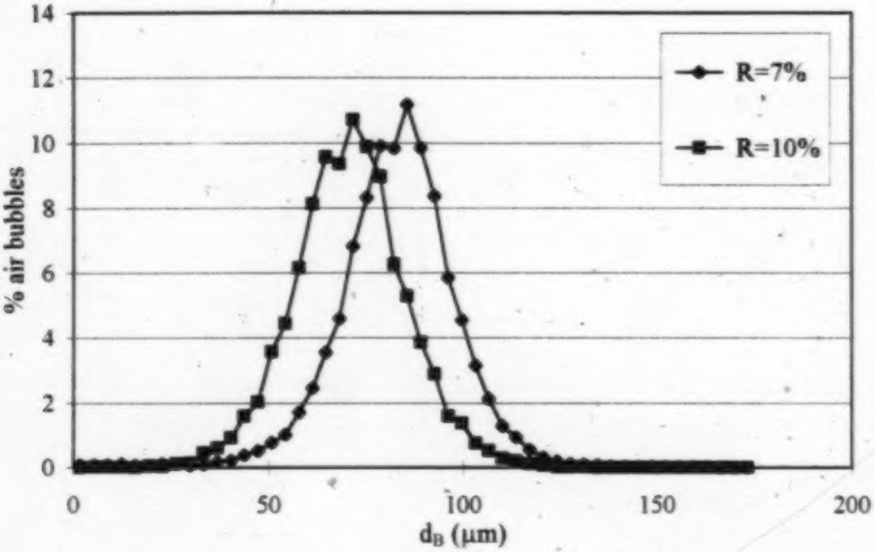

Figure 5.14 Effect of recycle ratio on BSD for hydraulic loading rate of 30 m/h, $d_{Orifice}$ = 0.55 mm, 20°C, P_{Sat} = 484 kPa and probe volume coordinates (900,0,25)

Table 5.11 Effect of recycle ratio on bubble size, concentration and rise velocity for hydraulic loading rate of 50 m/h, $d_{Orifice}$ = 0.55 mm, 20°C, P_{Sat} = 484 kPa and probe volume coordinates (900,0,25)

R_R (%)	5	7
d_B (μm)	68.8	63.3
σ_{dB}(μm)	19.1	12.6
$U_{B\ Inst}$ (m/s)	1.93E-02	1.84E-02
U_{RMS} (m/s)	2.32E-03	2.11E-03
U_L (m/s)	1.65E-02	1.65E-02
$U_{B\ Relative}$ (m/s)	2.80E-03	1.90E-03
$U_{B\ Stoke}$ (m/s)	2.62E-03	2.22E-03
Measured N_B (bubbles/mL)	1.12E+04	1.70E+04
Theoretical N_B (bubbles/mL)	2.18E+04	3.86E+04
Measured Φ_B (ppm)	2056	2898
Theoretical Φ_B (ppm)	3727	5120

Table 5.12 **Effect of recycle ratio on bubble size, concentration and rise velocity for hydraulic loading rate of 70 m/h, d $_{\text{Orifice}}$ = 0.55 mm, 20°C, P_{Sat} = 484 kPa and probe volume coordinates (900,0,25)**

R_R (%)	3	5
d_B (μm)	66.0	63.4
σ_{dB}(μm)	22.7	19.9
$U_{B\ \text{inst}}$ (m/s)	2.49E-02	2.44E-02
U_{RMS} (m/s)	3.00E-03	2.58E-03
U_L (m/s)	2.18E-02	2.18E-02
$U_{B\ \text{Relative}}$ (m/s)	3.05E-03	2.56E-03
$U_{B\ \text{Stoke}}$ (m/s)	2.41E-03	2.22E-03
Measured N_B (bubbles/mL)	5.97E+03	1.41E+04
Theoretical N_B (bubbles/mL)	1.52E+04	2.80E+04
Measured Φ_B (ppm)	1560	1877
Theoretical Φ_B (ppm)	2279	3727

Table 5.13 **Effect of recycle ratio on bubble size, concentration and rise velocity for hydraulic loading rate of 90 m/h, $d_{Orifice}$ = 1.03 mm, 20°C, P_{Sat} = 484 kPa and probe volume coordinates (900,0,25)**

R_R (%)	3	5	7
d_B (μm)	74.4	68.2	67.1
σ_{dB}(μm)	27.1	22.5	19.8
$U_{B\,inst}$ (m/s)	2.99E-02	2.94E-02	2.84E-02
U_{RMS} (m/s)	3.60E-03	3.34E-03	2.99E-03
U_L (m/s)	2.55E-02	2.55E-02	2.55E-02
$U_{B\,Relative}$ (m/s)	4.37E-03	3.90E-03	2.90E-03
$U_{B\,Stoke}$ (m/s)	3.06E-03	2.57E-03	2.49E-03
Measured N_B (bubbles/mL)	6.80E+03	1.04E+04	1.30E+04
Theoretical N_B (bubbles/mL)	1.06E+04	2.25E+04	3.24E+04
Measured Φ_B (ppm)	1468	1721	2239
Theoretical Φ_B (ppm)	2279	3727	5120

hydraulic loading rate was 30 m/h. That could be due to the fact that at higher hydraulic loading rates, the saturated flow rate, Q_{Sat}, at the required R_R is higher and therefore smaller bubbles were expected to be produced. However, for contact zone hydraulic loading rate of 90 m/h, the nozzle orifice diameter 1.03 mm had to be used. Therefore, bubbles with larger d_B were produced, especially at lower R_R. Also, the results showed that as R_R increased the standard deviation of the BSD became smaller, as shown in Figures 5.15 and 5.16. This means more uniform bubble size with mean volume diameter d_B were produced. The results also show that the U_{RMS} decreased as R_R was increased for contact zone hydraulic loading rates 50, 70 and 90 m/h.

Regarding the effect of R_R on bubble volume and number concentrations, the results in Tables 5.11 to 5.13 indicate that, for all contact zone hydraulic loading rates investigated, Φ_B and N_B increased as R_R was increased.

To summarize, increasing the recycle ratio at constant contact zone hydraulic loading rate and saturator pressure caused the bubble mean diameter to decrease and at the same time the standard deviation of BSD decreased, therefore, producing more uniform bubble size. As a result, bubble volume and number concentration increased. Also, the increase in the recycle ratio decreased the U_{RMS} due to the decrease in σ_{dB}.

5.2.3.3 Effect of contact zone hydraulic loading rate

The third important operational parameter that was investigated in this study was the hydraulic loading rate inside the contact zone. The effect of contact zone hydraulic loading rate on bubble size, concentration and $U_{B\,inst}$ was measured by varying the hydraulic loading rate at constant R_R and P_{Sat}. Hydraulic loading rates in this study were varied from 30 to 90 m/h. All experiments were performed at P_{Sat} of 484 kPa and the measurements were taken at probe volume coordinates (900,0,25).

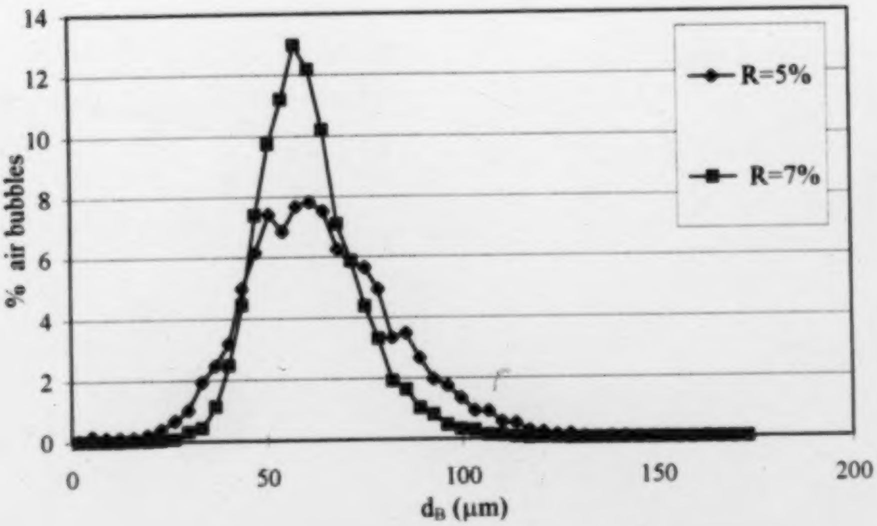

Figure 5.15 Effect of recycle ratio on BSD for hydraulic loading rate of 50 m/h, $d_{Orifice}$ = 0.55 mm, 20°C, P_{Sat} = 484 kPa and probe volume coordinates (900,0,25)

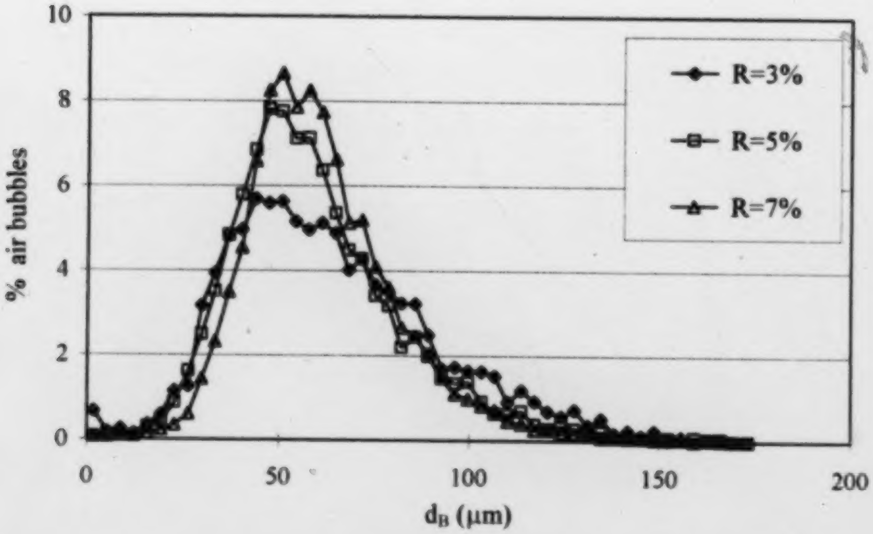

Figure 5.16 Effect of recycle ratio on BSD for hydraulic loading rate of 90 m/h, $d_{Orifice}$ = 1.03 mm, 20°C, P_{Sat} = 484 kPa and probe volume coordinates (900,0,25)

The effect of contact zone hydraulic loading rate on bubble size, concentration and $U_{B\ inst}$ for hydraulic loading rates of 30 and 50 m/h is shown in Table 5.14. These experiments were performed at recycle ratio of 7 % while $d_{Orifice}$ of 0.55 mm. The results showed that as contact zone hydraulic loading rate increased from 30 to 50 m/h, the mean bubble diameter decreased significantly. This is illustrated in Figure 5.17 which shows BSD at both hydraulic loading rates. As hydraulic loading rate increased, at the same R_R, the saturated water flow rate, Q_{Sat}, increased and as a result bubbles with smaller diameters were produced.

The results in Table 5.14 show that the mean relative rise velocity of the bubbles $U_{B\ rel}$ decreased as hydraulic loading rate was increased. This is in agreement with the calculated Stokes' rise velocity. As hydraulic loading rate increased, mean d_B decreased and therefore $U_{B\ Stoke}$ decreased, based on Equation 2.13. As expected, the mean instantaneous rise velocity of the bubbles increased as contact zone hydraulic loading rate increased. In addition, the U_{RMS} decreased.

Regarding the effect of contact zone hydraulic loading rate on bubble number concentrations (N_B), the results in Table 5.14 indicate that the measured N_B increased. Higher hydraulic loading rates produced bubbles with smaller d_B and therefore N_B increased. On the other hand, the results indicated that the measured bubble volume concentration Φ_B decreased as hydraulic loading increased for the same R_R and P_{Sat}. These results are in contradiction with the theoretical value based on Equations 2.6, 2.7 and 2.8. The differences between the theoretical and the experimental values could be due to the method that was used to calculate the Φ_B experimental. The experimental Φ_B value was calculated by multiplying the measured N_B values by the mean bubble volume, which is based on the measured mean d_B. Since the mean bubble diameter was less than 100 μm, the bubbles could be assumed to be spherical in shape (Clift et al., 1978). Also, the measured mean values of d_B using the PDA were verified using the video photographic method. Therefore, the main source of the discrepancy could be due to the measured N_B

Table 5.14 Effect of hydraulic loading rate on bubble size, concentration and rise velocity at $R_R = 7$ %, $d_{Orifice} = 0.55$ mm, 20°C, $P_{Sat} = 484$ kPa and probe volume coordinates (900,0,25)

Hydraulic loading rate (m/h)	30	50
d_B (µm)	85.5	63.3
σ_{dB}(µm)	15.4	12.6
$U_{B\ inst}$ (m/s)	1.42E-02	1.84E-02
U_{RMS} (m/s)	5.57E-03	2.11E-03
U_L (m/s)	1.05E-02	1.65E-02
$U_{B\ Relative}$ (m/s)	3.73E-03	1.90E-03
$U_{B\ Stoke}$ (m/s)	4.04E-03	2.22E-03
Measured N_B (bubbles/mL)	1.04E+04	1.70E+04
Theoretical N_B (bubbles/mL)	1.57E+04	3.86E+04
Measured Φ_B (ppm)	3405	2898
Theoretical Φ_B (ppm)	5120	5120

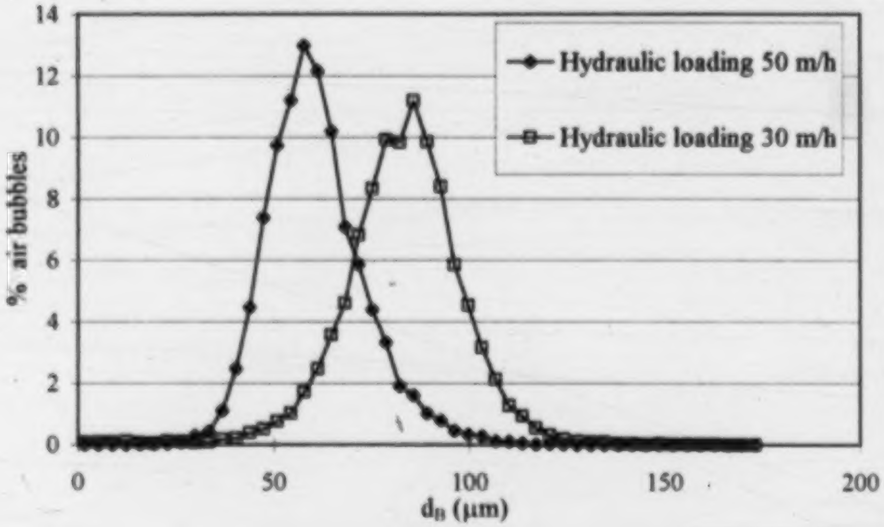

Figure 5.17 Effect of hydraulic loading rate on BSD at R_R = 7 %, P_{Sat} = 484 kPa, $d_{Orifice}$ = 0.55 mm, 20°C and probe volume coordinates (900,0,25)

values. Personal communication with DANTEC technical services verified that the differences in measured N_B values using the PDA could be as high as 50%.

Table 5.15 summarizes the results for experiments conducted at hydraulic loading rates 50 and 70 m/h. These experiments were performed at recycle ratio of 5 % and using $d_{Orifice}$ of 0.55 mm. The results again show that the mean bubble diameter decreased as contact zone hydraulic loading rate increased, which is illustrated by the BSD curves in Figure 5.18. As a result, the measured N_B increased while Φ_B decreased as the hydraulic loading rate increased. The results also show that the mean relative rise velocity of the bubbles $U_{B\ rel}$ decreased as hydraulic loading increased.

Table 5.16 summarizes the results for experiments conducted at hydraulic loading rates of 70 and 90 m/h. These experiments were performed at recycle ratio of 3 % and using $d_{Orifice}$ of 0.55 mm. These experiments show that the mean d_B decreased as a result of increasing the hydraulic loading rate. Figure 5.19 shows the BSD curves for both hydraulic loading rates. It was observed that both BSD curves had higher σ_{dB} and were more skewed to the right when compared to those at lower hydraulic loading rates, i.e. 30 and 50 m/h. At higher hydraulic loading rates, larger portions of bubbles with mean d_B larger than 150 μm, which were formed in the mixing column, will enter the contact zone column.

Table 5.16 show that N_B increased with increasing the hydraulic loading and Φ_B decreased. The results also show that the mean relative rise velocity of the bubbles $U_{B\ rel}$ decreased as hydraulic loading rate increased and at the same time the U_{RMS} of the bubbles decreased.

Table 5.17 summarizes the results for experiments conducted al at hydraulic loading rates of 70 and 90 m/h, with a recycle ratio of 7 % and using $d_{Orifice}$ of 1.03 mm. In these experiments, the results clearly show the effect of increasing the hydraulic loading

Table 5.15 **Effect of hydraulic loading rate on bubble size, concentration and rise velocity at $R_R = 5$ %, $d_{Orifice} = 0.55$ mm, 20°C, $P_{Sat} = 484$ kPa and probe volume coordinates (900,0,25)**

Hydraulic loading rate (m/h)	50	70
d_B (μm)	68.8	63.4
σ_{dB}(μm)	19.9	19.9
$U_{B\,inst}$ (m/s)	1.93E-02	2.44E-02
U_{RMS} (m/s)	2.32E-03	2.58E-03
U_L (m/s)	1.65E-02	2.18E-02
$U_{B\,Relative}$ (m/s)	2.80E-03	2.56E-03
$U_{B\,Stoke}$ (m/s)	2.62E-03	2.22E-03
Measured N_B (bubbles/mL)	1.12E+04	1.41E+04
Theoretical N_B (bubbles/mL)	2.19E+04	2.79E+04
Measured Φ_B (ppm)	2056	1877
Theoretical Φ_B (ppm)	3728	3728

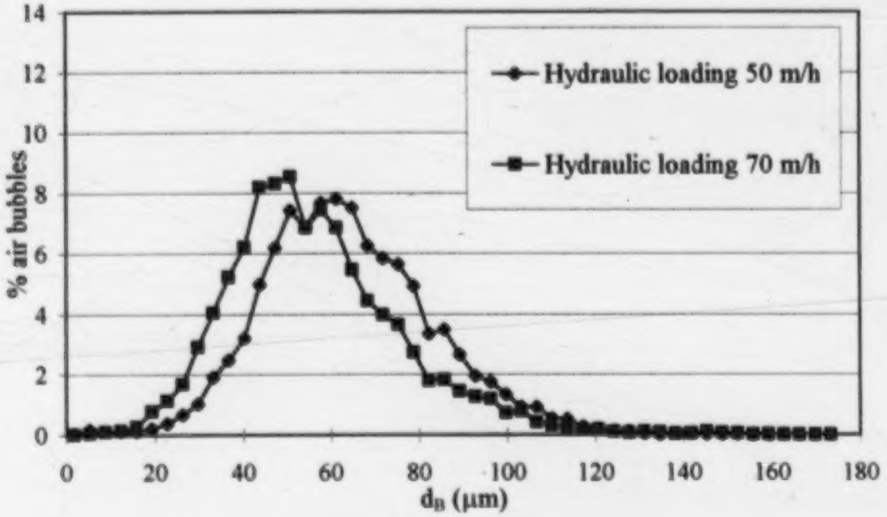

Figure 5.18 Effect of hydraulic loading rate on BSD at R_R = 5 %, P_{Sat} = 484 kPa, $d_{Orifice}$ = 0.55 mm, 20°C and probe volume coordinates (900,0,25)

Table 5.16 Effect of hydraulic loading rate on bubble size, concentration and rise velocity at R_R = 3 %, $d_{Orifice}$ = 0.55 mm, 20°C, P_{Sat} = 484 kPa and probe volume coordinates (900,0,25)

Hydraulic loading rate (m/h)	70	90
d_B (μm)	66.0	56.7
σ_{dB}(μm)	22.7	19.2
$U_{B\ inst}$ (m/s)	2.48E-02	2.74E-02
U_{RMS} (m/s)	3.00E-03	2.88E-03
U_L (m/s)	2.13E-02	2.55E-02
$U_{B\ Relative}$ (m/s)	3.53E-03	1.93E-03
$U_{B\ Stoke}$ (m/s)	2.41E-03	1.78E-03
Measured N_B (bubbles/mL)	5.97E+03	6.94E+03
Theoretical N_B (bubbles/mL)	1.51E+04	2.39E+04
Measured Φ_B (ppm)	1560	1432
Theoretical Φ_B (ppm)	2279	2279

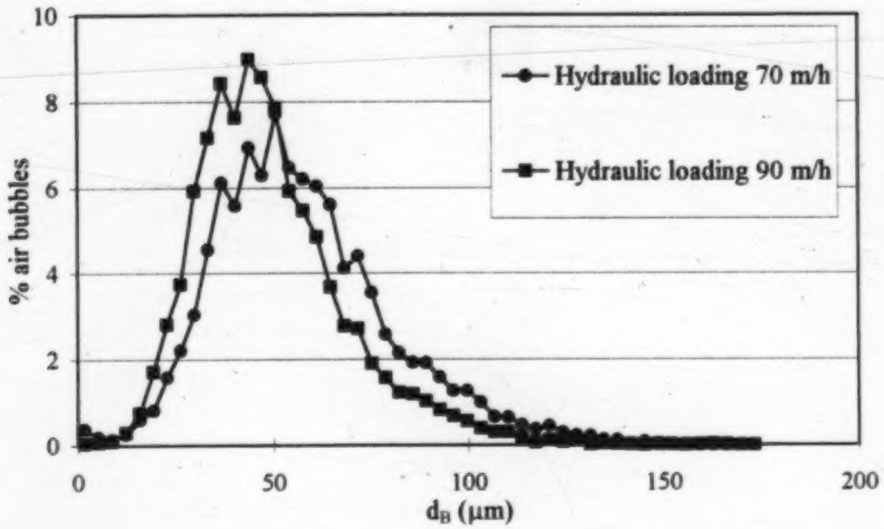

Figure 5.19 Effect of hydraulic loading rate on BSD at R_R = 3 %, P_{Sat} = 484 kPa, $d_{Orifice}$ = 0.55 mm, 20°C and probe volume coordinates (900,0,25)

Table 5.17 **Effect of hydraulic loading rate on bubble size, concentration and rise velocity at R_R = 7 %, d $_{Orifice}$ = 1.03 mm, 20°C, P_{Sat} = 484 kPa and probe volume coordinates (900,0,25)**

Hydraulic loading rate (m/h)	**70**	**90**
d_B (μm)	81.9	67.1
σ_{dB}(μm)	18.9	19.8
$U_{B\ inst}$ (m/s)	2.51E-02	2.84E-02
U_{RMS} (m/s)	3.81E-03	2.99E-03
U_L (m/s)	2.13E-02	2.55E-02
$U_{B\ Relative}$ (m/s)	3.80E-03	2.90E-03
$U_{B\ Stoke}$ (m/s)	3.71E-03	2.49E-03
Measured N_B (bubbles/mL)	1.37E+04	1.42E+04
Theoretical N_B (bubbles/mL)	1.78E+04	3.24E+04
Measured Φ_B (ppm)	3927	2239
Theoretical Φ_B (ppm)	5120	5120

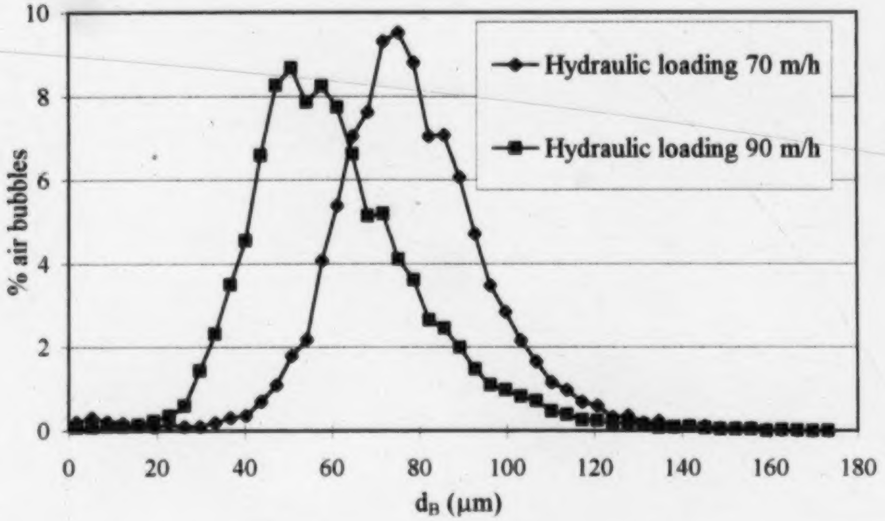

Figure 5.20 Effect of hydraulic loading rate on BSD at R_R = 7 %, P_{Sat} = 484 kPa, $d_{Orifice}$ = 1.03 mm, 20°C and probe volume coordinates (900,0,25)

rate on the mean d_B especially when using larger $d_{Orifice}$. As illustrated in Figure 5.20, the BSD curves showed that the mean d_B decreased as contact zone hydraulic loading rate increased. The results in Table 5.17 also show that N_B increased with increasing the hydraulic loading rate while Φ_B decreased. In addition, the mean relative rise velocity of the bubbles $U_{B\,rel}$ decreased as hydraulic loading rate increased and at the same time the U_{RMS} of the bubble decreased.

To summarize, increasing the contact zone hydraulic loading rate at constant recycle ratio and saturator pressure decreased the mean bubble diameter. As a result, bubble number concentration increased. Although the theoretical bubble volume concentration remained unchanged as the hydraulic loading rate was increased, the experimental bubble volume concentration had decreased. Also, the increase in the hydraulic loading rate increased both the instantaneous bubble rise velocity and the superficial liquid velocity and at the same time the relative bubble rise velocity decreased.

5.2.3.4 Effect of nozzle orifice diameter

The fourth important operating parameter that was investigated in this study was the nozzle orifice diameter $d_{Orifice}$. In this study, the effect of two values of $d_{Orifice}$ on bubble size, concentration and $U_{B\,inst}$ were investigated: $d_{Orifice}$ of 0.55 mm and 1.03 mm. These experiments were performed at constant contact zone hydraulic loading rate and R_R and at P_{sat} of 484 kPa.

The effect of increasing the $d_{Orifice}$ on bubble size, concentration, and $U_{B\,inst}$ is shown in Table 5.18. These experiments were performed at contact zone hydraulic loading of 50 m/h and R_R of 7 %. The probe volume coordinates were (400,0,25). The results show that as the $d_{Orifice}$ increased from 0.55 to 1.03 mm, the mean d_B increased significantly. At the same time the standard deviation of d_B increased as $d_{Orifice}$ increased, as shown in Figure 5.21. The BSD curve for $d_{Orifice}$ of 1.03 mm is more skewed to the right suggesting that higher percentage of larger bubbles were present.

Table 5.18 **Effect of nozzle orifice diameter on bubble size, concentration and rise velocity for hydraulic loading rate = 50 m/h, R_R = 7 %, 20°C, P_{Sat} = 484 kPa and probe volume coordinates (400,0,25)**

Nozzle orifice diameter (mm)	0.55	1.03
d_B (μm)	52.7	70.1
σ_{dB}(μm)	14.1	21.6
$U_{B\ inst}$ (m/s)	1.72E-02	1.81E-02
U_{RMS} (m/s)	3.64E-03	5.34E-03
U_L (m/s)	1.62E-02	1.62E-02
$U_{B\ Relative}$ (m/s)	9.77E-04	1.86E-03
$U_{B\ Stoke}$ (m/s)	1.54E-03	2.72E-03
Measured N_B (bubbles/mL)	2.36E+04	1.12E+04
Theoretical N_B (bubbles/mL)	6.68E+04	2.84E+04
Measured Φ_B (ppm)	1810	2025
Theoretical Φ_B (ppm)	5120	5120

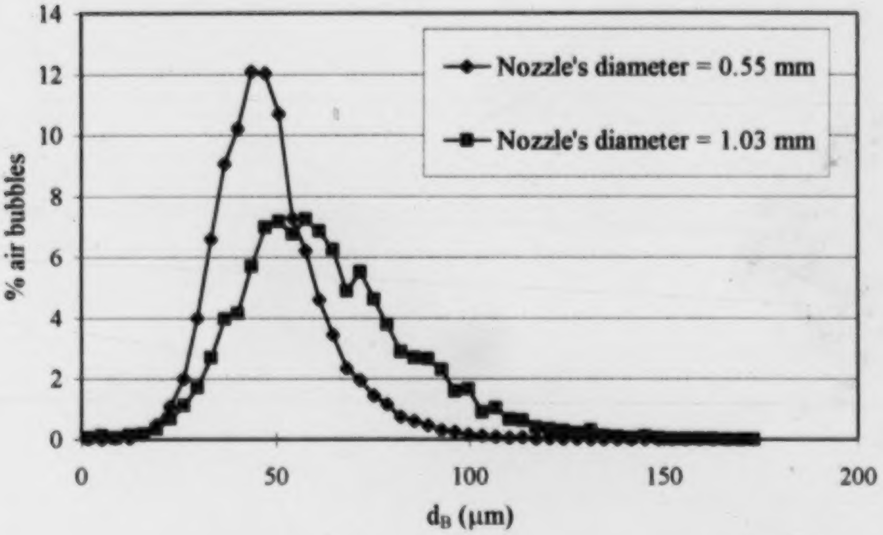

Figure 5.21 Effect of nozzle orifice diameter on BSD for hydraulic loading rate = 50 m/h, R_R = 7 %, P_{Sat} = 484 kPa, 20°C and probe volume coordinates (400,0,25)

Table 5.18 shows that as d $_{Orifice}$ increased, the mean $U_{B\ inst}$ increased. At the same time, the U_{RMS} increased as a result of increasing σ_{dB}. The relative rise velocity increased as the d $_{Orifice}$ increased due to the production of bubbles with larger mean d_B.

In addition, the results in Table 5.18 indicate that the measured N_B decreased with increasing d $_{Orifice}$ as a result of the increase in the bubble mean d_B. Also, the results showed that the experimental Φ_B increased as the result of using larger d $_{Orifice}$. Theoretically, Φ_B should have remained unchanged as d $_{Orifice}$ increased, based on Equations 2.6, 2.7 and 2.8. However, the increase in the experimental Φ_B as d $_{Orifice}$ increased may be explained as follow: as d $_{Orifice}$ had increased, bubbles with larger diameters were produced. Therefore, the mean bubble volume increased and as a result the experimental Φ_B, which is based on the experimental N_B multiplied by the experimental mean bubble volume, increased.

Tables 5.19 and 5.20 summarize the results for experiments conducted for hydraulic loading rate of 70 m/h, R_R = 5 %, P_{Sat} of 484 kPa and probe volume coordinates (400,0,0) and (900,0,0), respectively. These experiments showed that the mean d_B increased as the d $_{Orifice}$ increased from 0.55 to 1.03 mm. Also, the results show that the mean d_B for both d $_{Orifice}$ were larger at probe volume coordinates (900,0,0) than those at (400,0,0). At both probe volume coordinates, the bubble diameter standard deviation increased as the d $_{Orifice}$ increased from 0.55 to 1.03 mm. This is illustrated in Figures 5.22 and 5.23 which show BSD for both d $_{Orifice}$ at probe volume coordinates (400,0,0) and (900,0,0), respectively.

Tables 5.19 and 5.20 show that as d $_{Orifice}$ increased, the mean $U_{B\ inst}$ increased for both probe volume coordinates . At the same time, the U_{RMS} increased as a result of increasing σ_{dB}. Also, the relative rise velocity increased as the d $_{Orifice}$ increased due to the production of bubbles with larger mean d_B. In addition, the results indicated that the measured N_B decreased with increasing d $_{Orifice}$ and the experimental Φ_B increased as the result of using larger d $_{Orifice}$.

Table 5.19 Effect of nozzle orifice diameter on bubble size, concentration and rise velocity for hydraulic loading rate = 70 m/h, R_R = 5 %, 20°C, P_{Sat} = 484 kPa and probe volume coordinates (400,0,0)

Nozzle orifice diameter (mm)	0.55	1.03
d_B (μm)	54.1	61.1
σ_{dB}(μm)	18.6	22.9
$U_{B\ inst}$ (m/s)	2.28E-02	2.41E-02
U_{RMS} (m/s)	5.97E-03	7.90E-03
U_L (m/s)	2.16E-02	2.16E-02
$U_{B\ Relative}$ (m/s)	1.24E-03	2.45E-03
$U_{B\ Stoke}$ (m/s)	1.62E-03	2.06E-03
Measured N_B (bubbles/mL)	1.45E+04	1.09E+04
Theoretical N_B (bubbles/mL)	4.50E+04	3.12E+04
Measured Φ_B (ppm)	1198	1303
Theoretical Φ_B (ppm)	3728	3727

Table 5.20 Effect of nozzle orifice diameter on bubble size, concentration and rise velocity for hydraulic loading rate = 70 m/h, R_R = 5 %, 20°C, P_{Sat} = 484 kPa and probe volume coordinates (900,0,0)

Nozzle orifice diameter (mm)	0.55	1.03
d_B (μm)	64.5	79.1
σ_{dB}(μm)	18.0	22.7
$U_{B\,abs}$ (m/s)	2.39E-02	2.49E-02
U_{RMS} (m/s)	2.22E-03	2.69E-03
U_L (m/s)	2.22E-02	2.22E-02
$U_{B\,Relative}$ (m/s)	1.66E-03	2.72E-03
$U_{B\,Stokes}$ (m/s)	2.30E-03	3.46E-03
Measured N_B (bubbles/mL)	1.31E+04	9.68E+03
Theoretical N_B (bubbles/mL)	2.65E+04	1.44E+04
Measured Φ_B (ppm)	1841	2504
Theoretical Φ_B (ppm)	3727	3727

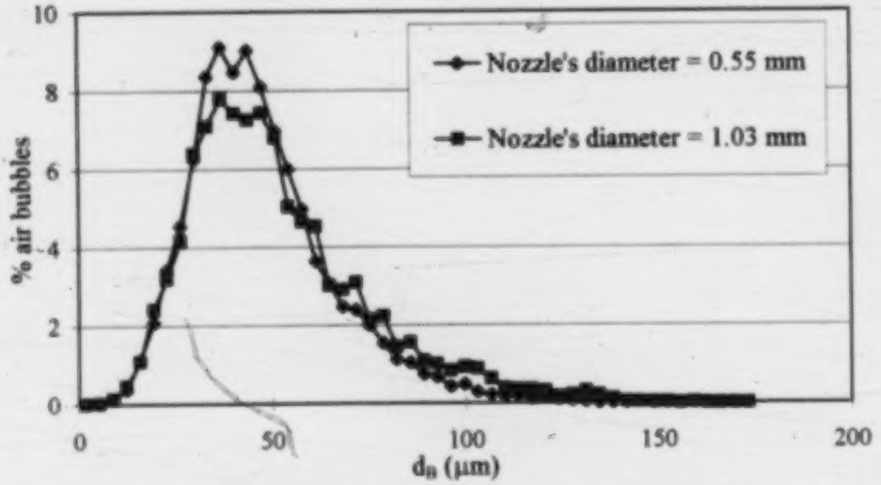

Figure 5.22 Effect of nozzle orifice diameter on BSD for hydraulic loading rate= 70 m/h, R_R = 5 %, P_{Sat} = 484 kPa, 20°C and probe volume coordinates (400,0,0)

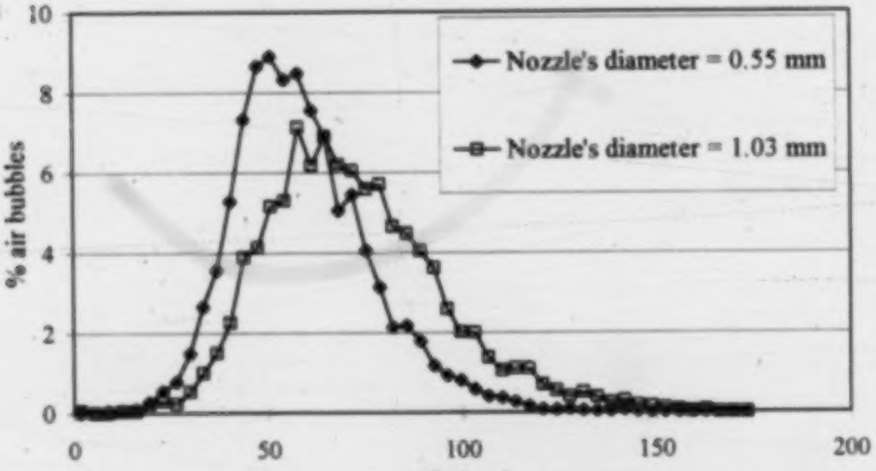

Figure 5.23 Effect of nozzle orifice diameter on BSD for hydraulic loading rate = 70 m/h, R_R = 5 %, P_{Sat} = 484 kPa, 20°C and probe volume coordinates (900,0,0)

Table 5.21 summarizes the results of experiments conducted for hydraulic loading of 90 m/h, R_R = 3 %, P_{Sat} of 484 kPa and probe volume coordinates (900,0,25). The results show that as the $d_{Orifice}$ increased from 0.55 to 1.03 mm, the mean d_B increased significantly. At the same time the standard deviation of d_B increased as $d_{Orifice}$ increased, as shown in Figure 5.24. The BSD curve for $d_{Orifice}$ of 1.03 mm was more skewed to the right suggesting that higher portion of larger bubbles were present.

Table 5.21 shows that the mean $U_{B\,inst}$ increased as $d_{Orifice}$ increased. The relative rise velocity increased as the $d_{Orifice}$ increased and the U_{RMS} of the bubbles increased. In addition, the results indicated that the measured N_B decreased with increasing $d_{Orifice}$ and the experimental Φ_B increased as the result of using larger $d_{Orifice}$.

To summarize, increasing the size of the nozzle orifice diameter increased the mean bubble diameter at constant hydraulic loading rate, recycle ratio and saturator pressure. As a result, bubble number concentration decreased. Although the theoretical bubble volume concentration remained unchanged as the nozzle orifice diameter was increased, the experimental bubble volume concentration increased. In addition, the instantaneous and relative bubble rise velocity increased as a result of increasing the size of the nozzle orifice diameter.

5.2.3.5 Effect of contact zone height

To study the effect of contact zone height on bubble size, concentration and rise velocity, PDA measurements were taken at two different heights. The PDA set-up was elevated 1500 mm from the ground and since the set-up was stationary, the first measurement was taken at 900 mm from the base of the DAF column. This corresponded to the maximum height that the PDA measurements could be taken. To take measurements at lower contact zone heights, and taking into consideration the maximum ceiling height, the DAF column could be elevated only by 500 mm from the ground.

Table 5.21 Effect of nozzle orifice diameter on bubble size, concentration and rise velocity for hydraulic loading rate= 90 m/h, R_R = 3 %, 20°C, P_{Sat} = 484 kPa and probe volume coordinates (900,0,25)

Nozzle orifice diameter (mm)	0.55	1.03
d_B (µm)	56.7	74.4
σ_{dB}(µm)	19.2	27.1
$U_{B\,net}$ (m/s)	2.74E-02	2.90E-02
U_{RMS} (m/s)	2.88E-03	3.60E-03
U_L (m/s)	2.55E-02	2.55E-02
$U_{B\,Relative}$ (m/s)	1.93E-03	3.50E-03
$U_{B\,Stoke}$ (m/s)	1.78E-03	3.06E-03
Measured N_B (bubbles/mL)	6.94E+03	6.80E+03
Theoretical N_B (bubbles/mL)	2.39E+04	1.06E+04
Measured Φ_B (ppm)	1432	1468
Theoretical Φ_B (ppm)	2279	2279

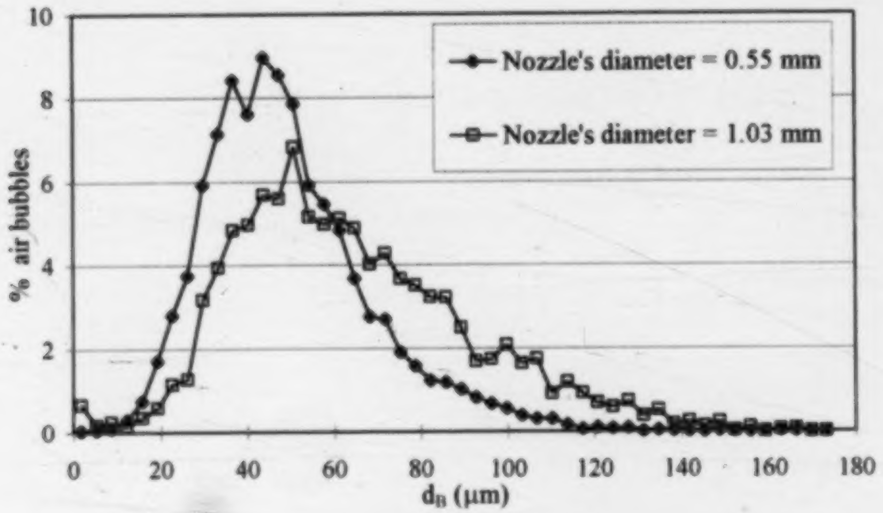

Figure 5.24 Effect of nozzle orifice diameter on BSD for hydraulic loading rate = 90 m/h, R_R = 3 %, P_{Sat} = 484 kPa, 20°C and probe volume coordinates (900,0,25)

Therefore, the minimum height that the PDA measurements could be taken was 400 mm from the base of the DAF column.

The effects of contact zone height on bubble size, concentration and $U_{B\,inst}$ for hydraulic loading rate of 30 m/h are shown in Table 5.22. These experiments were performed at two value of R_R: 7 % and 10 % and the probe volume coordinates were (900,0,25) for contact zone height of 900 mm and (400,0,25) for contact zone height of 400 mm. All experiments were conducted using $d_{Orifice}$ = 0.55 mm and P_{Sat} was 484 kPa. The results, for both recycle ratios, showed that the mean d_B increased significantly as the contact zone height increased. This is illustrated clearly in the BSD curves shown in Figures 5.25 and 5.26 for R_R = 7 % and R_R = 10 %, respectively. As expected, the values of the mean d_B and σ_{dB} were lower when measured at R_R = 10 %, for both heights. Calculations showed that the increase in the mean d_B as the contact zone height increased is due mainly to the coalescence of bubbles as they rise.

In addition, the results in Table 5.22 indicate that N_B decreased as the contact zone height had increased while Φ_B increased, for both recycle ratios. The reduction in N_B may be due to the coalescence of bubbles as they rise inside the column.

The effect of contact zone height was also investigated at higher hydraulic loading rates. As shown in Table 5.23, the results indicate again that the mean d_B decreased as the contact zone height increased for hydraulic loading rate of 50 m/h. These experiments were performed at two values of R_R: 5 % and 7 % and the probe volume coordinates were (900,0,25) for contact zone height of 900 mm and (400,0,25) for contact zone height of 400 mm. All experiments were conducted using $d_{Orifice}$ = 0.55 mm and P_{Sat} was 484 kPa. Figures 5.27 and 5.28 illustrate the BSD curves for R_R =5 % and 7 %, respectively. These figures show that BSD's for R_R = 7 %, for both heights, have lower mean d_B and σ_{dB} than those for R_R = 5 %.

Table 5.22 **Effect of contact zone height and recycle ratio on bubble size, concentration and rise velocity for hydraulic loading rate = 30 m/h, 20°C, P_{Sat} = 484 kPa, $d_{Orifice}$ = 0.55 mm and probe volume coordinates (900,0,25) and (400,0,25)**

	R_R = 7 %		R_R = 10 %	
Contact zone height (mm)	900	400	900	400
d_B (μm)	85.5	65.4	73.7	64.2
σ_{dB}(μm)	15.4	12.3	14.4	11.0
$U_{B\,inst}$ (m/s)	1.42E-02	1.35E-02	1.40E-02	1.32E-02
U_{RMS} (m/s)	5.57E-03	5.54E-03	4.68E-03	5.25E-03
U_L (m/s)	1.05E-02	1.07E-02	1.05E-02	1.07E-02
$U_{B\,Relative}$ (m/s)	3.73E-03	2.80E-03	3.50E-03	2.50E-03
$U_{B\,Stoke}$ (m/s)	4.04E-03	2.36E-03	3.00E-03	2.28E-03
Measured N_B (bubbles/mL)	1.04E+04	1.44E+04	1.79E+04	2.15E+04
Theoretical N_B (bubbles/mL)	1.57E+04	3.50E+04	3.40E+04	5.14E+04
Measured Φ_B (ppm)	3405	2108	3748	2979
Theoretical Φ_B (ppm)	5120	5120	7114	7114

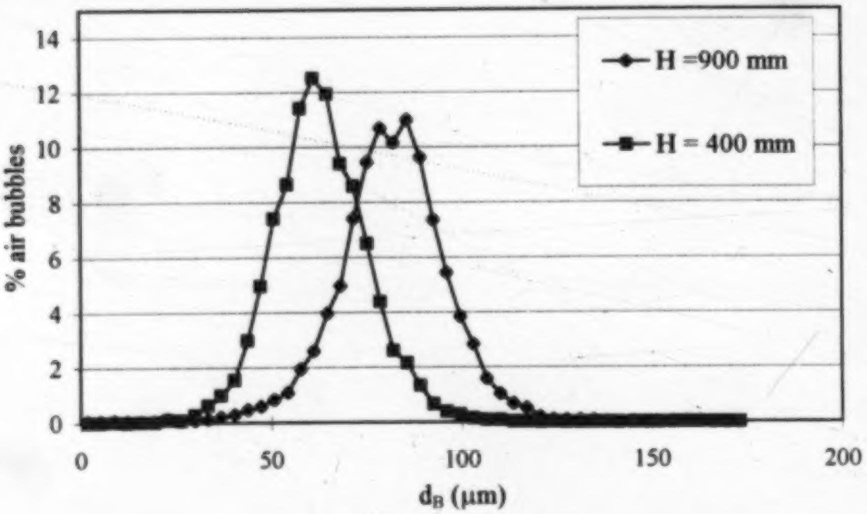

Figure 5.25 Effect of contact zone height on BSD for hydraulic loading rate = 30 m/h, R_R = 7 %, P_{Sat} = 484 kPa, 20°C, $d_{Orifice}$ 0.55 mm and probe volume coordinates (900,0,25) and (400,0,25)

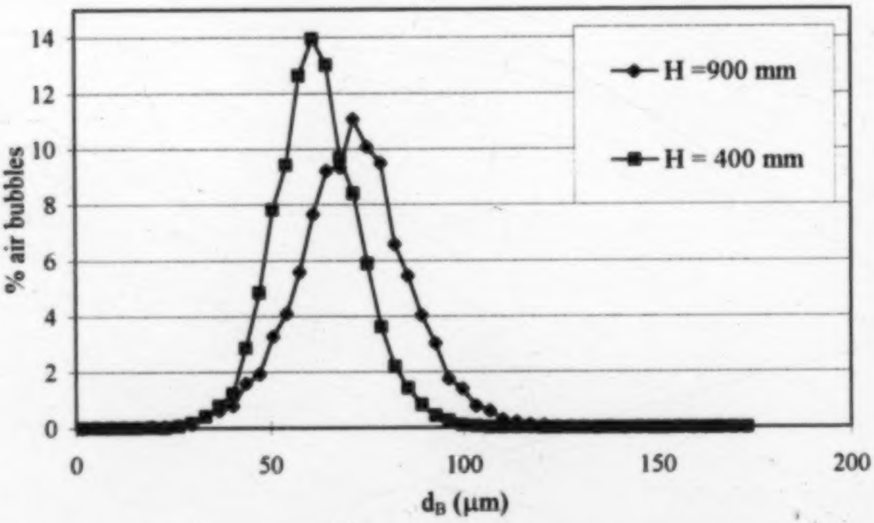

Figure 5.26 Effect of contact zone height on BSD for hydraulic loading rate = 30 m/h, R_R = 10 %, P_{Sat} = 484 kPa, 20°C, $d_{Orifice}$ 0.55 mm and probe volume coordinates (900,0,25) and (400,0,25)

Table 5.23 **Effect of contact zone height and recycle ratio on bubble size, concentration and rise velocity for hydraulic loading rate = 50 m/h, 20°C, P_{Sat} = 484 kPa, $d_{Orifice}$ = 0.55 mm and probe volume coordinates (900,0,25) and (400,0,25)**

	R_R =5 %		R_R = 7 %	
Contact zone height (mm)	900	400	900	400
d_B (μm)	68.8	54.1	63.3	52.7
σ_{dB}(μm)	19.1	17.1	12.6	11.9
$U_{B\,inst}$ (m/s)	1.93E-02	1.76E-02	1.84E-02	1.72E-02
U_{RMS} (m/s)	2.32E-03	3.86E-03	2.11E-03	3.64E-03
U_L (m/s)	1.65E-02	1.62E-02	1.65E-02	1.62E-02
$U_{B\,Relative}$ (m/s)	2.80E-03	1.35E-03	1.90E-03	9.77E-04
$U_{B\,Stoke}$ (m/s)	2.62E-03	1.62E-03	2.22E-03	1.54E-03
Measured N_B (bubbles/mL)	1.12E+04	1.52E+04	2.66E+04	2.36E+04
Theoretical N_B (bubbles/mL)	2.19E+04	4.50E+04	3.86E+04	6.68E+04
Measured Φ_B (ppm)	2056	1260	2198	1810
Theoretical Φ_B (ppm)	3728	3728	5120	5120

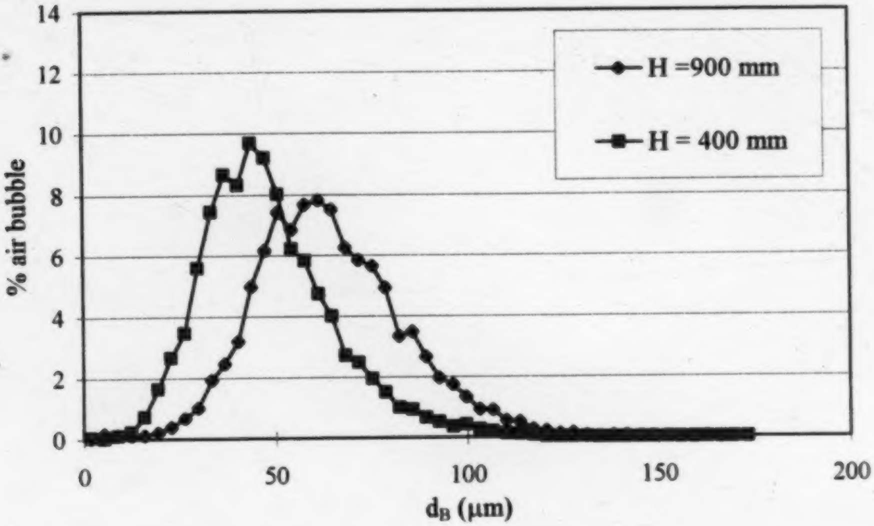

Figure 5.27 Effect of contact zone height on BSD for hydraulic loading rate = 50 m/h, R_R = 5 %, P_{Sat} = 484 kPa, 20°C, $d_{Orifice}$ 0.55 mm and probe volume coordinates (900,0,25) and (400,0,25)

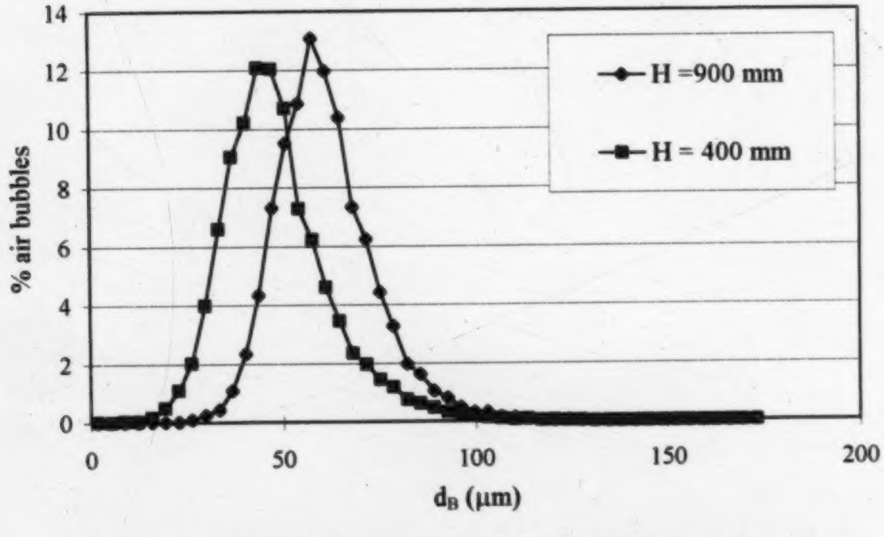

Figure 5.28 Effect of contact zone height on BSD for hydraulic loading rate = 50 m/h, R_R = 7 %, P_{Sat} = 484 kPa, 20°C, $d_{Orifice}$ 0.55 mm and probe volume coordinates (900,0,25) and (400,0,25)

To illustrate the effect of $d_{Orifice}$ on bubble size distribution for both contact zone heights, experiments were performed at R_R = 10 %, and $d_{Orifice}$ was 1.03 mm. As shown in Table 5.24, mean d_B for both heights were larger than d_B measured using the $d_{Orifice}$ = 0.55 mm and also the reduction in the mean bubble size, as the contact zone height decreased, was more significant. This is illustrated in Figure 5.29 which shows the BSD curves for both contact zone heights.

In addition, Tables 5.23 and 5.24 show that the mean $U_{B\,inst}$ decreased as the contact zone height decreased, for all R_R investigated. Also, these results indicate that the N_B decreased as the contact zone increased while Φ_B increased.

The effect of contact zone height on bubble size, concentration and $U_{B\,Inst}$ for hydraulic loading rate of 70 m/h is shown in Table 5.25. These experiments were performed at two R_R: 3 % and 5 % and the probe volume coordinates were (900,0,25) for contact zone height of 900 mm and (400,0,25) for contact zone height of 400 mm. All experiments were conducted using $d_{Orifice}$ = 0.55 mm and P_{Sat} was 484 kPa.

The results, for both recycle ratios, showed that the mean d_B increased as the contact zone height increased. However, the reduction in bubble size was not as significant as that observed for hydraulic loading rates of 30 and 50 m/h. This is illustrated in the BSD curves shown in Figures 5.30 and 5.31 for R_R = 3 % and R_R = 5 %, respectively.

In addition, Table 5.25 show that the mean $U_{B\,inst}$ decreased as the contact zone height decreased, for all R_R and $d_{Orifice}$ investigated. Also, these results indicate again that the N_B decreased as the contact zone increased while Φ_B increased.

To summarize, decreasing the contact zone height at constant hydraulic loading rates, recycle ratios and saturator pressures would decrease the mean bubble size. The reduction was more significant at lower hydraulic loading rates and recycle ratios. Also,

Table 5.24 Effect of contact zone height on bubble size, concentration and rise velocity for hydraulic loading rate = 50 m/h, R_R = 10 %, 20°C, P_{Sat} = 484 kPa, $d_{Orifice}$ = 1.03 mm and probe volume coordinates (900,0,25) and (400,0,25)

Contact zone height (mm)	900	400
d_B (μm)	100.7	80.0
σ_{dB}(μm)	21.0	16.0
$U_{B\,inst}$ (m/s)	2.44E-02	1.92E-02
U_{RMS} (m/s)	5.45E-03	5.08E-03
U_L (m/s)	1.70E-02	1.62E-02
$U_{B\,Relative}$ (m/s)	7.36E-03	3.00E-03
$U_{B\,Stoke}$ (m/s)	5.61E-03	3.54E-03
Measured N_B (bubbles/mL)	1.13E+04	1.85E+04
Theoretical N_B (bubbles/mL)	1.33E+04	2.66E+04
Measured Φ_B (ppm)	6037	4962
Theoretical Φ_B (ppm)	7114	7114

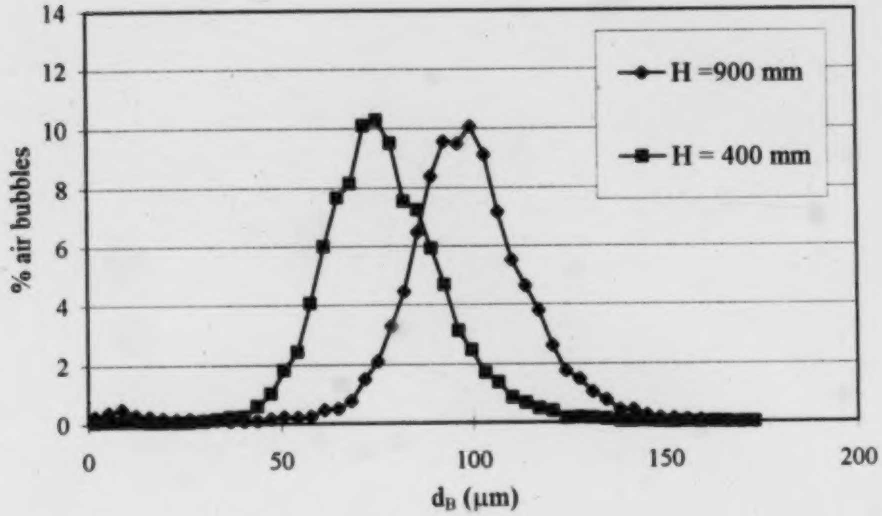

Figure 5.29 Effect of contact zone height on BSD at hydraulic loading rate = 50 m/h, R_R =10 %, P_{Sat} = 484 kPa, 20°C, $d_{Orifice}$ 1.03 mm and probe volume coordinates (900,0,25) and (400,0,25)

Table 5.25 **Effect of contact zone height and recycle ratio on bubble size, concentration and rise velocity for hydraulic loading rate = 70 m/h, 20°C, P_{Sat} = 484 kPa, d $_{Orifice}$ = 0.55 mm and probe volume coordinates (900,0,25) and (400,0,25)**

	$R_R = 3\ \%$		$R_R = 5\ \%$	
Contact zone height (mm)	900	400	900	400
d_B (μm)	66.0	54.8	64.5	54.1
σ_{dB}(μm)	22.7	20.7	18.0	18.6
$U_{B\ inst}$ (m/s)	2.48E-02	2.25E-02	2.39E-02	2.28E-02
U_{RMS} (m/s)	3.00E-03	6.90E-03	2.22E-03	5.97E-03
U_L (m/s)	2.13E-02	2.13E-02	2.22E-02	2.16E-02
$U_{B\ Relative}$ (m/s)	3.53E-03	1.20E-03	1.66E-03	1.24E-03
$U_{B\ Stoke}$ (m/s)	2.41E-03	1.66E-03	2.30E-03	1.62E-03
Measured N_B (bubbles/mL)	5.97E+03	6.21E+03	1.31E+04	1.45E+04
Theoretical N_B (bubbles/mL)	1.51E+04	2.65E+04	2.65E+04	4.50E+04
Measured Φ_B (ppm)	1560	1211	1841	1198
Theoretical Φ_B (ppm)	2279	2279	3727	3727

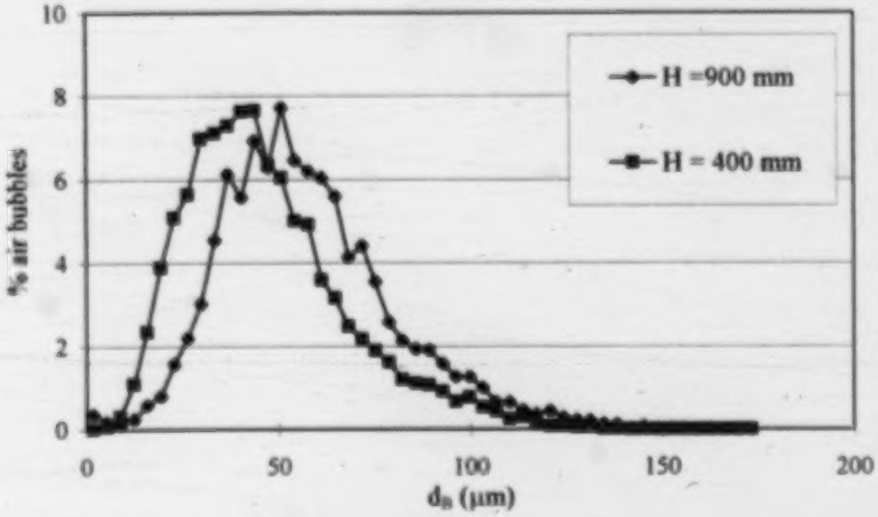

Figure 5.30 Effect of contact zone height on BSD for hydraulic loading rate = 70 m/h, R_R =3 %, P_{Sat} = 484 kPa, 20°C, $d_{Orifice}$ 0.55 mm and probe volume coordinates (900,0,25) and (400,0,25)

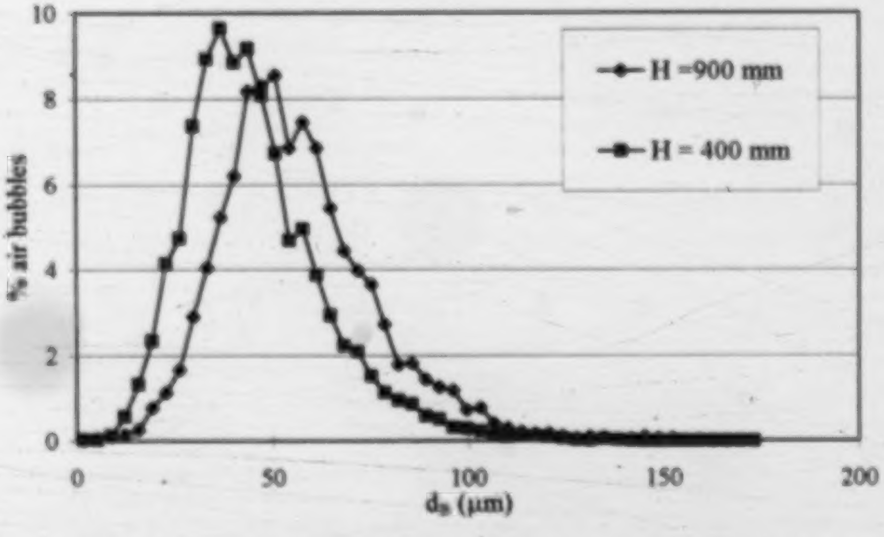

Figure 5.31 Effect of contact zone height on BSD for hydraulic loading rate = 70 m/h, R_R =5 %, P_{Sat} = 484 kPa, 20°C, $d_{Orifice}$ 0.55 mm and probe volume coordinates (900,0,25) and (400,0,25)

using larger nozzle orifice diameter had a more significant effect on bubble size with change in the contact zone height. As the contact zone height increased, the hydrostatic pressure decreased resulting in bubbles with larger d_B. However, calculations showed that the effect of the hydrostatic pressure on bubble size was insignificant. Also, bubbles coalesced as they rose inside the contact zone column and as a result bubbles with larger mean volume were produced. As a result, the bubble number concentration decreased while the bubble volume concentration increased. In addition, the mean instantaneous bubble rise velocity decreased as the contact zone height decreased.

5.2.3.6 Contact zone wall effect

These experiments were conducted for hydraulic loading rate of 70 m/h, R_R = 5 % and P_{Sat} = 484 kPa and using $d_{Orifice}$ = 0.55 mm. The measurements were taken at probe volume coordinates of (900,0,0), which represented the center of the column, (900,0,25) and (900,0,45), respectively.

The results of these experiments, summarized in Table 5.26, indicate that both mean $U_{B\ inst}$ and U_L decreased as the measurements were taken closer to the column's wall. In addition, the BSD curves, illustrated in Figure 5.32, showed that the measured mean d_B was almost the same for all probe volume coordinates. However, the measured bubble number concentration and the experimental bubble volume concentration increased slightly as the measurements were taken closer to the column's wall.

Table 5.26 Contact zone wall effects on bubble size, concentration and rise velocity for hydraulic loading rate = 70 m/h, R_R = 5 %, 20°C, $d_{Orifice}$ = 0.55 mm and P_{Sat} = 484 kPa

Probe volume coordinates (mm)	(900,0,0)	(900,0,25)	(900,0,45)
d_B (μm)	64.5	63.4	64.1
σ_{dB}(μm)	18.0	19.9	18.4
$U_{B\,inst}$ (m/s)	2.39E-02	2.44E-02	1.98E-02
U_{RMS} (m/s)	2.22E-03	2.58E-03	3.09E-03
U_L (m/s)	2.22E-02	2.18E-02	1.71E-02
$U_{B\,Relative}$ (m/s)	1.66E-03	2.56E-03	2.73E-03
$U_{B\,Stoke}$ (m/s)	2.30E-03	2.22E-03	2.27E-03
Measured N_B (bubbles/mL)	1.31E+04	1.41E+04	1.66E+04
Theoretical N_B (bubbles/mL)	2.65E+04	2.79E+04	2.70E+04
Measured Φ_B (ppm)	1841	1877	2297
Theoretical Φ_B (ppm)	3727	3727	3727

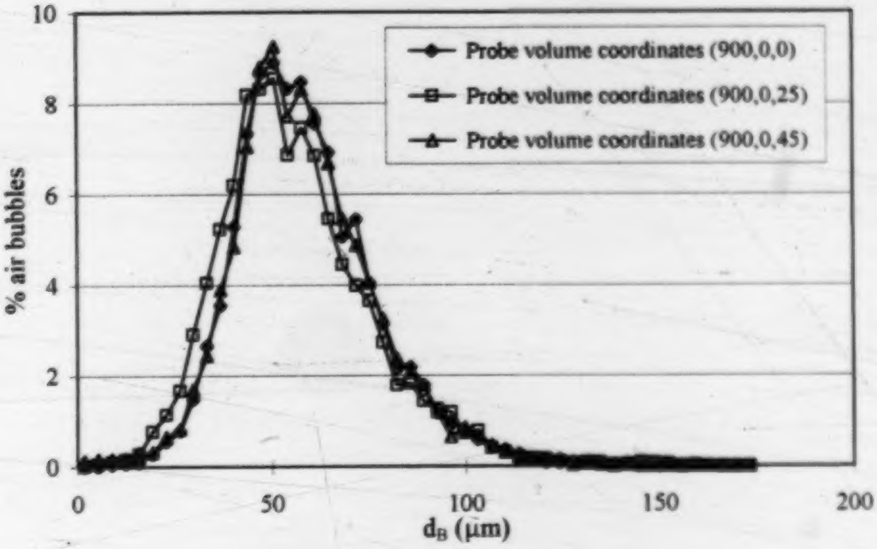

Figure 5.32 contact zone wall effect on BSD for hydraulic loading rate = 70 m/h, R_R =5 %, P_{Sat} = 484 kPa, 20°C and $d_{Orifice}$ = 0.55 mm

5.3 DAF Kinetic Studies

DAF kinetic experiments were performed on synthetic water spiked with algae as described in Section 4.4. In this section, the results of the optimum coagulant dose experiments, the effect of different operational conditions, on DAF performance, and the results of the overall DAF removal efficiency, R_{DAF}, and contact zone removal efficiency, R_{CZ}, at different operational conditions are presented.

5.3.1 Optimum coagulant dose

The optimum dose of the PACl was determined by using the bench-scale DAF unit and by following the procedures outlined in Section 4.4. The optimum dose was determined based on treated water turbidity of 0.1 NTU or lower and on the lowest number concentration of particles, i.e. highest particle log reduction. In these experiments, the PACl dose was varied from 0.5 to 5.0 mg/L as aluminum and there was no pH adjustment after the addition of the coagulant to the synthetic water. These experiments had to be performed in three different runs in order to locate the optimum dose.

The results of these experiments, which are summarized in Table 5.27, indicated that the optimum PACl dose was in the range of 2.9 to 3.14 mg/L as aluminum. At that dose, treated water turbidity was 0.09 NTU, a reduction of almost 92 %. Also, the number concentration of the particles in the treated water was 458 particles/mL, a reduction of 99.5 % or 2.3 log reduction. These results are also illustrated in the percentage reduction bar graphs shown in Figure 5.33.

Table 5.27 Optimum coagulant dose experimental results

	Experiment I				Experiment II				Experiment III			
	Jar#1	Jar#2	Jar#3	Jar#4	Jar#1	Jar#2	Jar#3	Jar#4	Jar#1	Jar#2	Jar#3	Jar#4
PACl dose (mg/L)	0	0.50	1.00	1.50	0	2.00	2.50	3.00	0	3.25	3.75	5.00
PACl Stock concentration (mg/L)	0	774	774	774	0	774	774	7740	0	7740	7740	7740
PACl volume (mL)	0	520	1035	1550	0	1810	1940	310	0	336	388	520
pH (before adding PACl)	7.88	7.88	7.88	7.88	7.89	7.93	7.91	7.95	8.01	7.97	7.97	7.97
pH (after adding PACl)	7.88	7.68	7.60	7.55	7.86	7.52	7.41	7.52	8.05	7.51	7.43	7.36
Raw water turbidity (NTU)	1.0	1.0	1.0	1.0	1.0	1.0	1.0	1.1	1.1	1.1	1.1	1.1
Treated water turbidity (NTU)	0.80	0.91	0.23	0.21	0.9	0.18	0.12	0.09	0.8	0.16	0.19	0.22
Initial particle concentration(#/mL	90718	90718	90718	90718	91658	91658	91658	91658	92063	92063	92063	92063
Final particle concentration(#/mL)	88450	84459	4808	1724	89658	1650	1100	458	89853	644	921	1197
Turbidity % removal	20	9	77	79	10	82	88	92	27	85	83	80
Particle concentration % removal	2.5	6.9	94.7	98.1	2.2	98.2	98.8	99.5	2.4	99.3	99.0	98.7
Particles log reduction	0.0	0.0	1.3	1.7	0.0	1.7	1.9	2.3	0.0	2.2	2.0	1.9

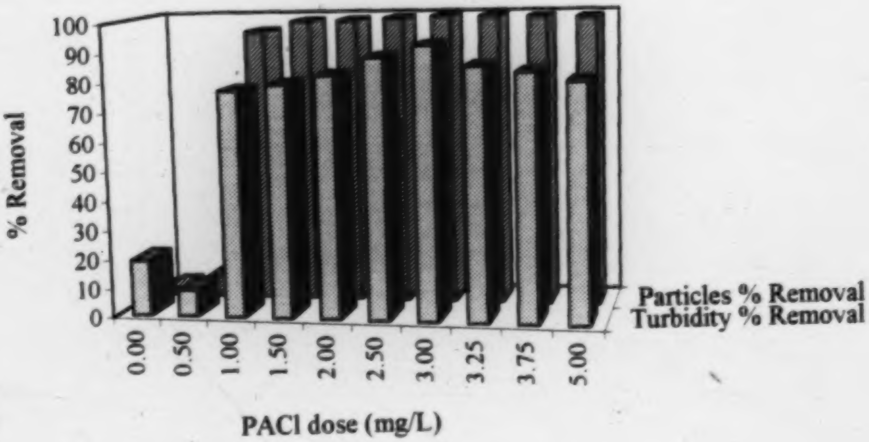

Figure 5.33 Turbidity and particles removal efficiency as a function of PACl dose

5.3.2 DAF Removal Efficiency

To determine the effect of different operating parameters on DAF removal efficiency, a 2^2 factorial design was employed in the pilot-scale experiments. Two levels of the independent variables: hydraulic loading rate and recycle ratio were studied simultaneously. Two 2^2 factorial designs were performed at two different nozzle orifice diameters. This arrangement was necessary to cover all possible hydraulic loading rates and recycle ratios in this study. The dependent or performance variable used to assess the effect of the independent variables was the overall percentage of DAF particle removal efficiency, R_{DAF}.

The overall percentage of DAF removal efficiency was calculated by summing $R_{DAF\,i}$ for particles of size, d_{Pi}, for the applied particle size range measured by the particle counter. The R_{DAF} was calculated by using the following formula:

$$R_{DAF} = \sum_{i=1}^{i=n} R_{DAFi} \times 100\% = \left\{1 - \sum_{i=1}^{i=n} \left(\frac{N_{DAFe}}{N_{CZo}}\right)_i \right\} \times 100\ \% \qquad (5.1)$$

Experiments in each factorial design were replicated by measuring the R_{DAF} at hydraulic loading rate and recycle ratio which corresponded to the midpoint of the two levels. These replicates were used to calculate the mean square error that was used in the analysis of variance, ANOVA. Table 5.28 summarizes the experimental arrangements for the pilot-scale DAF kinetic study.

The experimental results for the overall removal, R_{DAF}, are summarized in descending order in Figure 5.34. The highest R_{DAF} was achieved at a hydraulic loading of 90 m/h, R_R = 7 % and $d_{Orifice}$ = 1.03 mm, where about 76 % overall removal efficiency was achieved. On the other hand, when operating the DAF at a hydraulic loading rate of 30 m/h, R_R = 3 % and $d_{Orifice}$ = 0.55 mm, only 32 % of particle removal efficiency was

Table 5.28 Experimental arrangments for the pilot-scale DAF kinetic study

Factorial Design	$d_{Orifice}$ (mm)	Factor	Level Studied		
			Low	Midpoint	High
I	0.55	Hydraulic loading rate (m/h)	30	50	70
		Recycle ratio (%)	3	5	7
II	1.03	Hydraulic loading rate (m/h)	70	80	90
		Recycle ratio (%)	3	5	7

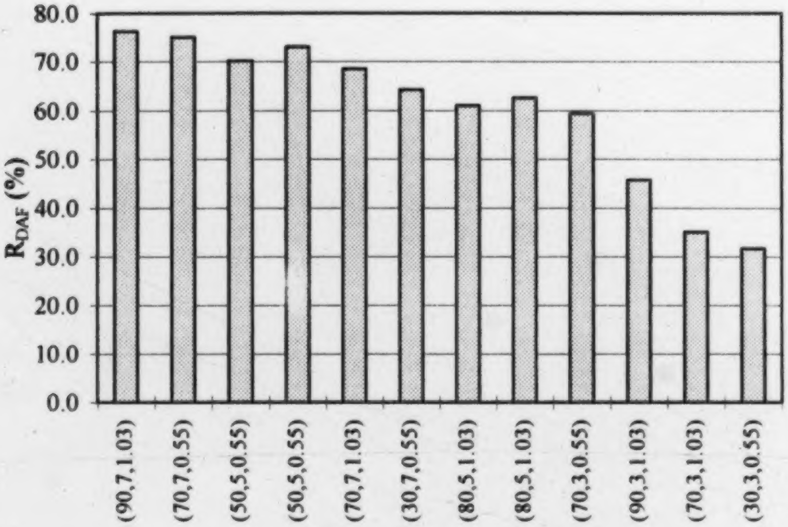

Figure 5.34 R_{DAF} removal efficinecy results for different hydraulic loading rates, recycle ratios and nozzle orifice diameters. Note: the values between the brackets represent hydraulic loading rate, R_R and $d_{Orifice}$, respectively

achieved. Experiments replicated at hydraulic loading rate of 50 m/h, $R_R = 5$ % and $d_{Orifice} = 0.55$ mm and at hydraulic loading rate of 80 m/h, $R_R = 5$ % and $d_{Orifice} = 1.03$ mm showed little variations in the results.

The values of R_{DAF} were calculated based on Equation 5.1. This required the measurement of the cumulative particle counts and the PSD for both the flocculated water and DAF effluent water. Table 5.29 summarizes the results of PSD analysis and R_{DAF} calculations for hydraulic loading of 90 m/h, $R_R = 7$ % and $d_{Orifice} = 1.03$ mm. One can notice the much higher particle numbers for the 1 to 150 μm size range, when compared to 2 to 150 μm size range, which indicate a large number of particles between 1 and 2 μm. In practice, most particle counting is performed with instruments that detect particles of 2 μm and larger; therefore, cumulative particle count will be based on particle size range 2 to 150 μm.

The effect of different operational conditions on DAF performance can be examined better using the PSD plots. The PSD data are presented using the number distribution function, which is one type of a normalized absolute PSD plot based on Standard Method number 2560 (APHA, AWWA and WEF, 1992). The number distribution is formed by plotting ΔN_i divided by $\Delta \log d_{Pi}$ versus $\log d_{Pi}$ in which ΔN_i is the particle count per milliliter in channel i, d_{Pi} is the average particle size for channel i and $\Delta \log d_{Pi} = \log d_{Pi+1} - \log d_{Pi}$ is the width of the size channel. This type of distribution usually illustrates the presence of more numerous smaller particles. The area under the PSD curve represents the total number of particles between any two sizes.

Figure 5.35 shows PSD, based on number distribution, for raw water (synthetic water with algae), flocculated water and DAF effluent water for hydraulic loading rate of 90 m/h, $R_R = 7$ % and $d_{Orifice} = 1.03$ mm. The PSD plot shows that floc particles were generally small, on a number basis. The particles were mostly smaller than 12 μm. Also, it shows that the number concentration of raw water particles increased after the addition of 3 mg/L of PACl followed by 5 minutes of flocculation.

Table 5.29 Particle size distribution analysis (PSD) for the pilot-scale kinetic study for the following operational conditions: hydraulic loading = 90 m/h, R_R = 7% and $d_{Orifice}$ = 1.03 mm.

i	d_{pi} (μm)	ΔLog d_{Pi} (μm)	$\Delta N_{Raw,i}$ * (particle/mL	$\Delta N_{Raw\,i} / \Delta \log d_{Pi}$ (particle/mL.μm)	$\Delta N_{CZ\,o,i}$ (particle/mL)	$\Delta N_{CZ\,o,i} / \Delta \log d_{Pi}$ (particle/mL.μm)	$\Delta N_{DAF\,e,i}$ (particle/mL)	$\Delta N_{DAF\,e,i} / \Delta \log d_{Pi}$ (particle/mL.μm)
1	1.5	0.30	91325	303375	48263	160326	30245	100472
2	2.5	0.18	4256	24169	4879	27707	1782	10120
3	4.0	0.22	2154	9709	3526	15894	504	2272
4	6.0	0.15	758	5187	1853	12681	251	1718
5	8.5	0.15	253	1633	658	4248	80	516
6	12.0	0.15	53	363	521	3565	79	541
7	17.0	0.15	12	77	56	362	26	168
8	85.0	0.88	1	1	5	6	3	3
$\Sigma \Delta N_i$ for d_{Pi} 1 to150 μm =			98812		59761		32970	
$\Sigma \Delta N_i$ for d_{Pi} 2 to150 μm =			7487		11498		2725	
R_{DAF} (%) =			76.3					

* $\Delta N_{RAW,i}$ is the particle count per milliliter for synthetic water with algae

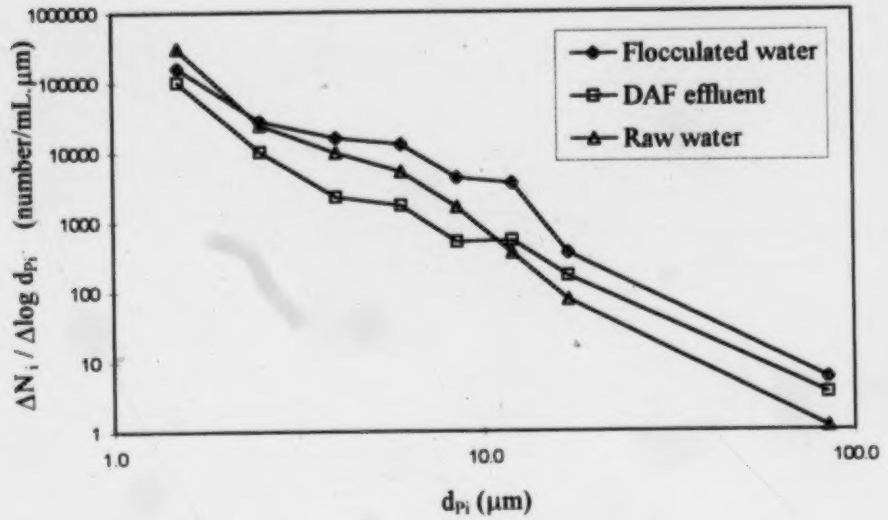

Figure 5.35 Particle size number distribution for pilot-scale kinetic study for the following operational conditions: hydraulic loading rate = 90 m/h, R_R = 7 % and $d_{Orifice}$ = 1.03 mm

DAF effluent particle counts, based on 2 to 150 μm size range, were generally between 2000 to 4000 particles/mL. The lowest DAF removal efficiencies occurred for particles lower than 2 μm in size while the highest was achieved for particles with d_{Pi} ranging from 4 to 12 μm. This is clearly illustrated in Figure 5.36 which shows R_{DAFi} for particle size, d_{Pi}, for hydraulic loading rate of 90 m/h, $R_R = 7$ % and $d_{Orifice} = 1.03$ mm. This finding is in agreement with the SCE model where total removal efficiency is proportional to d_P^2 for interception. Figure 5.36 also shows that R_{DAFi} for particles of size, d_{Pi}, larger than 12 μm decreased. That may be due to fewer particles of these sizes entering the DAF contact zone.

The direct effects of each independent variable, i.e. hydraulic loading rate and R_R, on each dependent variable, i.e. R_{DAF}, as well as the effects of two and three-way interactions were examined using ANOVA. The data collected in the 2^2 factorial experimental design were described by the following linear fixed effect ANOVA model:

$$Y_{ij} = \mu_\alpha + \alpha_i + \beta_j + (\alpha\beta)_{ij} + \varepsilon_{ij} \tag{5.2}$$

where Y_{ij} is the measured dependent variable, i.e. the overall percentage of DAF particle removal efficiency, R_{DAF}, μ_α is the overall average effect, α_i is the effect of the i^{th} level of the first independent variable or factor, i.e. hydraulic loading rate, β_j is the effect of the j^{th} level of the second treatment variable, i.e. the recycle ratio. The model also includes two-way interactions, $\alpha\beta_{ij}$, and also the random error of the experiment, ε_{ij}, which consists of the pure errors, PE, and the lack of fit errors, LOF.

Since all factors in the model were fixed, the ANOVA could be used to test hypotheses for each main effect and interaction by conducting test statistics. The hypothesis tested for main treatment effects were of the form:

Ho: $\alpha_1 = \alpha_2$ (Null hypothesis, effects are insignificant)

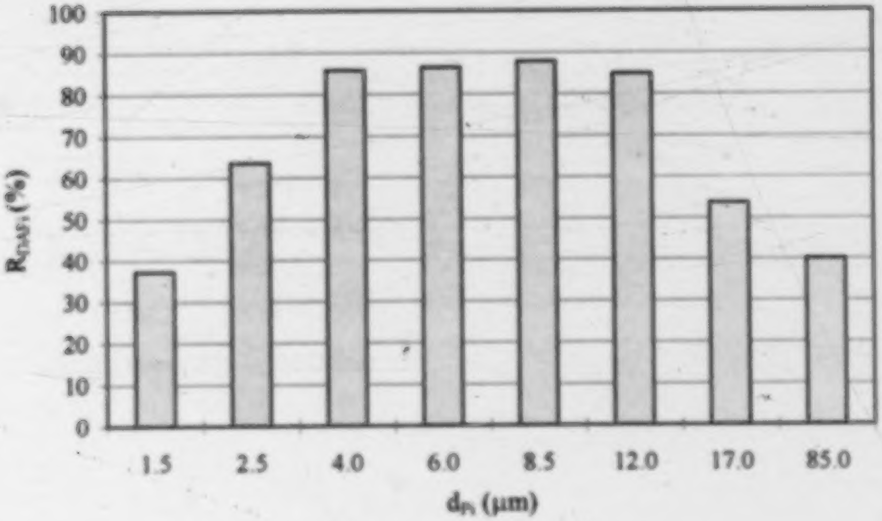

Figure 5.36 Particle removal efficiency $R_{DAF,i}$ for $d_{P,i}$ for the following operational conditions: hydraulic loading rate = 90 m/h, R_R = 7 % and $d_{Orifice}$ = 1.03 mm

H1: $\alpha_1 \neq \alpha_2$ (Alternative hypothesis, significant effect)

where α_1 and α_2 represent the two levels of the first treatment, e.g. hydraulic loading 30 and 50 m/h, respectively. The same hypotheses were used to test the two -way interactions. The test statistics for each main effect and interactions were developed by dividing the corresponding mean square by an estimate of the mean square error. The resulting statistical F-tests were upper-tail, one-sided test where the number of degrees of freedom for any effect,v_1, was equal to one. The mean square error, which had three degrees of freedom, v_2, was estimated from the replicated experiments. The main effects and interactions were considered significant if the calculated ratio of mean square by mean square error, F_o, was larger than the F-value calculated from the F-distribution curves with v_1 and v_2 degree of freedom at the 2 % level of significance.

Table 5.30 summarizes the ANOVA results for the pilot-scale DAF kinetic study using $d_{Orifice} = 0.55$ mm. The results indicate that both the main effect variables and interactions were significant at 2 % level of significance. Increasing the hydraulic loading rate from 30 to 70 m/h resulted in a 24 % increase in particle removal efficiency. Also, increasing the recycle ratio from 3 to 7 % increased the particle removal efficiency by about 20 %.

Similar ANOVA analyses were performed in the pilot-scale DAF kinetic study using $d_{Orifice} = 1.03$ mm. The results, which are summarized in Table 5.31, indicate that both the main effect variables and interactions were significant at the 2 % level of significance. Increasing the hydraulic loading rate from 70 to 90 m/h resulted in a 32 % increase in particle removal efficiency. Also, increasing the recycle ratio from 3 to 7 % increased the particle removal efficiency by about 10 %.

One of the main objectives of the kinetic study was to determine, experimentally, the contact zone removal efficiency, R_{CZ}, for different hydraulic loading rates and recycle

Table 5.30 ANOVA results for pilot-scale DAF kinetic study using $d_{Orifice} = 0.55$ mm

Source *	Sum of Squares (SS)	Degrees of Freedom		Mean Square (MS)	F_o #
μ_a	1325	1		1325	-
A	4747	1		4747	53
B	4096	1		4096	46
AB	6368	1		6368	71
PE =	179	1		179	-
LOF "	88	2		44	-
ε	267	3	MS_E	89	-
Total	16536	3		-	-

* μ_a represents overall average effect, A represents effect of α, B represents effect of β and AB represents effect of αβ

# F_o was calculated by dividing MS for each effect by mean square of error MS_E

= PE is the experimental pure errors

" LOF is the experimental lack of fit

Table 5.31 ANOVA results for pilot-scale DAF kinetic study using $d_{Orifice} = 1.03$ mm

Source	Sum of Squares (SS)	Degrees of Freedom		Mean Square (MS)	F_o
μ_o	1225	1		1225	-
A	4942	1		4942	371
B	2247	1		2247	169
AB	6099	1		6099	457
PE	27	1		27	-
LOF	13	2		6	-
ε	40	3	MS_E	13	-
Total	14513	3		-	-

ratios. This measurement can be used to estimate the experimental particle removal rate constant, k_P, using Equation 3.51.

As was explained earlier, there is a critical bubble-particle agglomerate diameter $d_{PBi\ Critical}$ for particle size, d_{Pi}, that enters the bottom of the DAF separation tank where $U_{PBi\ aggl} = U_{OS}$. Agglomerates having d_{PBi} larger than $d_{PBi\ Critical}$ would have higher $U_{PBi\ aggl}$ than U_{OS} and therefore will be separated from the effluent. On the other hand, agglomerates with $d_{PBi} < d_{PBi\ Critical}$ would be conveyed with the effluent together with those particles that are free of attached bubbles.

Therefore, by calculating d_{PBi} for each particle size d_{Pi}, one could determine the number concentration of the fraction of particles that would be separated and the number concentration of the fraction of particles that would conveyed with the effluent. To simplify, the particle mass balance diagram for the DAF contact and the separation zones, shown in Figure 5.37, will be used to calculate R_{CZ} .

In Figure 5.37, both particles free of attached bubbles, represented by number concentration of $N_{CZ\ e,j}$, and particles attached to air bubbles, represented by number concentration of $(N_{CZ\ o,j} - N_{CZ\ e,j})$, enter the bottom of the DAF separation zone. In this study, the number of attached air bubbles n_B was assumed to be one. This is based on the fact that the mean d_B was larger than the mean d_P for the PSD.

Bubble-particle agglomerates with $d_{PBi} > d_{PBi\ Critical}$ will be separated and collected on the top of the DAF separation tank forming the sludge layer. The particle number concentration of this fraction would be $(N_{CZ\ o,j} - N_{CZ\ e,j})_2$ for agglomerates with d_{PBi} larger than $d_{PBi\ Critical}$.

On the other hand, bubble-particle agglomerates with $d_{PBi} < d_{PBi\ Critical}$, which have number concentration of $(N_{CZ\ o,j} - N_{CZ\ e,j})_1$, will be conveyed with the effluent in addition to those particles with no attached bubbles. Therefore, the particle number concentration

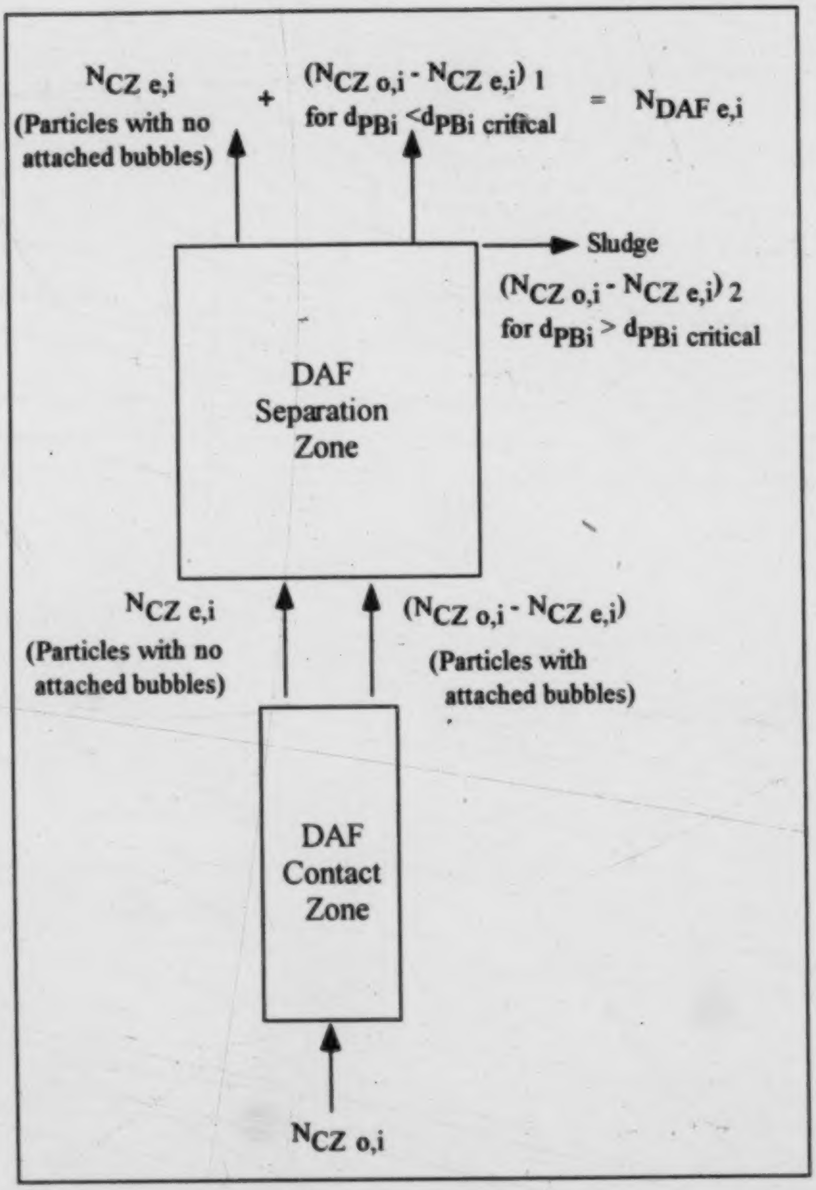
$N_{CZ\ e,i}$
(Particles with no attached bubbles)
+
$(N_{CZ\ o,i} - N_{CZ\ e,i})_1$
for $d_{PBi} < d_{PBi\ critical}$
= $N_{DAF\ e,i}$
Sludge
$(N_{CZ\ o,i} - N_{CZ\ e,i})_2$
for $d_{PBi} > d_{PBi\ critical}$
DAF Separation Zone
$N_{CZ\ e,i}$
(Particles with no attached bubbles)
$(N_{CZ\ o,i} - N_{CZ\ e,i})$
(Particles with attached bubbles)
DAF Contact Zone
$N_{CZ\ o,i}$

Figure 5.37 Hypothetical particle mass balance for contact and separation zones of the DAF process

of the DAF effluent $N_{DAF\ e,i}$ would be $N_{CZ\ e,i} + (N_{CZ\ o,i} - N_{CZ\ e,i})_1$ for agglomerates with d_{PBi} smaller than $d_{PBi\ Critical}$.

In order to calculate the overall percentage of the contact zone removal efficiency, R_{CZ}, based on Equation 3.41, the particle number concentration, $N_{CZ\ e,i}$, for particle size, d_{Pi}, has to be estimated. This was achieved by comparing d_{PBi} with $d_{PBi\ Critical}$ for each particle size, d_{Pi}, and calculating the fraction of $(N_{CZ\ o,i} - N_{CZ\ e,i})$ with $d_{PBi} < d_{PBi\ Critical}$. This is shown in Table 5.32, which summarizes the contact zone removal efficiency calculations for hydraulic loading rate = 90 m/h, R_R = 7% and $d_{Orifice}$ = 1.03 mm. As shown in Table 5.32, when $d_{PBi} < d_{PBi\ Critical}$ for particle size, d_{Pi}, the fraction of $(N_{CZ\ o,i} - N_{CZ\ e,i})_1$ is equal to 50% of the $N_{DAF\ e,i}$. This was based on the assumption that α_{PB} was equal to 0.5, i.e. 50% of the particles in the effluent are not attached to bubbles and the remaining 50% are conveyed with the effluent because they have $U_{PBi\ aggl}$ lower than U_{OS}. Table 5.33 summarizes the R_{CZ} results for all operational conditions investigated in this part of the study.

Table 5.32 Contact zone removal efficiency calculations for hydraulic loading 90 m/h, $R_R = 7$ % and $d_{Orifice} = 1.03$ mm. The limiting overflow rate of the DAF separation zone U_{OS} is 5.6 m/h.

i	d_{pi} µm	$\Delta N_{CZ\,o,i}$ number/mL	$\Delta N_{DAF\,e,i}$ number/mL	ρ_{PBi} g/mL	d_{PBi} µm	$U_{PBi\,aggl}$ m/h	Re_{PBi}	$d_{PBi\,critical}$* µm	$(\Delta N_{CZo,i} - \Delta N_{CZe,i})$ for $d_{PiB} < d_{PiB\,critical}$	$\Delta N_{CZ\,e,i}$ number/mL	$R_{CZ\,i}$ (%)
1	1.5	48263	30245	0.0012	67.0	8.9	0.0002	52.4	0	30245	37.3
2	2.5	4879	1782	0.0012	67.0	8.9	0.0002	52.4	0	1782	63.5
3	4.0	3526	504	0.0014	67.0	8.9	0.0002	52.4	0	504	85.7
4	6.0	1853	251	0.0019	67.0	8.9	0.0003	52.4	0	251	86.5
5	8.5	658	80	0.0032	67.0	8.9	0.0005	52.4	0	80	87.8
6	12.0	521	79	0.0069	67.1	8.9	0.0011	52.5	0	79	84.8
7	17.0	56	26	0.0174	67.4	8.9	0.0029	52.8	0	26	53.6
8	85.0	5	3	0.6784	97.1	6.0	0.1092	92.5	0	3	40.0
$\Sigma \Delta N_i$ for d_{Pi} 2 to150 µm =		11498	2725						0	2725	
	R_{CZ} (%) =	76.3									

---

* $d_{PBi\,critical}$ was calculated based on Equation 2.28 for $Re_{PBi} < 1$ and equation 2.29 for $1 < Re_{PBi} < 50$ assuming one bubble attached to particle of size d_{Pi}, i.e. $n_B = 1$.

Table 5.33 Summary of Contact zone removal efficiency results for DAF kinetic study

Hydraulic Loading rate (m/h)	R_R (%)	$d_{Orifice}$ (mm)	R_{CZ} (%)
90	7	1.03	76.3
70	7	0.55	75.1
50	5	0.55	70.2
50	5	0.55	73.1
70	7	1.03	68.5
30	7	0.55	64.2
80	5	1.03	61.0
80	5	1.03	62.5
70	3	0.55	59.3
90	3	1.03	45.6
70	3	1.03	35.0
30	3	0.55	31.7

CHAPTER 6

DISCUSSION OF RESULTS

The results presented in Chapter 5 are discussed in this chapter. Four subject areas will be discussed: (1) evaluation of DAF contact zone hydrodynamics; (2) evaluation of bubble size, concentration and velocity in DAF contact zone; (3) evaluation and discussion of particle removal efficiency for DAF contact zone with respect to the kinetic model; and (4) comparison of theoretical and experimental particle removal rate constants, k_P. The objective of this chapter is to incorporate the theoretical principles into the evaluation of the results and to identify the practical implications of the research data.

6.1 Hydrodynamic Characterization Study Results

In this research, it was important to characterize the hydrodynamics inside the contact zone, in terms of residence time and degree of mixing. Under actual operational conditions, the flow conditions inside the DAF contact zone are neither perfect plug flow nor completely mixed. Plug flow conditions are more efficient than completely mixed contact zone, in terms of particle removal, provided that first order kinetics applies and k_P and HRT are the same. In order to model the particle removal kinetics in the contact zone, the mean residence, t_m, has to be determined under different operational conditions. As expected, the results have shown that t_m was always larger than the HRT for all hydraulic loading rates investigated in this study.

The second important parameter needed for modeling the particle removal kinetics in the contact zone is the degree of mixing, or the Pe. The results in this study have confirmed that Pe was directly proportional to U_L and that the degree of mixing in the contact zone decreased as U_L increased.

In order to examine correlations between the variables t_m and U_L, and Pe and U_L, the simple linear regression one-parameter model was used. It can be written as:

$$y_u = \beta x_u + \varepsilon_u \qquad (6.1)$$

where y_u is the response variable, x_u is the fixed regressor variable, β is the slope of the best fitting line and ε_u is the random experimental error. The parameter β, termed regression coefficient, is unknown and is estimated by using the method of least squares. This method considers the best fitting model to be the one that comes closest to the data in the sense of minimizing the quantity:

$$S = \sum_{u=1}^{n} (y_u - \eta_u)^2 \qquad (6.2)$$

where S is the sum of squared discrepancies between the observed values y_u and the values given by the model $\eta_u = \beta x_u$. By substituting η_u in Equation 6.2, the best fitting straight line can be obtained by finding the value of β that would minimize:

$$S = S(\beta) = \sum_{u=1}^{n} (y_u - \beta x_u)^2 \qquad (6.3)$$

The resulting least squares regression equation must be evaluated to determine the significance of the regression. The approach used in this study was to calculate the coefficient of determination, r^2, using the statistical analysis program provided with Microsoft Excel software. The r^2 value is a measure of the fraction of the variation in y_u which can be attributed to a linear relationship with x_u. If r^2 is equals to 1.0 then 100 % of the variation in y_u can be explained by x_u and the linear regression is a good fit to the data. On the other hand, if r^2 equals to 0 then the variation in y_u is not explained by x_u and the linear regression is a poor fit to the data.

Correlation between contact zone mean residence time, t_m, and hydraulic loading rate, U_L, can be expressed in the following equation:

$$t_m = A\, U_L^{-1} \qquad (6.4)$$

where A is correlation parameter to be determined by regression analysis using the experimental results for different contact zone heights. Statistical analyses performed for top, middle and bottom ports data are summarized in Tables B1.5 to B1.7 in Appendices B1.

The following empirical equations were obtained for the contact zone top, middle and bottom ports, respectively:

$$t_m = 1.815\, U_L^{-1} \qquad (6.5)$$

$$t_m = 1.275\, U_L^{-1} \qquad (6.6)$$

$$t_m = 0.999\, U_L^{-1} \qquad (6.7)$$

The r^2 values were 0.986, 0.982 and 0.941 for top, middle and bottom ports, respectively, which indicate that the linear regression is a good fit to the experimental data.

The regression parameter, A, which represents the distance from the point of the tracer injection to the port where the measurements were taken, L, was close to the actual values. The actual distance from the point of the tracer injection to the top, middle and bottom ports were 1750, 1300 and 830 mm, respectively, while the regression parameter A for the top, middle and bottom ports were 1815, 1275 and 999 mm, respectively. Figure 6.1 shows a plot for the best fit of the experimental results for the correlation

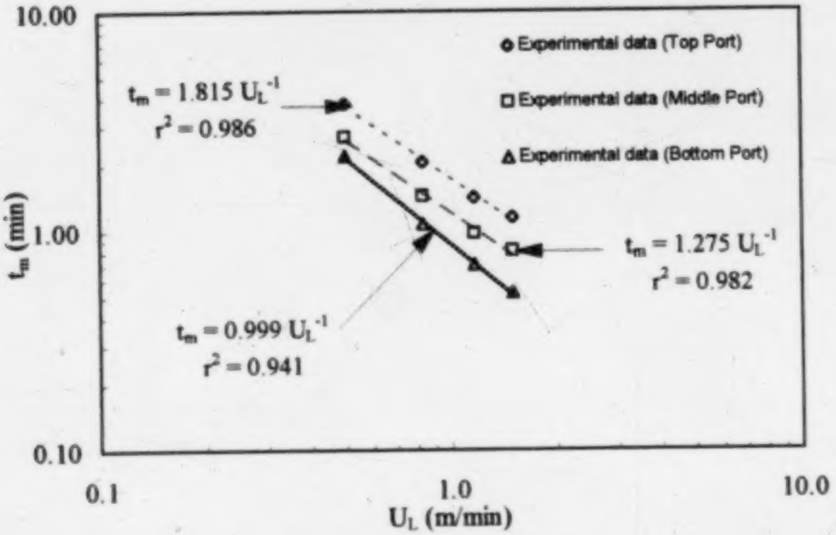

Figure 6.1 Plot of best fit of the experimental results for the correlation between t_m and U_L for contact zone top, middl and bottom ports, respectively.

between contact zone mean residence time and hydraulic loading rate for the top, middle and bottom ports, respectively.

Correlation between Pe and hydraulic loading rate, U_L, can be expressed in the following equation:

$$Pe = B\ U_L \tag{6.8}$$

were B is correlation parameter to be determined by regression analysis using the experimental results for different contact zone heights and recycle ratios. Statistical analyses performed for top, middle and bottom ports data and for different recycle ratios are summarized in Tables B1.8 to B1.16 in Appendix B1. The plots for the best fit of the experimental results for Pe as a function of U_L and R_R for the top, middle and bottom ports of the contact zone are shown in Figures 6.2 to 6.4.

The following empirical equations for contact zone top port and for different R_R were obtained:

$$Pe = 0.52\ U_L \qquad \text{for } R_R = 0\ \% \tag{6.9}$$

$$Pe = 0.47\ U_L \qquad \text{for } R_R = 5\ \% \tag{6.10}$$

$$Pe = 0.44\ UL \qquad \text{for } R_R = 10\ \% \tag{6.11}$$

The r^2 values were 0.863, 0.879 and 0.919 for R_R = 0 %, 5 % and 10 %, respectively, which indicate that the linear regression for the correlation between Pe and U_L for the contact zone top port is good fit to the experimental data.

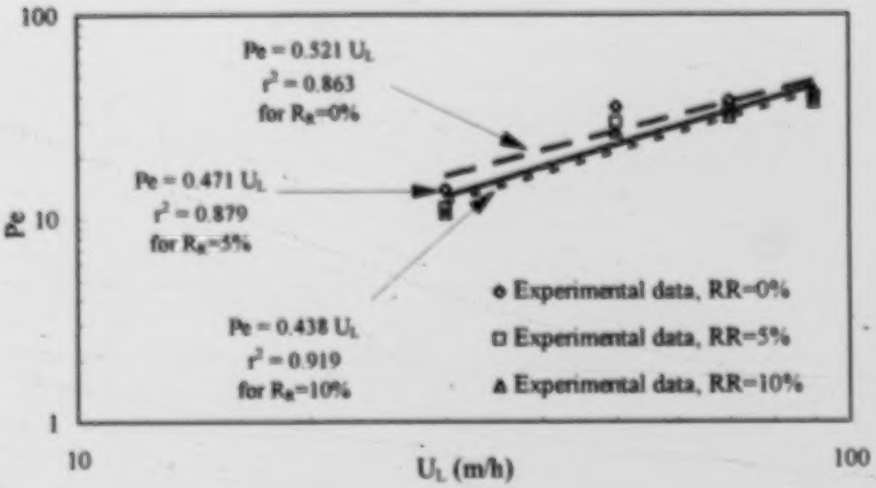

Figure 6.2 Plot for the best fit of the experimental results for the Pe and hydraulic loading rate correlation for contact zone top port and for different recycle ratios (Note: RR=R_R)

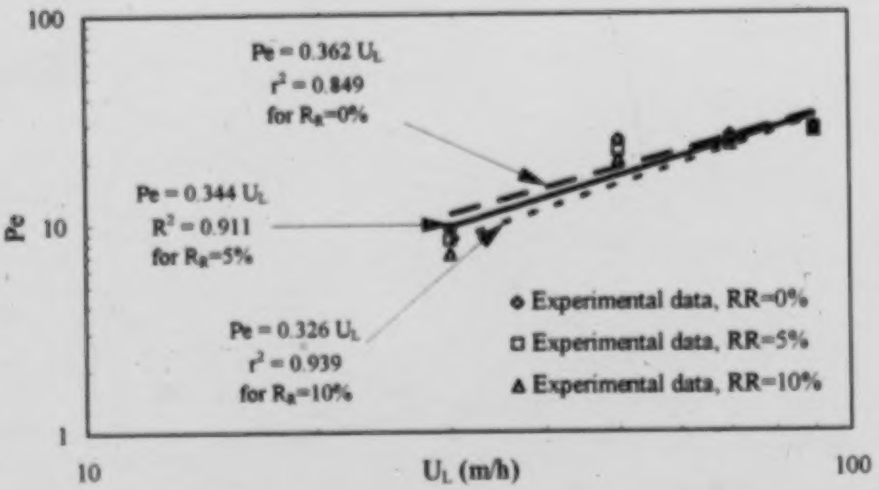

Figure 6.3 Plot for the best fit of the experimental results for the Pe and hydraulic loading rate correlation for contact zone middle port and for different recycle ratios (Note: $RR=R_R$)

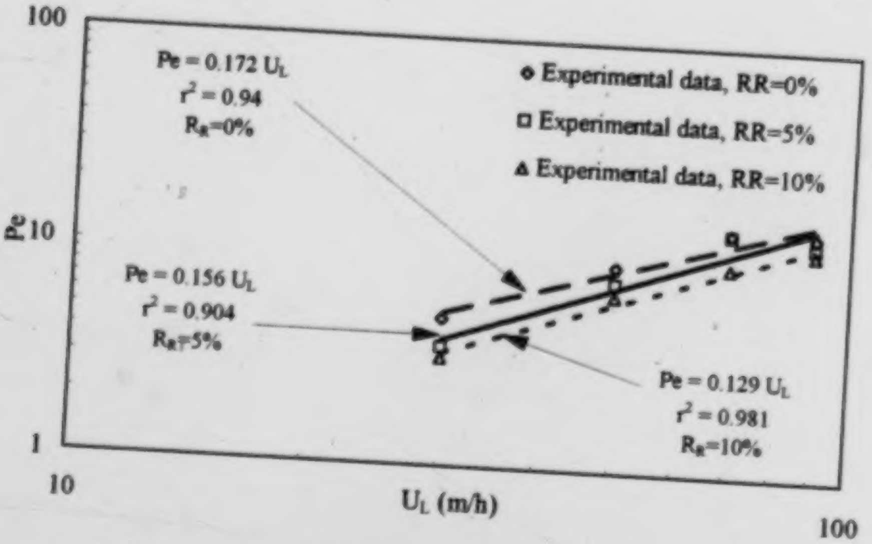

Figure 6.4 Plot for the best fit of the experimental results for the Pe and hydraulic loading rate correlation for contact zone bottom port and for different recycle ratios (Note: RR=R_R)

The theoretical relationship between Pe and U_L was presented in Equation 3.14. The regression parameter B in Equation 6.8 represents the ratio of the distance between the point of the tracer injection and the port where the measurements were taken, L, to the axial dispersion coefficient, D_a. The experimental results indicated that D_a, which was calculated by dividing L for each port by the regression parameter B, increased as the recycle ratio increased. The calculated D_a for the contact zone top port for different R_R are summarized in Table 6.1.

The resulting empirical equations for contact zone middle port for different R_R were as follow:

$$Pe = 0.36\ U_L \qquad \text{for } R_R = 0\ \% \qquad (6.12)$$

$$Pe = 0.34\ U_L \qquad \text{for } R_R = 5\ \% \qquad (6.13)$$

$$Pe = 0.33\ U_L \qquad \text{for } R_R = 10\ \% \qquad (6.14)$$

The r^2 values were 0.849, 0.911 and 0.939 for R_R = 0 %, 5 % and 10 %, respectively, which indicate that the linear regression for the correlation between Pe and U_L for the middle port is good fit to the experimental data.

The experimental results indicate that D_a values increased as R_R increased and also they were slightly higher than those calculated for the top port. The calculated D_a for the contact zone middle port for different R_R are summarized in Table 6.1.

The resulting empirical equations for contact zone bottom port for different R_R were as follow:

$$Pe = 0.17\ U_L \qquad \text{for } R_R = 0\ \% \qquad (6.15)$$

$$Pe = 0.16\ U_L \qquad \text{for } R_R = 5\ \% \qquad (6.16)$$

$$Pe = 0.13\ U_L \qquad \text{for } R_R = 10\ \% \qquad (6.17)$$

The r^2 values were 0.940, 0.904 and 0.981 for R_R = 0 %, 5 % and 10 %, respectively, which indicate good correlation between Pe and U_L for the bottom port.

The experimental results indicate that D_a values increased as the recycle ratio increased and also they were higher than those calculated for the top and the middle ports. The calculated D_a for the contact zone bottom port for different R_R are summarized in Table 6.1.

6.2 Bubble size, Concentration and Velocity Results

The results of this part of the study have provided important information regarding the size, concentration and rise velocity of air bubbles in the contact zone, which were measured simultaneously and under different operational conditions. These results were used to calculate the theoretical k_P based on Equation 3.37.

The results for superficial liquid velocity, bubble size, concentration and velocity, measured by the PDA, for different operational conditions are summarized in Table 6.2. These results show that the saturator pressure, recycle ratio, hydraulic loading rate , nozzle orifice diameter, and contact zone height have all affected contact zone model parameters, i.e. d_B, Φ_B, $U_{B\,inst}$ and U_L. Therefore, it is expected that they will also affect the DAF performance in terms of particles removal.

In general, the results show that d_B decreased as the contact zone hydraulic loading rate increased for experiments conducted at the same R_R, P_{Sat}, $d_{Orifice}$ and H_{CZ}. Also, d_B

Table 6.1 Effect of contact zone height and recycle ratio on contact zone axial dispersion coefficient D_a

Contact Zone Port	L^* (mm)	R_R (%)	Regression coefficient B	$Da^\#$ (m^2/h)
Top	1750	0	0.52	3.4
	1750	5	0.47	3.7
	1750	10	0.44	4.0
Middle	1300	0	0.36	3.6
	1300	5	0.34	3.8
	1300	10	0.33	3.9
Bottom	830	0	0.17	4.9
	830	5	0.16	5.2
	830	10	0.13	6.4

* L is actual the distance between the point of the tracer injection and the port where the measurements were taken

# D_a was calculated by dividing L by the regression parameter B

Table 6.2 Summary of results for superficial liquid velocity, bubble diameter, concentration and velocity measured by the PDA for different operational conditions

Hydraulic oading (m/h	R_R (%)	P_{Sat} (kPa)	$d_{Orifice}$ (mm)	(x,y,z) coordinates, mm	d_B (μm)	σ_{dB} (μm)	N_B (#/mL)	Φ_B ppm	$U_{B\,inst}$ (m/s)	U_{RMS} (m/s)	U_L (m/s)	$U_{B\,rel}$ (m/s)
90	7	484	1.03	(900,0,25)	67.1	19.8	1.3E+04	2239	2.84E-02	2.99E+03	2.55E-02	2.90E-03
90	5	484	1.03	(900,0,25)	68.2	22.5	1.0E+04	1721	2.94E-02	3.34E-03	2.55E-02	3.90E-03
90	3	484	0.55	(900,0,25)	56.7	19.2	6.9E+03	1432	2.74E-02	3.49E-03	2.55E-02	1.90E-03
90	3	484	1.03	(900,0,25)	74.4	27.1	6.8E+03	1468	2.99E-02	3.60E-03	2.55E-02	4.40E-03
70	7	484	1.03	(400,0,25)	63.6	19.0	1.6E+04	2087	2.43E-02	6.31E-03	2.13E-02	3.00E-03
70	7	484	1.03	(900,0,25)	81.9	18.9	1.4E+04	3927	2.51E-02	3.81E-03	2.18E-02	3.30E-03
70	5	345	0.55	(900,0,0)	63.0	21.9	5.4E+03	710	2.34E-02	2.20E-03	2.22E-02	1.20E-03
70	5	484	0.55	(900,0,0)	64.5	18.0	1.3E+04	1841	2.39E-02	2.22E-03	2.22E-02	1.70E-03
70	5	587	0.55	(900,0,0)	64.1	15.5	1.5E+04	2038	2.37E-02	3.25E-03	2.22E-02	1.50E-03
70	5	484	0.55	(400,0,0)	54.1	18.6	1.5E+04	1198	2.28E-02	5.97E-03	2.13E-02	1.50E-03
70	5	484	1.03	(400,0,0)	61.1	22.9	1.1E+04	1303	2.41E-02	7.90E-03	2.13E-02	2.80E-03
70	5	484	0.55	(900,0,25)	63.4	19.9	1.4E+04	1877	2.44E-02	2.58E-03	2.18E-02	2.60E-03
70	5	484	0.55	(900,0,45)	64.1	18.6	1.7E+04	2297	1.98E-02	3.09E-03	1.71E-02	2.70E-03
70	5	484	1.03	(900,0,0)	79.1	22.7	9.7E+03	2504	2.49E-02	2.69E-03	2.22E-02	2.70E-03
70	3	484	0.55	(400,0,25)	54.8	20.7	6.2E+03	1211	2.25E-02	6.90E-03	2.13E-02	1.20E-03
70	3	484	0.55	(900,0,25)	66.0	22.7	6.0E+03	1560	2.49E-02	3.00E-03	2.18E-02	3.10E-03

Table 6.2 (continued)

Hydraulic oading (m/h	R_R (%)	P_{Sat} (kPa)	$d_{Orifice}$ (mm)	(x,y,z) coordinates, mm	d_B (μm)	σ_{dB} (μm)	N_B (#/mL)	Φ_B ppm	$U_{B\,inst}$ (m/s)	U_{RMS} (m/s)	U_L (m/s)	$U_{B\,rel}$ (m/s)
50	10	484	1.03	(400,0,25)	80.0	16.0	1.9E+04	4962	1.92E-02	5.08E-03	1.62E-02	3.00E-03
50	10	484	1.03	(900,0,25)	100.7	21.0	1.1E+04	6037	2.44E-02	5.45E-03	1.65E-02	7.90E-03
50	7	484	0.55	(400,0,25)	52.7	11.9	2.4E+04	1810	1.72E-02	3.64E-03	1.62E-02	1.00E-03
50	7	484	0.55	(900,0,25)	63.3	12.6	1.7E+04	2898	1.84E-02	2.11E-03	1.65E-02	1.90E-03
50	7	484	1.03	(400,0,25)	70.1	21.6	1.1E+04	2025	1.81E-02	3.70E-03	1.62E-02	1.90E-03
50	5	484	0.55	(400,0,25)	54.1	17.1	1.5E+04	1260	1.76E-02	3.86E-03	1.62E-02	1.40E-03
50	5	484	0.55	(900,0,25)	68.8	19.1	1.1E+04	2056	1.93E-02	2.32E-03	1.65E-02	2.80E-03
30	10	484	0.55	(400,0,25)	64.2	11.0	2.2E+04	2979	1.32E-02	5.25E-03	1.07E-02	2.50E-03
30	10	484	0.55	(900,0,25)	73.7	14.1	1.8E+04	3748	1.40E-02	4.68E-03	1.05E-02	3.50E-03
30	7	484	0.55	(400,0,25)	65.4	12.3	1.4E+04	2108	1.35E-02	5.54E-03	1.07E-02	2.80E-03
30	7	484	0.55	(900,0,25)	85.5	15.4	1.0E+04	3405	1.42E-02	5.57E-03	1.05E-02	3.70E-03

decreased as the recycle ratio increased for all experiments performed at the same hydraulic loading rate, P_{Sat}, $d_{Orifice}$ and H_{CZ}. On the other hand, d_B increased as the nozzle orifice diameter increased for experiments conducted at the same hydraulic loading rate, R_R, P_{Sat}, and H_{CZ}.

The saturator pressure P_{Sat}, for the range investigated in this study, had no significant effect on d_B. Increasing P_{Sat} resulted in the production of higher percentage of bubbles with uniform size for all experiments performed at the same hydraulic loading rate, R_R, $d_{Orifice}$ and H_{CZ},. Also, bubbles with smaller d_B and uniform size distribution were produced as the R_R increased for the experiments conducted at the same hydraulic loading rate, P_{Sat}, $d_{Orifice}$ and H_{CZ}. In addition, using the nozzle with smaller $d_{Orifice}$ resulted in the formation of bubbles with uniform size distribution and smaller d_B.

Number concentrations of air bubbles N_B were measured directly using the PDA while the experimental bubble volume concentration Φ_B was calculated by multiplying the measured N_B values by the measured d_B values. Both N_B and Φ_B increased as a result of increasing P_{Sat} for all experiments performed at the same hydraulic loading rate, R_R, $d_{Orifice}$ and H_{CZ}. They also increased as a result of increasing the R_R for experiments conducted at the same hydraulic loading rate, P_{Sat}, $d_{Orifice}$ and H_{CZ}.

Contact zone wall effect has somewhat different effect on N_B and Φ_B. The results showed that both N_B and Φ_B increased when PDA measurements were taken closer to the column's wall for all experiments performed at the same hydraulic loading rate, R_R, H_{CZ}, $d_{Orifice}$ and P_{sat}. In addition, it was observed that for all N_B and Φ_B results, the theoretical calculations were always larger than the measured values.

The measured instantaneous bubble rise velocity decreased as a result of increasing R_R for experiments conducted at the same hydraulic loading rate, H_{CZ}, $d_{Orifice}$ and P_{sat}. On the other hand, increasing the contact zone hydraulic loading rate resulted in the increase of $U_{B\,inst}$ and U_L and the decrease of $U_{B\,rel}$ for experiments performed at the same R_R, H_{CZ}, $d_{Orifice}$ and P_{Sat}. In addition, using larger $d_{Orifice}$ resulted in an increase in both $U_{B\,inst}$ and $U_{B\,rel}$ for experiments performed at the same hydraulic loading rate, R_R, H_{CZ} and P_{Sat}.

One of the important correlations obtained in this study was between the relative bubble rise velocity $U_{B\,rel}$ and d_B. Theoretically, $U_{B\,Rel}$ is proportional to d_B^2 for spherical bubbles and under laminar flow conditions, i.e. $Re_B \leq 1$. Correlation between $U_{B\,Rel}$ and d_B can be expressed as follow:

$$U_{B\,rel} = C\, d_B^2 \tag{6.18}$$

where C is correlation parameter to be determined by regression analysis using the experimental results. Statistical analysis performed for all experimental data are summarized in Table B2.29 in Appendix B.2.

The following empirical equation for all the experimental data (n=27) was obtained:

$$U_{B\,Rel} = 5.93 \times 10^5\, d_B^2 \tag{6.19}$$

The r^2 value was 0.846, which indicate that the linear regression is relatively good fit to the experimental data. Figure 6.5 shows the line for the best fit of the experimental results for the correlation between bubble relative rise velocity and the mean diameter.

Also, correlation between bubble Reynolds number, Re_B, and bubble drag coefficient ,$C_{D\,B}$, was obtained in this study. The theoretical relationship between Re_B and $C_{D\,B}$ was defined in Equation 2.16 for spherical bubbles and for laminar flow conditions. Experimental Re_B and $C_{D\,B}$ were calculated using Equations 2.15 and 2.17 after substituting U_B with the $U_{B\,rel}$. Correlation between Re_B and $C_{D\,B}$ can be expressed as follow:

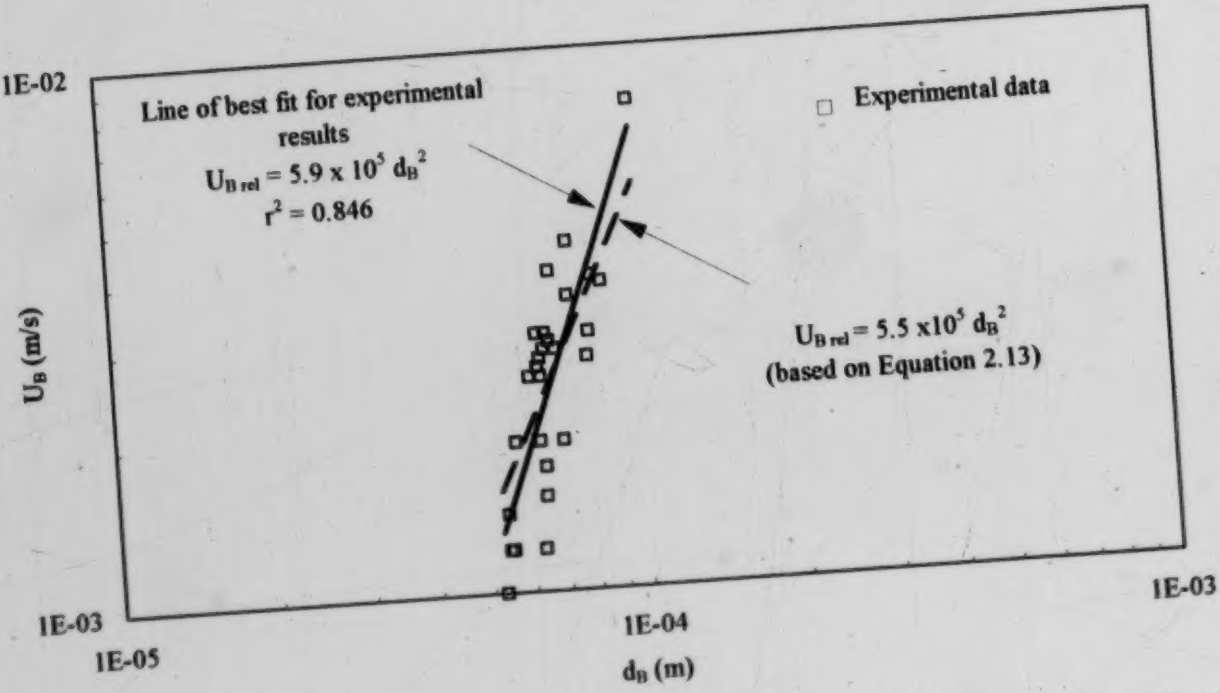

Figure 6.5 Plot for the best fit of the experimental results for the correlation between bubble relative rise velocity and the mean diameter for all data points (n=27)

$$C_{DB} = E\, Re_B^{-1} \tag{6.20}$$

where E is correlation parameter to be determined by regression analysis using the experimental results. Statistical analysis performed for all experimental data is summarized in Table B2.30 in Appendix B.2.

The following empirical equation for all the experimental data (n=27) was obtained:

$$C_{DB} = 31.4\, Re_B^{-1} \tag{6.21}$$

The r^2 value was 0.885, which indicates good correlation between C_{DB} and Re_B. Figure 6.6 shows the line for the best fit of the experimental results for the correlation between C_{DB} and Re_B.

6.3 Particle Removal Efficiency Results and Model Predictions

The results of DAF kinetic study using synthetic water are discussed and related to the theoretical DAF removal efficiency predicted by the contact zone kinetic model, Equation 3.39.

Experimental results showed that the optimum DAF removal efficiency was achieved when particles were destabilized at the optimum coagulant dosage predicted by the DAF bench-scale study. The results confirm the kinetic model predictions that the DAF performance depends on the collision efficiency factor α_{PB} and that particle-bubble attachment is favored under optimum coagulation conditions. The data generated by this study agree with results presented by Edzwald and Malley (1989) for coagulation and flotation of algae and by Valade et al. (1996) for dissolved air flotation of natural waters.

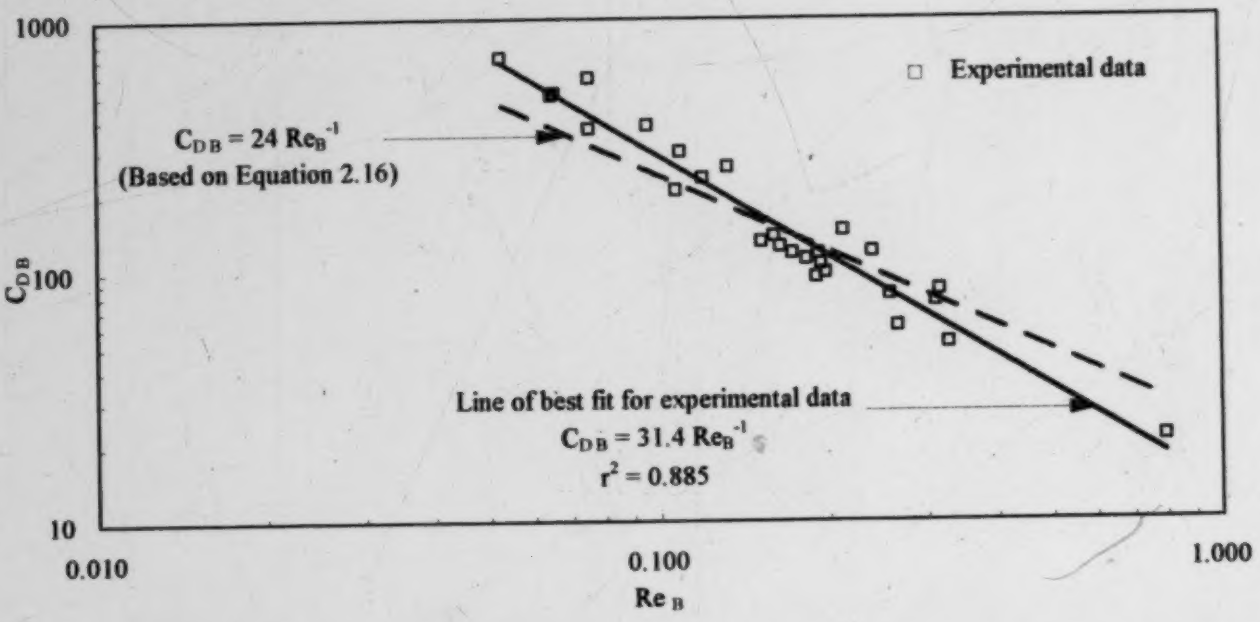

Figure 6.6 Plot for the best fit of the experimental results for the correlation between bubble drag coefficient and Re_B for all data points (n=27)

The pH conditions also affect α_{PB} and therefore the DAF performance; however, pH effect was not investigated in this study.

In this study, no attempt was made to measure α_{PB} experimentally. It was assumed that performing all kinetic experiments using the optimum coagulant dose would guarantee the maximum α_{PB} value. For the purpose of model predictions, α_{PB} value of 0.5 was assumed based on study performed by Edzwald (1993) on synthetic water spiked with algae.

The theoretical effect of floc particle size on DAF removal efficiency was presented in Equations 3.4 to 3.7 in the contact zone kinetic model. The theory suggests that floc particles of about 1 μm should be avoided. The model suggests that larger particles are transported more efficiently to the bubble surface. The model does not apply for particle sizes larger than 100 μm because detachment forces for large flocs on small bubbles must be considered.

Floc particles larger than 100 μm require larger number of bubbles to attach so that the bubble-particle agglomerate density is reduced. For these considerations, the model suggest the production of floc particles smaller than 100 μm before flotation. This could be achieved by using flocculation tanks ahead of the flotation unit which would have small detention times and high mixing conditions. Although flocculation of particles reduces their number concentration, N_P, which would reduce the collision rate between particles and bubbles, the particle diameters, d_P, increases. Since the overall particle removal efficiency predicted by the kinetic model depends on d_P^2, this would produce higher removal efficiencies for particles of 10's of micrometers.

The particle removal kinetic study was performed at the optimum coagulant dose following 5 minutes of flocculation at mixing intensity G of 70 s^{-1}. The flocculation intensity was based on many studies performed using different type of waters and coagulants. These studies showed that the optimum G value for DAF water treatment applications was in the range of 55 to 100 s^{-1}(Edzwald, 1995). The flocculation time was based on a recent study by Valade et al. (1996) which showed that DAF performance was almost the same after 5 and 20 minutes of flocculation despite the higher particle concentration with 5 minutes flocculation.

The results of this study showed that particle number concentration for the 1 to 150 µm size range was much higher than the 2 to 150 µm size range, as shown in Table 5.29. The difference between the two particle number concentration indicates that the largest fraction of the particles occurred between 1 and 2 µm. Also, it was noticed that N_P had increased from raw water to flocculated water due to the precipitation of $Al(OH)_3$ particles.

Comparison of N_P for both size ranges indicates that particles larger than 2 µm are removed more efficiently as compared to particles of 1 to 2 µm. This is illustrated in Figure 5.36 which indicates that the lowest removal efficiencies occurred for particles of approximately 1 µm as compared to larger particles in the 3 to 12 µm size range. This agrees with studies performed by other researchers (Valade et al., 1996) and also agrees with the contact zone kinetic model. The removal efficiency had decreased above 12 µm because fewer particles of these sizes entered the DAF contact zone.

The DAF removal efficiency based on the kinetic model presented in Equation 3.39 and the experimental R_{DAF} were compared for different operational conditions. Table 6.3 summarizes the results of the comparison, where α_{PB} was varied from 0.3 to 1.0. The results show that theoretical R_{DAF} were higher than the experimental R_{DAF} for α_{PB} value of 0.5 and higher for all operational conditions investigated. For lower α_{PB} values, the experimental R_{DAF} were higher than the theoretical values. The value of α_{PB} for which both theoretical and experimental R_{DAF} were equal was between 0.35 and 0.40. Since the experimental α_{PB} value for this study could not be determined, it is reasonable to assume that the α_{PB} range would be 0.35 to 0.40 for the system investigated in this study.

Table 6.3 Results of comparison between theoritical DAF removal efficiencies based on the contact zone kinetic model and experimental R_{DAF} for different operational conditions

Hydraulic loading (m/h)	R_R (%)	$d_{Orifice}$ (mm)	d_B (μm)	Φ_B (ppm)	Theoretical R_{DAF} (%) α_{PB} 0.3	0.5	1.0	Experimental R_{DAF} (%)
90	7	1.03	67.0	5120	71.9	87.9	98.5	76.3
70	7	0.55	63.0	3727	67.9	84.9	97.7	75.1
50	5	0.55	69.0	3727	60.8	79.0	95.6	73.1
70	7	1.03	82.0	5120	53.6	72.2	92.3	68.5
30	7	0.55	86.0	5120	52.3	70.9	91.5	64.2
70	3	0.55	66.0	2279	45.8	64.0	87.1	59.3
90	3	1.03	74.0	2279	35.2	51.4	76.4	45.6
70	3	1.03	83.4	2279	27.9	42.0	66.3	35.0
30	3	0.55	89.5	2279	25.5	38.8	62.5	31.7

6.4 Comparison of Theoretical and Experimental Removal Rate Constant

The main objective of the DAF kinetic study was to measure experimentally the overall particle removal rate constant and compare it with theoretical value, based on the derived kinetic model , under different operational conditions. This comparison should validate the kinetic model.

In order to perform the comparison, the contact zone removal efficiency R_{CZ} was first measured experimentally under different operational conditions. These results were summarized in Table 5.33. Later, the experimental k_P values were determined by trial and error using Equation 3.51, and the mean residence times and Pe were obtained from the hydrodynamic characterization study. At the same time, theoretical k_P values for different operational conditions were calculated using Equation 3.37.

Table 6.4 summarizes the results of the comparison between theoretical and experimental k_P values for different α_{PB} values under different operational conditions. The results show that the experimental k_P values were always higher than the theoretical values for α_{PB} of 0.35 and lower values. The highest experimental and theoretical k_P values were achieved for hydraulic loading rate of 90 m/h and R_R = 7 % while the lowest value was achieved for hydraulic loading rate of 30 m/h and R_R = 3 %. These results confirm that higher hydraulic loading rate and recycle ratios can improve DAF performance by increasing the particle removal rate constant.

Also, the results in Table 6.4 indicate that the nozzle orifice diameter had significant effect on DAF performance. Smaller $d_{Orifice}$ produced smaller bubbles and therefore increased the DAF particle removal efficiency as the contact zone kinetic model had predicted. When kinetic experiments were performed at hydraulic loading of 70 m/h and R_R = 7 %, the experimental k_P value for $d_{Orifice}$ = 0.55 mm was 0.965 min^{-1} while for $d_{Orifice}$ = 1.03 mm the k_P value was 0.796 min^{-1}.

The results of Table 6.4 show the importance of α_{PB} on predicting particles removal efficiency by DAF for different operational conditions. Since α_{PB} is determined empirically and it ranges from 0 to 1.0, with values closer to 1.0 for optimum coagulant dose and pH conditions, it is imperative that α_{PB} be determined experimentally.

Table 6.4 Results of comparison between theoritical overall particle removal rate constant based on the contact zone kinetic model and experimental k_P for different operational conditions

Hydraulic loading (m/h)	R_R (%)	$d_{Orifice}$ (mm)	d_B (μm)	Φ_B (ppm)	Pe	t_m (min)	R_{CZ}	Experimental k_P (min^{-1})	Theoretical k_P (min^{-1}) α_{PB}		
									0.30	0.35	0.40
90	7	1.03	67	5120	37	1.3	0.763	1.148	0.901	1.051	1.201
70	7	0.55	63	3727	32	1.5	0.751	0.965	0.617	0.720	0.823
50	5	0.55	69	2947	30	2.1	0.702	0.599	0.274	0.320	0.366
70	7	1.03	82	5120	32	1.5	0.685	0.796	0.398	0.464	0.530
30	7	0.55	86	5120	11	3.8	0.642	0.291	0.167	0.194	0.222
70	3	0.55	66	2279	35	1.5	0.593	0.614	0.330	0.385	0.440
90	3	1.03	74	2279	40	1.2	0.456	0.515	0.300	0.350	0.401
70	3	1.03	83.4	2279	35	1.5	0.350	0.291	0.169	0.197	0.225
30	3	0.55	89.5	2279	13	3.7	0.317	0.106	0.067	0.078	0.089

CHAPTER 7

CONCLUSIONS AND RECOMMENDATIONS

7.1 Limitations of the Study

As with any study, there are number of limitations which must be considered when using the result of this research. The following is a list of these limitations:

(1) The pilot-scale DAF process used in this research was designed with a mixing column which was attached to the DAF contact zone. The purpose of this column was to provide adequate mixing between the flocculated water and the super saturated water. Also, the mixing column served to separate the macro bubbles, i.e. $d_B > 150$ μm, from the micro bubbles. Larger bubbles had rise velocities larger than the hydraulic loading and therefore rose to the top of the mixing column. As a result, floc particles attached to those bubbles were separated from the bubble-particle suspension entering the DAF contact zone. Although the observed particles collected on the top of the mixing column were negligible, several attempts were made to measure the concentration of these particles. However, these attempts failed because of the difficulty encountered in the collection of these particles. Therefore, the concentration of the particles collected on the top of the mixing column was not included in the calculation of the contact zone removal efficiency.

(2) The measurements of bubble size, concentration and velocity was performed by using the particle dynamic analyzer, PDA. The PDA measurement required the presence of particles or seeds, in this case the air bubbles, in the water. Low concentration of air bubbles would compromise the PDA efficiency and would require a very long time to collect data. On the other hand, high concentration of bubbles would obscure the laser beam and no data could be collected. Therefore, in this research the measurement of

bubble size, concentration and velocity at recycle ratios R_R lower than 3% and higher than 10% could not be achieved.

(3) In this research, the saturator system used in pilot-scale DAF system was considered semi-continuous, i.e. continuous in compressed air and batch in water. This means that the saturator would have limited efficiency in terms of dissolving air in water and therefore would affect the bubble volume concentration.

7.2 Conclusions

In this research, a kinetic model for DAF contact zone has been developed based on the SCE model and flotation principles and fundamentals. The key model variables have been identified and their effect on DAF performance has been examined. Important model parameters, such as bubble number concentration, N_B, bubble mean diameter, d_B, the instantaneous bubble rise velocity, $U_{B\,inst}$, and the hydraulic loading rate, U_L, were measured simultaneously for different operational conditions. DAF kinetic studies using synthetic water spiked with algae were used, with the measured model parameters, to estimate the overall particle removal rate constant under different operational conditions. These were compared to the theoretical rate constant predicted by the kinetic model. The major findings of this research are as follow:

(1) A kinetic model for DAF contact zone based on the single collector efficiency, SCE, model was developed which was incorporated into a continuous flow DAF system. The model included parameters whidh describe bubble-particle transport and attachment efficiencies, particle size, bubble size and volume concentration, bubble rise velocity and contact zone hydraulic loading rate and height.

(2) Model simulation indicates that the DAF performance, in terms of particles removal efficiency, increases as the particle-bubble attachment efficiency, α_{PB}, increases. DAF kinetic study confirmed that α_{PB} was strongly dependent on the coagulant dosage.

The results showed that the highest DAF removal efficiency, and therefore α_{PB}, was achieved under optimum coagulation conditions which produced particles of little or no charge and relatively hydrophobic.

(3) The value of α_{PB} for the synthetic water system investigated in the DAF kinetic study was estimated by comparing the theoretical DAF removal efficiency, R_{DAF}, based on the kinetic model and the experimental R_{DAF} for different operational conditions. The kinetic study results indicated that the theoretical and experimental R_{DAF} were equal when α_{PB} was in the range of 0.35 to 0.40.

(4) Sensitivity analyses performed on the contact zone kinetic model indicated that particle removal improved sharply as the particle size, d_P, increased. This was confirmed by the kinetic study results which showed that the overall DAF removal efficiency increased as d_P increased from 2 μm to 12 μm. This is in agreement with the SCE model where the total single collector efficiency η_T is proportional to d_P^2 for particles larger than 1 μm.

(5) The DAF kinetic study results showed that the particle number concentration N_P following 5 minutes of flocculation with mixing at G value of 70 s^{-1} produced high fraction of particles between 1 and 2 μm. This may explain the low values of the experimental DAF removal efficiencies for all operational conditions investigated.

(6) Model simulation performed on the kinetic model indicated that the DAF particle removal efficiency increased as the bubble size, d_B, decreased. The contact zone kinetic model shows that the DAF particle removal rate is proportional to d_B^{-3}. This was confirmed by the kinetic study results which showed that the estimated value of the contact zone removal rate constant k_P increased from 0.106 min^{-1} to 0.965 min^{-1} as d_B decreased from 90 μm to 60 μm.

(7) Sensitivity analyses performed on the kinetic model showed that as the bubble volume concentration, Φ_B, increased the DAF removal efficiency increased sharply. The Φ_B is controlled by the saturator pressure, P_{Sat}, and the recycle ratio, R_R. In practice, changing the R_R has more significant effect on Φ_B than changing P_{Sat}. The DAF kinetic study results showed that the estimated value of k_P increased from 0.515 min^{-1} to 1.148 min^{-1} as R_R increased from 3% to 7% for hydraulic loading rate of 90 m/h and P_{Sat} of 484 kPa.

(8) Model simulation performed on the kinetic model indicated that the DAF removal efficiency decreased slightly as the contact zone hydraulic loading rate, U_L, increased. The simulation showed that as U_L increased from 10 m/h to 100 m/h, the DAF removal efficiency decreased from almost 100% to about 99.8%. According to the kinetic model, as U_L increases the contact time required for bubble-particle collision and attachment decreases and, therefore, particle removal rate decreases. However, increasing contact zone U_L would increase Pe. As a result, the flow conditions inside the contact zone approach plug flow which would favor higher DAF removal efficiency. This was confirmed by the DAF kinetic study results which showed that the estimated k_P value increased from 0.106 min^{-1} to 0.614 min^{-1} as U_L increased from 30 m/h to 70 m/h for $R_R = 3\%$ and $P_{Sat} = 484$ kPa.

(9) Sensitivity analyses conducted on the kinetic model showed that DAF removal efficiency increased as a result of increasing contact zone height. The simulation showed that more than 95% removal was expected for contact zone height of 1750 mm when $\alpha_{PB} = 0.4$, $d_B = 60$ μm, $\Phi_B = 4000$ ppm, $d_P = 10$ μm and $U_L = 70$ m/h.

(10) The DAF kinetic study results showed that the highest particle removal rate constant k_P was 1.148 min^{-1} for experiments performed at $U_L = 90$ m/h, $R_R = 7\%$ and $P_{Sat} = 484$ kPa. On the other hand, the lowest k_P value was 0.106 min^{-1} for experiments performed at $U_L = 30$ m/h, $R_R = 3\%$ and $P_{Sat} = 484$ kPa.

The following conclusions can be drawn on the supplemental objectives of this research:

(1) Contact zone hydrodynamic characterization results indicated that the degree of mixing or the Pe were always lower than 100 (or $N_d > 0.01$) indicating that the flow conditions inside the contact zone deviated from plug flow conditions. As the contact zone hydraulic loading rate increased, Pe increased and the flow approached plug flow conditions. These conditions favor higher particulate removal and consequently higher DAF efficiency, which was confirmed by the kinetic study results. This would suggest designing the DAF contact zone based on high hydraulic loading rates in the range of 70 to 90 m/h.

(2) The hydrodynamic characterization experimental results confirmed that the axial dispersion model can be used to estimate the degree of mixing inside the DAF contact zone.

(3) Linear regression for the correlation between experimental Pe and U_L indicated that intercept of the linear regression model, which represent the ratio of the distance between the point of the tracer injection and the contact zone port where the measurements were taken, L, to the axial dispersion coefficient, D_a, decreased from the top to the bottom of the contact zone. Also, the tracer study results indicated that the L/D_a decreased as R_R increased. The results suggest that the degree of mixing decreased from the bottom to the top of the contact zone and increased as R_R increased.

(4) The results of the particle dynamic analyzer, PDA, study showed that the saturator pressure, recycle ratio, hydraulic loading rate, nozzle orifice diameter and contact zone wall effects and height affected the measured bubble size, concentration and rise velocity.

(5) The results of the PDA study indicated that bubble size decreased as a result of increasing recycle ratio and hydraulic loading rate and decreasing the nozzle orifice diameter. Also, increasing the saturator pressure resulted in the production of high percentage of small and uniform size air bubbles.

7.2 Recommendation

Based on this research, a number of recommendations are made for further study:

(1) The results of this study showed the importance of the bubble-particle collision efficiency factor, α_{PB}, for predicting particle removal efficiency by DAF for different operational conditions. However, α_{PB} is determined empirically and in this study it was estimated by comparing the theoretical and the experimental particle removal rate constant. Since α_{PB} can range from 0 to 1.0 with values closer to 1.0 for optimum coagulation conditions, it is imperative that α_{PB} be determined experimentally. Simple and direct methods for determining α_{PB} for the system under investigation is required.

(2) In this study, the geometry of the DAF contact zone was fixed and therefore the effect of different configuration and geometry on DAF performance were not investigated. Future work should include contact zone geometry as one of the independent variables in the study.

(3) In this research, the contact zone kinetic model was calibrated by using model water that contained laboratory grown green algae which represented the particles to be removed by the DAF process. Due to time limitation, natural waters were not used. In future work, the kinetic model must be tested and verified using natural water that contains suspended and dissolved particles of organic and inorganic nature.

APPENDIX A Detailed Analytical Methods

A1. Determination of Saturator Efficiency

The procedure followed below is similar to that followed by Henry J. and Gehr R. (1981). It is used to determine the volume of air dissolved in the liquid in the saturator tank and to estimate the saturator efficiency.

Equipment list:

- saturator tank equipped with pressure gauge;
- one 4000 mL beaker;
- one 500 mL graduated cylinder which provides enough volume to enable the released air volume to be read on an accuracy of about 2 mL;
- one small valve;
- 1 meter long plastic tubing;
- thermometer; and
- barometer.

Procedure:

1. allow the DAF saturator to reach steady state conditions at saturator pressure P_{Sat} = 484 kPa;
2. fill the graduated cylinder to the top and the beaker with about 2 L of water;
3. invert the cylinder, placing the palm of the hand over its mouth to prevent water from escaping and place the inverted cylinder into the partially filled beaker. When the palm is removed a vacuum will be formed above the water in the graduated cylinder;
4. mark the water level in the beaker as B;
5. add exactly 1 L of water to the beaker and mark the second level A;
6. pour out the water in the beaker to the original mark B, taking care not to permit air to enter the cylinder;
7. record the volume of the vacuum in the cylinder (V_1);

8. record the air temperature(T), atmospheric pressure (P_{atm}) and the saturator gage pressure (P_{Sat});
9. insert carefully the plastic tubing, which is connected to the saturator tank effluent line, below the cylinder and crack open the valve and allow saturated water to enter the cylinder. The flow should be slow enough that air bubbles do not leak out around the bottom of the cylinder;
10. close the valve when the water level reaches mark A;
11. when all the air bubbles have disappeared and the liquid in the cylinder is clear again, record the volume of air in the top of the graduated cylinder (V_2); and
12. repeat the procedure three times and record the average value.

Calculations:

1. Calculate the volume of air released in the cylinder (V_{air}) in mL:

$$V_{air} = V_1 - V_2 \qquad (A.1.1)$$

2. Determine the saturated vapor pressure (P_{SV}) in mm Hg at room temperature

3. Calculate the partial pressure of air (P_{air}) in mm Hg:

$$P_{air} = P_{atm} - P_{SV} \qquad (A.1.2)$$

4. Calculate the volume of dry air released per L of water ($V_{dry\ air}$) in L

$$V_{dry\ air} = V_{air} \times [(273+20)/(T/273)] \times (P_{air}/760) \qquad (A.1.3)$$

5. Determine the density of dry air ($\rho_{dry\ air}$) in mg/L at 760 mm Hg and 20°C

6. Calculate the experimental total mass of air released per liter of water ($M_{A\ Exp}$) in mg/L

$$M_{A\,Exp} = V_{dry\,air} \times \rho_{dry\,air} \qquad \text{(A.1.4)}$$

7. Calculate the theoretical mass of air released at atmospheric pressure using the following equations:

(a) From Henry's law:

$$x = (P_{atm}/H) \qquad \text{(A.1.5)}$$

where x is the mole fraction of air in water defined as the ratio of the number of moles of gas (n_g) in 1 L of water divided by the number of mole of gas and water ($n_g + n_w$) in 1 L of water, n_w is the number of moles of water in 1 L of water which is equal to 55.6 mole/L, and H is Henry's constant which is equal to 6.64×10^4 (atm/mole fraction) at 20°C. Using equation A.1.5, the value of n_g is equal to 8.4×10^{-4} mole/L.

(b) the saturation concentration of air is calculated as: 8.4×10^{-4} (mole/L) x 28.96 (g/mole) x 1000 (mg/gm) and is equal to 24.33 mg/L

(c) therefore, the theoretical mass of air released per L of water ($M_{A\,Theor}$) in mg/L is:

$$M_{A\,Theor} = 24.33 \times [(273+20)/(T/273)] \times (P_{Sat}/760) \qquad \text{(A.1.6)}$$

8. Calculate the saturator efficiency factor (f):

$$f = (M_{A\,Exp} / M_{A\,Theor}) \qquad \text{(A.1.7)}$$

Table A.1.1 summarizes the data analysis and the results for the saturator efficiency experiment.

Table A.1.1 Data analysis and results for the DAF saturator efficiency experiment

Parameter	Units	Trial 1	Trial 2	Trial 3
V_2	mL	120	120	120
V_1	mL	210	214	208
V_{air}	mL	90	94	88
T	°C	25	25	25
P_{Sat}	kPa	484	484	484
P_{Sat}	Psi	70.1	70.1	70.1
P_{atm}	mm Hg	697	697	697
P_{SV}	mm Hg	17.5	17.5	17.5
P_{air}	mm Hg	679.5	679.5	679.5
$V_{dry\ air}$	L of air/L water	0.0791	0.0826	0.0774
$\rho_{dry\ air}$	mg/L	1205	1205	1205
$M_{A\ Exp}$	mg/L	95.3	99.6	93.2
$M_{A\ Theo}$	mg/L	114.1	114.1	114.1
f	-	0.84	0.87	0.82
Avg. f		0.84		

APPENDIX B Summary of Data

B.1 Tracer Study Data

Table B1.1 Tracer study results for hydraulic loading 30 m/h

R_R (%)	Contact Zone Port #	HRT (min)	Parameter	Trial#1	Trial#2	Trial#3	Trial#4	Avg.
0	Top	2.9	t_m (min)	3.8	3.5	3.6	3.9	3.7
			σ_t^2 (min^2)	1.35	1.11	1.16	1.10	1.18
			Pe	15.3	12.5	19.4	8.4	13.9
	Middle	1.9	t_m (min)	2.6	2.5	2.8	2.9	2.7
			σ_t^2 (min^2)	1.44	1.21	1.54	1.25	1.36
			Pe	10.2	8.4	9.2	9.8	9.4
	Bottom	1.0	t_m (min)	2.2	2.3	1.8	2.1	2.1
			σ_t^2 (min^2)	1.56	1.63	1.41	1.56	1.54
			Pe	3.7	3.9	5.4	6.6	4.9
5	Top	2.9	t_m (min)	3.6	3.7	3.7	4.1	3.8
			σ_t^2 (min^2)	1.13	1.07	1.46	1.11	1.19
			Pe	9.5	11.6	13.5	10.2	11.2
	Middle	1.9	t_m (min)	2.9	3.0	2.7	2.6	2.8
			σ_t^2 (min^2)	1.19	1.09	1.14	2.10	1.38
			Pe	7.5	8.8	10.3	6.6	8.3
	Bottom	1.0	t_m (min)	2.0	2.3	2.3	1.3	2.0
			σ_t^2 (min^2)	1.64	1.73	1.63	1.44	1.61
			Pe	2.9	4.0	3.8	3.7	3.6
10	Top	2.9	t_m (min)	3.8	3.9	3.9	3.5	3.8
			σ_t^2 (min^2)	1.18	1.21	1.07	1.30	1.19
			Pe	10.5	11.4	10.7	9.7	10.6
	Middle	1.9	t_m (min)	3.1	2.6	2.6	2.9	2.8
			σ_t^2 (min^2)	1.24	1.27	1.25	1.80	1.39
			Pe	9.6	8.4	6.8	3.5	7.1
	Bottom	1.0	t_m (min)	2.0	2.2	2.0	2.6	2.2
			σ_t^2 (min^2)	1.49	1.71	1.62	1.50	1.58
			Pe	1.7	4.4	3.0	3.7	3.2

Table B1.2 Tracer study results for hydraulic loading 50 m/h

R_R (%)	Contact Zone Port #	HRT (min)	Parameter	Trial#1	Trial#2	Trial#3	Trial#4	Avg.
0	Top	1.7	t_m (min)	2.0	2.2	2.1	2.1	2.1
			σ_t^2 (min^2)	0.46	0.28	0.49	0.24	0.37
			Pe	34.2	36.3	35.4	34.5	35.1
	Middle	1.1	t_m (min)	1.3	1.5	1.3	1.6	1.4
			σ_t^2 (min^2)	0.49	0.25	0.38	0.40	0.38
			Pe	27.4	24.1	23.8	24.3	24.9
	Bottom	0.6	t_m (min)	1.4	1.0	1.4	0.7	1.1
			σ_t^2 (min^2)	0.82	0.70	0.69	0.04	0.56
			Pe	10.1	7.4	9.6	9.7	9.2
5	Top	1.7	t_m (min)	2.3	2.1	2.1	1.9	2.1
			σ_t^2 (min^2)	0.27	0.38	0.50	0.40	0.39
			Pe	30.6	31.3	31.2	25.4	29.6
	Middle	1.1	t_m (min)	1.7	1.4	1.6	1.6	1.6
			σ_t^2 (min^2)	0.42	0.60	0.50	0.08	0.40
			Pe	22.5	23.8	24.3	18.6	22.3
	Bottom	0.6	t_m (min)	0.8	0.9	0.9	1.1	0.9
			σ_t^2 (min^2)	0.50	0.42	0.57	0.83	0.58
			Pe	7.4	6.8	8.6	8.1	7.7
10	Top	1.7	t_m (min)	2.1	2.2	1.9	2.6	2.2
			σ_t^2 (min^2)	0.40	0.37	0.17	0.62	0.39
			Pe	25.9	25.3	25.5	28.5	26.3
	Middle	1.1	t_m (min)	1.9	1.7	1.7	1.2	1.6
			σ_t^2 (min^2)	0.31	0.53	0.52	0.32	0.42
			Pe	21.4	25.2	19.0	15.2	20.2
	Bottom	0.6	t_m (min)	0.9	1.2	0.9	1.3	1.1
			σ_t^2 (min^2)	0.70	0.68	0.63	0.31	0.58
			Pe	5.5	5.4	6.4	9.6	6.7

Table B1.3 Tracer study results for hydraulic loading 70 m/h

R_R (%)	Contact Zone Port #	HRT (min)	Parameter	Trial#1	Trial#2	Trial#3	Trial#4	Avg.
0	Top	1.2	t_m (min)	1.4	1.5	1.4	1.3	1.4
			σ_t^2 (min^2)	0.21	0.25	0.24	0.10	0.20
			Pe	33.9	35.1	35.6	42.2	36.7
	Middle	0.8	t_m (min)	0.9	1.0	1.3	0.9	1.0
			σ_t^2 (min^2)	0.23	0.23	0.21	0.17	0.21
			Pe	27.0	25.0	22.2	28.9	25.8
	Bottom	0.4	t_m (min)	0.6	0.7	0.8	0.7	0.7
			σ_t^2 (min^2)	0.56	0.25	0.24	0.15	0.30
			Pe	12.3	13.9	12.0	6.2	11.1
5	Top	1.2	t_m (min)	1.5	1.6	1.7	1.3	1.5
			σ_t^2 (min^2)	0.18	0.19	0.22	0.29	0.22
			Pe	33.1	36.0	30.2	35.4	33.7
	Middle	0.8	t_m (min)	0.9	0.9	1.0	1.3	1.0
			σ_t^2 (min^2)	0.33	0.12	0.18	0.33	0.24
			Pe	21.7	26.3	26.1	25.8	25
	Bottom	0.4	t_m (min)	0.4	0.5	0.4	1.1	0.6
			σ_t^2 (min^2)	0.24	0.42	0.19	0.39	0.31
			Pe	12.4	11.9	17.3	12.8	13.6
10	Top	1.2	t_m (min)	1.4	1.6	1.7	1.3	1.5
			σ_t^2 (min^2)	0.25	0.22	0.22	0.15	0.21
			Pe	32.4	32.6	29.7	31.2	31.5
	Middle	0.8	t_m (min)	0.9	1.0	1.0	1.5	1.1
			σ_t^2 (min^2)	0.23	0.24	0.21	0.28	0.24
			Pe	25.1	21.6	25.0	23.1	23.7
	Bottom	0.4	t_m (min)	0.6	0.9	0.6	0.7	0.7
			σ_t^2 (min^2)	0.21	0.22	0.19	0.58	0.30
			Pe	8.8	8.3	10.4	10.4	9.5

Table B1.4 Tracer study results for hydraulic loading 90 m/h

R_R (%)	Contact Zone Port #	HRT (min)	Parameter	Trial#1	Trial#2	Trial#3	Trial#4	Avg.
0	Top	1.0	t_m (min)	1.2	1.3	1.3	1.0	1.2
			σ_t^2 (min^2)	0.13	0.10	0.09	0.08	0.10
			Pe	41.4	44.1	40.0	40.1	41.4
	Middle	0.6	t_m (min)	0.7	0.7	1.0	0.8	0.8
			σ_t^2 (min^2)	0.10	0.14	0.08	0.16	0.12
			Pe	29.9	28.3	27.1	29.6	28.7
	Bottom	0.3	t_m (min)	0.6	0.5	0.7	0.2	0.5
			σ_t^2 (min^2)	0.13	0.16	0.18	0.17	0.16
			Pe	14.0	15.4	12.7	13.2	13.8
5	Top	1.0	t_m (min)	1.2	0.9	1.3	1.4	1.2
			σ_t^2 (min^2)	0.15	0.10	0.11	0.12	0.12
			Pe	38.5	43.0	41.6	34.9	39.5
	Middle	0.6	t_m (min)	0.9	1.0	1.0	0.7	0.9
			σ_t^2 (min^2)	0.12	0.18	0.10	0.16	0.14
			Pe	29.3	24.3	28.6	30.2	28.1
	Bottom	0.3	t_m (min)	0.5	0.5	0.4	0.6	0.5
			σ_t^2 (min^2)	0.18	0.22	0.15	0.21	0.19
			Pe	10.8	10.5	13.9	14.0	12.3
10	Top	1.0	t_m (min)	1.3	1.2	1.5	1.2	1.3
			σ_t^2 (min^2)	0.13	0.11	0.09	0.11	0.11
			Pe	37.4	38.4	38.9	34.1	37.2
	Middle	0.6	t_m (min)	0.8	0.8	0.8	0.8	0.8
			σ_t^2 (min^2)	0.10	0.14	0.15	0.13	0.13
			Pe	24.9	27.9	25.4	31.1	27.3
	Bottom	0.3	t_m (min)	0.4	0.8	0.5	0.7	0.6
			σ_t^2 (min^2)	0.22	0.13	0.19	0.22	0.19
			Pe	9.6	11.8	11.2	13.4	11.5

Table B1.5 Statistical analysis for contact zone residence time and hydraulic loading rate for the top port

β=A **1.815**

SS = 0.058442

U_L (m/min) x_i	x_i^{-1}	t_m (min) y_i	Predicted y_i	Residuals
0.50	2.000	3.78	3.631	0.149
0.83	1.200	2.06	2.178	-0.118
1.17	0.857	1.42	1.556	-0.136
1.50	0.667	1.15	1.210	-0.060

Regression Statistics	
r^2	0.986
Standard Error	0.140
Observations	4

	Coefficients	*Lower 95%*	*Upper 95%*
β	1.815	1.643	1.988

Table B1.6 Statistical analysis for contact zone residence time and hydraulic loading rate for the middle port

β=A **1.275**

SS = 0.039194

U_L (m/min) x_i	x_i^{-1}	t_m (min) y_i	Predicted y_i	Residuals
0.50	2.000	2.67	2.550	0.120
0.83	1.200	1.44	1.530	-0.090
1.17	0.857	0.97	1.093	-0.123
1.50	0.667	0.81	0.850	-0.040

Regression Statistics	
r^2	0.982
Standard Error	0.024
Observations	4

	Coefficients	*Lower 95%*	*Upper 95%*
β	1.275	1.336	1.416

Table B1.7 Statistical analysis for contact zone residence time and hydraulic loading rate for the bottom port

β=A 0.999
SS = 0.099194

U_L (m/min) x_i	x_i^{-1}	t_m (min) y_i	Predicted y_i	Residuals
0.50	2.000	2.19	1.997	0.193
0.83	1.200	1.07	1.198	-0.128
1.17	0.857	0.70	0.856	-0.156
1.50	0.667	0.52	0.666	-0.146

Regression Statistics	
r^2	0.941
Standard Error	0.182
Observations	4

	Coefficients	*Lower 95%*	*Upper 95%*
β	0.999	0.774	1.223

Table B1.8 Statistical analysis for Pe and hydraulic loading rate for the top port and at R_R = 0%

β = B 0.52
SS = 116.545061

U_L (m/h) x_i	Pe y_i	Predicted y_i	Residuals
30	13.9	15.616	-1.716
50	35.1	26.027	9.073
70	37.7	36.438	1.262
90	41.4	46.849	-5.449

Regression Statistics	
r^2	0.863
Standard Error	6.233
Observations	4

	Coefficients	*Lower 95%*	*Upper 95%*
β	0.521	0.366	0.675

Table B1.9 Statistical analysis for Pe and hydraulic loading rate for the top port and at R_R = 5%

β = B 0.471
SS = 54.070488

U_L (m/h) x_i	Pe y_i	Predicted y_i	Residuals
30	11.2	14.140	-2.940
50	29.6	23.567	6.033
70	33.7	32.994	0.706
90	39.5	42.421	-2.921

Regression Statistics	
r^2	0.879
Standard Error	4.245
Observations	4

	Coefficients	*Lower 95%*	*Upper 95%*
β	0.471	0.366	0.577

Table B1.10 Statistical analysis for Pe and hydraulic loading rate for the top port and at R_R = 10%

β = B 0.438
SS = 31.445122

U_L (m/h) x_i	Pe y_i	Predicted y_i	Residuals
30	10.6	13.145	-2.545
50	26.3	21.909	4.391
70	31.5	30.672	0.828
90	37.2	39.435	-2.235

Regression Statistics	
r^2	0.919
Standard Error	3.238
Observations	4

	Coefficients	*Lower 95%*	*Upper 95%*
β	0.438	0.358	0.519

Table B1.11 Statistical analysis for Pe and hydraulic loading rate for the middle port and at $R_R = 0\%$

β = B 0.362
SS = 64.003598

U_L (m/h) x_i	Pe y_i	Predicted y_i	Residuals
30	9.4	10.860	-1.460
50	24.9	18.101	6.799
70	26.1	25.341	0.759
90	28.7	32.581	-3.881

Regression Statistics	
R Square	0.849
Standard Error	4.618
Observations	4

	Coefficients	*Lower 95%*	*Upper 95%*
β	0.362	0.247	0.477

Table B1.12 Statistical analysis for Pe and hydraulic loading rate for the middle port and at $R_R = 5\%$

β = B 0.344
SS = 39.116280

U_L (m/h) x_i	Pe y_i	Predicted $\log_{10}(y_i)$	Residuals
30	8.3	10.323	-2.023
50	22.3	17.204	5.096
70	25.0	24.086	0.914
90	28.1	30.968	-2.868

Regression Statistics	
R Square	0.911
Standard Error	3.611
Observations	4

	Coefficients	*Lower 95%*	*Upper 95%*
β	0.344	0.254	0.433

Table B1.13 Statistical analysis for Pe and hydraulic loading rate for the middle port and at $R_R = 10\%$

β = B 0.326

SS = 27.325061

U_L (m/h) x_i	Pe y_i	Predicted y_i	Residuals
30	7.1	9.766	-2.666
50	20.2	16.277	3.923
70	23.7	22.788	0.912
90	27.3	29.299	-1.999

Regression Statistics	
R Square	0.939
Standard Error	3.018
Observations	4

	Coefficients	*Lower 95%*	*Upper 95%*
β	0.326	0.251	0.401

Table B1.14 Statistical analysis for Pe and hydraulic loading rate for the bottom port and at $R_R = 0\%$

β = B 0.172

SS = 6.345549

U_L (m/h) x_i	Pe y_i	Predicted $\log_{10}(y_i)$	Residuals
30	4.9	5.149	-0.249
50	9.2	8.582	0.618
70	13.8	12.015	1.785
90	13.8	15.448	-1.648

Regression Statistics	
R Square	0.940
Standard Error	1.454
Observations	4

	Coefficients	*Lower 95%*	*Upper 95%*
β	0.172	0.136	0.208

Table B1.15 Statistical analysis for Pe and hydraulic loading rate for the bottom port and at R_R = 5%

β = B 0.156
SS = 11.383902

U_L (m/h) x_i	Pe y_i	Predicted y_i	Residuals
30	3.6	4.668	-1.068
50	7.7	7.780	-0.080
70	13.6	10.893	2.707
90	12.3	14.005	-1.705

Regression Statistics	
R Square	0.904
Standard Error	1.947
Observations	4

	Coefficients	*Lower 95%*	*Upper 95%*
β	0.156	0.107	0.204

Table B1.16 Statistical analysis for Pe and hydraulic loading rate for the bottom port and at R_R = 10%

β = B 0.130
SS = 0.729939

U_L (m/h) x_i	Pe y_i	Predicted y_i	Residuals
30	3.2	3.898	-0.698
50	6.7	6.497	0.203
70	9.5	9.096	0.404
90	11.5	11.695	-0.195

Regression Statistics	
R Square	0.981
Standard Error	0.493
Observations	4

	Coefficients	*Lower 95%*	*Upper 95%*
β	0.129	0.118	0.142

B.2 PDA Study Data

Table B2.1 PDA raw data for hydraulic loading 30 m/h, R_R = 10 %, P_{Sat} = 484 kPa, $d_{Orifice}$ = 0.55 mm and probe volume coordinates (900,0,25)

Exp# J31.1	Trial 1	Trial 2	Trial 3	Avg
Attempted samples	5813	7317	7257	6796
Validated Samples	4911	6239	6212	5787
Validation %	84	85	86	85
Data Rate (Hz)	85	83	79	82
$U_{B\,Inst}$ (m/s)	1.35E-02	1.46E-02	1.39E-02	1.40E-02
σ_{UB} (m/s)	4.00E-03	5.56E-03	4.48E-03	4.68E-03
d_B (μm)	72.5	74.0	74.6	73.7
Variance	204	210.2	206.0	206.7
σ_{dB}(μm)	14.3	14.5	14.4	14.4
Concentration (#/mL)	2.1E+04	1.6E+04	1.7E+04	1.8E+04

Table B2.2 PDA raw data for hydraulic loading 30 m/h, R_R = 7 %, P_{Sat} = 484 kPa, $d_{Orifice}$ = 0.55 mm and probe volume coordinates (900,0,25)

Exp# J27.2	Trial 1	Trial 2	Trial 3	Trial 4	Avg
Attempted samples	7179	9437	9135	9761	8878
Validated Samples	5541	7141	6973	7228	6721
% Validation	77	76	76	74	76
Data Rate (Hz)	102	102	96	94	99
$U_{B\,Inst}$ (m/s)	1.53E-02	1.48E-02	1.31E-02	1.36E-02	1.42E-02
σ_{UB} (m/s)	6.58E-03	5.91E-03	5.37E-03	4.44E-03	5.57E-03
d_B (μm)	84.5	84.7	83.6	89.2	85.5
Variance	217.3	225.1	216.7	290.8	237.5
σ_{dB}(μm)	14.7	15.0	14.7	17.1	15.4
Concentration (#/mL)	8.5E+03	9.6E+03	1.3E+04	8.9E+03	1.0E+04

Table B2.3 PDA raw data for hydraulic loading 30 m/h, R_R = 7 %, P_{Sat} = 484 kPa, $d_{Orifice}$ = 0.55 mm and probe volume coordinates (400,0,25)

Exp# A19.2	Trial 1	Trial 2	Trial 3	Trial 4	Avg
Attempted samples	6584	6837	6660	6684	6691
Validated Samples	5762	5835	5840	5777	5804
% Validation	88	85	88	86	87
Data Rate (Hz)	71	72	75	72	73
$U_{B\,last}$ (m/s)	1.38E-02	1.35E-02	1.34E-02	1.33E-02	1.35E-02
σ_{UB} (m/s)	5.56E-03	5.53E-03	5.59E-03	5.48E-03	5.54E-03
d_B (µm)	63.7	64.5	66.5	66.8	65.4
Variance	143	156.6	148.0	153.0	150.2
σ_{dB}(µm)	12.0	12.5	12.2	12.4	12.3
Concentration (#/mL)	1.2E+04	1.3E+04	1.8E+04	1.3E+04	1.4E+04

Table B2.4 PDA raw data for hydraulic loading 30 m/h, R_R = 10 %, P_{Sat} = 484 kPa, $d_{Orifice}$ = 0.55 mm and probe volume coordinates (400,0,25)

Exp# A19.3	Trial 1	Trial 2	Trial 3	Trial 4	Avg
Attempted samples	6077	5945	6003	6004	6007
Validated Samples	5543	5543	5556	5490	5533
% Validation	91	93	93	91	92
Data Rate (Hz)	50	48	44	42	46
$U_{B\,last}$ (m/s)	1.30E-02	1.27E-02	1.38E-02	1.33E-02	1.32E-02
σ_{UB} (m/s)	5.21E-03	5.19E-03	5.31E-03	5.29E-03	5.25E-03
d_B (µm)	64.9	63.5	63.9	64.6	64.2
Variance	133.4	111.7	116.9	119.7	120.4
σ_{dB}(µm)	11.5	10.6	10.8	10.9	11.0
Concentration (#/mL)	2.0E+04	2.3E+04	2.4E+04	2.1E+04	2.2E+04

Table B2.5 PDA raw data for hydraulic loading 50 m/h, $R_R = 5$ %, $P_{Sat} = 484$ kPa, $d_{Orifice} = 0.55$ mm and probe volume coordinates (900,0,25)

Exp# A8.3	Trial 1	Trial 2	Trial 3	Trial 4	Trial 5	Avg
Attempted samples	2214	2242	2348	3785	5123	3142
Validated Samples	2096	2127	2157	3384	4595	2872
% Validation	95	95	92	89	90	92
Data Rate (Hz)	81	78	71	75	90	79
$U_{B\ Inst}$ (m/s)	1.96E-02	1.97E-02	1.92E-02	1.88E-02	1.92E-02	1.93E-02
σ_{UB} (m/s)	2.41E-03	2.40E-03	2.31E-03	2.25E-03	2.23E-03	2.32E-03
d_B (μm)	67.8	68.8	67.9	69.2	70.5	68.8
Variance	418	391.6	348.6	319.0	350.0	365.4
σ_{dB}(μm)	20.4	19.8	18.7	17.9	18.7	19.1
Concentration (#/mL)	1.2E+04	1.4E+04	8.1E+03	1.1E+04	9.3E+03	1.1E+04

Table B2.6 PDA raw data for hydraulic loading 50 m/h, $R_R = 7$ %, $P_{Sat} = 484$ kPa, $d_{Orifice} = 0.55$ mm and probe volume coordinates (900,0,25)

Exp# J27.1	Trial 1	Trial 2	Trial 3	Trial 4	Avg
Attempted samples	2730	3912	3966	3765	3593
Validated Samples	2366	3455	3474	3399	3174
% Validation	87	88	88	90	88
Data Rate (Hz)	67	38	39	23	42
$U_{B\ Inst}$ (m/s)	1.87E-02	1.87E-02	1.99E-02	1.72E-02	1.84E-02
σ_{UB} (m/s)	2.15E-03	2.13E-03	2.18E-03	1.98E-03	2.11E-03
d_B (μm)	62.5	63.2	64.0	63.5	63.3
Variance	156.4	158.8	172.0	153.0	160.1
σ_{dB}(μm)	12.5	12.6	13.1	12.4	12.6
Concentration (#/mL)	1.8E+04	1.8E+04	1.7E+04	1.5E+04	1.7E+04

Table B2.7 PDA raw data for hydraulic loading 50 m/h, R_R = 10 %, P_{Sat} = 484 kPa, $d_{Orifice}$ = 1.03 mm and probe volume coordinates (900,0,25)

Exp# J29.5	Trial 1	Trial 2	Trial 3	Trial 4	Avg
Attempted samples	11708	11355	11577	11559	11550
Validated Samples	8154	8175	8331	8281	8235
% Validation	70	72	72	72	71
Data Rate (Hz)	86	81	79	82	82
$U_{B\,Inst}$ (m/s)	2.35E-02	2.31E-02	2.52E-02	2.58E-02	2.44E-02
σ_{UB} (m/s)	5.24E-03	5.13E-03	5.72E-03	5.74E-03	5.45E-03
d_B (μm)	101.5	100.4	100.6	100.4	100.7
Variance	506.2	427.0	403.5	426.0	440.7
σ_{dB}(μm)	22.5	20.7	20.1	20.6	21.0
Concentration (#/mL)	9.1E+03	1.5E+04	1.3E+04	1.5E+04	1.1E+04

Table B2.8 PDA raw data for hydraulic loading 50 m/h, R_R = 7 %, P_{Sat} = 484 kPa, $d_{Orifice}$ = 1.03 mm and probe volume coordinates (400,0,25)

Exp# A14.3	Trial 1	Trial 2	Trial 3	Trial 4	Avg
Attempted samples	1666	1737	2369	3712	2371
Validated Samples	1565	1595	2148	3284	2148
% Validation	94	92	91	88	91
Data Rate (Hz)	51	69	60	72	63
$U_{B\,Inst}$ (m/s)	1.79E-02	1.83E-02	1.77E-02	1.84E-02	1.81E-02
σ_{UB} (m/s)	4.23E-03	3.78E-03	3.66E-03	3.11E-03	3.70E-03
d_B (μm)	70.5	70.3	69.8	69.6	70.1
Variance	535	498.0	435.0	423.0	472.8
σ_{dB}(μm)	23.1	22.3	20.9	20.6	21.7
Concentration (#/mL)	1.5E+04	1.0E+04	8.1E+03	1.1E+04	1.1E+04

Table B2.9 PDA raw data for hydraulic loading 50 m/h, R_R = 10 %, P_{Sat} = 484 kPa, $d_{Orifice}$ = 1.03 mm and probe volume coordinates (400,0,25)

Exp# A14.4	Trial 1	Trial 2	Trial 3	Trial 4	Avg
Attempted samples	7799	7960	9571	9572	8726
Validated Samples	6252	6353	7610	7628	6961
% Validation	80	80	80	80	80
Data Rate (Hz)	81	88	83	82	84
$U_{B\ Inst}$ (m/s)	1.83E-02	1.89E-02	1.96E-02	2.00E-02	1.92E-02
σ_{UB} (m/s)	4.74E-03	5.00E-03	5.43E-03	5.14E-03	5.08E-03
d_B (μm)	78.6	79.4	81.2	80.9	80.0
Variance	278.4	243.7	268.1	240.1	257.6
σ_{dB}(μm)	16.7	15.6	16.4	15.5	16.0
Concentration (#/mL)	2.2E+04	1.6E+04	2.1E+04	1.7E+04	1.9E+04

Table B2.10 PDA raw data for hydraulic loading 50 m/h, R_R = 5 %, P_{Sat} = 484 kPa, $d_{Orifice}$ = 0.55 mm and probe volume coordinates (400,0,25)

Exp# A18.2	Trial 1	Trial 2	Trial 3	Trial 4	Trial 5	Avg
Attempted samples	2125	3231	5794	5912	5990	4610
Validated Samples	2051	3081	5278	5296	5329	4207
% Validation	97	95	91	90	89	92
Data Rate (Hz)	10	22	48	54	61	39
$U_{B\ Inst}$ (m/s)	1.75E-02	1.87E-02	1.77E-02	1.66E-02	1.74E-02	1.76E-02
σ_{UB} (m/s)	4.51E-03	4.80E-03	3.51E-03	3.25E-03	3.23E-03	3.86E-03
d_B (μm)	54.3	52.5	54.8	54.7	54.4	54.1
Variance	359.9	287.8	285.8	278.2	256.5	293.6
σ_{dB}(μm)	19.0	17.0	16.9	16.7	16.0	17.1
Concentration (#/mL)	1.6E+04	1.7E+04	1.4E+04	1.1E+04	1.7E+04	1.5E+04

Table B2.11 PDA raw data for hydraulic loading 50 m/h, R_R = 7 %, P_{Sat} = 484 kPa, $d_{Orifice}$ = 0.55 mm and probe volume coordinates (400,0,25)

Exp# A18.3	Trial 1	Trial 2	Trial 3	Trial 4	Trial 5	Avg
Attempted samples	6262	7631	12929	9008	8622	8890
Validated Samples	5406	6526	11052	7777	7710	7694
% Validation	86	86	85	86	89	87
Data Rate (Hz)	85	88	108	110	90	96
$U_{B\,Inst}$ (m/s)	1.63E-02	1.69E-02	1.75E-02	1.64E-02	1.89E-02	1.72E-02
σ_{UB} (m/s)	3.06E-03	3.51E-03	4.00E-03	3.03E-03	4.58E-03	3.64E-03
d_B (μm)	54.2	53.3	51.5	51.2	53.3	52.7
Variance	257.9	245.4	185.1	163.0	154.0	201.1
σ_{dB}(μm)	16.1	15.7	13.6	12.8	12.4	14.1
Concentration (#/mL)	2.8E+04	2.3E+04	2.2E+04	2.6E+04	2.1E+04	2.4E+04

Table B2.12 PDA raw data for hydraulic loading 70 m/h, R_R = 3 %, P_{Sat} = 484 kPa, $d_{Orifice}$ = 0.55 mm and probe volume coordinates (900,0,25)

Exp# J24.2	Trial 1	Trial 2	Trial 3	Trial 4	Avg
Attempted samples	1392	1972	2143	2158	1916
Validated Samples	1354	1888	2076	2101	1855
% Validation	97	96	97	97	97
Data Rate (Hz)	31	39	31	43	36
$U_{B\,Inst}$ (m/s)	2.53E-02	2.54E-02	2.41E-02	2.44E-02	2.48E-02
σ_{UB} (m/s)	3.12E-03	3.17E-03	2.77E-03	2.96E-03	3.00E-03
d_B (μm)	66.0	68.8	63.8	65.4	66.0
Variance	510.2	586.6	450.0	518.8	516.4
σ_{dB}(μm)	22.6	24.2	21.2	22.8	22.7
Concentration (#/mL)	6.2E+03	5.5E+03	6.5E+03	5.8E+03	6.0E+03

Table B2.13 PDA raw data for hydraulic loading 70 m/h, R_R = 5 %, P_{Sat} = 484 kPa, $d_{Orifice}$ = 0.55 mm and probe volume coordinates (900,0,25)

Exp# A8.1	Trial 1	Trial 2	Trial 3	Avg
Attempted samples	2250	3464	3522	3079
Validated Samples	2123	3236	3252	2870
% Validation	94	93	92	93
Data Rate (Hz)	52	49	37	46
$U_{B\,Inst}$ (m/s)	2.49E-02	2.45E-02	2.38E-02	2.44E-02
σ_{UB} (m/s)	2.81E-03	2.66E-03	2.26E-03	2.58E-03
d_B (µm)	63.5	62.7	64.0	63.4
Variance	406	378.7	407.0	397.2
σ_{dB}(µm)	20.1	19.5	20.2	19.9
Concentration (#/mL)	1.6E+04	1.3E+04	1.3E+04	1.4E+04

Table B2.14 PDA raw data for hydraulic loading 70 m/h, R_R = 7 %, P_{Sat} = 484 kPa, $d_{Orifice}$ = 1.03 mm and probe volume coordinates (900,0,25)

Exp# J29.4	Trial 1	Trial 2	Trial 3	Trial 4	Avg
Attempted samples	8247	8259	8530	8938	8494
Validated Samples	6483	6476	6561	6818	6585
% Validation	79	78	77	76	78
Data Rate (Hz)	74	73	85	90	81
$U_{B\,Inst}$ (m/s)	2.57E-02	2.37E-02	2.56E-02	2.55E-02	2.51E-02
σ_{UB} (m/s)	3.39E-03	3.94E-03	4.54E-03	3.37E-03	3.81E-03
d_B (µm)	81.0	82.1	82.5	82.0	81.9
Variance	368.7	392.8	327.9	334.5	356.0
σ_{dB}(µm)	19.2	19.8	18.1	18.3	18.9
Concentration (#/mL)	1.2E+04	1.9E+04	1.4E+04	1.1E+04	1.4E+04

Table B2.15 PDA raw data for hydraulic loading 70 m/h, R_R = 5 %, P_{Sat} = 484 kPa, $d_{Orifice}$ = 0.55 mm and probe volume coordinates (900,0,45)

Exp# A4.1	Trial 1	Trial 2	Trial 3	Avg
Attempted samples	5586	5259	5476	5440
Validated Samples	4601	4487	4558	4549
% Validation	82	85	83	84
Data Rate (Hz)	64	51	67	61
$U_{B\,Inst}$ (m/s)	1.93E-02	1.97E-02	2.05E-02	1.98E-02
σ_{UB} (m/s)	2.71E-03	3.17E-03	3.39E-03	3.09E-03
d_B (μm)	63.7	63.9	64.8	64.1
Variance	318.7	348.5	349.7	339.0
σ_{dB}(μm)	17.9	18.7	18.7	18.4
Concentration (#/mL)	1.2E+04	1.8E+04	2.1E+04	1.7E+04

Table B2.16 PDA raw data for hydraulic loading 70 m/h, R_R = 5 %, P_{Sat} = 345 kPa, $d_{Orifice}$ = 0.55 mm and probe volume coordinates (900,0,0)

Exp# A4.3	Trial 1	Trial 2	Trial 3	Avg
Attempted samples	1026	1542	1049	1206
Validated Samples	1012	1524	1025	1187
% Validation	99	99	98	98
Data Rate (Hz)	25	33	23	27
$U_{B\,Inst}$ (m/s)	2.31E-02	2.38E-02	2.33E-02	2.34E-02
σ_{UB} (m/s)	2.18E-03	2.23E-03	2.19E-03	2.20E-03
d_B (μm)	63.1	62.6	63.3	63.0
Variance	506	455.7	479.9	480.5
σ_{dB}(μm)	22.5	21.3	21.9	21.9
Concentration (#/mL)	5.5E+03	5.2E+03	5.5E+03	5.4E+03

Table B2.17 PDA raw data for hydraulic loading 70 m/h, R_R = 5 %, P_{Sat} = 484 kPa, $d_{Orifice}$ = 0.55 mm and probe volume coordinates (900,0,0)

Exp# A4.4	Trial 1	Trial 2	Trial 3	Avg
Attempted samples	4336	4588	4688	4537
Validated Samples	4148	4243	4284	4225
% Validation	96	92	91	93
Data Rate (Hz)	22	40	45	36
$U_{B\ Inst}$ (m/s)	2.43E-02	2.36E-02	2.36E-02	2.39E-02
σ_{UB} (m/s)	2.17E-03	2.19E-03	2.31E-03	2.22E-03
d_B (μm)	63.3	65.6	64.5	64.5
Variance	325.4	339.4	310.0	324.9
σ_{dB}(μm)	18.0	18.4	17.6	18.0
Concentration (#/mL)	1.5E+04	1.3E+04	1.1E+04	1.3E+04

Table B2.18 PDA raw data for hydraulic loading 70 m/h, R_R = 5 %, P_{Sat} = 587 kPa, $d_{Orifice}$ = 0.55 mm and probe volume coordinates (900,0,0)

Exp# A4.5	Trial 1	Trial 2	Trial 3	Avg
Attempted samples	6158	6230	6132	6173
Validated Samples	5424	5510	5488	5474
% Validation	88	88	89	89
Data Rate (Hz)	73	84	84	80
$U_{B\ Inst}$ (m/s)	2.33E-02	2.28E-02	2.21E-02	2.37E-02
σ_{UB} (m/s)	2.90E-03	3.68E-03	3.15E-03	3.25E-03
d_B (μm)	64.5	64.1	63.6	64.1
Variance	269.5	236.8	215.8	240.7
σ_{dB}(μm)	16.4	15.4	14.7	15.5
Concentration (#/mL)	1.9E+04	1.4E+04	1.2E+04	1.5E+04

Table B2.19 PDA raw data for hydraulic loading 70 m/h, R_R = 5 %, P_{Sat} = 484 kPa, $d_{Orifice}$ = 1.03 mm and probe volume coordinates (900,0,0)

Exp# A4.7	Trial 1	Trial 2	Trial 3	Avg
Attempted samples	1611	1600	2194	1802
Validated Samples	1561	1562	2119	1747
% Validation	97	98	97	98
Data Rate (Hz)	48	55	56	53
$U_{B\ Inst}$ (m/s)	2.49E-02	2.52E-02	2.47E-02	2.49E-02
σ_{UB} (m/s)	2.62E-03	2.72E-03	2.71E-03	2.69E-03
d_B (μm)	79.1	79.8	78.3	79.1
Variance	539.6	518.4	489.3	515.8
σ_{dB}(μm)	23.2	22.8	22.1	22.7
Concentration (#/mL)	9.2E+03	9.7E+03	1.1E+04	1.0E+04

Table B2.20 PDA raw data for hydraulic loading 70 m/h, R_R = 5 %, P_{Sat} = 484 kPa, $d_{Orifice}$ = 0.55 mm and probe volume coordinates (400,0,0)

Exp# A12.3	Trial 1	Trial 2	Trial 3	Trial 4	Avg
Attempted samples	3183	4296	4457	5742	4420
Validated Samples	3065	4087	4135	5222	4127
% Validation	96	95	93	91	94
Data Rate (Hz)	43	31	51	55	45
$U_{B\ Inst}$ (m/s)	1.74E-02	1.76E-02	1.83E-02	2.04E-02	2.28E-02
σ_{UB} (m/s)	6.77E-03	6.16E-03	6.35E-03	4.31E-03	5.97E-03
d_B (μm)	56.6	54.8	53.0	52.0	54.1
Variance	430.8	380.5	317.0	269.0	349.3
σ_{dB}(μm)	20.8	19.5	17.8	16.4	18.6
Concentration (#/mL)	1.4E+04	1.3E+04	1.9E+04	1.4E+04	1.5E+04

Table B2.21 PDA raw data for hydraulic loading 70 m/h, R_R = 3 %, P_{Sat} = 484 kPa, $d_{Orifice}$ = 0.55 mm and probe volume coordinates (400,0,25)

Exp# A13.4	Trial 1	Trial 2	Trial 3	Trial 4	Avg
Attempted samples	1533	1538	1548	1543	1541
Validated Samples	1514	1515	1548	1517	1524
% Validation	99	99	100	98	99
Data Rate (Hz)	29	35	25	35	31
$U_{B\,Inst}$ (m/s)	2.28E-02	2.26E-02	2.14E-02	2.31E-02	2.25E-02
σ_{UB} (m/s)	7.08E-03	6.48E-03	7.51E-03	6.52E-03	6.90E-03
d_B (μm)	52.8	55.2	55.6	55.5	54.8
Variance	386.8	442.0	438.0	451.8	429.7
σ_{dB}(μm)	19.7	21.0	20.9	21.3	20.7
Concentration (#/mL)	6.4E+03	6.1E+03	6.0E+03	6.3E+03	6.2E+03

Table B2.22 PDA raw data for hydraulic loading 70 m/h, R_R = 7 %, P_{Sat} = 484 kPa, $d_{Orifice}$ = 1.03 mm and probe volume coordinates (400,0,25)

Exp# A14.1	Trial 1	Trial 2	Trial 3	Trial 4	Avg
Attempted samples	4576	6144	6127	6209	5764
Validated Samples	4241	5459	5401	5428	5132
% Validation	93	89	88	87	89
Data Rate (Hz)	59	58	62	64	61
$U_{B\,Inst}$ (m/s)	2.33E-02	2.37E-02	2.53E-02	2.48E-02	2.43E-02
σ_{UB} (m/s)	6.47E-03	7.09E-03	5.69E-03	5.98E-03	6.31E-03
d_B (μm)	63.4	64.6	62.6	63.7	63.6
Variance	430	383.0	361.0	373.7	386.9
σ_{dB}(μm)	20.7	19.6	19.0	19.3	19.7
Concentration (#/mL)	1.9E+04	1.6E+04	1.2E+04	1.7E+04	1.6E+04

Table B2.23 **PDA raw data for hydraulic loading 70 m/h, R_R = 5 %, P_{Sat} = 484 kPa, $d_{Orifice}$ = 1.03 mm and probe volume coordinates (400,0,0)**

Exp# A14.2	Trial 1	Trial 2	Trial 3	Avg
Attempted samples	1546	1551	1360	1486
Validated Samples	1516	1518	1322	1452
% Validation	98	98	97	98
Data Rate (Hz)	71	83	65	73
$U_{B\,Inst}$ (m/s)	2.22E-02	2.19E-02	2.16E-02	2.41E-02
σ_{UB} (m/s)	8.19E-03	8.61E-03	6.89E-03	7.90E-03
d_B (μm)	60.6	59.9	62.9	61.1
Variance	533	485.1	558.0	525.4
σ_{dB}(μm)	23.1	22.0	23.6	22.9
Concentration (#/mL)	1.1E+04	1.0E+04	1.2E+04	1.1E+04

Table B2.24 **PDA raw data for hydraulic loading 90 m/h, R_R = 3 %, P_{Sat} = 484 kPa, $d_{Orifice}$ = 0.55 mm and probe volume coordinates (900,0,25)**

Exp# J27.3	Trial 1	Trial 2	Trial 3	Trial 4	Avg
Attempted samples	2098	3164	3289	3279	2958
Validated Samples	2052	3097	3135	3113	2849
% Validation	98	98	95	95	96
Data Rate (Hz)	31	43	40	26	35
$U_{B\,Inst}$ (m/s)	2.76E-02	2.71E-02	2.74E-02	2.75E-02	2.74E-02
σ_{UB} (m/s)	3.51E-03	3.38E-03	3.58E-03	4.44E-03	3.49E-03
d_B (μm)	56.5	58.4	56.0	55.8	56.7
Variance	357.9	408.0	354.0	350.3	367.6
σ_{dB}(μm)	18.9	20.2	18.8	18.7	19.2
Concentration (#/mL)	6.8E+03	6.7E+03	7.2E+03	6.9E+03	6.9E+03

Table B2.25 PDA raw data for hydraulic loading 90 m/h, R_R = 5 %, P_{Sat} = 484 kPa, $d_{Orifice}$ = 1.03 mm and probe volume coordinates (900,0,25)

Exp# J29.1	Trial 1	Trial 2	Trial 3	Trial 4	Avg
Attempted samples	2208	2225	2200	2213	2212
Validated Samples	2134	2130	2116	2135	2129
% Validation	97	96	96	96	96
Data Rate (Hz)	46	49	48	59	48
$U_{B\,Inst}$ (m/s)	2.91E-02	2.94E-02	2.96E-02	2.95E-02	2.94E-02
σ_{UB} (m/s)	3.32E-03	3.33E-03	3.36E-03	3.35E-03	3.34E-03
d_B (μm)	70.2	67.9	67.7	66.8	68.2
Variance	562	484.0	507.0	467.6	505.2
σ_{dB}(μm)	23.7	22.0	22.5	21.6	22.5
Concentration (#/mL)	9.3E+03	1.3E+04	1.1E+04	1.1E+04	1.1E+04

Table B2.26 PDA raw data for hydraulic loading 90 m/h, R_R = 7 %, P_{Sat} = 484 kPa, $d_{Orifice}$ = 1.03 mm and probe volume coordinates (900,0,25)

Exp# J29.2	Trial 1	Trial 2	Trial 3	Trial 4	Avg
Attempted samples	6034	6579	5992	4997	5901
Validated Samples	5463	5654	5460	4454	5258
% Validation	91	86	91	89	89
Data Rate (Hz)	29	58	25	40	38
$U_{B\,Inst}$ (m/s)	2.88E-02	2.84E-02	2.83E-02	2.80E-02	2.84E-02
σ_{UB} (m/s)	2.81E-03	3.32E-03	2.84E-03	3.01E-03	2.99E-03
d_B (μm)	66.5	66.7	68.3	67.0	67.1
Variance	378.5	339.0	440.8	409.0	391.8
σ_{dB}(μm)	19.5	18.4	21.0	20.2	19.8
Concentration (#/mL)	1.4E+04	1.2E+04	1.2E+04	1.4E+04	1.3E+04

Table B2.27 PDA raw data for hydraulic loading 90 m/h, R_R = 3 %, P_{Sat} = 484 kPa, $d_{Orifice}$ = 1.03 mm and probe volume coordinates (900,0,25)

Exp# J30.1	Trial 1	Trial 2	Trial 3	Avg
Attempted samples	1050	1312	1355	1239
Validated Samples	1033	1296	1335	1221
% Validation	98	99	99	99
Data Rate (Hz)	25	28	26	26
$U_{B\ Inst}$ (m/s)	2.90E-02	2.93E-02	2.87E-02	2.90E-02
σ_{UB} (m/s)	3.72E-03	3.45E-03	3.64E-03	3.60E-03
d_B (μm)	75.4	76.0	71.9	74.4
Variance	813	744.6	645.0	734.2
σ_{dB}(μm)	28.5	27.3	25.4	27.1
Concentration (#/mL)	6.7E+03	6.5E+03	7.2E+03	6.8E+03

Table B2.28 PDA superficial liquid velocity raw data for different hydraulic loadings

Exp# A19.1

Hydraulic loading = 30 m/h, probe volume coordinates (400,0,25)

	Trial 1	Trial 2	Trial 3	Trial 4	Avg
U_L (m/s)	1.11E-02	1.01E-02	1.05E-02	1.11E-02	1.07E-02
σ_{UL} (m/s)	4.15E-03	4.10E-03	4.08E-03	4.07E-03	4.10E-03
σ_{UL} / U_L	0.374	0.406	0.389	0.367	0.384

Exp# J31.2

Hydraulic loading = 30 m/h, probe volume coordinates (900,0,25)

	Trial 1	Trial 2	Trial 3	Trial 4	Avg
U_L (m/s)	1.09E-02	1.13E-02	9.84E-03	9.84E-03	1.05E-02
σ_{UL} (m/s)	3.39E-03	2.46E-03	3.11E-03	2.82E-03	2.95E-03
σ_{UL} / U_L	0.311	0.217	0.317	0.287	0.283

Exp# A8.4

Hydraulic loading = 50 m/h, probe volume coordinates (900,0,25)

	Trial 1	Trial 2	Trial 3	Trial 4	Avg
U_L (m/s)	1.56E-02	1.73E-02	1.65E-02	1.66E-02	1.65E-02
σ_{UL} (m/s)	2.52E-03	2.21E-03	2.25E-03	2.35E-03	2.33E-03
σ_{UL} / U_L	0.161	0.128	0.136	0.141	0.142

Exp# A14.5

Hydraulic loading = 50 m/h, probe volume coordinates (400,0,25)

	Trial 1	Trial 2	Trial 3	Trial 4	Avg
U_L (m/s)	1.53E-02	1.69E-02	1.66E-02	1.61E-02	1.62E-02
σ_{UL} (m/s)	4.02E-03	4.39E-03	4.28E-03	5.04E-03	4.43E-03
σ_{UL} / U_L	0.263	0.260	0.258	0.313	0.273

Table B2.28 Continue

Exp# J24.4

Hydraulic loading = 70 m/h, probe volume coordinates (900,0,-25)

	Trial 1	Trial 2	Trial 3	Trial 4	Avg
U_L (m/s)	2.14E-02	2.19E-02	2.08E-02	2.11E-02	2.13E-02
σ_{UL} (m/s)	2.49E-03	2.47E-03	2.55E-03	2.57E-03	2.52E-03
σ_{UL} / U_L	0.116	0.113	0.123	0.122	0.118

Exp# J31.3

Hydraulic loading = 70 m/h, probe volume coordinates (900,0,0)

	Trial 1	Trial 2	Trial 3	Avg
U_L (m/s)	2.19E-02	2.23E-02	2.24E-02	2.22E-02
σ_{UL} (m/s)	2.70E-03	2.51E-03	2.34E-03	2.52E-03
σ_{UL} / U_L	0.123	0.113	0.104	0.114

Exp# J31.5

Hydraulic loading = 70 m/h, probe volume coordinates (900,0,45)

	Trial 1	Trial 2	Trial 3	Avg
U_L (m/s)	1.73E-02	1.70E-02	1.70E-02	1.71E-02
σ_{UL} (m/s)	2.93E-03	3.40E-03	3.64E-03	3.32E-03
σ_{UL} / U_L	0.169	0.200	0.214	0.194

Exp# A8.2

Hydraulic loading = 70 m/h, probe volume coordinates (900,0,25)

	Trial 1	Trial 2	Trial 3	Avg
U_L (m/s)	2.17E-02	2.14E-02	2.21E-02	2.18E-02
σ_{UL} (m/s)	2.75E-03	2.90E-03	2.84E-03	2.83E-03
σ_{UL} / U_L	0.127	0.135	0.128	0.130

Table B2.28 Continue

Exp# A13.1
Hydraulic loading = 70 m/h, probe volume coordinates (400,0,25)

	Trial 1	Trial 2	Trial 3	Trial 4	Avg
U_L (m/s)	2.10E-02	2.15E-02	2.10E-02	2.16E-02	2.13E-02
σ_{UL} (m/s)	7.52E-03	6.93E-03	7.14E-03	7.02E-03	7.15E-03
σ_{UL} / U_L	0.358	0.323	0.340	0.324	0.336

Exp# A13.6
Hydraulic loading = 70 m/h, probe volume coordinates (900,0,-45)

	Trial 1	Trial 2	Trial 3	Trial 4	Avg
U_L (m/s)	1.77E-02	1.65E-02	1.61E-02	1.65E-02	1.67E-02
σ_{UL} (m/s)	3.51E-03	3.47E-03	3.41E-03	3.41E-03	3.45E-03
σ_{UL} / U_L	0.198	0.210	0.212	0.207	0.207

xp# J29.3
Hydraulic loading = 90 m/h, probe volume coordinates (900,0,25)

	Trial 1	Trial 2	Trial 3	Trial 4	Avg
U_L (m/s)	2.59E-02	2.46E-02	2.57E-02	2.56E-02	2.55E-02
σ_{UL} (m/s)	3.36E-03	3.39E-03	3.25E-03	3.26E-03	3.31E-03
σ_{UL} / U_L	0.130	0.137	0.126	0.127	0.130

Exp# A23.2
Hydraulic loading = 90 m/h, probe volume coordinates (400,0,25)

	Trial 1	Trial 2	Trial 3	Trial 4	Avg
U_L (m/s)	2.39E-02	2.41E-02	2.45E-02	2.47E-02	2.43E-02
σ_{UL} (m/s)	7.42E-03	7.45E-03	7.49E-03	7.68E-03	7.51E-03
σ_{UL} / U_L	0.310	0.309	0.306	0.311	0.309

Table B2.29 Statistical analysis for the correlation between $U_{B\,rel}$ and d_B for all data (n=27)

β = C = 5.93E+05

SS = 0.0000143

d_B (m) x_i	d_B^2 x_i^2	$U_{B\,rel}$ (m/s) y_i	Predicted y_i	Residuals
8.55E-05	7.31E-09	3.7E-03	4.33E-03	-6.34E-04
7.37E-05	5.43E-09	3.5E-03	3.22E-03	2.80E-04
6.54E-05	4.28E-09	2.8E-03	2.54E-03	2.64E-04
6.42E-05	4.12E-09	2.5E-03	2.44E-03	5.64E-05
6.88E-05	4.73E-09	2.8E-03	2.81E-03	-6.29E-06
6.33E-05	4.01E-09	1.9E-03	2.38E-03	-4.76E-04
1.01E-04	1.01E-08	7.9E-03	6.01E-03	1.89E-03
7.01E-05	4.91E-09	1.9E-03	2.91E-03	-1.01E-03
8.00E-05	6.40E-09	3.0E-03	3.79E-03	-7.94E-04
5.41E-05	2.93E-09	1.4E-03	1.74E-03	-3.35E-04
5.27E-05	2.78E-09	1.0E-03	1.65E-03	-6.47E-04
6.60E-05	4.36E-09	3.0E-03	2.58E-03	4.17E-04
6.34E-05	4.02E-09	2.6E-03	2.38E-03	2.17E-04
8.19E-05	6.71E-09	3.8E-03	3.98E-03	-1.77E-04
6.41E-05	4.11E-09	2.7E-03	2.44E-03	2.64E-04
6.30E-05	3.97E-09	1.2E-03	2.35E-03	-1.15E-03
6.45E-05	4.16E-09	1.7E-03	2.47E-03	-7.66E-04
6.41E-05	4.11E-09	1.5E-03	2.44E-03	-9.36E-04
7.91E-05	6.26E-09	2.7E-03	3.71E-03	-1.01E-03
5.41E-05	2.93E-09	1.2E-03	1.74E-03	-5.35E-04
5.48E-05	3.00E-09	1.2E-03	1.78E-03	-5.80E-04
6.36E-05	4.04E-09	3.0E-03	2.40E-03	6.02E-04
6.11E-05	3.73E-09	2.5E-03	2.21E-03	2.87E-04
5.67E-05	3.21E-09	1.9E-03	1.91E-03	-6.00E-06
6.82E-05	4.65E-09	3.9E-03	2.76E-03	1.14E-03
6.71E-05	4.50E-09	2.9E-03	2.67E-03	2.31E-04
7.44E-05	5.54E-09	4.4E-03	3.28E-03	1.12E-03

Regression Statistics	
R Square	0.846
Standard Error	7.40E-04
Observations	27

	Coefficients	*Lower 95%*	*Upper 95%*
β	5.93E+05	5.33E+05	6.52E+05

Table B2.30 Statistical analysis for the correlation between U_{BRel} and d_B for hydraulic loading 50 m/h data (n=7)

$\beta_1 = \log_{10}(C) = 9.203$
C= 1.6E+09
$\beta2 = p = 2.8434$
SS = 0.035655

d_B (m) x_i	$\log_{10}(x_i)$	U_{BRel} (m/s) y_i	$\log_{10}(y_i)$	Predicted $\log_{10}(y_i)$	Residuals
6.88E-05	-4.162	2.8E-03	-2.553	-2.632	0.079
6.33E-05	-4.199	1.9E-03	-2.721	-2.735	0.014
1.01E-04	-3.997	7.9E-03	-2.102	-2.162	0.059
7.01E-05	-4.154	1.9E-03	-2.721	-2.609	-0.112
8.00E-05	-4.097	3.0E-03	-2.523	-2.446	-0.077
5.41E-05	-4.267	1.4E-03	-2.854	-2.929	0.075
5.27E-05	-4.278	1.0E-03	-3.000	-2.961	-0.039

Regression Statistics	
R Square	0.929
Standard Error	0.0844
Observations	7

	Coefficients	*S.E*	*Lower 95%*	*Upper 95%*
β1	9.203	1.4697	5.425	12.981
β2	2.843	0.3528	1.937	3.750

REFERENCES

Adkins M. (1997). Dissolved air flotation and the Canadian experience, *CIWEM International Conference on Dissolved Air Flotation Technology in Water Treatment-An Art or a Science*?, London, England, pp: 289-307.

American Water Works Association (1990). *Water Quality and Treatment, a Handbook of Community Water Supply*, F. W. Pontius (ed.), 4th. edition, McGraw-Hill Inc., New York.

American Water Works Association Research Foundation (1991). *Mixing in Coagulation and Flocculation*, A. Amirtharajah, M. M. Clark and R. R. Trussel (eds.), Denver, Co, USA.

Anderson M. A. and Rubin A. J. (1981). *Adsorption of Inorganics at Solid-Liquid Interfaces*, Ann Arbor Science Pupl., Inc., Ann Arbor, MI.

APHA, AWWA, WEF (1992). *Standard Methods*, 19th Edition, Washington, D.C.

Arora H., De Wolfe J. R., Lee R. and Grubb T. 1994. Evaluation of dissolved air flotation process for water clarification and sludge thickening, *IAWQ/IWSA/AWWA Joint Specialized Conference on Flotation Processes in Water and Sludge Treatment*, Conference Preprints, Orlando, Florida, pp: 115-127.

Baeyens J., I. Y. Mochtar, S. Liers, and H. De Wit. 1995. Plug flow dissolved air flotation, *Water Environment Research*, 67(7):1027-1035.

Bratby J. and Marais G. V. R. (1975). Dissolved air flotation: an evaluation of inter-relationship between process variables and their optimization for design, *Water SA*, 1(2):57-69

Bunker D. Q. Jr., J. K. Edzwald, J. Dahlquist, and L. Gillberg. 1994. Pretreatment considerations for dissolved air flotation: water type, coagulants, and flocculation, *IAWQ/IWSA/AWWA Joint Specialized Conference on Flotation Processes in Water and Sludge Treatment*, Conference Preprints, Orlando, Florida, pp: 35-44.

Camp T. R. (1955). Flocculation and flocculation basins, *Trans. American Soc. of Civil Eng.*, 120, 1-16.

Camp T. R. and Stein P.C. (1943). Velocity gradient and internal work in fluid motion, *Jour. Boston Soc. Civil Eng.*, 30(4):219-237.

Clift R., Grace J. and Weber M. (1978). *Bubbles, Drops and Particles*, Academic press, New York.

Chang R. (1981). *Physical Chemistry with Applications to Biological Systems*, 2nd edition, Macmillan Publication Co., New York.

Collins G. and Jameson G. (1976). Experiments on the flotation of fine particles: the influence of particle size and charge, *Chemical Eng. Sci.* , 31:985-991.

Collins G. L. and Jameson G. (1977). Double-layer effects in the flotation of fine particles, *Chemical Eng. Sci.* , 32:239-246.

Derjaguin B. V. and Landau L. (1941). Theory of stability of strongly charged lyophobic sols and of the adhesion of strongly charged particles in solutions of electrolytes, *Acta Physicochimical*, 14: 633-662.

Derjaguin B. V., Dunkin S. S. and Rulyov N. N. (1984). Kinetic theory of flotation of small particles, *Surface and Colloid Sciences*, 13:17-113.

DANTEC (1989). *Particle Dynamic Analyzer: Users Manual*, DANTEC.

Edzwald J. K. (1985). Cationic polyelectrolytes in water treatment, *Proceedings of the Engineering Foundation Conference on Flocculation, Sedimentation and Consolidation*, B. M. Moudgil and P. Somasundaran (eds.), *Amer. Inst. Chem. Engr.*, pp. 171-180.

Edzwald J. K. and Wingler B. J. (1990). Chemical and physical aspects of dissolved-air flotation for the removal of algae, *Aqua*, 39:24-35.

Edzwald J. K. and Malley J. P. (1990). *Removal of Humic Substances and Algae by Dissolved Air Flotation*, USEPA Research and Development Project Summary. EPA/600/S2-89/032.

Edzwald J. K., Malley J. and Yu C. (1990). A Conceptual model for dissolved air flotation in water treatment, *IWSA/IAWPRC joint Specialized Conference on Coagulation, Flocculation, Filtration, Sedimentation and Flotation*, Bernhardt H. and Ives K.(Editors), 9(1):141-150.

Edzwald J. K and Walsh J. P. (1992). *Dissolved Air Flotation: Laboratory and Pilot Plant Investigations*, AWWA Research Foundation, Denver, Co., USA

Edzwald J. K., Walsh J. P., Kaminski G. S. and Dunn H. J. (1992). Flocculation requirements for dissolved-air flotation, *AWWA*, 84(3):92-100.

Edzwald J. K. (1993). Algae, bubbles, coagulants, and dissolved-air flotation, *Wat. Sci. Tech.* 27(30):67-81.

Edzwald K. J., Bunker D. Q., Dahlquist J., Gillberge L. and Hedberg T. (1994a). Dissolved air flotation: pretreatment and comparison to sedimentation, *Proceedings of the 6th. International Gothenburge Symposium on Chemical Treatment*, Gothenburg, Sweden.

Edzwald J. K. (1995). Principles and applications of dissolved air flotation, *Wat. Sci. Tech.*, 31(3-4), 1-23.

Edzwald J. K. (1997). Contact zone modeling and the role of pretreatment in dissolved air flotation performance, *CIWEM International Conference on Dissolved Air Flotation Technology in Water Treatment-An Art or a Science*?, London, England, pp: 9-23.

Fawcett N. S. (1997). The hydraulics of flotation tanks: computational modeling, *CIWEM International Conference on Dissolved Air Flotation Technology in Water Treatment-An Art or a Science*?, London, England, pp: 51-71.

Flint L. R. and Howarth W. J. (1971). The collision efficiency of small particles with spherical air bubbles, *Chemical Eng. Sci.*, 26:1155-1168.

Finch J. A. and Dobby G. S. (1990). *Column Flotation*. Pergamon Press, Oxford.

Fukushi K., Tambo N. and Matsui Y. (1994). A kinetic model for dissolved air flotation in water and wastewater treatment, *Wat. Sci. Tech.*, 31(3-4): 54-68.

Gochin R. J. (1981). Flotation. *In: Solid-Liquid Separation*, 2nd edition, L. Svarovsk (ed), Butterworths.

Gregory J. (1969). The calculation of Hamaker constants, *Advances in Colloid and Interface Sci.*, 2:396-417.

Gregory R. and Zabel T. F. (1990). Sedimentation and flotation, In: *Water Quality and Treatment, AWWA*, 4th. edition, McGraw-Hill Inc., New York.

Gregory R. (1997). Summary of general development in DAF for water treatment since 1976, *CIWEM International Conference on Dissolved Air Flotation Technology in Water Treatment-An Art or a Science?*, London, England, pp: 1-87.

Gaudin A.M. (1957). *Flotation*, 2nd Edition, McGraw Hill Book Co., New York

Haarhoff J. and van Vuuren L (1994). Design parameters for dissolved air flotation in South Africa, *IAWQ/IWSA/AWWA Joint Specialized Conference on Flotation Processes in Water and Sludge Treatment*, Conference Preprints, Orlando, Florida, pp: 197-207.

Haarhoff J. and Steinbach S. (1997). Towards the maximal utilization of air in dissolved air flotation, *CIWEM International Conference on Dissolved Air Flotation Technology in Water Treatment-An Art or a Science*?,London, England, pp:25-34.

Henry J. and R. Gehr. (1981). *Dissolved Air Flotation for Primary and Secondary Clarification*, Canada Mortgage and Housing Corporation, Environment Canada.

Heinanen J., Jokela P. and Pettokanas J. (1992). Experimental studies on the kinetics of flotation, *Chemical Water and Wastewater Treatment* (H. H. Hahn and R. Klute, Editors), Springer Verlag, Berlin: 247-262.

Heinanen J. (1988). Use of dissolved-air flotation in potable water treatment in Finland, *Aqua Fennica* 18,2:113-123.

Himmelblau D. and Bischoff K. (1968). *Process Analysis and Simulation: Deterministic Systems*, Wiley, New York.

Hyde R. A., Miller D. G., Packham R. F. and Richards W. N. (1977). Water clarification by flotation, *AWWA*, 69(7) , pp. 369-374.

Janssens J. (1991). The application of dissolved air flotation in drinking water production, in particular for removing algae. *DVGW-Schrifrtenreiche Wasser.*, 67, Eschborn.

Johnson P.N. and Amirtharajah A. (1983). Ferric chloride and alum as single and dual coagulants, *AWWA*, 75(5), 232.

Johnson B. A., Gong B., Bellamy W. and Tran T. (1994). Pilot plant testing of dissolved air flotation for treating Boston's low-turbidity surface water supply, *IAWQ/IWSA/AWWA Joint Specialized Conference on Flotation Processes in Water and Sludge Treatment*, Conference Preprints, Orlando, Florida, pp: 55-66.

Kitchener J. A. and Gochin R. J. (1981). The mechanism of dissolved air flotation for potable water: Basic analysis and proposal, *Wat. Res.*, 15:585-590.

Kitchener J. A. (1984). The froth flotation process: Past, present and future - in brief. In: *The scientific basis of flotation*, K. J. Ives (ed.), NATO ASI Series, Martinas Nijhoff, Boston, USA, pp. 3-51.

Klute R., Langer S. and Pfeifer R. (1994). Optimization of coagulation processes prior to DAF, *IAWQ/IWSA/AWWA Joint Specialized Conference on Flotation Processes in Water and Sludge Treatment*, Conference Preprints, Orlando, Florida, pp:31-34.

Lading L. and Anderson K. (1988). A covariance processor for laser anemometry and particle sizing, *Proceedings of the 4th. International Symposium on Applications of Laser Anemometry to Fluid Mechanics*, Lisbon, Spain.

Letterman R. D. (1981). Flocculation, In: *Coagulation and Filtration: Back to the Basics, Proceedings AWWA Annual Conference*, St. Louis, Mo.

Levich V. G. (1962). *Physiochemical Hydrodynamics*, Prentice Hall, N. J.

Levenspiel O. (1972). *Chemical Reaction Engineering*, Second edition, John Wiley and Sons, Inc, N.Y.

Liers S., Baeyens J. and Mochtar I. (1996). Modeling dissolved air flotation, *Water Environment Research*, 68(6):1061-1075.

Longhurst S. J. and Graham N. J .D. (1987). Dissolved air flotation for potable water treatment: a survey of operational units in Great Britain, *Public Health Engineer*, 14(6), 71-76.

Malley J. P. (1988). *A Fundamental Study of Dissolved Air Flotation for Treatment of Low Turbidity Waters Containing Natural Organic Matter*, Ph.D. Thesis, University of Massachusetts, Amherst.

Malley J. P. and Edzwald J. K. (1991). Concepts of dissolved-air flotation for the treatment of drinking waters, *J. Water SRT-Aqua*. 40(1):7-17.

Mangravite F. J. et al. (1972). The microflotation of Silica, *Jour. of Colloid and Interface Science*, 39(2):357-366.

Mavros P. (1992). Technical note: validity and limitations of the closed-vessel analytical solution to the axial dispersion model, *Mineral Eng.*, 5(9): 1053-1060.

Mavros P. and A. Daniilidon (1993). Mixing in flotation columns: Part II. Liquid-phase residence time distribution studies, *Mineral Eng.*, 6(7):707-719.

Metcalf and Eddy, Inc. (1979). *Wastewater Engineering: Treatment, Disposal and Reuse*, 2nd edition, McGraw-Hill Book Co., New York.

Nickols D. (1997). The current status of dissolved air flotation in the USA. *CIWEM International Conference on Dissolved Air Flotation Technology in Water Treatment-An Art or a Science*?, London, England, pp: 308-319.

Ødegaard H. (1994). Optimization of flocculation/flotation in chemical wastewater treatment, *IAWQ/IWSA/AWWA Joint Specialized Conference on Flotation Processes in Water and Sludge Treatment*, Conference Preprints, Orlando, Florida, pp: 45-54.

O'Melia C. (1972). Coagulation and flocculation, Chapter 2, *Physiochemical Processes for Water Quality Control*, Weber W.J,Jr (author), John Wiley and Sons, New York.

O'Melia C. (1985). Particles, pretreatment and performance in water filtration, *Jour. Environ. Eng.* (ASCE), 111(6):874-890.

Reay D. and Ratcliff G. (1973). Removal of fine particles from water by dispersed air flotation, *Canadian Jour. Chem. Eng.* , 51:178-185.

Rubin A. J. and Johnson J. D. (1967). Effect of pH and ion and precipitate flotation systems, *Anal. Chem.*, 39:298-302.

Rubin A. J. (1968). Removal of trace metals by foam separation processes, *AWWA*, 60(7):832-846.

Rubin A. J. and Lackey S. C. (1969). Effect of coagulation on the microflotation of Bacillus Cereus, *AWWA*, 60(10):1156-1166.

Rubin A. J. and Lapp W. L. (1969). Foam separation of Lead III with Sodium Lauryl Sulfate, *Anal. chem.*, 41:1133-1135.

Rykaart E. M. and Haarhoof J. (1995). Behavior of air injection nozzles in dissolved air flotation, *Wat. Sci. Tech.*, 31(3-4):67-79.

Saffman M., Buchhave P. and Tanger H. (1984). Simultaneous Measurement of Size, Concentration and Velocity of Spherical Particles by a Laser Doppler Method, *Proceedings of the second International Symposium on Applications of Laser Anemometry to Fluid Mechanics*, Lisbon.

Shah Y. T., Kelkar B. G., Godbole S. P. and Deckwer W. D. (1982). Design parameters estimations for bubble column reactors, *AIChE Journal*, 28: 353-379.

Stumm W. and Morgan J. (1981). *Aquatic Chemistry*, Prentice Hall, N.J.

Stumm W. (1967). Metal ions in aqueous solutions, *Principles and applications of water chemistry*, J.V. Hunter and S.D. Faust (eds.), John Wiley and Sons, New York.

Sutherland K. (1948). Physical chemistry of flotation, Part XI: Kinetics of the flotation process, *Jour. Phys. chem.*, 52: 394-425.

Tambo N. and Matsui Y. (1986). A kinetic study of dissolved air flotation, *World Congress of Chem. Engr.*, Tokyo, Japan, pp: 200-203.

Tampo N. (1990). Optimization of flocculation in connection with various solid-liquid separation processes, In: *Chemical Water and Wastewater Treatment*, H.H. Hahn and R. Klute (eds.), Spring-Verlag Berlin Heidelberge, pp: 17-32.

Tylor G. (1953). Dispersion of soluble matter in solvent flowing slowly through a tube, *Proceedings of the Royal Society*, 219: 186-203.

Takahashi T., Miyahara T. and Mochizuki H. (1979). Fundamental study of bubble formation in dissolved air pressure flotation, *Journal of Chemical Eng. of Japan*, 12:275-280.

Tsukada T. et al. (1984). Computer simulations of deformation of moving drops and bubbles by use of finite element method, *Jour. of Chem. Engr. of Japan*, 17(3):246-251.

Valade M. T., Edzwald J. K., Tobiason J. E., Dahlquist J., Hedberge T. and Amato T. (1996). Pretreatment effects on particle removal by flotation and filtration, *AWWA*, 88(12):35-47.

van Craenebroek W., van den Bogart W. and Ceulemans J. (1993). The use of dissolved air flotation for the removal of algae-the antwerp experience, *Water Supply*, 11(3/4):123-133

Verwey E. J. and Overbeek J. (1948). *Theory of the Stability of Lyophobic Colloids*, Elesvier, Amsterdam.

Westertrep R., W. van Swaaij and A. Beenackers. (1984). *Chemical Reactor Design and Operation*, John Wiley and Sons, N.Y.

Yao K., Habibian M. T. and O'Melia C. R. (1971). Water and wastewater filtration: concepts and applications, *Envir. Sci. and Tech.* , 5:1105-1112.

Yuu S., Fukui Y. and Jotaki T. (1977). Collection of submicron particles by the H_2 bubbles, *Chem. Eng. Sci.*, 32: 1389-1396.

Zabel T.(1984). Flotation in water treatment, *The Scientific Basis of Flotation* (Ives K.J., Editor), NATO ASI Series, Martinus Nijhoff Publications, Boston, MA.

Zabel T. (1985). The advantages of dissolved air flotation for water treatment, *AWWA*, 77(5):42-46.